Aix*Marseille université
Initiative d'excellence

THÈSE DE DOCTORAT

Soutenue à Aix-Marseille Université
le 5 novembre 2020 par

Raúl BALDERRAMA
MARTíNEZ SOTOMAYOR

Développement de ligands de cuivre pour des applications thérapeutiques

Discipline

Sciences chimiques

École doctorale

ED 250 – Sciences chimiques de Marseille

Laboratoire/Partenaires de recherche

Institute des Sciences Moléculaires de Marseille UMR 7313 / Biosciences
Consejo Nacional de Ciencia y Tecnología (CONACyT)

Composition du jury

Peter FALLER	Rapporteur
Université Strasbourg	
Institut de Chimie UMR 7177	
María Amelia SANTOS	Rapporteuse
Universidade de Lisboa	
Centro de Química Estrutural	
Instituto Superior Técnico	
Sara LACERDA	
Université d'Orléans	Examinatrice
Centre de Biophysique Moléculaire	
CNRS-UPR 4301	
Karine ALVAREZ	Présidente du jury
Aix-Marseille Université	et examinatrice
Laboratoire Architecture et Fonction	
des Macromolécules Biologiques	
UMR 7257, Campus de Luminy	
Olga IRANZO	
Aix-Marseille Université	Directrice de thèse
Institute des Sciences Moléculaires	
de Marseille UMR 7313	

Contents

Acknowledgements

Résumé

Le cuivre (Cu) est un métal endogène et redox actif présent dans plusieurs protéines et enzymes essentielles à la vie et joue un rôle important dans différents processus biologiques. Cependant, son activité redox rend également le Cu potentiellement toxique car il peut favoriser la formation d'espèces réactives de l'oxygène (ROS). Ce comportement à double tranchant intéresse les chercheurs depuis longtemps et son exploitation est cruciale pour développer des complexes de Cu aux propriétés biologiques, catalytiques, diagnostiques et thérapeutiques uniques. Dans ce travail de thèse, différents ligands pour la coordination du Cu ont été conçus et explorés dans deux contextes différents : le cancer et la maladie d'Alzheimer (MA). La première partie de cette thèse est consacrée à approfondir les connaissances relatives aux effets cytotoxiques produits par les complexes de Cu(II) (C1, C2) de deux ligands (L1, L2). Bien que les complexes aient montré de faibles interactions avec l'ADN, des études *in vitro* réalisées sur des lignées cellulaires normales (IMR-90, HUVEC) et cancéreuses (A2780, MCF-7) ont indiqué que C1 et C2 internalisaient les cellules et favorisaient la formation de ROS. Bien que les effets cytotoxiques n'aient pas été détectés dans les cellules MCF-7, ceux-ci étaient plus élevés dans A2780 que dans les cellules normales. L1 et L2 ont été modifiés afin d'améliorer la cytotoxicité. La deuxième partie de la thèse évalue les capacités de chélation du Cu de L1 et L2 en tant qu'agents thérapeutiques potentiels pour la MA. Les données ont montré que L1 peut arrêter efficacement la production de ROS catalysée par Cu(I)/Cu(II) en présence et en l'absence de peptide Aβ16 et de zinc. Les données suggèrent que le rapport L1 : Cu joue un rôle important dans l'efficacité de L1 pour arrêter la production de ROS. L1 a été modifié avec succès sans altérer ses propriétés de chélation du Cu pour fournir une perméabilité à la barrière hémato-encéphalique.

Mots clés : chimie médicinale inorganique, cancer, maladie d'Alzheimer, complexes métalliques, cuivre, peptides, espèces réactives de l'oxygène

Abstract

Copper (Cu) is a versatile redox active endogenous metal that is present in many proteins and enzymes critical for life and plays important roles in different biological processes. However, its redox activity also renders Cu potentially toxic because it can promote the formation of reactive oxygen species (ROS). This double-edged sword behavior has interested researchers for long time and its harnessing is crucial to develop Cu complexes with unique biological, catalytic, diagnostic and therapeutic properties. In this Ph.D. thesis different ligands for Cu coordination have been designed and explored in two different contexts: cancer and Alzheimer disease (AD). The first part of this thesis is devoted to providing more insights into the cytotoxic effects produced by the Cu(II) complexes (C1, C2) of two ligands (L1, L2). The complexes showed weak interactions with DNA, but *in vitro* studies performed in normal (IMR-90, HUVEC) and cancer cell lines (A2780, MCF-7) indicated that C1 and C2 internalize into the cells and promote the production of ROS. While cytotoxic effects were not detected in MCF-7 cells, in line with very low internalization, they were higher in A2780 than in normal cells. L1 and L2 were further modified to improve cytotoxicity. The second part of the thesis evaluates the Cu chelating abilities of L1 and L2 as potential therapeutic agents for AD. Data showed that L1 can arrest efficiently the generation of ROS catalyzed by Cu(I)/Cu(II) in presence and absence of Aß16 peptide and zinc. The presence of excess of L1 lessened this effect but it was counterbalanced by the co-presence of Zn. A mechanism that involves the redox reaction between Cu(II)L1 and Cu(I)(L1)$_2$ is proposed to explain this behavior. L1 was successfully modified, without altering its Cu chelating properties and ROS arresting capabilities, to attain blood-brain-barrier permeability.

Keywords: medicinal inorganic chemistry, cancer, Alzheimer's disease, metal complexes, copper, peptides, reactive oxygen species

Preface

The work presented in this thesis is related to different ligands designed for Cu coordination and explored in two different contexts: Cancer and Alzheimer's disease. The first two chapters are focus specifically on the cancer context, while the two subsequent chapters are related to Alzheimer's disease (AD).

The first chapter aims to collect existing literature regarding the efforts of the medicinal inorganic chemistry community in cancer therapy, providing an overview of these efforts through the early years of the field and concluding with the most representative advances in terms of Cu(II) complexes of the last decades. Lastly, it concludes by describing the thesis objectives relative to this topic.

The second chapter comprises all the work related to the investigation of the anticancer properties of two Cu(II) complexes developed and characterized in the group (C1 and C2). It includes the studies of their interactions with *ct*-DNA, their internalization capabilities and their cytotoxic activities exhibited in two human cancer cell lines in comparison with two normal cell lines. It also discusses these results and their relationship with the capabilities of these Cu(II) complexes to generate intracellular reactive oxygen species (ROS). Subsequently, the chapter describes the modification of one ligand and the limitations encountered regarding its Cu(II) complexation. This chapter ends by mentioning the conclusions and final remarks on the studies.

Chapter 3 introduces the topic of AD. It opens describing this neurodegenerative disease, its main histopathological criteria, symptoms and risk factors. Later, it describes the amyloid cascade hypothesis and the link between Cu and other metal ions with the pathogenesis and progression of AD. Afterwards, it reviews the state of art in Cu chelation therapy and concludes with the objectives of the study in this topic.

The fourth chapter presents the work devoted to explore the potential of a histidine containing phenanthroline based ligand (L1) as Cu targeting candidate for AD therapy. This work was carried out in collaboration with Dr. Charlène

Esmieu and Dr. Christelle Hureau from the *Laboratoire de Chimie de Coordination* (LCC) in Toulouse. Herein, it is described the results obtained regarding the abilities of L1 to stop the production of ROS and their potential to remove Cu(II) and Cu(I) from the harmful complex CuAβ, both in the absence and in the presence of Zn(II). The selectivity of L1 towards Cu ions was studied through the determination of the affinity constants of Cu(II), Cu(I) and Zn(II) to L1. This chapter also explores the effect of using excess of L1 versus Cu In the arrest of ROS production, and discusses the potential mechanism responsible for the observed effect. Chapter 4 also includes the design, synthesis and characterization of L1AB, a ligand that merges L1 with a peptide sequence able to access the central nervous system. Its Cu(II) chelation properties and ROS arresting capabilities in presence of Aβ peptide and Zn(II) are reported. Lastly, this chapter ends with the conclusions relative to this part of the work.

Chapter 5 critically relates the two different approaches of this work to provide a general conclusion considering the key aspects of each topic.

The last chapter describes the experimental procedures and methods used in this work.

Abbreviations & symbols

8HQ	8-hydroxyquinoline
A	Absorbance
A2780	Human ovarian cancer cells
aa	Amino acid
Aβ	Amyloid-beta peptide
ACh	Acetylcholine
AChE	Acetylcholinesterase
ACN	Acetonitrile
AD	Alzheimer's disease
API	Atmospheric pressure ionization
APP	Amyloid precursor protein
AscH$^-$	Ascorbic acid
ATCUN	Amino-terminal Cu(II)- and Ni(II)- binding
BACE-1	Beta-site APP cleaving enzyme 1
BBB	Blood-brain-barrier
Boc	Tert-butyloxycarbonyl
ca.	Circa
CDCl$_3$	Deuterated chloroform
CHCl$_3$	Chloroform
cm	Centimeters
CNS	Central nervous system
CQ	Clioquinol
CR	Congo red
ct-**DNA**	*calf Thymus* DNA
Cu(I)	Cuprous ion
Cu(II)	Cupric ion
d	Doublet
DCF	Dichlorofluorescein
DCFDA	Dichlorofluorescin diacetate
DCM	Dichloromethane
DFP	Defiprone
DIEA	N,N-Diisopropylethyl amine
DMEM	Dulbecco's modified Eagle's medium
DMF	Dimethylformamide
DMSO	Dimethylsulphoxide
DNP	Donepezil
ε	Extinction coefficient
E$_{1/2}$	Half-wave potential
EBr	Ethidium bromide
EDC	1-ethyl-3-(3-dimethylaminopropyl)carbodiimide
EDTA	Ethylenediamine tetra-acetic acid

E_{pa}	Anodic peak potential
E_{pc}	Cathodic peak potential
EPR	Electron Paramagnetic resonance
equiv.	Molar equivalents
ESI-MS	Electrospray ionization mass spectrometry
ET3N	Triethylamine
EtOH	Ethanol
FBS	Fetal bovine serum
FDA	US Food and Drug Administration
Fmoc	Fluorenylmethyloxycarbonyl chloride
GSH	Glutathione
HBTU	Hexafluorophosphate benzotriazole tetramethyl uronium
HEPES	4-(2-hydroxyethyl)-1-piperazineethanesulfonic acid
HPLC	High performance liquid chromatography
HSA	Human serum albumin
HUVEC	human umbilical vein endothelial cells
IC_{50}	Concentration of an inhibitor where the response is reduced by half
ICP-MS	Coupled induced plasma mass spectrometry
IMR-90	human lung fibroblast
J	Coupling constant
K	Kelvin
K_b	Binding constant
$K_{M-L,app}$	Apparent affinity constant metal to ligand
$K_{M-L,cond}$	Conditional affinity constant metal to ligand
K_{sv}	Stern-Volmer quenching constant
λ	Wavelength
ℓ	Path length
L:M	Ligand per metal ratio
M	Molar
m/z	Mass per charge ratio
MAO	Monoamine oxidase
MBHA	4-Methylbenzhydrylamine hydrochloride
MCF-7	Human breast cancer cells
MeOH	Methanol
MT	Metallothionein
MTT	3-(4,5-dimethylthiazol-2-yl)-2,5-diphenyltetrazolium bromide
N	Asparagine or nitrogen
NFTs	Neurofibrillary tangles
nm	Nanometers
NMP	N-Methyl-2-pyrrolidone
NMR	Nuclear magnetic resonance
NOESY	Nuclear Overhauser effect spectroscopy
PBS++	Phosphate buffer saline containing calcium and magnesium
PET	Positron emission tomography

pH	Potential of hydrogen
Phen	Phenanthroline
PyBOP	Benzotriazol-1-yl-oxytripyrrolidinophosphonium hexafluorophosphate
RAGE	Receptor for advanced glycation endproducts
ROS	Reactive oxygen species
R_t	Retention time
RT	Room temperature 25° C
s	Singlet
SMC	Subjective memory complaint
SPECT	Single photon emission computed tomography
SPPS	Solid phase peptide synthesis
SPs	Senile plaques
t	Time
T	Temperature
TAC	Tacrine
TFA	Trifluoroacetic acid
ThT	Thioflavin-T
TIS	Triisopropyl silane
TLC	Thin layer chromatography
TRIS	Trisaminomethane
Trt	Trityl
UV-vis	Ultraviolet visible spectroscopy
V	Volts
📖	Pages containing bibliographic references

Amino Acids Abbreviations

Ala (A)	Alanine
Arg (R)	Arginine
Asn (N)	Asparagine
Asp (D)	Aspartic acid
Glu (E)	Glutamic acid
Gln (Q)	Glutamine
Gly (G)	Glycine
His (H)	Histidine
Ile (I)	Isoleucine
Leu (L)	Leucine
Met (M)	Methionine
Phe (F)	Phenylalanine
Ser (S)	Serine
Tyr (Y)	Tyrosine
Val (V)	Valine

CHAPTER 1.

Cancer & Bioinorganic Chemistry

1.1. Metals in life.

Metal ions are always present in biological systems playing important roles in structure, catalysis and metabolic processes including cellular replication, signaling pathways, respiration and transport.[1] Metal ions such as sodium (Na), potassium (K), copper (Cu) and iron (Fe), among others (**Figure 1.1**) are defined nowadays as bio-metals and their application to medicinal purposes is described by the interdisciplinary fields of bioinorganic chemistry or biological inorganic chemistry. Both fields comprehend the knowledge in biochemistry, inorganic chemistry, coordination chemistry, molecular and structural biology, environment chemistry, physiology, toxicology, pharmacy, medicine and more.[2]

Figure 1.1. Reduced form of the Periodic Table of the Elements indicating the essential d metals for life.

1.2. Bioinorganic chemistry in medicine.

The Medicinal inorganic chemistry is still considered a young field, but many ancient civilizations (Egypt, India and China) have proof the use of metal ions in mixtures with medicinal intentions.[2–4] In the last decades, especially after the discovery of cisplatin (see Section 1.2.1) the field of the bioinorganic chemistry has shown a notable potential for the design of therapeutic and diagnostic agents.[5] The introduction of metal ions in molecules allows a wide range of reactivities not accessible otherwise. These reactivities can be modulated by the properties of both the ligand and the metal ion. The identity of the metal ion, its oxidation state, the

type and number of donor atoms in the ligand, the coordination geometry and other intrinsic characteristics of the metal ion are determinant in the activity and behavior of the final metal complex (**Figure 1.2**).[6,7]
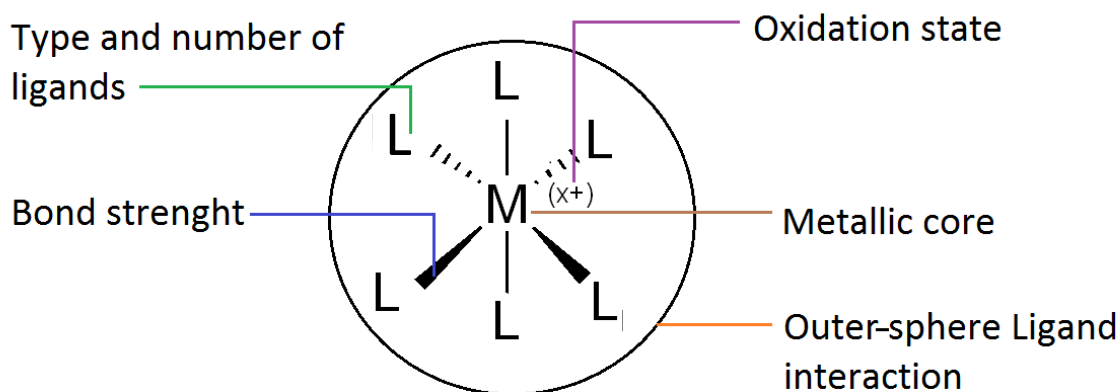
Figure 1.2. Tunable characteristics in the design of a metallodrug.

In the last decades[5] many metal-containing drugs have been designed, developed and studied (**Figure 1.3**). Salvarsan is one of the first metal-based antimicrobial agents developed described by Paul Ehrlich. In 1920 Ehrlich published the potential of the 3-amino-4-hydroxyphenyl-arsenic(III) for the treatment of syphilis.[8] Since then, this arsenic-based drug was widely used in humans until its replacement by penicillin after the World War II.[9]
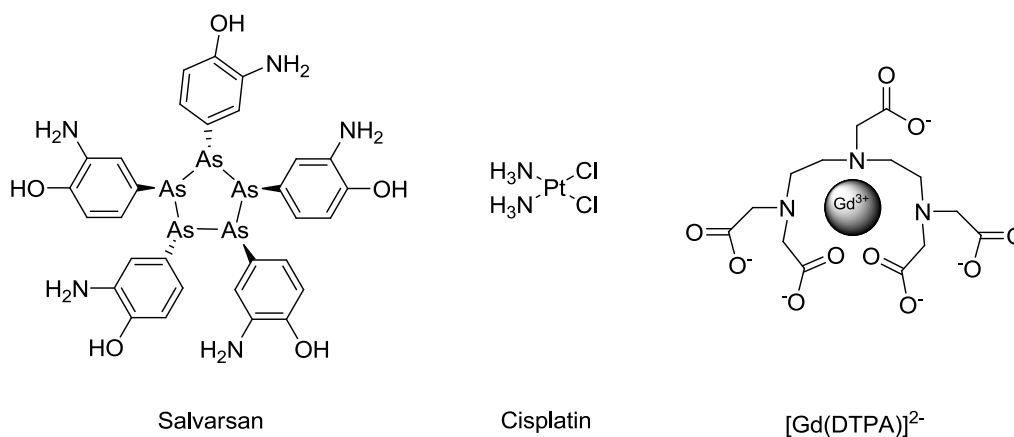
Figure 1.3. Metal-based drugs approved by FDA

The diethylenetriaminepentaacetic acid [H_5DTPA] is a metal chelator used complexed with Gd^{3+} as an injectable macrocycle contrast agent [$Gd(DTPA)$]$^{2-}$ for magnetic resonance imaging scans (MRI). It was approved by the US Food and Drug Administration (FDA) in 1988 and its use as a radiopharmaceutical in imaging modalities such as single photon emission computed tomography (SPECT) and positron emission tomography (PET) has paved the way to theranostics agents.[10]

Particularly, the field of metal-based anticancer drugs, is one of the most successful domains in bioinorganic chemistry: nowadays, about 50 % of cancer chemotherapy agents in use are metal-based drugs.[11]

1.2.1. Cancer and the potential of platinum-based compounds in chemotherapy.

According to estimates from the World Health Organization (WHO) in 2015, cancer is the first or second leading cause of death (before 70 years old) in 91 of 172 countries.[12] Additionally, it is expected that by 2030, the number of cancer cases reaches up to 21.6 million, 21.6 % higher than the reported cases for 2012.[13]

The cis-diammine-dichloroplatinum(II), best-known as cisplatin (**Figure 1.3**), was synthesized in 1845 by Michel Peyrone but it was not until 1960 when Rosenberg discovered its anticancer properties. Two decades later, in 1978, the FDA approved its use to treat cancer. Since then, the Pt^{2+} squared planar complex has been one of the most successful metal-based antitumor drugs.[14]

After the enormous impact of cisplatin, huge efforts were made to understand the mechanism of action of the drug. Studies indicate that cisplatin enter the cells by passive diffusion (**Figure 1.4**), and the uptake is non-saturable and concentration dependent. Nevertheless, evidence also suggest that the copper transporter 1 (CTR1) (a transmembrane protein involved in Cu homeostasis) plays also an important role in the uptake of cisplatin in ovarian carcinoma cells.[15] Once inside the cell, where the chloride concentration decreases from 100 mM to 4-6 mM, the complex hydrolyzes into the active mono-aqua [$Pt(NH_3)_2Cl(H_2O)$]$^+$ and di-aqua [$Pt(NH_3)_2(H_2O)_2$]$^{2+}$ complexes.[16] These complexes can react with the

nucleophilic centers on purine bases of DNA, mainly with the N7 sites of guanosine, leading to the formation of cross-links between these nucleotides.[17] The distortion caused by Pt triggers the signal transduction pathways that ultimately will lead to apoptosis. Additionally, these complexes bind to different nucleophilic species in the cytoplasm catalyzing the formation of reactive oxygen species (ROS) causing oxidative stress.[18]
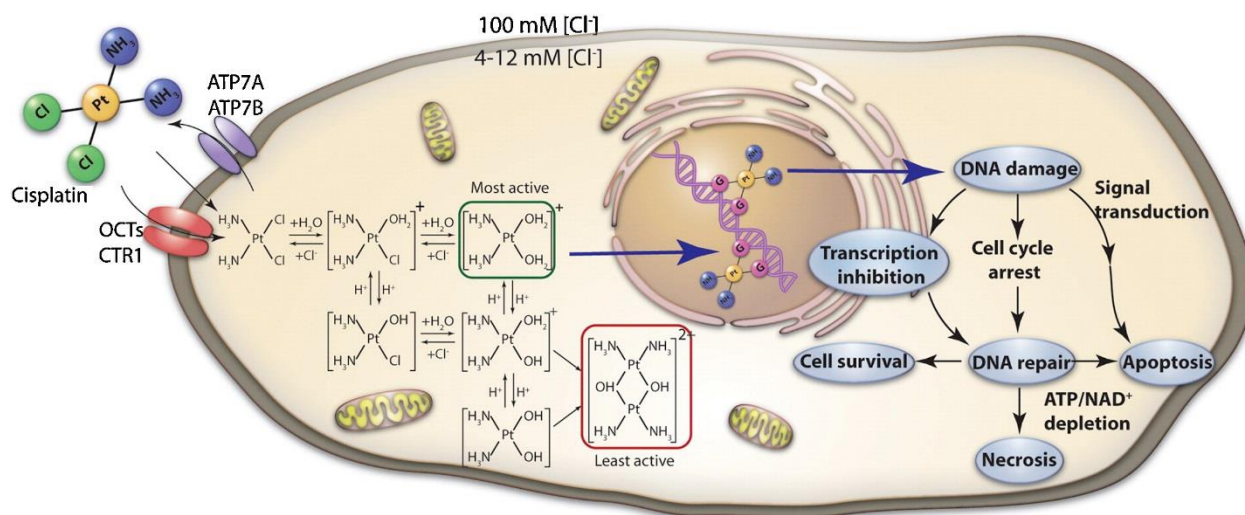
Figure 1.4.The mechanism of action of cisplatin. Figure from ref 19.

Unfortunately, cisplatin causes many side effects such as hair loss, nauseas and vomit, it is nephro-, neuro- and ototoxic.[15,20] Peripheral neurotoxicity is the most important dose-limiting issue linked to cisplatin.[21] Data suggest that cisplatin kills cancer cells but also peripheral neurons.[22] The symptoms and signs of peripheral neurotoxicity include the loss of taste, of position sense, loss of vibration sense, tingling, paraesthesia, weakness and tremor.[23–25]

To overcome the drawbacks of cisplatin a new generation of platinum-based compounds appeared: among the new compounds the oxaliplatin, carboplatin and nedaplatin (**Figure 1.5**), that exhibit same potential as anticancer agents.[6] Carboplatin is considered to be less neurotoxic than cisplatin.[26]

Carboplatin   Oxaliplatin   Nedaplatin
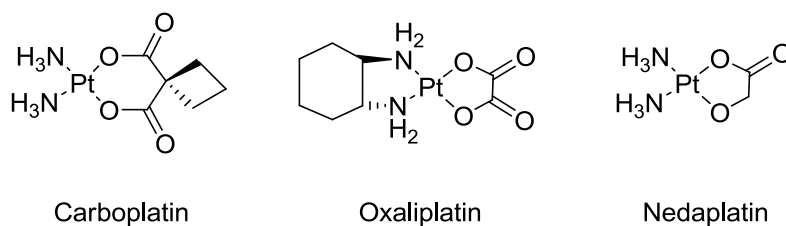
Figure 1.5. Second generation Platinum-based anticancer agents.

Although cisplatin and its analogs are highly effective in the treatment of many different tumors and nowadays an estimated of 50 - 70 % of cancer therapies involves Pt metallodrugs[27] the toxicity of the platinum-based drugs persist limiting the dosage. Evidence has shown that there is still no effective strategy for the regulation of the neurotoxicity and other side effects induced by these platinum-based agents.[28] Consequently, new strategies to overcome the high toxicity of the platinum-based drugs are needed.

1.2.2. Copper as an alternative for platinum-based anticancer agents.

Recently, the investigation of copper complexes with medicinal properties has increased considerably.[6] Cu is an endogenous and essential metal ion, present in a huge number of proteins and enzymes, and plays a crucial role in many biological processes such as angiogenesis, response to hypoxia and neuromodulation. The essentiality of Cu for animals and humans has been known for nearly a century.[29] In fact, Cu concentrations are well regulated by different mechanisms such as ceruloplasmin and albumin in the liver to regulate blood levels and also copper transporter proteins (CTR1 and Cu ATP7A/B).[30] In addition Cu acts as a cofactor of many enzymes involved in energy metabolism, melanin (tyrosinase) synthesis, dopamine synthesis (dopamine-β-hydroxylase), cross-linking of collagen and elastin (lysyl oxidase).[29] Nutritional copper deficit gives rise to anemia and different neuropathies.[31] It has been associated with Parkinson's disease, Huntington's disease and Alzheimer's disease.[31,32]

Cu has interesting and versatile properties that makes it a potential alternative to overcome the limitations of other metal cores in metallodrugs under the assumption that endogenous metals may be less toxic.[4,6,33,34] Copper can form

a wide variety of coordination complexes with mainly oxidation states Cu(I) and Cu(II).[35] Cu(I) complexes show, in general, a tetrahedral geometry by the coordination of four species. For the case of Cu(II) complexes the coordination can involve from four to six species: i) the four-coordinate square-planar (SP-4), ii) the five-coordinate trigonal bipyramidal (TBPY-5) and square-pyramidal (SPY-5), and the iii) six-coordinate octahedral (OC-6) geometry. Cu is a redox-active metal mainly in the form of the couple Cu(II)/Cu(I). If it is not complexed (free Cu) it causes oxidative damage in cells due to its potential to catalyze the formation of reactive oxygen species (ROS).[31]

Overall, Cu has proven its great potential in the medicinal inorganic chemistry encouraging the design and development of many copper-based drugs aimed against a wide spectrum of diseases.[6,7,36–40]

1.2.2.1. Advances in copper-based anticancer agents.

Regarding cancer chemotherapy, copper complexes hold the capability to catalyze the production of ROS causing damage to cells.[41] In terms of chemo-selectivity, the use of Cu to do redox chemistry inside tumor cells is advantageous since cancer cells present most likely a reductive environment. This is due to the increased rate of proliferation compared to normal cells, causing a dramatic increase on the glucose uptake. This feature produces a shift in the metabolism known as the "Warburg effect".[42] The metabolism of glucose is essential for sustaining all mammalian life, the final products are lactate, or over the full oxidation of glucose, CO_2. During the 1920's Otto Warburg established that in malignant cells the uptake of glucose is dramatically increased, and lactate is produced even in the presence of oxygen. Elevated glucose metabolism slightly decreases the pH in the intracellular environment due to lactate secretion. This aerobic fermentation is one of the signatures of cancer.[43]

The reductive environment found into cancer cells can promote the reduction of Cu(II) to Cu(I) facilitating the production of ROS and inducing cell death.[44] These mechanisms are possible due to the biologically accessible Cu(II)/Cu(I) redox cycling. However, this important feature could represent also a

drawback for the copper complexes if the ligands cannot stabilize both oxidation states and avoid the destruction of the copper complexes. In this regard, earlier this year, it has been reported that the glutathione (GSH)/metallothionein (MT) system represents an important threat for Cu complexes aimed to do redox chemistry inside cells.[44] GSH and MTs are two abundant Cu(I) chelators, they can bind Cu(I) with log K values around 17 and 20 respectively[45,46] and they can found intracellularly in the nucleus and cytosol.[47–49] Specifically MTs compromises Cu-based anti-cancer agents effectiveness due to their role in metal ions homeostasis[50] and their reported overexpression in some cancer cell lines.[51–53]

Regardless, in the last decades, copper-based complexes have shown great potential as an alternative for Pt-based anticancer agents and the field has been well reviewed by different research groups[6,38,39,54]

Herein we provide an overview of the different families of copper complexes designed for putative application in cancer treatment. Particularly, the review of Santini *et al.*[6] highlights the large number of family ligands that have been designed to develop Cu complexes with putative anticancer properties (**Figure 1.6**).

Families
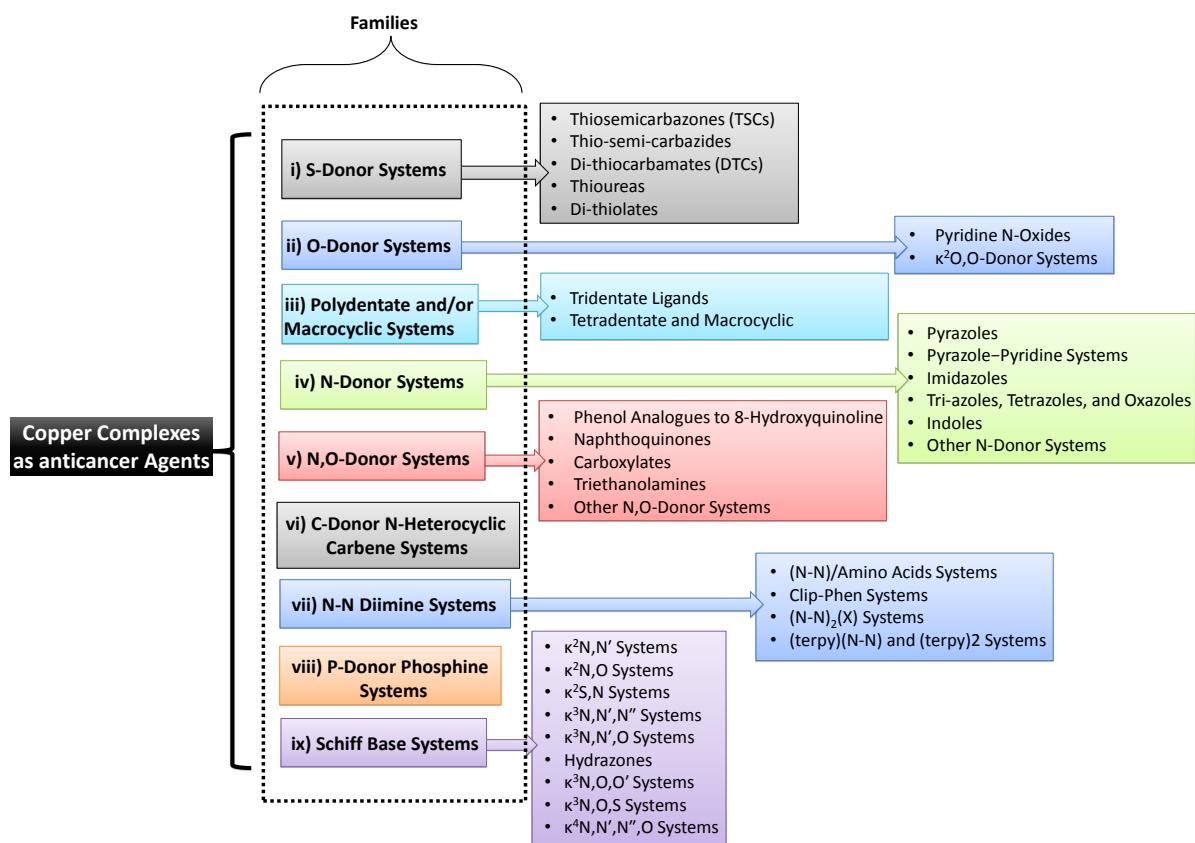
Figure 1.6. Classification of copper complexes as anticancer agents proposed by Santini *et al.*[6]

Some recent promising examples of copper complexes with efficacy against different types of cancer are shown in **Figure 1.7**. The thiosemicarbazone Cu(II) complex (**1**) exhibited 95% tumor growth inhibition on human colon carcinoma cells (HCT116)[55] Carter *et al.* reported the activity in cell culture and animal models of the two bis(thiosemicarbazonato) copper complexes (**2**) and (**3**)[56] showing a 70 % tumor growth reduction on male transgenic adenocarcinoma of the mouse prostate (TRAMP). Moreover, the biotin- and nano- conjugated complex (**4**), exhibited high toxicity against human cervical cancer cells (HeLa), *in vivo* studies showed 3.8-fold reduction in tumor volume.[57] Sathisha *et al.* reported the synthesis and cytotoxic activities of the Cu(II) complexes (**5**) and (**6**).[58] The thiocarbohydrazone complexes presented promising cytotoxic activity against Ehrlich Ascites Carcinoma cells (EAC) and additionally, inhibitory effects against bacterial and fungal strains. Another example is the complex (**7**), which induces apoptotic cell death *in vitro* on human leukemia cell lines; *in vivo* studies showed

that the compound can inhibit 92.4 % of tumor growth after 12 mg kg^{-1} treatment on male nude mice.[59]
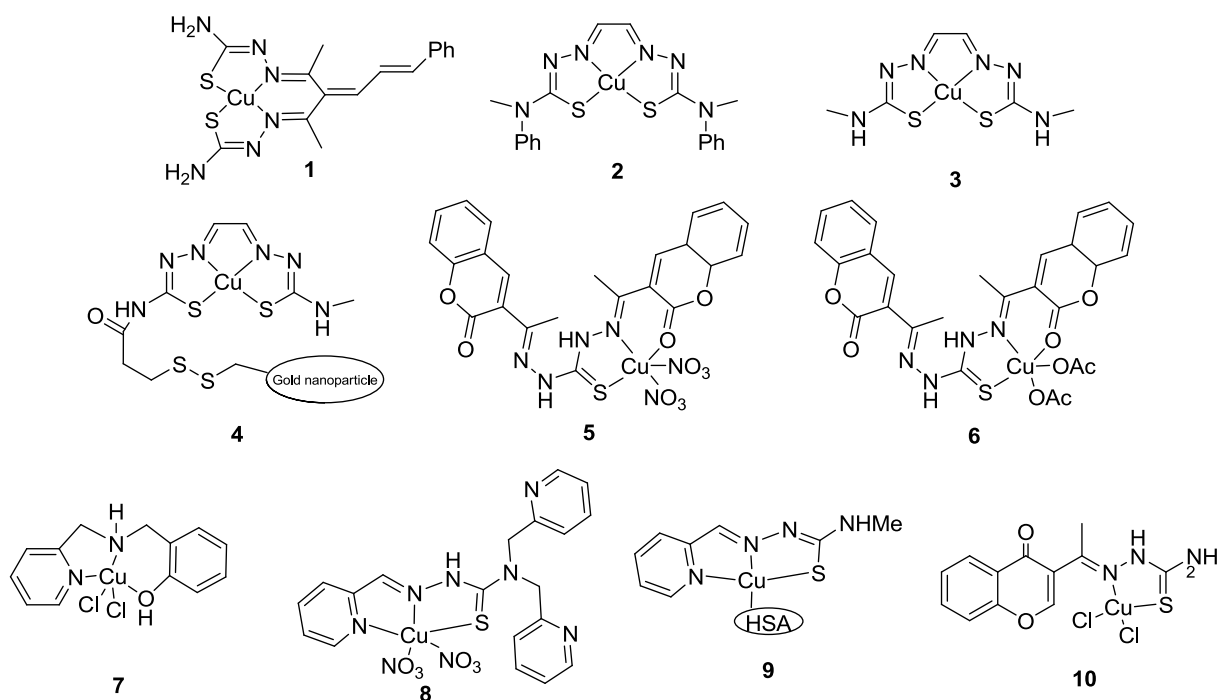
Figure 1.7. Some remarkable examples of Cu complexes with *in vivo* cytotoxicity activity in mice.[44-52]

Hancock *et al.*[60] also reported a thiosemicarbazone (**8**) (**Figure 1.7**) able to induce cell death by increasing the oxidative stress levels on mouse melanoma cells (B16-F10) and showed 87 % inhibition of growth tumor. A recent study by Qi *et al.* indicated that complex (**9**) is cytotoxic on human leukemia cells (HL-60), reflecting an increased selectivity and capacity of inhibiting tumor growth compared to its non-bound to serum albumin (HSA) analogue.[61] Another example of active copper complexes is the 3-formylchromone derivate (**10**), which exhibits significant reduction of tumor growth on human pancreatic cancer cells (COLO 357) tested on female nude mice.[62]

Elesclomol (N-malonyl-bis(N'-methyl-N'-thiobenzoylhydrazide) is a chemotherapeutic agent (mitochondria-targeted) that exhibits anticancer activity *in vitro* against a wide range of cancer cell types such as lung, melanoma and leukemia (**Figure 1.8**). In addition, enhances the potency of other anticancer

agents in human tumor models *in vivo,* therefore exhibiting encouraging therapeutic potential.[63–68] This prodrug has been examined in a phase II trial against ovarian, fallopian, and peritoneal cancers.[69] Elesclomol binds to Cu(II) in the serum and once inside the cancer cell, Cu(II) is reduced to Cu(I) inducing DNA cleavage and elevate levels of ROS production, exhausting the tumor cell antioxidant capacity. This results in the induction of the mitochondrial apoptosis.[70–72]
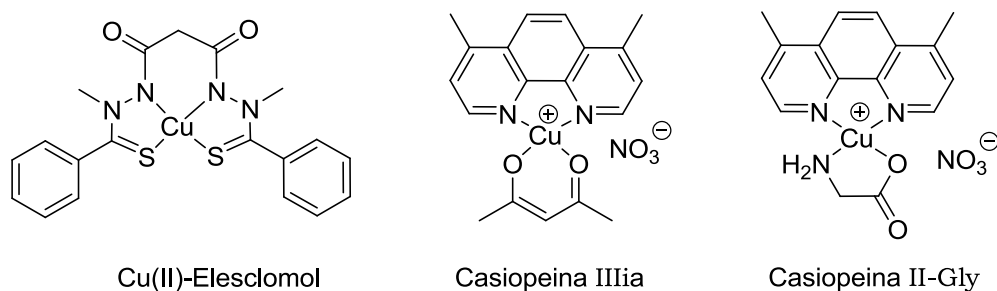
Figure 1.8. Copper complexes studied in clinical trials.

Another representative example is Casiopeina IIIia (**Figure 1.8**). A complex that belongs to Casiopeinas, a family of copper complexes developed by Ruiz-Azuara *et al.*[73–78] This type of complexes have the formula $[Cu(N-N)(N-O)]^+$ and $[Cu(N-N)(O-O)]^+$, where N−N is an aromatic substituted diamine (Phen, bipyridine or extended planar heterocyclic bases), N−O is an α-L-amino acidato and O−O is acetylacetonate or salicyaldehydate. Many amino acids such as L-glycine, L-alanine, L-valine, L-leucine, L-isoleucine, L-proline, L-phenylalanine, L-tryptophan have been tested. In general these complexes are able to bind and cleave DNA through the generation of ROS and the effect in biological activity of exchanging the amino acid unit is weaker compared to the effect of changing the aromatic substituted diamine[6,77] Casiopeina IIIia has entered into a phase I clinical trial against acute myeloid leukemia.[79] This agent induces DNA fragmentation and base oxidation, indicating that its mode of action involves ROS generation. In 2016, the group of Ruiz-Azuara and co-workers used transcriptomic approaches and pathway analysis tools to proof that the analogue, Casiopeina II-

gly, enhances the metabolism of metal ions and inhibits the migration and proliferation of HeLa cells. It is currently studied in a phase I trial.[80]

These Cu complexes encouraged the current investigations in this domain with the goal to overcome the challenges in the anticancer therapy by the rational design and development of new Cu ligands.

1.3. Objectives of the study.

One of the main purposes of this thesis is the study of the anticancer properties of the copper(II) complexes developed previously in the group[81] in order to better understand and modulate their interactions with biological systems.

The following chapter describes the work done devoted to the achievement of the following objectives:

i)   Study the interactions and intercalation abilities of the complexes **C1** and **C2** with *ct*-DNA.

ii)   Reevaluate the cytotoxic activity of these complexes in human cancer cells A2780 and MCF-7 and explore their cytotoxicity in normal cells IMR-90 and HUVEC.

iii) Explore the capabilities of these complexes to internalize into these cancer and normal cell lines.

iv)   Evaluate the capabilities of the complexes to induce intracellular ROS production in these cancer and normal cells.

v)   Redesign and synthesize novel ligands and characterize their Cu(II) complexes.

vi)   Evaluate the redox and biological activities of the new Cu(II) complexes.

1.4. Bibliography.

(1)   Sigel, H.; Sigel, A. The Bio-Relevant Metals of the Periodic Table of the Elements. *Z. Für Naturforschung B* **2019**, *74* (6), 461–471. https://doi.org/10.1515/znb-2019-0056.

(2)   Magner, L. N.; Kim, O. J. *A History of Medicine*; CRC Press, 2017.

(3)   Orvig, C.; Abrams, M. J. Medicinal Inorganic Chemistry: Introduction. *Chem. Rev.* **1999**, *99* (9), 2201–2204. https://doi.org/10.1021/cr980419w.

(4)   Metzler-Nolte, N.; Kraatz, H. B. *Concepts and Models in Bioinorganic Chemistry*; Wiley-Vch New York, 2006.

(5)   Mjos, K. D.; Orvig, C. Metallodrugs in Medicinal Inorganic Chemistry. *Chem. Rev.* **2014**, *114* (8), 4540–4563. https://doi.org/10.1021/cr400460s.

(6)   Santini, C.; Pellei, M.; Gandin, V.; Porchia, M.; Tisato, F.; Marzano, C. Advances in Copper Complexes as Anticancer Agents. *Chem. Rev.* **2014**, *114* (1), 815–862. https://doi.org/10.1021/cr400135x.

(7)   Brissos, R. F.; Caubet, A.; Gamez, P. Possible DNA-Interacting Pathways for Metal-Based Compounds Exemplified with Copper Coordination Compounds: Possible DNA-Interacting Pathways for Metal-Based Compounds. *Eur. J. Inorg. Chem.* **2015**, *2015* (16), 2633–2645. https://doi.org/10.1002/ejic.201500175.

(8)   Ehrlich, P.; Bertheim, A. Über das salzsaure 3.3′-Diamino-4.4′-dioxy-arsenobenzol und seine nächsten Verwandten. *Berichte Dtsch. Chem. Ges.* **1912**, *45* (1), 756–766. https://doi.org/10.1002/cber.191204501110.

(9)   *The Practice of Medicinal Chemistry*, 3rd ed.; Wermuth, C. G., Ed.; Elsevier/Academic Pr: Amsterdam, 2008.

(10)   Heffern, M. C.; Matosziuk, L. M.; Meade, T. J. Lanthanide Probes for Bioresponsive Imaging. *Chem. Rev.* **2014**, *114* (8), 4496–4539. https://doi.org/10.1021/cr400477t.

(11)   Hannon, M. J. Metal-Based Anticancer Drugs: From a Past Anchored in Platinum Chemistry to a Post-Genomic Future of Diverse Chemistry and Biology. *Pure Appl. Chem.* **2007**, *79* (12), 2243–2261. https://doi.org/10.1351/pac200779122243.

(12)   GBD 2015 Mortality and Causes of Death Collaborators. Global, Regional, and National Life Expectancy, All-Cause Mortality, and Cause-Specific Mortality for 249 Causes of Death, 1980-2015: A Systematic Analysis for the Global Burden of Disease Study 2015. *Lancet Lond. Engl.* **2016**, *388* (10053), 1459–1544. https://doi.org/10.1016/S0140-6736(16)31012-1.

(13)   Kelland, L. The Resurgence of Platinum-Based Cancer Chemotherapy. *Nat. Rev. Cancer* **2007**, *7* (8), 573.

(14)   Lippert, B. *Cisplatin: Chemistry and Biochemistry of a Leading Anticancer Drug*; John Wiley & Sons, 1999.

(15)   Kalayda, G. V.; Wagner, C. H.; Jaehde, U. Relevance of Copper Transporter 1 for Cisplatin Resistance in Human Ovarian Carcinoma Cells. *J. Inorg. Biochem.* **2012**, *116*, 1–10.

(16)   Wheate, N. J.; Walker, S.; Craig, G. E.; Oun, R. The Status of Platinum Anticancer Drugs in the Clinic and in Clinical Trials. *Dalton Trans.* **2010**, *39* (35), 8113–8127.

(17) Huang, J.-C.; Zamble, D. B.; Reardon, J. T.; Lippard, S. J.; Sancar, A. HMG-Domain Proteins Specifically Inhibit the Repair of the Major DNA Adduct of the Anticancer Drug Cisplatin by Human Excision Nuclease. *Proc. Natl. Acad. Sci.* **1994**, *91* (22), 10394–10398.

(18) Fong, C. W. Platinum Based Radiochemotherapies: Free Radical Mechanisms and Radiotherapy Sensitizers. *Free Radic. Biol. Med.* **2016**, *99*, 99–109. https://doi.org/10.1016/j.freeradbiomed.2016.07.006.

(19) Ma, P.; Xiao, H.; Li, C.; Dai, Y.; Cheng, Z.; Hou, Z.; Lin, J. Inorganic Nanocarriers for Platinum Drug Delivery. *Mater. Today* **2015**, *18* (10), 554–564. https://doi.org/10.1016/j.mattod.2015.05.017.

(20) Moroso, M.; Blair, R. A Review of Cis-Platinum Ototoxicity. *J. Otolaryngol.* **1983**, *12* (6), 365–369.

(21) Ozols, R. F.; Young, R. C. High-Dose Cisplatin Therapy in Ovarian Cancer.; 1985; Vol. 12, pp 21–30.

(22) Gill, J. S.; Windebank, A. J. Cisplatin-Induced Apoptosis in Rat Dorsal Root Ganglion Neurons Is Associated with Attempted Entry into the Cell Cycle. *J. Clin. Invest.* **1998**, *101* (12), 2842–2850.

(23) Thompson, S. W.; Davis, L. E.; Kornfeld, M.; Hilgers, R. D.; Standefer, J. C. Cisplatin Neuropathy. Clinical, Electrophysiologic, Morphologic, and Toxicologic Studies. *Cancer* **1984**, *54* (7), 1269–1275.

(24) Roelofs, R. I.; Hrushesky, W.; Rogin, J.; Rosenberg, L. Peripheral Sensory Neuropathy and Cisplatin Chemotherapy. *Neurology* **1984**, *34* (7), 934–934.

(25) Von Hoff, D.; Schilsky, R.; Reichert, C.; Reddick, R.; Rozencweig, M.; Young, R.; Muggia, F. Toxic Effects of Cis-Dichlorodiammineplatinum (II) in Man. *Cancer Treat. Rep.* **1979**, *63* (9–10), 1527.

(26) McKeage, M. J. Comparative Adverse Effect Profiles of Platinum Drugs. *Drug Saf.* **1995**, *13* (4), 228–244.

(27) Dyson, P. J.; Sava, G. Metal-Based Antitumour Drugs in the Post Genomic Era. *Dalton Trans.* **2006**, No. 16, 1929. https://doi.org/10.1039/b601840h.

(28) Amptoulach, S.; Tsavaris, N. Neurotoxicity Caused by the Treatment with Platinum Analogues. *Chemother. Res. Pract.* **2011**, *2011*, 1–5. https://doi.org/10.1155/2011/843019.

(29) Collins, J. F.; Klevay, L. M. Copper. *Adv. Nutr.* **2011**, *2* (6), 520–522. https://doi.org/10.3945/an.111.001222.

(30) Kim, B.-E.; Nevitt, T.; Thiele, D. J. Mechanisms for Copper Acquisition, Distribution and Regulation. *Nat. Chem. Biol.* **2008**, *4* (3), 176–185. https://doi.org/10.1038/nchembio.72.

(31) Scheiber, I.; Dringen, R.; Mercer, J. F. B. Copper: Effects of Deficiency and Overload. In *Interrelations between Essential Metal Ions and Human Diseases*; Sigel, A., Sigel, H., Sigel, R. K. O., Eds.; Springer Netherlands: Dordrecht, 2013; Vol. 13, pp 359–387. https://doi.org/10.1007/978-94-007-7500-8_11.

(32) Robert, A.; Benoit-Vical, F.; Liu, Y.; Meunier, B. Small Molecules: The Past or the Future in Drug Innovation? *Met. Ions Life Sci.* **2019**, *19.* https://doi.org/10.1515/9783110527872-008.

(33) Lippard, S. J.; Berg, J. M. *Principles of Bioinorganic Chemistry*; Univ. Science Books: Mill Valley, Calif, 1994.

(34) Da Silva, J. F.; Williams, R. J. P. *The Biological Chemistry of the Elements: The Inorganic Chemistry of Life*; Oxford University Press, 2001.

(35) Melník, M.; Kabešová, M.; Koman, M.; Macášková, L.; Holloway, C. E. Coordination Compounds: Classification and Analysis of Crystallographic and Structural Data. V. Polymeric Compounds. *J. Coord. Chem.* **2000**, *50* (1), 177–322. https://doi.org/10.1080/00958970008054937.

(36) Wang, T.; Guo, Z. Copper in Medicine: Homeostasis, Chelation Therapy and Antitumor Drug Design. *Curr. Med. Chem.* **2006**, *13* (5), 525–537.

(37) Wadas, T. J.; Wong, E. H.; Weisman, G. R.; Anderson, C. J. Coordinating Radiometals of Copper, Gallium, Indium, Yttrium, and Zirconium for PET and SPECT Imaging of Disease. *Chem. Rev.* **2010**, *110* (5), 2858–2902.

(38) Tisato, F.; Marzano, C.; Porchia, M.; Pellei, M.; Santini, C. Copper in Diseases and Treatments, and Copper-based Anticancer Strategies. *Med. Res. Rev.* **2010**, *30* (4), 708–749.

(39) Duncan, C.; White, A. R. Copper Complexes as Therapeutic Agents. *Metallomics* **2012**, *4* (2), 127–138.

(40) Franz, K. J. Application of Inorganic Chemistry for Non-Cancer Therapeutics. *Dalton Trans.* **2012**, *41* (21), 6333–6334.

(41) Graf, N.; Lippard, S. J. Redox Activation of Metal-Based Prodrugs as a Strategy for Drug Delivery. *Adv. Drug Deliv. Rev.* **2012**, *64* (11), 993–1004. https://doi.org/10.1016/j.addr.2012.01.007.

(42) Schwartz, L.; Supuran, C. T.; Alfarouk, K. O. The Warburg Effect and the Hallmarks of Cancer. *Anticancer Agents Med. Chem.* **2017**, *17* (2), 164–170.

(43) Warburg, O. On the Origin of Cancer Cells. *Science* **1956**, *123* (3191), 309–314.

(44) Santoro, A.; Calvo, J. S.; Peris-Díaz, M. D.; Krężel, A.; Meloni, G.; Faller, P. The Glutathione/Metallothionein System Challenges the Design of Efficient O2-activating Cu-complexes. *Angew. Chem.* **2020**, ange.201916316. https://doi.org/10.1002/ange.201916316.

(45) Atrián-Blasco, E.; Santoro, A.; Pountney, D. L.; Meloni, G.; Hureau, C.; Faller, P. Chemistry of Mammalian Metallothioneins and Their Interaction with Amyloidogenic Peptides and Proteins. *Chem. Soc. Rev.* **2017**, *46* (24), 7683–7693.

(46) Morgan, M. T.; Nguyen, L. A. H.; Hancock, H. L.; Fahrni, C. J. Glutathione Limits Aquacopper (I) to Sub-Femtomolar Concentrations through Cooperative Assembly of a Tetranuclear Cluster. *J. Biol. Chem.* **2017**, *292* (52), 21558–21567.

(47) McRae, R.; Bagchi, P.; Sumalekshmy, S.; Fahrni, C. J. In Situ Imaging of Metals in Cells and Tissues. *Chem. Rev.* **2009**, *109* (10), 4780–4827.

(48) Xiao, Z.; Gottschlich, L.; van der Meulen, R.; Udagedara, S. R.; Wedd, A. G. Evaluation of Quantitative Probes for Weaker Cu (I) Binding Sites Completes a Set of Four Capable of Detecting Cu (I) Affinities from Nanomolar to Attomolar. *Metallomics* **2013**, *5* (5), 501–513.

9)   Barnard, P.; Bayly, S.; Holland, J.; Dilworth, J.; Waghorn, P. In Vitro Assays for Assessing the Potential for Copper Complexes to Function as Radiopharmaceutical Agents. *QJ Nucl Med Mol Imaging* **2008**, *52* (3), 235.

(50) Suzuki, K. T.; Someya, A.; Komada, Y.; Ogra, Y. Roles of Metallothionein in Copper Homeostasis: Responses to Cu-Deficient Diets in Mice. *J. Inorg. Biochem.* **2002**, *88* (2), 173–182.

(51) Uozaki, H.; Horiuchi, H.; Ishida, T.; Iijima, T.; Imamura, T.; Machinami, R. Overexpression of Resistance-related Proteins (Metallothioneins, Glutathione-S-transferase π, Heat Shock Protein 27, and Lung Resistance-related Protein) in Osteosarcoma: Relationship with Poor Prognosis. *Cancer Interdiscip. Int. J. Am. Cancer Soc.* **1997**, *79* (12), 2336–2344.

(52) Sutoh, I.; Kohno, H.; Nakashima, Y.; Hishikawa, Y.; Tabara, H.; Tachibana, M.; Kubota, H.; Nagasue, N. Concurrent Expressions of Metallothionein, Glutathione S-Transferase-π, and P-Glycoprotein in Colorectal Cancers. *Dis. Colon Rectum* **2000**, *43* (2), 221–232.

(53) Surowiak, P.; Materna, V.; Kaplenko, I.; Spaczyński, M.; Dietel, M.; Lage, H.; Zabel, M. Augmented Expression of Metallothionein and Glutathione S-Transferase Pi as Unfavourable Prognostic Factors in Cisplatin-Treated Ovarian Cancer Patients. *Virchows Arch.* **2005**, *447* (3), 626–633.

(54) Tabti, R.; Tounsi, N.; Gaiddon, C.; Bentouhami, E.; Desaubry, L. Progress in Copper Complexes as Anticancer Agents. *Med. Chem.* **2017**, *07* (05). https://doi.org/10.4172/2161-0444.1000445.

(55) Raman, N.; Jeyamurugan, R.; Rajkapoor, B.; Magesh, V. Metal-based Antitumor, Cytotoxic and Antimicrobial Activity: Pharmacological Evaluation of Knoevenagel Condensate B-diketone Schiff Base Thiosemicarbazone Cu (II) and Zn (II) Complexes. *Appl. Organomet. Chem.* **2009**, *23* (7), 283–290.

(56) Cater, M. A.; Pearson, H. B.; Wolyniec, K.; Klaver, P.; Bilandzic, M.; Paterson, B. M.; Bush, A. I.; Humbert, P. O.; La Fontaine, S.; Donnelly, P. S.; Haupt, Y. Increasing Intracellular Bioavailable Copper Selectively Targets Prostate Cancer Cells. *ACS Chem. Biol.* **2013**, *8* (7), 1621–1631. https://doi.org/10.1021/cb400198p.

(57) Pramanik, A. K.; Siddikuzzaman; Palanimuthu, D.; Somasundaram, K.; Samuelson, A. G. Biotin Decorated Gold Nanoparticles for Targeted Delivery of a Smart-Linked Anticancer Active Copper Complex: In Vitro and In Vivo Studies. *Bioconjug. Chem.* **2016**, *27* (12), 2874–2885. https://doi.org/10.1021/acs.bioconjchem.6b00537.

(58) Sathisha, M. P.; Shetti, U. N.; Revankar, V. K.; Pai, K. S. R. Synthesis and Antitumor Studies on Novel Co(II), Ni(II) and Cu(II) Metal Complexes of Bis(3-Acetylcoumarin)Thiocarbohydrazone. *Eur. J. Med. Chem.* **2008**, *43* (11), 2338–2346. https://doi.org/10.1016/j.ejmech.2007.10.003.

(59) Borges, L. J. H.; Bull, É. S.; Fernandes, C.; Horn, A.; Azeredo, N. F.; Resende, J. A. L. C.; Freitas, W. R.; Carvalho, E. C. Q.; Lemos, L. S.; Jerdy, H.; Kanashiro, M. M. In Vitro and in Vivo Studies of the Antineoplastic Activity of Copper (II) Compounds against Human Leukemia THP-1 and Murine Melanoma B16-F10 Cell Lines. *Eur. J. Med. Chem.* **2016**, *123*, 128–140. https://doi.org/10.1016/j.ejmech.2016.07.018.

(60) Hancock, C. N.; Stockwin, L. H.; Han, B.; Divelbiss, R. D.; Jun, J. H.; Malhotra, S. V.; Hollingshead, M. G.; Newton, D. L. A Copper Chelate of Thiosemicarbazone NSC 689534 Induces Oxidative/ER Stress and Inhibits Tumor Growth in Vitro and in Vivo. *Free Radic. Biol. Med.* **2011**, *50* (1), 110–121. https://doi.org/10.1016/j.freeradbiomed.2010.10.696.

(61) Qi, J.; Zhang, Y.; Gou, Y.; Zhang, Z.; Zhou, Z.; Wu, X.; Yang, F.; Liang, H. Developing an Anticancer Copper(II) Pro-Drug Based on the His242 Residue of the Human Serum Albumin Carrier IIA Subdomain. *Mol. Pharm.* **2016**, *13* (5), 1501–1507. https://doi.org/10.1021/acs.molpharmaceut.5b00938.

(62) Barve, V.; Ahmed, F.; Adsule, S.; Banerjee, S.; Kulkarni, S.; Katiyar, P.; Anson, C. E.; Powell, A. K.; Padhye, S.; Sarkar, F. H. Synthesis, Molecular Characterization, and Biological Activity of Novel Synthetic Derivatives of Chromen-4-One in Human Cancer Cells. *J. Med. Chem.* **2006**, *49* (13), 3800–3808. https://doi.org/10.1021/jm051068y.

(63) Wangpaichitr, M.; Wu, C.; You, M.; Maher, J.; Dinh, V.; Feun, L.; Savaraj, N. N′ 1, N′ 3-Dimethyl-N′ 1, N′ 3-Bis (Phenylcarbonothioyl) Propanedihydrazide (Elesclomol) Selectively Kills Cisplatin Resistant Lung Cancer Cells through Reactive Oxygen Species (ROS). *Cancers* **2009**, *1* (1), 23–38.

(64) Chen, S.; Sun, L.; Koya, K.; Tatsuta, N.; Xia, Z.; Korbut, T.; Du, Z.; Wu, J.; Liang, G.; Jiang, J. Syntheses and Antitumor Activities of N′ 1, N′ 3-Dialkyl-N′ 1, N′ 3-Di-(Alkylcarbonothioyl) Malonohydrazide: The Discovery of Elesclomol. *Bioorg. Med. Chem. Lett.* **2013**, *23* (18), 5070–5076.

(65) Hedley, D.; Shamas-Din, A.; Chow, S.; Sanfelice, D.; Schuh, A. C.; Brandwein, J. M.; Seftel, M. D.; Gupta, V.; Yee, K. W.; Schimmer, A. D. A Phase I Study of Elesclomol Sodium in Patients with Acute Myeloid Leukemia. *Leuk. Lymphoma* **2016**, *57* (10), 2437–2440.

(66) Berkenblit, A.; Eder, J. P.; Ryan, D. P.; Seiden, M. V.; Tatsuta, N.; Sherman, M. L.; Dahl, T. A.; Dezube, B. J.; Supko, J. G. Phase I Clinical Trial of STA-4783 in Combination with Paclitaxel in Patients with Refractory Solid Tumors. *Clin. Cancer Res.* **2007**, *13* (2), 584–590.

(67) Korn, E. L.; Liu, P.-Y.; Lee, S. J.; Chapman, J.-A. W.; Niedzwiecki, D.; Suman, V. J.; Moon, J.; Sondak, V. K.; Atkins, M. B.; Eisenhauer, E. A. Meta-Analysis of Phase II Cooperative Group Trials in Metastatic Stage IV Melanoma to Determine Progression-Free and Overall Survival Benchmarks for Future Phase II Trials. *J. Clin. Oncol.* **2008**, *26* (4), 527–534.

(68) O'Day, S. J.; Eggermont, A. M.; Chiarion-Sileni, V.; Kefford, R.; Grob, J. J.; Mortier, L.; Robert, C.; Schachter, J.; Testori, A.; Mackiewicz, J. Final Results of Phase III SYMMETRY Study: Randomized, Double-Blind Trial of Elesclomol plus Paclitaxel versus Paclitaxel Alone as Treatment for Chemotherapy-Naive Patients with Advanced Melanoma. *J. Clin. Oncol.* **2013**, *31* (9), 1211–1218.

(69) Elesclomol Sodium and Paclitaxel in Treating Patients With Recurrent or Persistent Ovarian Epithelial Cancer, Fallopian Tube Cancer, or Primary Peritoneal Cancer - Full Text View - ClinicalTrials.gov https://clinicaltrials.gov/ct2/show/NCT00888615 (accessed Aug 18, 2019).

(70) Kirshner, J. R.; He, S.; Balasubramanyam, V.; Kepros, J.; Yang, C.-Y.; Zhang, M.; Du, Z.; Barsoum, J.; Bertin, J. Elesclomol Induces Cancer Cell

Apoptosis through Oxidative Stress. *Mol. Cancer Ther.* **2008**, *7* (8), 2319–2327.

(71) Blackman, R. K.; Cheung-Ong, K.; Gebbia, M.; Proia, D. A.; He, S.; Kepros, J.; Jonneaux, A.; Marchetti, P.; Kluza, J.; Rao, P. E. Mitochondrial Electron Transport Is the Cellular Target of the Oncology Drug Elesclomol. *PloS One* **2012**, *7* (1), e29798.

(72) Modica-Napolitano; Bharath; Hanlon; Hurley. The Anticancer Agent Elesclomol Has Direct Effects on Mitochondrial Bioenergetic Function in Isolated Mammalian Mitochondria. *Biomolecules* **2019**, *9* (8), 298. https://doi.org/10.3390/biom9080298.

(73) Ruiz-Ramírez, L.; De La Rosa, M.; Gracia-Mora, I.; Mendoza, A.; Pérez, G.; Ferrer-Sueta, G.; Tovar, A.; Breña, M.; Gutierrez, P.; Martínez, M. C. Casiopeinas, Metal-Based Drugs a New Class of Antineoplastic and Genotoxic Compounds. *J. Inorg. Biochem.* **1995**, *59* (2–3), 207–207.

(74) Ruiz-Ramirez, L.; Gracia-Mora, I.; de la Rosa, M. E.; Sumano, H.; Gomez, C.; Arenas, F.; Gomez, E.; Pimentel, E.; Cruces, M. Cytostatic, Mutagenic, Antineoplastic Activities and Preliminar Toxicity of Copper (II) New Drugs: Casiopeinas I, II, III. *J. Inorg. Biochem.* **1993**, *51* (1–2), 406.

(75) Alemón-Medina, R.; Breña-Valle, M.; Muñoz-Sánchez, J. L.; Gracia-Mora, M. I.; Ruiz-Azuara, L. Induction of Oxidative Damage by Copper-Based Antineoplastic Drugs (Casiopeínas®). *Cancer Chemother. Pharmacol.* **2007**, *60* (2), 219–228. https://doi.org/10.1007/s00280-006-0364-9.

(76) Rivero-Müller, A.; De Vizcaya-Ruiz, A.; Plant, N.; Ruiz, L.; Dobrota, M. Mixed Chelate Copper Complex, Casiopeina IIgly®, Binds and Degrades Nucleic Acids: A Mechanism of Cytotoxicity. *Chem. Biol. Interact.* **2007**, *165* (3), 189–199.

(77) Bravo-Gómez, M. E.; García-Ramos, J. C.; Gracia-Mora, I.; Ruiz-Azuara, L. Antiproliferative Activity and QSAR Study of Copper (II) Mixed Chelate [Cu (N–N)(Acetylacetonato)] NO3 and [Cu (N–N)(Glycinato)] NO3 Complexes,(Casiopeínas®). *J. Inorg. Biochem.* **2009**, *103* (2), 299–309.

(78) Ruiz-Azuara, L.; Bravo-Gómez, M. E. Copper Compounds in Cancer Chemotherapy. *Curr. Med. Chem.* **2010**, *17* (31), 3606–3615.

(79) Ruiz-Azuara, L.; Bastian, G.; Bravo-Gómez, M. E.; Cañas, R. C.; Flores-Alamo, M.; Fuentes, I.; Mejia, C.; García-Ramos, J. C.; Serrano, A. Abstract CT408: Phase I Study of One Mixed Chelates Copper (II) Compound, Casiopeína CasIIIia with Antitumor Activity and Its Mechanism of Action. **2014**.

(80) Espinal-Enríquez, J.; Hernández-Lemus, E.; Mejía, C.; Ruiz-Azuara, L. Network Analysis Shows Novel Molecular Mechanisms of Action for Copper-Based Chemotherapy. *Front. Physiol.* **2016**, *6*, 406.

(81) Leite, S. M. G.; Lima, L. M. P.; Gama, S.; Mendes, F.; Orio, M.; Bento, I.; Paulo, A.; Delgado, R.; Iranzo, O. Copper(II) Complexes of Phenanthroline and Histidine Containing Ligands: Synthesis, Characterization and Evaluation of Their DNA Cleavage and Cytotoxic Activity. *Inorg. Chem.* **2016**, *55* (22), 11801–11814. https://doi.org/10.1021/acs.inorgchem.6b01884.

CHAPTER 2.

Exploring Deeper into the Anticancer Properties of the Cu(II) Complexes C1 and C2.

66 To be surprised, to wonder,
is to begin to understand."

José Ortega y Gasset

2.1. Background.

The ligands **HL1** and **H₂L2** (**Figure 2.1**, A) were previously developed in the group[1] and they contain two coordinating units: (i) phenanthroline (Phen), a bidentate classical metal chelator capable to coordinate Cu through the nitrogen atoms,[2] and an attractive scaffold used in anticancer agents since the discovery of the nuclease activity of Cu(Phen)₂ by Sigman *et al*,[3] and (ii) histidine (His) an amino acid that plays important roles on Cu coordination on peptides and metalloproteins providing high thermodynamic stability to the resulting complexes.[4–7] **HL1** and **H₂L2** were designed to study the effect that combining these two units in a single molecule, *vs* having them as independent units (i.e. Casiopeinas, see Section 1.2.2.1, Chapter 1), has in the coordination properties of Cu and how this can affect the cytotoxic properties and biological activity of the resulting Cu(II) complexes.
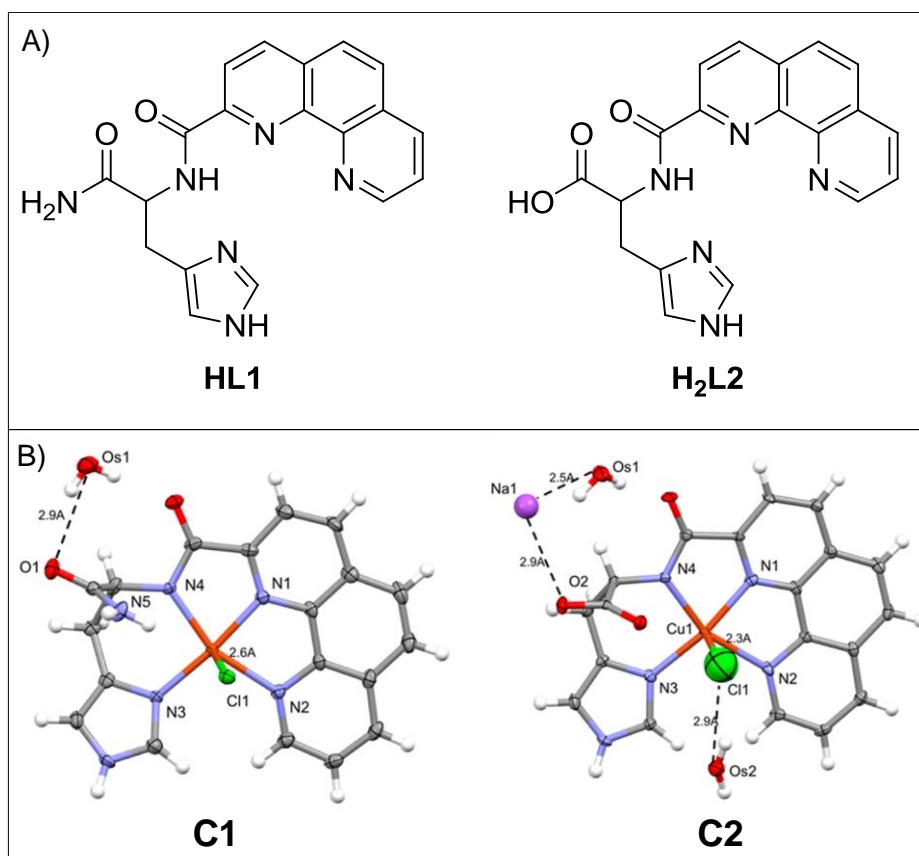
Figure 2.1. Structures of ligands **HL1** and **H₂L2** (A) and X-ray structures of the respective complexes [Cu**L1**·H₂O] (left) and [Cu(Na**L2**)·2H₂O] (right).

The ligands **HL1** and **H₂L2** bind Cu(II) with similar affinity constants at pH 7.4 (log K_{cond} = 14.55 and 13.89, respectively) forming a single major species on a wide range of pH ([**CuL1**] = **C1** from 3.0 to 9.0 and [**CuL2**] = **C2** from 5.0 to 10.0, see Annex **Figure A.1**). The Cu(II) atom is bound in a similar way in both complexes, (to the deprotonated amide, the N of the Phen unit and to the imidazole ring of His) and presents a distorted squared pyramidal geometry with a chloride ion occupying the axial position (**Figure 2.1**, **B**). Cyclic voltammetry indicated that the complexes **C1** and **C2** are reducible and that the **C2** complex has lower reduction potential (E_{pc} = –0.452 V *vs* –0.722 V for **C1** and **C2**, respectively). The large separation observed between the anodic and the cathodic peaks in both cases ($\Delta E_p = \Delta E_{pa} - \Delta E_{pc}$ = 0.653 V and 0.903 V for **C1** and **C2**, respectively) indicates a non-reversible Cu(II) $\rightleftarrows$ Cu(I) one electron redox process. Overall, the covalent attachment of the His to the Phen unit had a double impact: (i) it increased the Cu(II) binding affinity of **HL1** and **H₂L2** at pH 7.4 in relation to that observed for related ternary complexes and (ii) it lowered the reduction potential of the **C1** and **C2** complexes leading to non-reversible redox process.

The biological studies showed that both Cu(II) complexes are poorly active as DNA nucleases, indicating that there is a reduced contribution of hydrolytic pathways in the DNA cleavage. However, the addition of activators such as H_2O_2 or ascorbic acid enhanced their activities revealing the involvement of ROS in the process. Overall, the **C2** complex produces higher DNA cleavage. Consistently, **C2** also shows higher cytotoxic activity (**Table 2.1**). Cytotoxic activity was determined by a colorimetric method (MTT assay) on the human ovarian cancer (A2780) cell line, its cisplatin-resistant variant (A2780cisR) and on the human breast cancer cell line (MCF-7). The **HL1** and **H₂L2** ligands show no cytotoxicity. A direct and reliable comparison of the cytotoxic activity of the new complexes with the congeners of the "Casiopeínas" type is hampered by the fact that the different compounds have been tested against different cell lines with different responses to antitumor drugs. Nevertheless, the relative cytotoxicity values of **C1** and **C2** are in line with the QSAR studies reported for Casiopeínas and related Cu(II) complexes that pointed out for an increasing of the biological activity for the weaker oxidants.[8]

Table 2.1. Reported IC_{50} values at 72 h treatment of **C1**, **C2** and of their corresponding ligands obtained for different human tumor cell lines.

Compound	IC_{50} (μM)*		
	A2780	A2780cisR	MCF-7
HL1	>200	>200	>200
H₂L2	>200	>200	>200
C1	24.24 ± 1.85	>200	>200
C2	18.01 ± 1.59	152 ± 1.86	88 ± 1.55
Cu(NO₃)₂	42.31 ± 1.41	91.47 ± 1.77	>200
Cisplatin	0.5 ± 0.1	16.05 ± 1.12	38 ± 1.23

*IC_{50} values are mean ± SD of triplicates obtained after 72 h treatment (MTT assay).[1]

This work explores deeper into the potential therapeutic properties of the **C1** and **C2** complexes providing insights into their ways of interaction with DNA, their cellular uptake and their ability to produce ROS inside the cells.

2.1.1. Synthesis of HL1, H₂L2 and their Cu(II) complexes.

The synthesis of **HL1** and **H₂L2** was carried out following the published protocols[1] (**Scheme 2.1**). The common precursor material for both ligands, namely the 2-carboxy-1,10-phenanthroline (**14**) was synthesized from the Phen (**11**) as reported by Sun *et al.*[9] **HL1** and **H₂L2** were manually assembled on a rink amide MBHA and a 2-chlorotrityl chloride resins, respectively. The Fmoc-His(Trt)-OH (**15**) residue was firstly coupled to the resin (**16**) using the correspondent standard Fmoc solid-phase methods[10] followed by a Fmoc deprotection step (**17**) by treating the resin with 20 % piperidine in dimethylformamide (DMF) solution. The PhenCOOH was coupled in DMF using PyBOP as coupling agent and DIEA as base. The ligands were deprotected and cleaved from the resin by a treatment with a 95:2.5:2.5, $TFA/TIS/H_2O$. After filtration the mixtures were evaporated to a crude oil, from which a precipitate was obtained by addition of cold diethyl ether.

The ligands were purified as described in the experimental section (Sections 6.3.2 and 6.3.3, Chapter 6). The Cu(II) complexes were prepared *in situ* by mixing equimolar amounts of the corresponding ligands and the Cu salt directly from their stock solutions and adjusting manually the required pH.
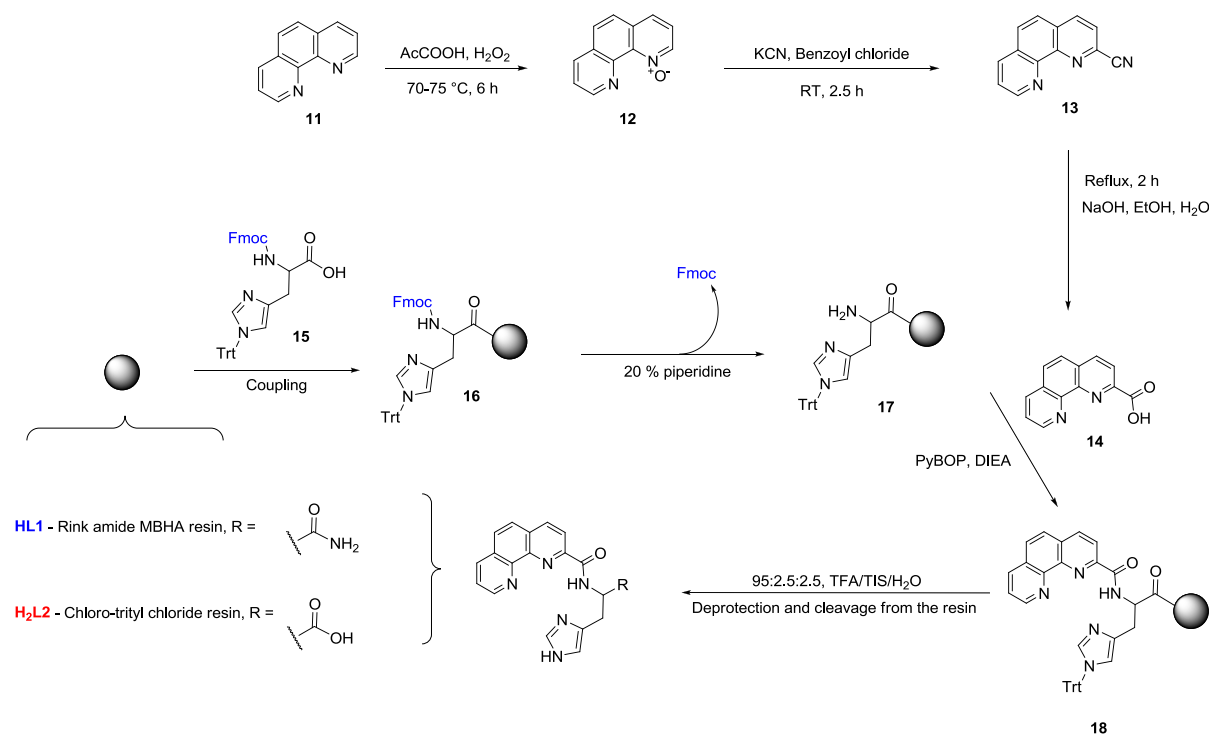
Scheme 2.1. Synthetic pathway to obtain **HL1** and **H₂L2**.

2.1.2. C1 and C2 DNA interaction studies.

Among the different structures found in cells, DNA is still one of the main targets for many chemotherapeutic compounds that are currently in clinical trials. Targeting DNA is a way to modulate transcription (protein synthesis and gene expression) or to affect replication and therefore cell division.[11] UV-VIS spectroscopy was used to decipher the DNA binding modes of **C1** and **C2**, and their DNA binding constants. The UV-vis spectra of **C1** and **C2** complexes were recorded from 200 - 500 nm (**Figure 2.2**) at a constant complex concentration of 25 μM, before (black line) and after each addition of *calf Thymus* DNA (*ct*-DNA). For both complexes, the results show a hypochromic effect upon *ct*-DNA addition but no significant bathochromism. These data suggest that **C1** and **C2** have mild DNA

binding capabilities, interacting with DNA most likely via groove binding or electrostatic interactions rather than via intercalation since the change in the absorbance does not show any shift in the absorption bands.[7,12] The slightly higher hypochromism value observed for **C1** (20 %) over the one of **C2** (16 %) correlates with the fact that **C1** at pH 7.4 is positively charged favoring it interaction with the partially negatively charged DNA.
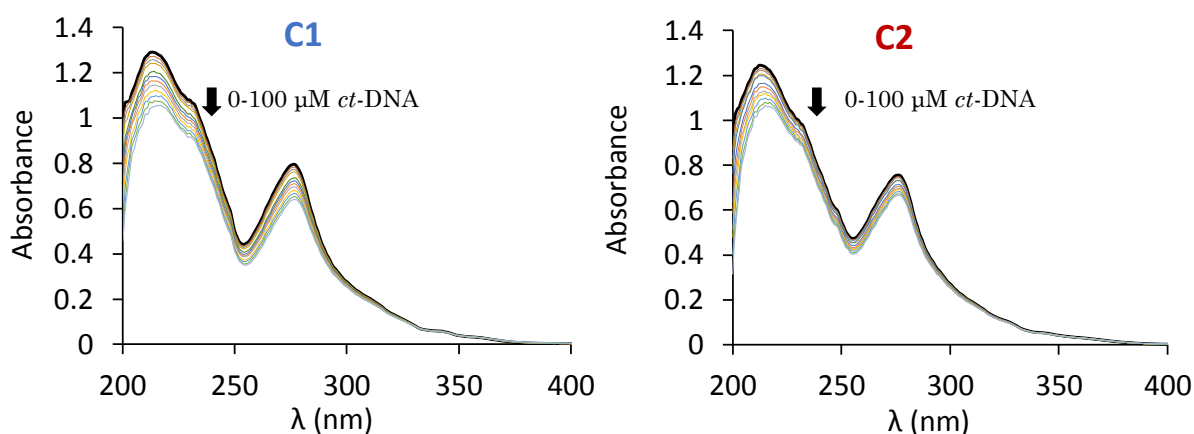
Figure 2.2. UV-vis spectra of complexes **C1** (left) and **C2** (right) (25 µM) in Tris-HCl pH 7.4 (5 mM) and NaCl (50 mM) upon additions of *ct*-DNA (0 - 100 µM). The arrows point the change in the absorbance of the complex after the addition of *ct*-DNA. The black bold line represents the initial absorbance of the complex (no *ct*-DNA). Data was corrected considering dilution factors and DNA blanks for each addition.

The Benesi-Hildebrand equation (**Equation 2.1**) was used to determine the binding constant K_b from the UV-vis spectroscopic data. In this equation A_0 represents the initial absorbance of the complex, A is the absorbance at each given DNA concentration and ε_G and ε_{H-G} are the extinction coefficients of the complex and complex-DNA system, respectively. The variation of absorbance at 212 nm ($A_0/(A - A_0)$) was plotted *vs* the inverse of the *ct*-DNA concentration ($1/[ct\text{-DNA}]$)[12] (**Figure 2.3**):

$$\frac{A_0}{A-A_0} = \frac{\varepsilon_G}{\varepsilon_{H-G}-\varepsilon_G} + \frac{\varepsilon_G}{\varepsilon_{H-G}-\varepsilon_G} \cdot \frac{1}{K_b[ct-\text{DNA}]}$$ (**Equation 2.1**)
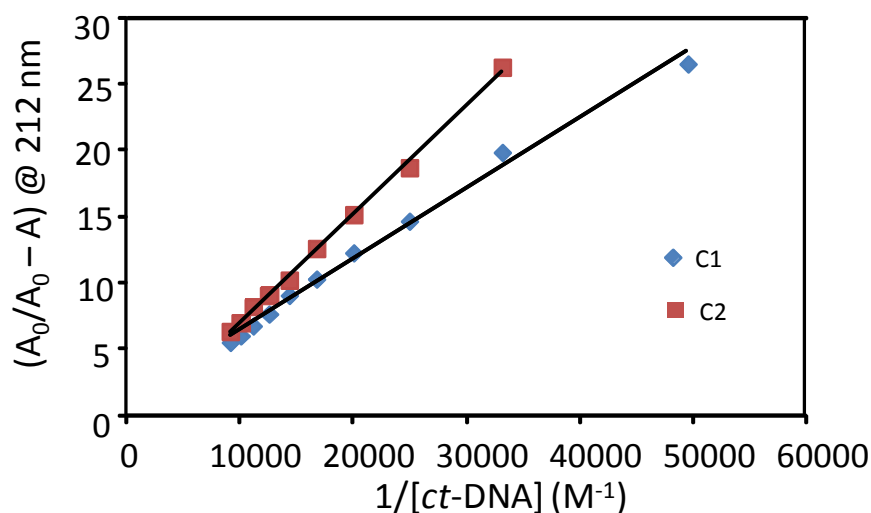
Figure 2.3. Plot of the change of the absorbance of **C1** (blue) and **C2** (red) at 212 nm ($A_0/(A - A_0)$) *vs* the inverse of the *ct*-DNA concentration (1/[*ct*-DNA]). Solid black lines are the fit of experimental data to the Benesi-Hildebrand equation (**Equation 2.1**).

The K_b values obtained are indicated on **Table 2.2**. and in both cases are in the order of 10^3. This K_b values are lower than the values known (around 10^6-10^7) for classical and strong metallo-intercalators (DAPI, HOECHST, GMB, etc.) [13–15] and indicate a mild *ct*-DNA binding affinity.

Table 2.2. Values of K_b (M^{-1}) and hypochromism obtained from the interaction between *ct*-DNA and the complexes **C1** and **C2**.

Compound	K_b (M^{-1})	log K_b	% hypochromism*
C1	2.97×10^3	3.47 ± 0.08	20 %
C2	1.48×10^3	3.17 ± 0.05	16 %

Hypochromism = ((A₀ − Aƒ) / A₀). Aƒ = final absorbance. Values are mean ± SD of 3 independent experiments.

2.1.3. Ethidium bromide competition studies.

Fluorescence spectroscopy is commonly used to investigate the interactions between DNA and small molecules. With fluorescence quenching experiments it is possible to obtain additional information regarding the localization of the molecule and their mode of interaction with DNA.[11] Fluorescence emission is enough sensible to the environment and given that the fluorophore transfer from high to low polarity environments, normally causes shifts from 10 to 20 nm in the excitation and emission spectra.[16]

Ethidium bromide (EBr) is probably one of the most well-known fluorescent DNA intercalating agents. When it binds to DNA enhances its fluorescence by around 20-fold in comparison with the free EBr. This change in fluorescence allows to follow the intercalation of molecules into DNA. A molecule that is able to displace EBr from the DNA will cause a decrease on the fluorescence intensity at 610 nm (EBr-DNA adduct).[17]

The EBr competition studies were carried out with the **C1** and **C2** complexes verifying that the complexes interact weakly with *ct*-DNA. The intensity of the band at 610 nm was not significantly affected by the addition of the complexes (0 - 160 μM) showing only around 10 % of hypochromism (**Figure 2.4**).
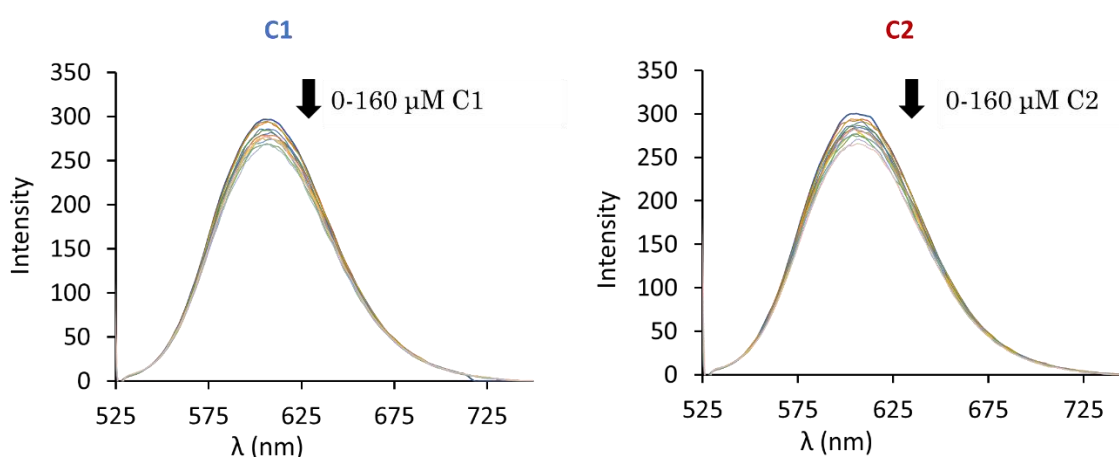
Figure 2.4. Fluorescence spectra (λ_{exc} = 514 nm and λ_{em} = 610 nm) of EBr:*ct*-DNA (12.5 μM:2.5μM) in Tris-HCl pH 7.4 (5 mM) and NaCl (50 mM) upon additions of complexes **C1** (left) and **C2** (right) (0 - 160 μM).

The Stern-Volmer equation (**Equation 2.2**) was used to calculate the Stern-Volmer constant *(K_{SV})*,[12] where I_o and I represent the emission intensities of the EBr-DNA complex before and after each **C1** and **C2** complex addition, respectively. The plot shows the intensities ratio (I_o/I) *vs* the complex concentration ([*Complex*]) (**Figure 2.5**):

$$\frac{I_o}{I} = K_{sv}[Complex] + 1 \qquad\qquad \textbf{Equation (2.2)}$$
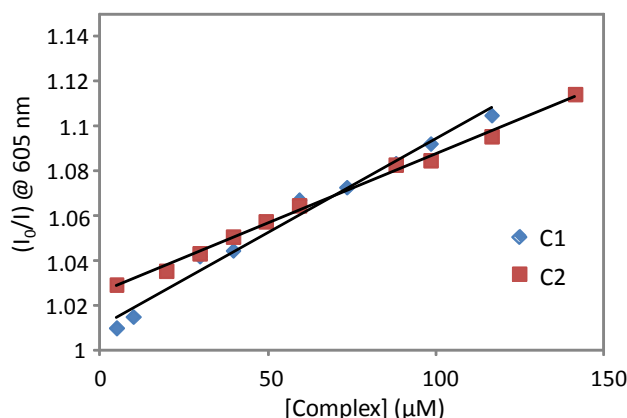
Figure 2.5. Plot of the I_o/I ratio *vs* the concentration of **C1** (blue) or **C2** (red) added. The K_{SV} is calculated from the slope of the linear fitting using the Stern-Volmer model (**Equation 2.2**).

Table 2.3. Values of K_{SV} (M^{-1}) and hypochromism obtained from the EBr competition studies for the complexes **C1** and **C2**.

Compound	K_{SV} (M^{-1})	% hypochromism*
C1	8 x 10^2	11
C2	6 x 10^2	10

*Hypochromism **=** (($I_0 - I_f$)/I_0). I_f = final fluorescence intensity. Values are mean of two experiments.

The values of K_{SV} obtained for the complexes **C1** and **C2** (**Table 2.1**) are around 10^2 and are in line with those obtained by UV-vis spectroscopy (**Table 2.2**) suggesting that **C1** and **C2** have poor DNA intercalation abilities and that interact weakly with DNA most likely through electrostatic interactions.

2.1.4. Evaluation of the biological activity of C1 and C2 inside human cells.

The biological assays were carried out with the cancer cell lines: human ovarian cancer cells (A2780), and human breast cancer cells (MCF-7). Furthermore, 2 normal cell lines were also used in order to compare the biological activities between normal and cancer cells and thus explore the selective cytotoxicity of the copper complexes. The normal cell lines used were human umbilical vein endothelial cells (HUVEC) and human lung fibroblast (IMR-90).

2.1.4.1. Cytotoxic activities of C1 and C2.

The antiproliferative activities of the complexes **C1** and **C2** and of their corresponding free ligands were previously evaluated in A2780, its cisplatin resistant variant A2780cisR and MCF-7 human cancer cell lines (**Table 2.1**).[1] However, at that point, their antiproliferative activities were not evaluated in normal cells. This is indeed an important point in terms of selective chemotherapy since poor activity in normal cells might provide less side-effects, and therefore could represent an *in vivo* advantage.

In order to obtain comparable data, the IC_{50} values of **C1**, **C2** and their correspondent ligands were reevaluated in parallel in the two human cancer cell lines and two non-cancerous (normal) human cell lines. Additionally, H_2O_2 and $CuCl_2$ were also assayed since they are used as a positive control and reference, respectively, in further experiments (see Section 2.1.4.2 and 2.1.4.3). The same colorimetric test, i.e. MTT assay, was used to determine the cell viability.

Dose-response curves after 72 h exposure of different concentrations of **C1**, **C2**, **HL1**, **H₂L2**, H_2O_2 and $CuCl_2$ (0 - 200 µM) were obtained (**Figure 2.6**). After their correspondent fittings the IC$_{50}$ values were calculated and are presented in **Table 2.4**.
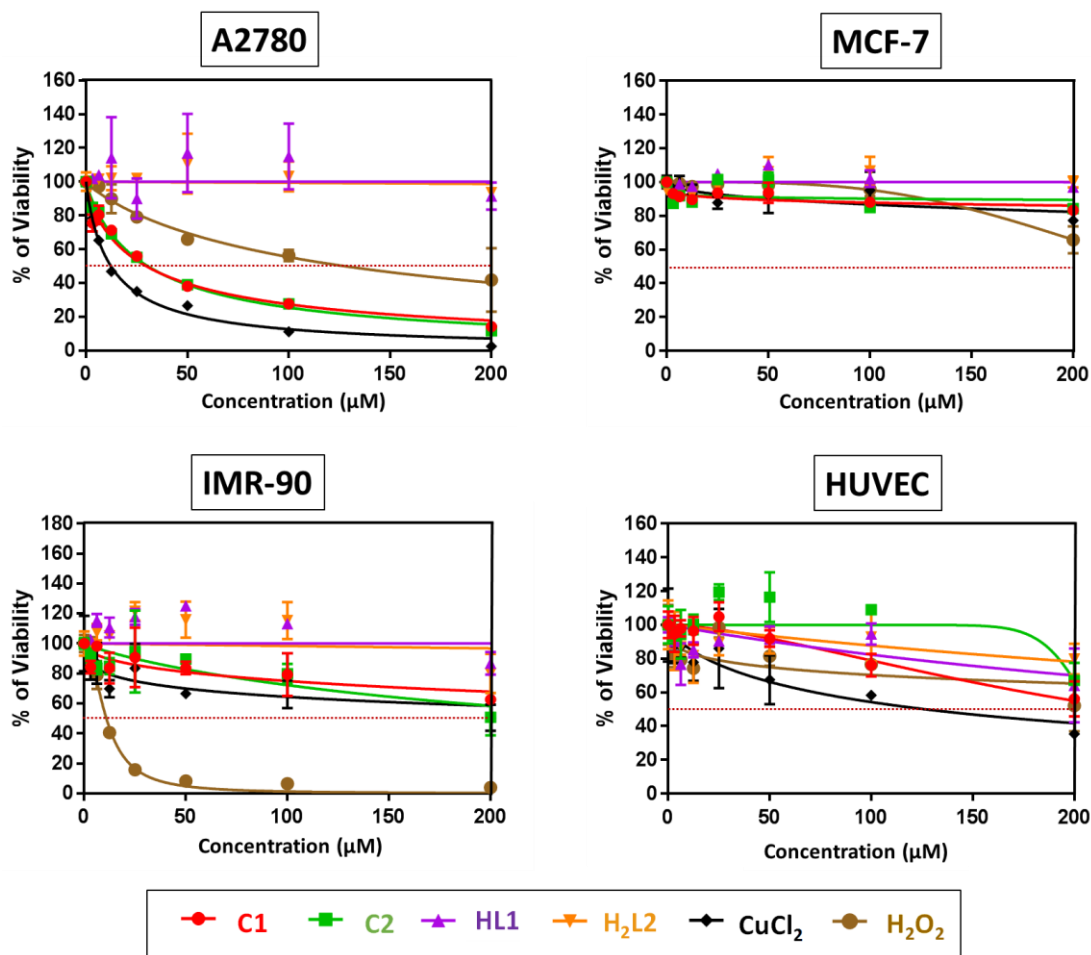
Figure 2.6. Dose-response cell viability assays on two human cancer cell lines (A2780 and MCF-7) and two normal human cell lines (IMR-90 and HUVEC) after 72 h treatment with **C1**, **C2**, **HL1**, **H₂L2**, $CuCl_2$ and H_2O_2 at different concentrations. The dashed red line indicates the 50 percent of viability.

For some cases, cytotoxicity (**Table 2.4**) was not detected (N.D.) under the used experimental conditions. This implies that in comparison with the control cells, the cell viability was not disturbed after 72 h treatment with the maximum concentration tested (200 µM). For other cases, where there is a cytotoxic effect, but the compound was not effective enough to inhibit the cell viability by half, the IC$_{50}$ values are considered over 200 µM (**Table 2.4**).

Table 2.4. IC$_{50}$ values (μM) after 72h treatment obtained for **C1**, **C2**, **HL1**, **H$_2$L2**, CuCl$_2$ and H$_2$O$_2$ in the human cell lines A2780, MCF-7, IMR-90 and HUVEC.

IC$_{50}$ values (μM)

	C1	C2	HL1	H$_2$L2	CuCl$_2$	H$_2$O$_2$
A2780	29.68 ± 2.15	30.43 ± 1.48	N.D.	N.D.	12.27 ± 0.51	127.6 ± 14.8
MCF-7	>200 (17)	>200 (16)	N.D.	N.D.	>200 (23)	>200 (34.0)
IMR-90	>200 (37)	>200 (49)	N.D.	N.D.	>200 (48)	10.66 ± 1.46
HUVEC	>200 (43)	>200 (33)	>200 (36)	>200 (20)	126.8 ± 33.8	>200 (48)

N.D. = Not detected. Values are mean ± SD of 3 experiments.
* Values between parenthesis refer to % inhibition at 200 μM.

The data obtained indicate that the ligands **HL1** and **H$_2$L2** have small or no cytotoxic effect over the cells tested, maintaining in most of the cases 100 % of cell viability. Only a decrease of 36 % for **HL1** and 20 % for **H$_2$L2** was observed for HUVEC cells. These results are in line with the previous results reported (**Table 2.1**).[1]

The IC$_{50}$ values obtained for the complexes **C1** and **C2** in A2780 are comparable to the ones reported previously by Leite *et al*. (**Table 2.1**) specially for **C1** (29.68 *vs* 24.24 μM). For **C2** the values differ more (30.43 *vs* 18.01 μM). In MCF-7 cells both complexes show very small inhibition activity (17 % for **C1** and 16 % for **C2**, **Table 2.1**). These results mismatch the results obtained by Leite *et al*.[1] where an IC$_{50}$ of 88 μM was observed for **C2** (**Table 2.1**).

For the case of the non-cancerous cell line IMR-90, **C1** and **C2** showed a maximum inhibition of 37 and 49 % respectively, at the maximum concentration tested (200 μM, **Figure 2.6**). A similar value is obtained for CuCl$_2$ (48 %). In contrast, for the case of H$_2$O$_2$ the calculated IC$_{50}$ value is 10.66 μM (**Table 2.4**). On HUVEC cells, **C1** and **C2** show a maximum inhibition of viability of 43 and 32 % respectively, while H$_2$O$_2$ produced 48 % at 200 μM. The IC$_{50}$ value calculated for CuCl$_2$ is 126.8 μM.

Despite the mismatching results obtained with MCF-7, the less sensitive cell line, the complexes **C1** and **C2** show a moderate cytotoxic effect over A2780 as previously reported,[1] while over the two non-cancerous cells assayed, this effect was milder. These results can be interesting in terms of selective cytotoxicity through a deeper study using more cancer and normal cells will be needed.

2.1.4.2. Cellular uptake of the complexes C1 and C2.

The biological activity of metal complexes is strongly influenced by their cellular internalization across the cell membrane. To be active, these compounds must reach the desired location inside the cell. The transportation processes of molecules through the cell membrane involve many different mechanisms, including passive diffusion and entry through organic and metal transporters, and they directly affect the rate of uptake and cellular distribution. Different methods have been used to study cellular uptake (**Table 2.5**),[18] and considering the intrinsic properties of the complexes **C1** and **C2**, inductively coupled plasma mass spectrometry (ICP-MS) was chosen to evaluate their uptake in A2780, MCF-7, IMR-90 and HUVEC.

Table 2.5. Comparison of methods for the study cellular accumulation.[18]

Method	Advantages	Disadvantages
ICP-MS	Applicable to non-luminescent complexes Quantitative (mean metal content per mg of protein)	Low throughput Cannot distinguish surface-bound *vs* internalized Sample is degraded
Flow cytometry	High throughput Semi-quantitative Provides population distribution of luminescence intensity Can distinguish live *vs* dead cells	Limited to luminescent complexes Cannot distinguish surface-bound *vs* internalized
Confocal microscopy	Provides subcellular localization Real-time monitoring *in situ* Can distinguish live *vs* dead cells	Limited to luminescent complexes Low throughput

Cells were incubated at 37 °C with 200 μM solutions of **C1** and **C2**. In addition, non-treated cells (control cells) and cells treated with a 200 μM $CuCl_2$ solution were also incubated as references. After 4 h treatment, the solutions were removed and the cells were collected and digested with HNO_3, as described in experimental section (Section 6.7.2), prior to Cu quantification through ICP-MS. The treatment time was chosen (4 h) to avoid cell death and consequently release of the intracellular medium affecting the reliability of the ICP-MS data.

The data obtained after the Cu quantification are presented in **Table 2.6**. The results reveal that in the three cases (**C1**, **C2** and $CuCl_2$), the cancer cells (A2780 and MCF-7) exhibit lower Cu uptake compared to the normal cells (IMR-90 and HUVEC). Moreover, all the cell lines treated with **C1** show higher Cu uptake in comparison with those treated with **C2** (see **Figure A.2**).

Table 2.6. ICP-MS quantification of the Cu uptake in four different cell lines after 4 h treatment.

Cell line	**Intracellular Cu** ($\mu g_{Cu}/mg_{protein}$)*		
	C1	**C2**	**CuCl₂**
A2780	8.24 ± 0.31	4.02 ± 0.11	35.97 ± 0.84
MCF-7	2.89 ± 0.44	1.54 ± 0.03	16.52 ± 0.93
IMR-90	55.83 ± 6.41	30.39 ± 1.1	238.98 ± 4.72
HUVEC	100.53 ± 3.24	55.46 ± 0.74	420.54 ± 14.74

*The experimental values are mean ± SD of 3 experiments.

For every cell line, there is a noticeable difference between the Cu uptake in the cells treated with the complexes **C1** and **C2**, and those treated with $CuCl_2$. This indicates that most likely, the complexes are not destroyed during the incubation time and that they are internalized as a whole unit.

On A2780 cells the internalization values of **C1** and **C2** are 8.24 and 4.02 $\mu g_{Cu}/mg_{protein}$, which means that **C2** internalizes 52 % less than **C1**. However, the IC$_{50}$ values for **C1** and **C2** are very similar. This reveals that **C2** may have more cytotoxic activity than **C1** but less internalization abilities.

The internalization values observed for MCF-7 cells were the lowest among the cell lines tested (**Table 2.6**). For instance, the complexes **C1** and **C2** internalize 65 and 61 % less respectively, in MCF-7 than in A2780 cells. The low internalization values obtained for MCF-7 cells may explain their low sensitive to all the compounds tested (**Figure 2.6** and **Table 2.6**).

The non-cancerous cells exhibited significantly higher Cu uptake values compared to the cancer cell lines, being HUVEC the ones with the higher uptake (100.53, 55.46 and 420.54 $\mu g_{Cu}/mg_{protein}$ for **C1**, **C2** and CuCl$_2$ respectively) (**Table 2.6**). These results together with the cytotoxic studies (**Table 2.4**, **Figure 2.6**) indicate that **C1** and **C2** are less toxic for HUVEC and IMR-90 cells than for A2780 because they inhibit less cell viability in spite of a higher internalization.

It was not possible to compare these values with other values reported in literature because of the differences in the conditions assayed, such as concentrations, times or cells. Overall, these data highlight the importance of carrying out Cu uptake studies when analyzing the cytotoxic effects of metal complexes.

2.1.4.3. Measurement of intracellular ROS by HL1, H$_2$L2, C1 and C2.

It was previously established (Section 2.1.2) that complexes **C1** and **C2** interact weakly with DNA, and they might not affect replication or induce cell-death by binding to DNA and changing its structure. Therefore, their cytotoxic activity should be induced by another mechanism of action. One of the main pathways involved in the cytotoxic activity of Cu-based anticancer molecules is to induce apoptosis/necrosis in cells via generation of intracellular ROS.[19,20] It has been reported that, overall, cancer cells present higher inner concentration levels of ROS compared to normal cells.[21] This is a consequence of their higher

metabolism rate and their genetic associated alterations. Considering this fact (higher basal ROS levels), cancer cells show higher vulnerability to ROS level changes than normal cells do, and this difference can be advantageous and represents a unique opportunity to selectively target cancer cells (**Figure 2.7**).[22]
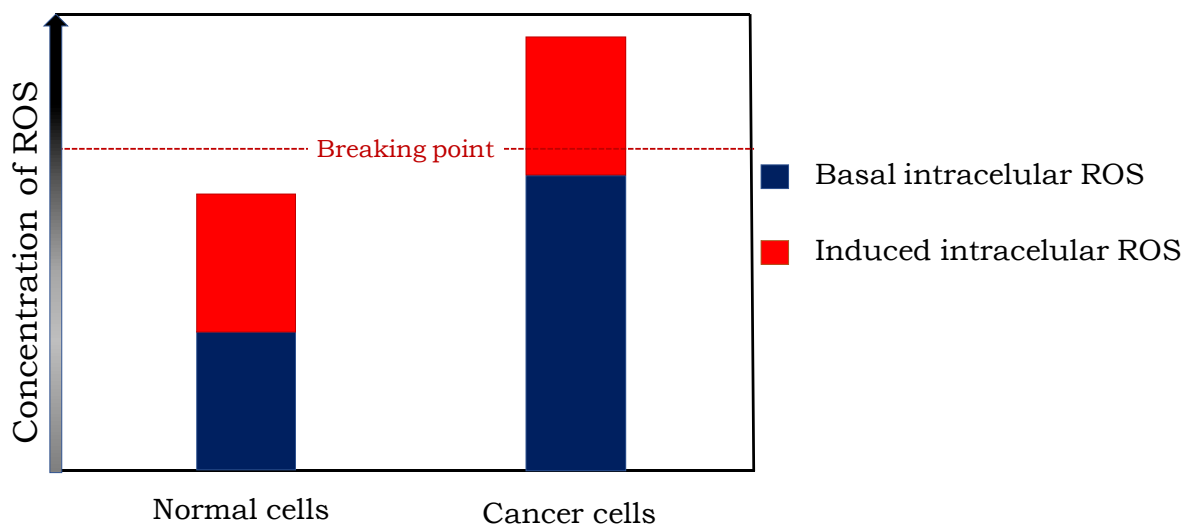
Figure 2.7. Illustration of the selective strategy by induction of intracellular ROS taking advantage of the different basal levels of oxidant stress between normal and malignant cancer cells.

Considering that the DNA cleaving studies carried out with the complexes **C1** and **C2** (Section 2.1) indicate an oxidative dependent mechanism of action, and that their calculated apparent half-wave potentials ($E_{1/2} = (E_{pc} - E_{pa})/2$) for the Cu(II)/Cu(I) redox pair -0.1255 and -0.2705 *vs* Ag/AgCl for **C1** and **C2**, respectively) are inside the window of biological redox chemistry (**Figure 2.8**), these complexes could most likely perform redox chemistry inside cells.[23] In this context, it was considered important to confirm the formation of intracellular ROS.
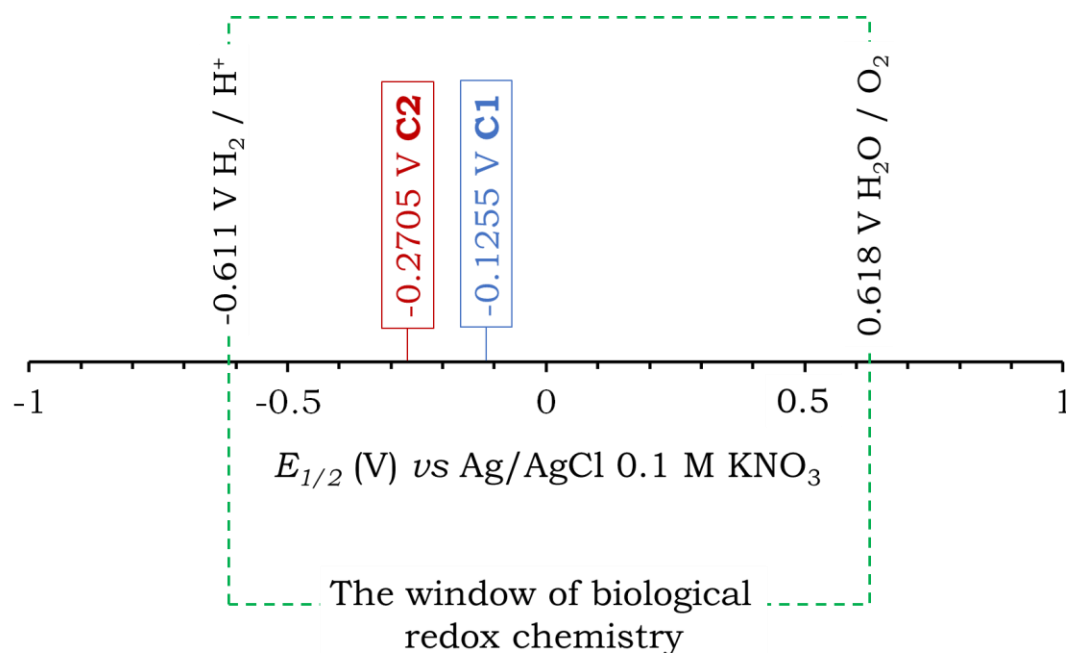
Figure 2.8. Calculated $E_{1/2}$ values for **C1** and **C2** placed in the window of biological redox window.[23]

An evaluation of the amount of the ROS produced inside the A2780, MCF-7, IMR-90 and HUVEC cell lines after treatment with the complexes **C1** and **C2** was carried out using 2′,7′-dichlorofluorescin diacetate (DCFDA), a permeable non-fluorescent dye that after being oxidized by ROS generates dichlorofluorescin (DCF), a non-permeable and fluorescent dye (**Scheme 2.2**). The experiments were also done with the respective ligands, **HL1** and **H₂L2**, and the two positive controls, CuCl₂ and H₂O₂. The experiments tested concentrations from 0.3 to 200 µM, and fluorescence was recorded at initial time after 4, (see Annex, **Figure A.3** and **A.4**) and 72 h of treatment (**Figure 2.9**).
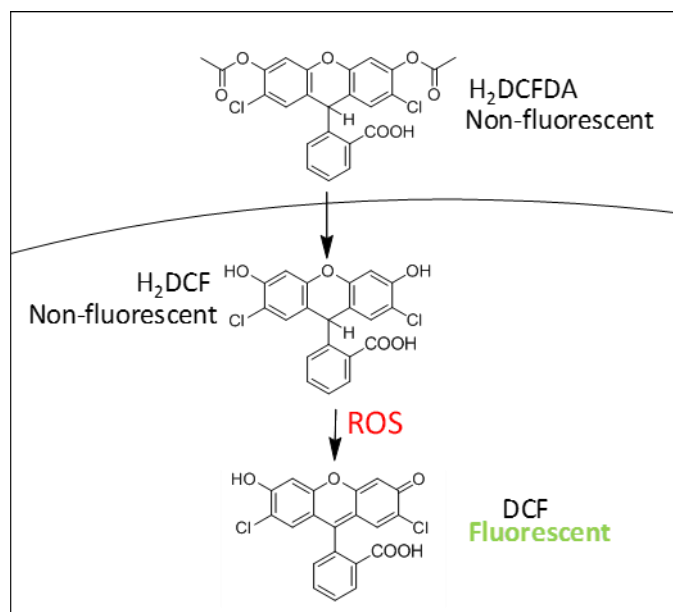
Scheme 2.2. Generation of the DCF by intracellular ROS.

The results obtained after 72 h treatment are presented herein (**Figure 2.9**) and reveal that, in general, **HL1** and **H₂L2** ligands are not producing intracellular ROS, this is in line with the fact that they are not redox active as previously reported.[1] Moreover, the ligands are not producing any cytotoxic effect on cells (Section 2.1.4.1). The controls H_2O_2 and $CuCl_2$ produce higher amounts of intracellular ROS compared to the control cells for the A2780 and IMR-90 cell lines. Different situation is observed for MCF-7 cells, where the production of ROS by these agents was not significant in comparison with the control cells. For the case of HUVEC cells $CuCl_2$ was able to produce intracellular ROS, while for H_2O_2 almost no effect was observed. (**Figure 2.9**). Overall, these data correlate with the IC_{50} data (**Table 2.4**).

The complexes **C1** and **C2** generate intracellular ROS in A2780 cells but not inside MCF-7 cells, in agreement with the cytotoxic data reported in **Table 2.4**. The ROS production in A2780 correlates with the cytotoxic activities of the complexes **C1** and **C2**, (IC_{50} = 29.68 and 30.43 μM, respectively).
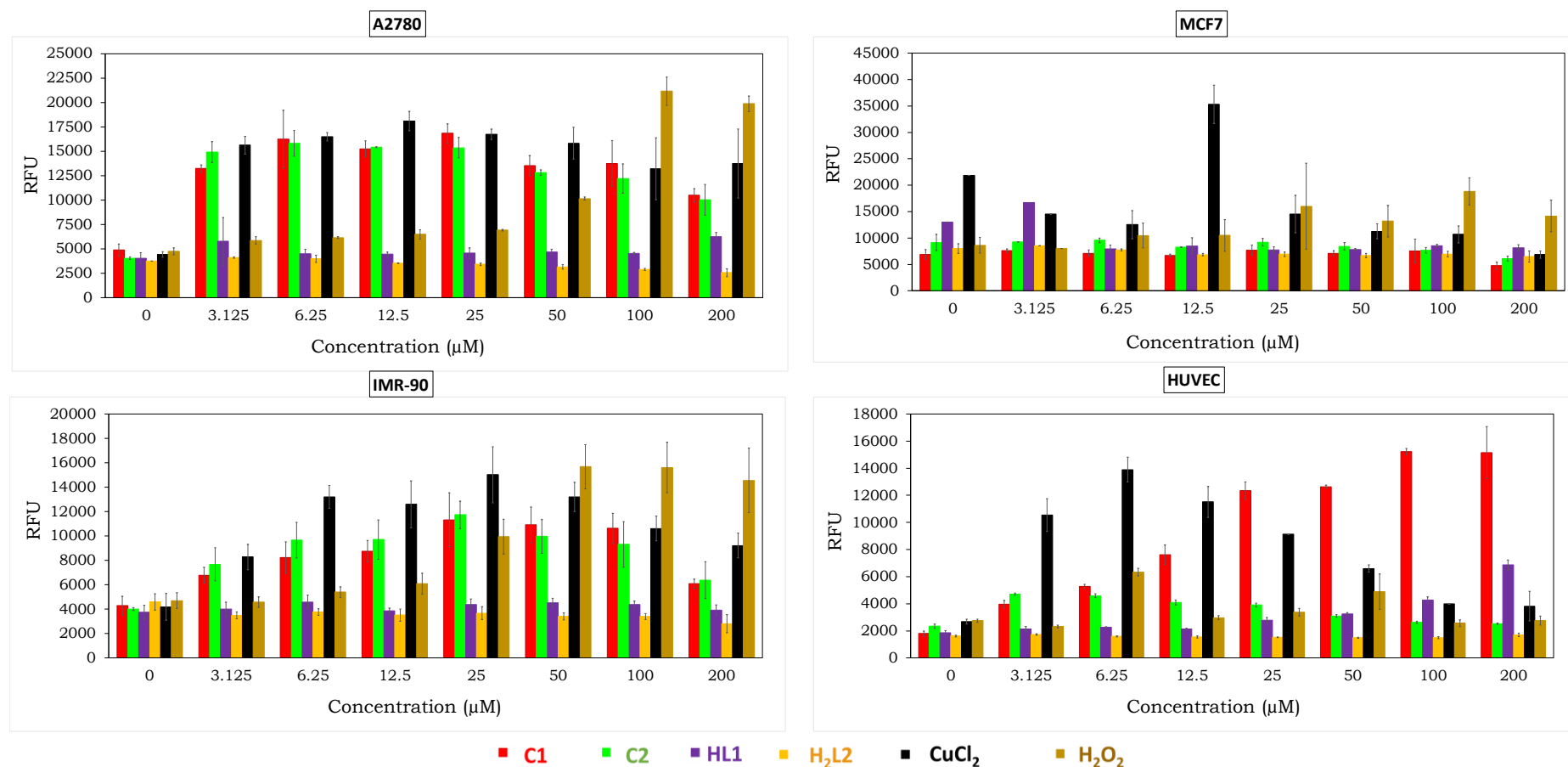
Figure 2.9. Intracellular induced ROS production assayed with DCFDA in A2780, MCF-7, IMR-90 and HUVEC cell lines after 72 h incubation with the **HL1**, **H₂L2**, **C1**, **C2**, and the controls H_2O_2 and $CuCl_2$ at different concentrations. Values (expressed in relative fluorescent units, RFU) are mean of 3 experiments.

The complexes **C1** and **C2** also generate ROS inside the IMR-90 cell line. The amount is lower than that produced by H_2O_2 at high concentrations and slightly lower than that produce by $CuCl_2$ in all the concentration range tested. This trend correlates with the cytotoxic data. In HUVEC, only **C1** produces significant intracellular ROS.

In summary, these results indicate that **C1** and **C2** complexes have a similar behavior. They can internalize into cancer and normal human cells (4 h) showing a higher uptake in the last cells (**Table 2.6**). Interestingly, their cytotoxicity in A2780 cells is higher than in normal cells (IMR-90 and HUVEC) indicating that indeed **C1** and **C2** are more toxic in these cancer cells than in normal ones.

The cytotoxic effect of **C1** and **C2** in A2780 cells is consistent with their abilities to generate intracellular ROS. The IC_{50} values for **C1** and **C2** in A2780 are respectively 29.68 and 30.43 μM and **Figure 2.10** summarizes the intracellular ROS production induced by the complexes at 25 mM (the closest assayed concentration to their IC_{50}). At 4 h, both **C1** and **C2** complexes can generate *ca.* twice the amount of ROS observed on control A2780 cells and similar amounts than the ones produced by the positive control H_2O_2 and $CuCl_2$. It should be noticed that the internalization values of **C1** and **C2** are largely lower than the internalization of $CuCl_2$. After 72 h of treatment, i.e. the same time of the cytotoxic assays, the intracellular ROS almost reached 4-fold in respect to the control cells. Under these conditions, **C1** and **C2** can produce a similar amount of ROS than $CuCl_2$

C2 is better to generate ROS in A2780 considering the low uptake of **C2** regarding **C1** in these cells (8.24 *vs* 4.02 $\mu g_{Cu}/mg_{protein}$, respectively for **C1** and **C2**) and the cytotoxicity values (**Table 2.4**).

On the contrary, on MCF-7 cells, no induction of ROS by the complexes is observed. This fact agrees with the cytotoxic experiments and with the low uptake of **C1** and **C2** by these cancer cells.
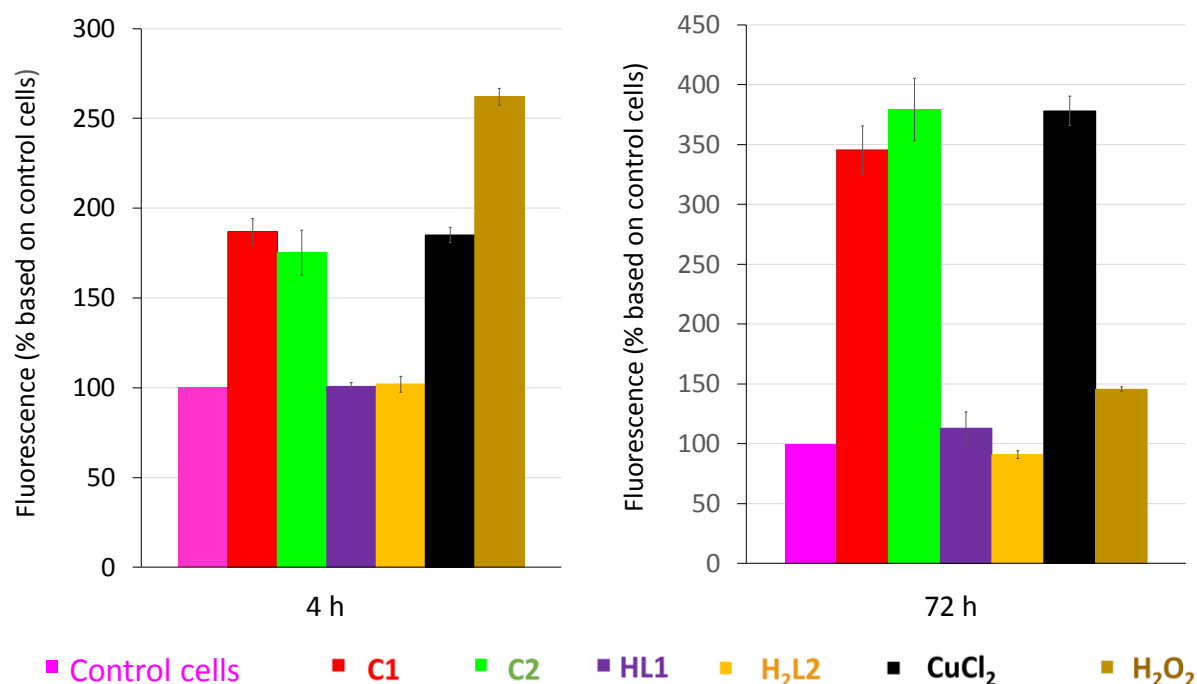
Figure 2.10. Intracellular induced ROS production assayed with DCFDA in A2780 cells after 4 and 72 h incubation with the **C1**, **C2**, **HL1**, **H₂L2** and the positive controls H_2O_2 and $CuCl_2$ at 25 μM. Values are mean of 3 experiments. Control cells = untreated cells.

All these results highlight that production of intracellular ROS and copper uptake are crucial aspects to consider in the final cytotoxicity of **C1** and **C2** complexes. Therefore, improving both or any of these aspects should enhance the final biological activity. The promising data obtained in A2780 cells where the cytotoxic effect of **C1** and **C2** is consistent with their abilities to generate intracellular ROS encouraged the modification of the ligands **HL1** and **H₂L2** in order to provide enhanced cytotoxic activities to the resulting complexes, i.e. improve their Cu(II)/Cu(I) redox cycling process.

2.2. Synthesis and characterization of the ligand L3.

The structure of the ligands **HL1** and **H₂L2** allows the formation of stable Cu(II) complexes, **C1** and **C2**, that have low redox potentials and present a nonreversible Cu(II) $\rightleftarrows$ Cu(I) one electron redox process (Section 2.1). This impacts their ability to produce ROS and therefore their cytotoxic activity. As a proof of

concept, the ligand **HL1** was modified in order to enhance the redox activity of the corresponding Cu(II) complex. For that aim, the amide nitrogen was methylated to block the formation of the amidate and weaken the Cu(II)-nitrogen amide bond.

The new ligand **L3** was prepared manually by standard solid phase peptide synthesis starting from the commercially available Fmoc-N-Me-His(Trt)-OH and using the rink amide resin. A similar method to the one used for the synthesis of its analog **HL1** was employed (**Scheme 2.3**).
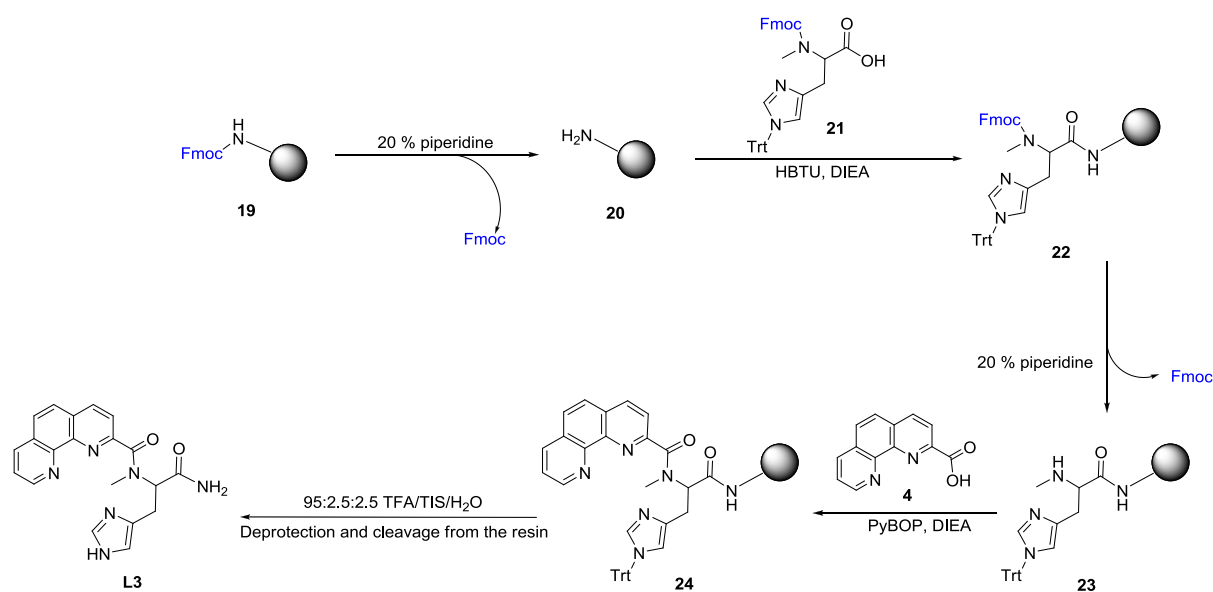
Scheme 2.3. Synthetic route of **L3**.

After the removal of the Fmoc protecting group of the rink amide MBHA resin with 20 % of piperidine, the Fmoc protected N-methylated His (**21**) was attached to the resin in NMP using HBTU as activator and DIEA as base. The Fmoc group was subsequently removed using 20% piperidine and the Phen unit (**14**) was coupled in NMP, using this time PyBOP as coupling agent. Simultaneous deprotection and cleavage from the resin were done by treating the resin with a solution containing TFA/TIS/ H$_2$O 95:2.5:2.5 (v/v/v) for 2 h. The resin was removed by filtration, the solution was concentrated using a steam of N$_2$ and the crude ligand was precipitated by addition of cold diethyl ether. The crude ligand was purified by preparative reversed-phase HPLC and the purity was verified by analytical reversed-phase HPLC (greater than 97 %). **L3** was characterized by

ESI-MS: m/z calc. for $[\textbf{L3} + H]^+$ = 375.16, found 375.1 ± 0.5. Interestingly, the ^{1}H and ^{13}C NMR spectra (see **Figure A.9** and **Figure A.10** in Annex) showed two set of chemical shifts for each expected signal with a 2:1 ratio (**Figure 2.11**).
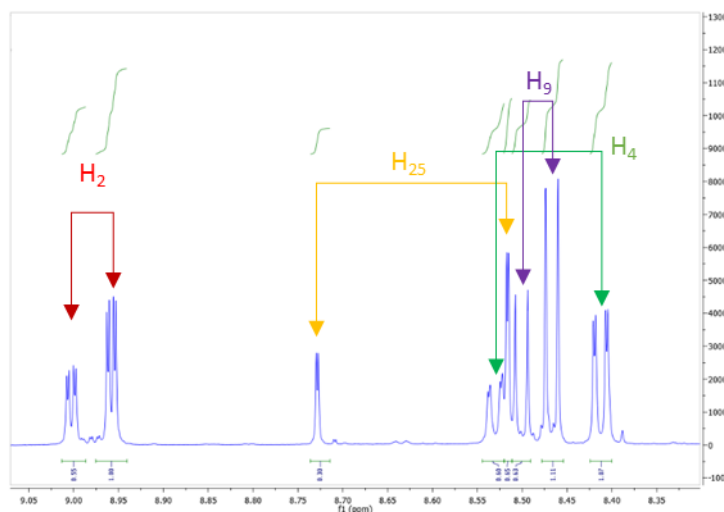
Figure 2.11. ^{1}H NMR (600 MHz, D$_2$O) spectrum (expansion). Arrows indicate the duplicated signals for H$_2$ (red) H$_{25}$ (yellow) H$_9$ (purple) and H$_4$ (green) (see **Figure 2.12** for numbering).

The presence of two times the number of signals expected in the ^{1}H and ^{13}C NMR spectra, but only one molecular weight according to ESI-MS and one single peak on analytical HPLC, suggested racemization or different conformers in solution. In order to gain insights into this fact, the ligand was analyzed in different chiral columns (i.e. Chiralpak IA, IB, IC, ID, IE, IF, IG, AD-H, AZ-H, Lux-Amylose-2, Lux-Cellulose-3, Lux-Cellulose-4 and Chiralcel OD-3) in the platform of chiral chromatography at Aix-Marseille University (https://ism2.univ-amu.fr/fr/plateforme-chromato-chirale) and in every case, a single peak was observed. These results excluded the possible racemization of the ligand during its synthesis.

Two-dimensional Nuclear Overhouser Effect NMR spectroscopy (2D NOESY) was then carried out in order to study the intramolecular through-space interactions of the ^{1}H nuclei in **L3** (**Figure A.11** in Annex). The NOESY data

indicate that the two sets of observed signals correspond to the same compound **L3** in two different conformations (**Figure 2.12**, A).
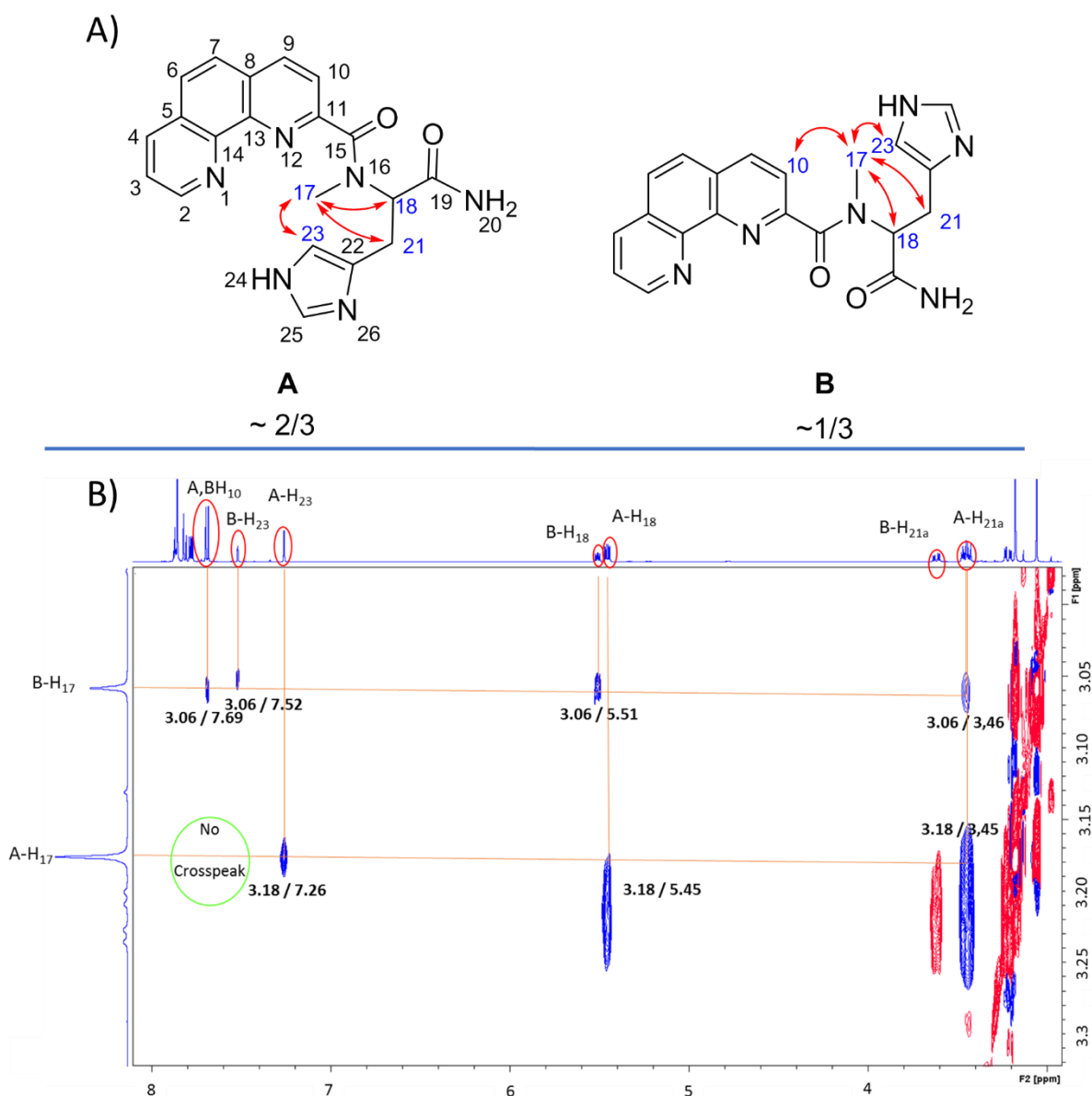
Figure 2.12. **L3** two major conformers in solution (A). 2D NOESY (partial) spectra recorded in D$_2$O at 600 MHz (B): Scalar coupled partners are shown in red while NOE cross peaks are shown in blue.

The structures for the conformers **A** and **B** (**Figure 2.12**, A) are proposed based on the different intramolecular through-space interactions (NOE cross peaks) seen between the ^{1}H of the conformer **A** and the ^{1}H of the conformer **B**; remarkably for the H$_{17}$ (methyl group) showing cross peaks with H$_{18}$, H$_{21}$ and H$_{23}$

for the conformer **A**, and cross peaks with H_{18}, $H_{21,}$ H_{23} and H_{10} for the conformer **B**. Additionally, it is possible to observe another small ^1H signals with weak cross peaks reflecting that there is at least another conformation of the **L3** ligand (~ 1/8). However, the intensity of these signals and of the correlations was too small to be analyzed.

Further NMR analysis were performed to check if temperature and solvents could affect the ratio of the conformers. A temperature dependent ^1H NMR experiment between 300 and 350 K was carried out. In addition, experiments replacing D_2O with MeOD-d4 and acetone-d6 were recorded. However, the differences observed respect to the initial ratio (2:1) between the two species were not significant in any case.

2.3. Study of the Cu coordination properties of L3.

The coordination of **L3** with Cu was studied under different conditions and using different spectroscopic techniques. Several issues were encountered during these studies and they are described on the following sections.

2.3.1. Cu(II) coordination of L3 in water.

The UV-Vis spectra of a solution containing equimolar amounts of **L3** and $CuCl_2$ (0.5 mM) were recorded at different pH values to investigate the coordination of Cu(II) to **L3** upon pH change. The pH value was increased by adding varying volumes of 0.5 M NaOH solution. UV-vis spectra were collected between pH 4.0 and 10.0 and showed a strong increasing absorption band at 470 nm. The band at 470 nm was intense enough to saturate the signal. The experiment was repeated at 0.1 mM concentration (**Figure 2.13**) and the same behavior was observed. Replacing the Cu(II) source for $Cu(NO_3)_2$ did not change anything. In all cases, the colorless solution turned yellowish between pH 4.0 and 6.0, subsequently it became yellow at pH 7.0 and finally turned red as the pH was increased. An absorption d-d band at 650 nm is observed indicating the formation of a Cu(II) specie, however this band is rapidly overlapped by the intense absorption band appearing at 470 nm. Re-adjusting the pH to 3.0 did not produce

any effect, i.e. the solution remained red and the band at 470 nm did not disappear. These results point most likely to an irreversible process that could or not affect the ligand.
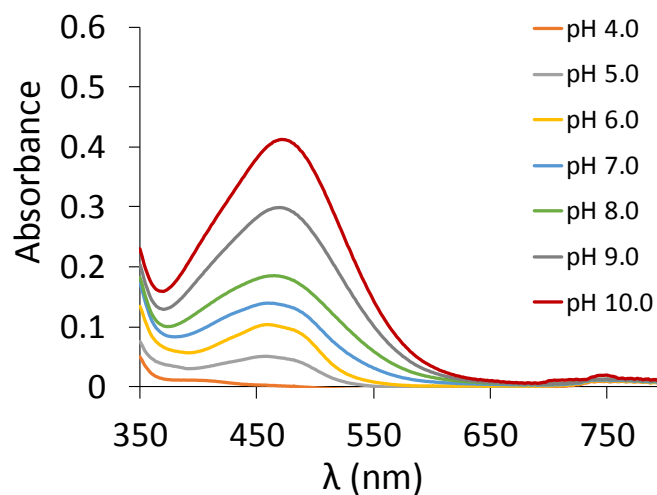
Figure 2.13. UV-vis spectra of a solution containing equimolar amounts of **L3** and $CuCl_2$ (0.1 mM) at different pH values.

In another experiment, the solution containing the equimolar amount (0.5 mM) of **L3** and $CuCl_2$ at pH 7.0 was monitored over time. It was observed an increase in the absorbance of the band at 470 nm indicating that this increase is independent of the pH changes (**Figure 2.14**).
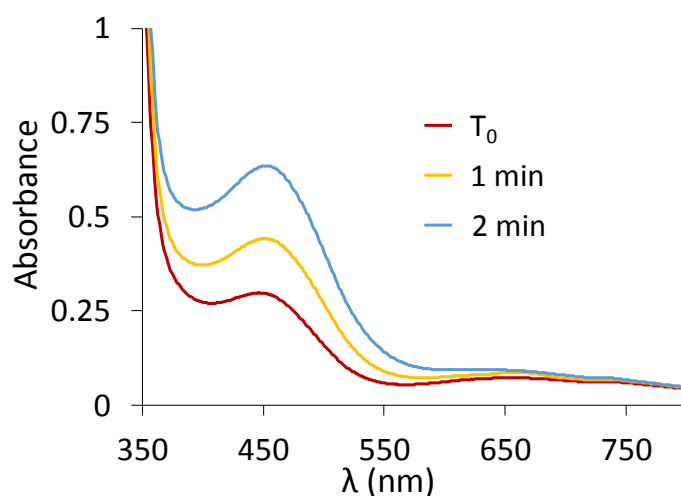
Figure 2.14. Evolution overtime of the UV-vis spectra of a solution containing equimolar amounts of **L3** and $CuCl_2$ (0.5 mM) at pH 7.0.

In order to discard the possibility that the effect was due to a change in the ligand upon increasing pH, a UV-vis pH titration was done only with the ligand. The formation of the band at 470 nm was not observed (**Figure 2.15**) and the solution remained colorless.
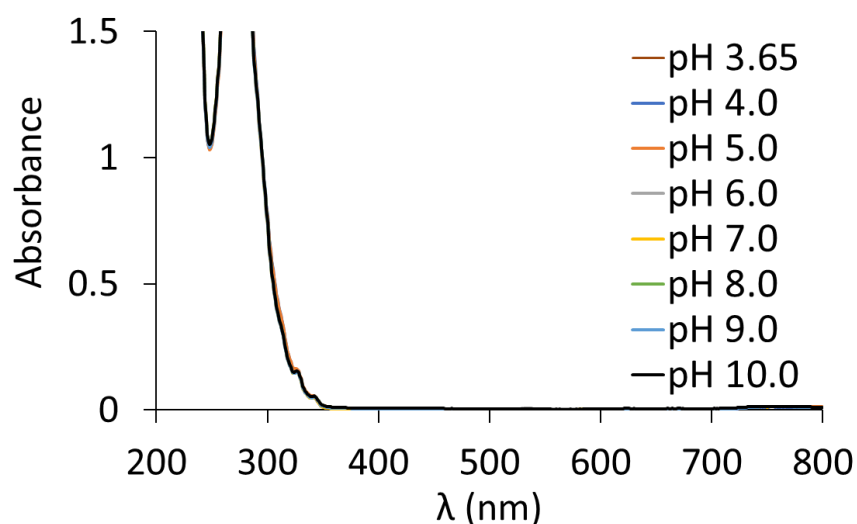
Figure 2.15. UV-vis pH titration spectra recorded at 298 K
of a solution containing **L3** (0.1 mM).

The data obtained so far indicate that the process is induced by the presence of Cu(II) at pH ≥ 4.0. Additionally, further experiments were done under anaerobic conditions, but no significant effect in the generation of the band at 470 nm was observed, suggesting that the reaction involved does not need O_2 to occur.

To obtain more information about the system Cu(II)-**L3**, electron paramagnetic resonance (EPR) spectra of a solution containing 1 mM of **L3** and 1 equiv. of $CuCl_2$ were recorded at different times after adjusting the pH to 7.0. For that, aliquots of 0.2 mL were collected at the initial time (t_0), after 40 mins, and after the stabilization of the UV-vis band at 470 nm (5 h) (**Figure 2.16**).
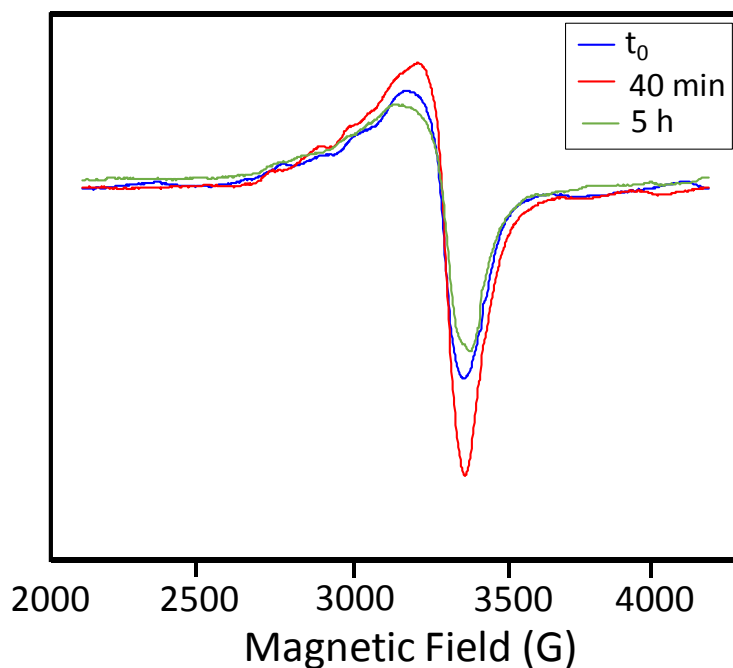
Figure 2.16. The X-band EPR spectra of the frozen solution at 120 K containing **L3** (1 mM) and 1 equivalent of $CuCl_2$ in H_2O at pH 7.0 recorded at the initial time (blue), after 40 minutes (red) and after 5 h (green). The solution contained 10% glycerol.

The obtained spectra are large and un-resolved. This indicates a mixture of species with different environments and/or copper centers that are close to each other (i.e. polymeric or weakly coupled species where the spin-spin dipolar interaction may lead to enlargement). Only from the EPR spectrum recorded at the initial time (**Figure 2.16**, blue curve) it was possible to estimate some parameters of the main species: $g_{//} = 2.23$, $g_{perp} > 2$, $A_{//} = 140 \times 10^{-4}$ cm^{-1} and $g_{//}/A_{//} = 140 \times 10^4$ cm.[1] It has to be noticed that these values were not extracted from simulation, they were estimated directly from the spectrum reading due to the fact that the EPR spectra were un-resolved. These parameters suggest that the Cu atom is in distorted square-planar or square pyramidal geometry with possible equatorial ligands containing 2 N and 2 O donors. Although the EPR spectra do not allow any further interpretation, the data support the presence of different Cu containing species and correlates with the UV-vis data where an absorbance band is observed at 650 nm.

2.3.2. Cu(II) coordination properties of L3 in methanol.

The coordination of Cu to **L3** was studied in anhydrous MeOH to check if H_2O could play a role in the behavior observed. For that, the UV-vis spectra of 0.5 mM **L3** in MeOH were recorded overtime (**Figure 2.17**), A) after the addition of 1 equiv. of anhydrous Cu acetate (anhydrous $Cu(OAc)_2$ in MeOH). After 40 h, no more changes were observed. The addition of Cu to **L3** produced the same effect than the one observed in H_2O, i.e. the appearance of an absorption band at 470 nm. The band increased slower in comparison with the experiments done in H_2O.
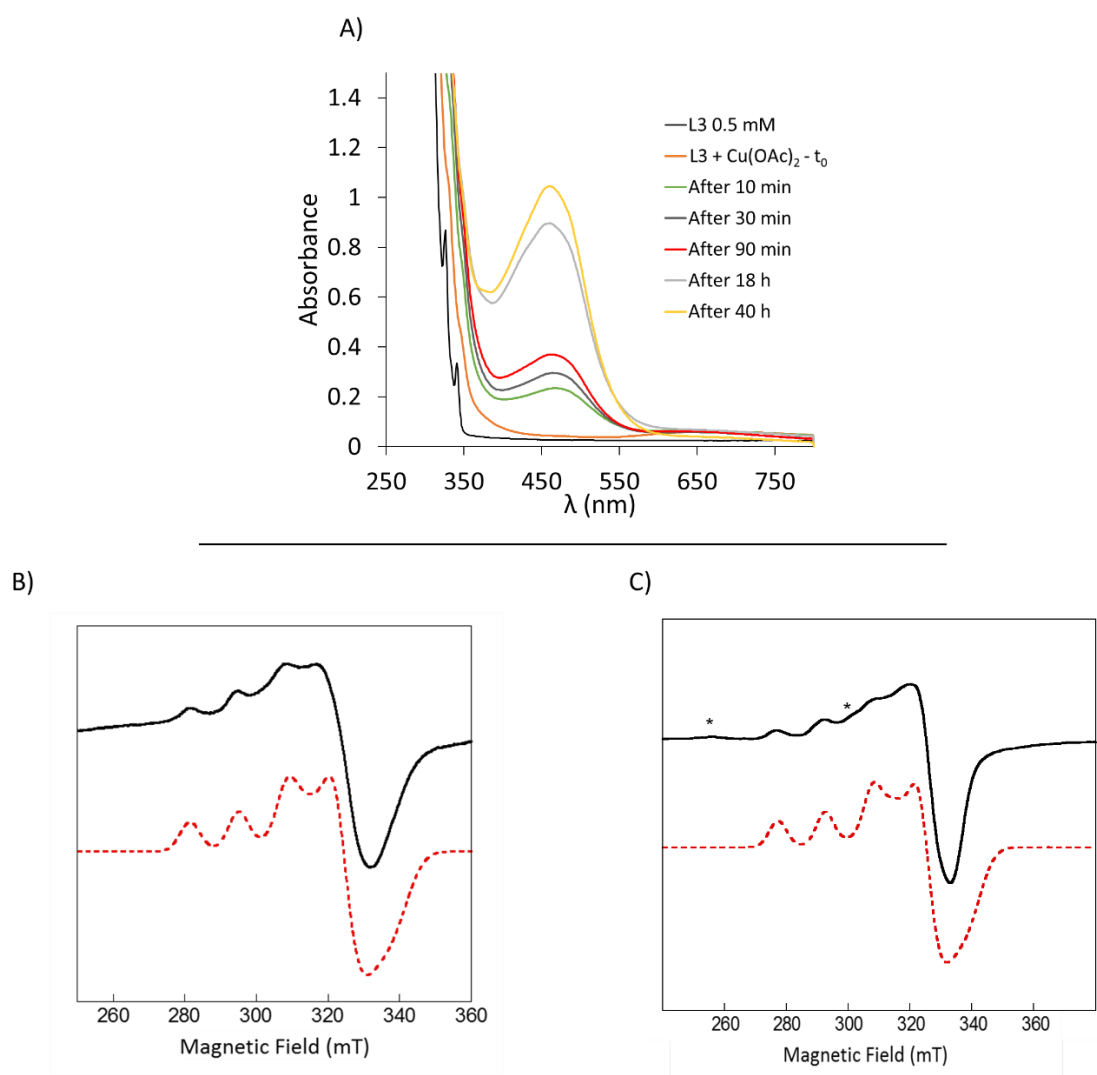
Figure 2.17. (A) UV-vis spectra of 0.5 mM **L3** with 1 equiv. of $Cu(OAc)_2$ in MeOH recorded at different times. (B) EPR spectra of a frozen solution at 120 K containing 0.5 mM **L3** with 1 equiv. of $Cu(OAc)_2$ in MeOH after 90 mins and (C) after stabilization of the UV-vis signal (40 h). Red dashed curves represent the simulated spectra of the major species, while * points the signals for the minor Cu(II) species.

EPR spectroscopy was also carried out. Aliquots for EPR analysis were sampled 90 min after the addition of $Cu(OAc)_2$ and after the stabilization of the UV-vis spectra (40 h). Both EPR spectra showed at least two different species in solution, (**Figure 2.17**, B and C). The parameters are indicative of an electron in d_{x2-y2} orbital and thus of Cu ions in distorted geometries from ideal square-planar or square pyramidal ($g_{//}/A_{//} > 130 \times 10^4$ cm)[24] (**Table 2.7**).

Table 2.7. EPR parameters obtained for solutions of **L3** (0.5 mM) and 1 equiv. of $Cu(OAc)_2$ in MeOH at 90 minutes and 40 h.

Sample	$g_{//}$	$A_{//}$ $(10^{-4}\,cm^{-1})$	g_{perp}	$g_{//}\,/\,A_{//}$ $(x\,10^4\,cm^1)$	Ligands[25]
90 min	2.223	139	*	161	N_3O or N_4
40 h	2.246	157	*	143	N_3O or N_2O_2

*Not determined

These data are in agreement with the data obtained in aqueous media and highlight the presence of different Cu species in solution.

2.3.3. Cu(I) coordination properties of L3 in water.

To obtain more insights about the effect observed when adding Cu(II) to the **L3**, the coordination experiment was repeated using Cu(I) and anaerobic conditions. Namely, the UV-Vis spectra of a solution containing **L3** (30 µM) in 50 mM HEPES buffer pH 7.0 were recorded before and after the addition of 1 equiv. of tetrakis(acetonitrile)copper(I) (**Figure 2.18**, A). The addition of Cu(I) produced a shift on the UV-Vis absorption band of **L3** at 270 nm suggesting the coordination of Cu(I). No changes on the spectra were observed for 4 h. Interestingly, these spectra did not show the band at 470 nm that appeared in presence of Cu(II). After 4 h air was added into the system and the solution was monitored by UV-vis for 4 additional hours. The band at 470 nm appeared over time after air exposure (**Figure 2.18**, B).

This is consistent with the oxidation of Cu(I) into Cu(II) and therefore the generation of the non-stable Cu(II)—**L3** system. The intensity of the UV-vis absorption band at 277 nm decreased as the new band at 470 nm appeared (**Figure 2.18**, B). The fact that the absorption band of the free **L3** ligand is not recovered suggests a chemical change in **L3** in the presence of Cu(II).
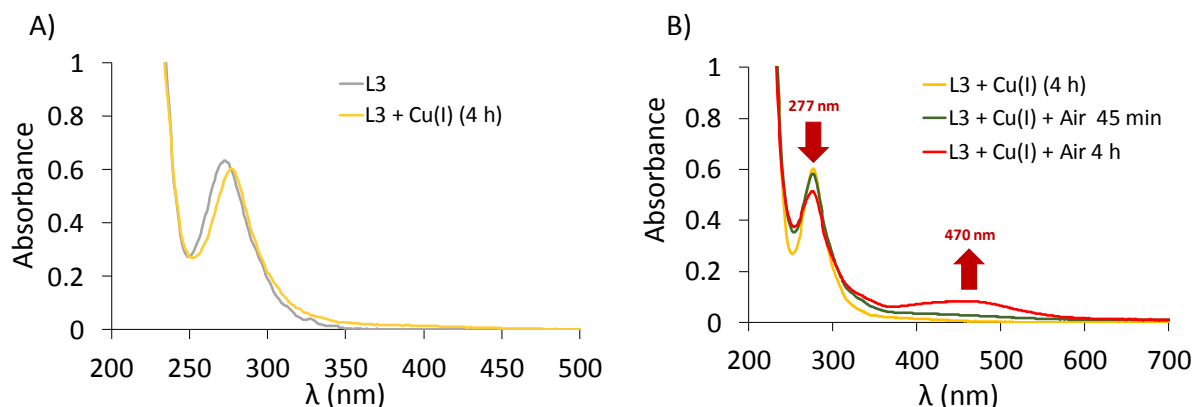
Figure 2.18. UV-vis spectra of **L3** (30 μM) in 50 mM HEPES buffer pH 7.0: A) before and 4 h after the addition of 1 equiv. of Cu(I) under anaerobic conditions; B) after the addition of air at different times.

2.4. L3 + Cu(II) → ?: ESI-MS and MS/MS analysis.

In order to obtain more insights about the process occurring after the interaction of **L3** with Cu(II), mass spectra analyses were carried out at different values of pH and different times.

Three solutions containing 1 mM of **L3** and 1 equiv. of CuCl$_2$ were prepared at different pH values (3.0, 7.0 and 10.0) and analyzed at different times (see Annex **Scheme A.1** and **A.2**). The different species found at the initial time (t$_0$) are shown in the **Table 2.8**. At pH 3.0, 5 major species were detected: the species (**1a**) corresponding to the Cu(II) complex of the ligand **L3** and with the higher signal intensity, the species (**2a**) found with a smaller signal intensity and corresponding to the Cu(I) complex of **L3**, the species (**3a**) and (**4a**) corresponding to the specie (**1a**) with a molecule of trifluoroacetic acid (TFA) and chloride, respectively, and finally, the species (**5a**), that corresponds to the free ligand **L3**.
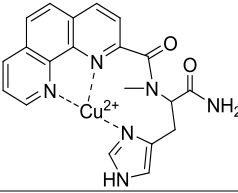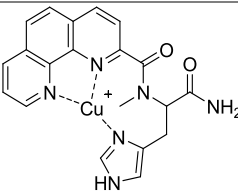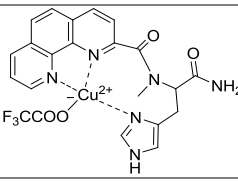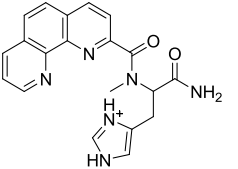
Table 2.8. Species and structures proposed for the m/z found by ESI-MS analysis after the addition (initial time) of 1 equiv. of CuCl$_2$ to **L3** at 298 K, and pH 3.0, pH 7.0 and 10.0.

pH	Species	m/z	m/z calc.	Condensed formula	Proposed structure	%*
				t_0		
3.0	**1a**	218.5417	437.0776	$[C_{20}H_{18}CuN_6O_2]^{2+}$		100.0
	2a	437.0835	437.0782	$[C_{20}H_{18}CuN_6O_2]^{+}$		34.0
	3a	550.0679	549.9739	$[C_{22}H_{18}CuF_3N_6O_4]^{+}$		25.0
	4a	472.0576	472.0476	$[C_{20}H_{18}ClCuN_6O_2]^{+}$		16.0
	5a	375.1613	375.1491	$[C_{20}H_{18}N_6O_2]^{+}$		6.0.
7.0, 10.0	**6a**	436.0782	436.0698	$[C_{20}H_{17}CuN_6O_2]^{+}$	[**1a** – H]	100.0
	1a	218.5417	437.0776	$[C_{20}H_{18}CuN_6O_2^2]^{+}$		3.0
	5a	375.1613	375.1491	$[C_{20}H_{18}N_6O_2]^{+}$		6.0

*Percentage of the signal intensity.

At pH 7.0 and pH 10.0, only 3 main species were found: the one with the highest intensity corresponds to the species (**1a**) minus a H⁺ (species (**6a**)), and the other two species that are present with very small intensities are the species (**1a**) and (**5a**). Since the spectra of the solution at pH 7.0 and the one at pH 10.0 contained the same species with similar intensities, it was decided to work further only with the solution at pH 3.0 and 7.0. All the solutions were again analyzed after 18 h at room temperature in order to check the evolution of the species overtime. The results are compiled in **Table 2.9**. At pH 3.0 the species and proportions found indicated small changes compared to the initial time, i.e., the species (**4a**) was detected with a higher signal intensity.

Table 2.9. Species and structures proposed for the *m/z* found by ESI-MS analysis after 18 h of the addition of 1 equiv. of CuCl$_2$ to **L3** at 298 K and pH 3.0.

		t = 18 h			
Species	*m/z*	*m/z* calc.	Condensed formula	Proposed structure	%*
1a	218.5417	437.0776	$[C_{20}H_{18}CuN_6O_2]^{2+}$		100.0
4a	472.0576	472.0476	$[C_{20}H_{18}ClCuN_6O_2]^+$		50.0
2a	437.0835	437.0782	$[C_{20}H_{18}CuN_6O_2]^+$		30.0
3a	550.0688	549.9739	$[C_{22}H_{18}CuF_3N_6O_4]^+$		16.0
5a	375.1613	375.1491	$[C_{20}H_{18}N_6O_2]^+$		4.0

*Percentage of the signal intensity.
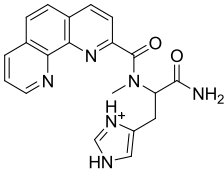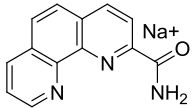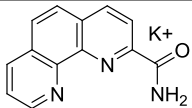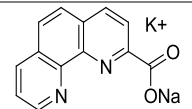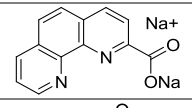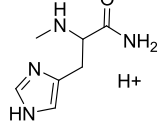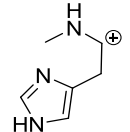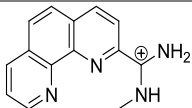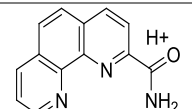
On the contrary, at pH 7.0, a mixture of several peaks (containing or not Cu(II) and Cu(I)) was found, unfortunately its complexity represented a limitation to elucidate the structures. These results are in line with the previous EPR experiments (**Figure 2.16**) where several Cu(II) species were observed in solution at pH 7.0.

In order to obtain more information of the species present in solution after 18 hours of the addition of Cu(II) at pH 7.0 and to know if it was possible to recover the intact ligand after 18 hours of the addition of Cu(II) at pH 3.0, EDTA was added to the solutions prior to the ESI-MS analysis. The results are shown in **Table 2.10**. The ligand **L3** (species (**5a**)) was recovered intact from the solution at pH 3.0 indicating that **L3** was stable under these conditions even after 18 h. On the other hand, for the sample at pH 7.0 many peaks were detected corresponding to different organic compounds and pointing to the degradation of the ligand **L3** in the presence of Cu(II). The fact that different Phen derivatives were observed (**Table 2.10**, species (species (**7a**) – (**14a**)), suggests that there is more than one pathway of degradation of the ligand.

Additionally, to verify that the compound observed in solution by ESI-MS at pH 3.0 after 18 h and after the addition of EDTA corresponds to the unmodified ligand **L3**, MS/MS experiments were performed on both: on the pure ligand **L3** and the compound recovered after the addition of EDTA.

The MS/MS spectra (**Figure 2.19**) show the same fragmentation pattern for both samples. These results demonstrate that the ligand **L3** is not modified by Cu(II) at pH 3.0. This fact was also confirmed by analytical reversed-phase HPLC analyzing the same solution used in ESI-MS analysis and comparing it with a solution containing pure **L3** (see **Figure A.14**).

Table 2.10. Species and structures proposed for the *m/z* peaks found by ESI-MS analysis after adding 3 equiv. of EDTA to the solutions incubated for 18 h after the addition of 1 equiv. of CuCl$_2$ to **L3** at 298 K and at pH 3.0 and 7.0.

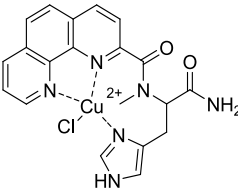| pH	Species	*m/z*	*m/z* calc.	Condensed formula	Proposed structure	%*
3.0	**5a**	375.1599	375.1491	[C$_{20}$H$_{18}$N$_6$O$_2$]$^+$		100.0
7.0	**7a**	246.0636	246.0637	[C$_{13}$H$_9$N$_3$ONa]$^+$		100.0
	8a	262.0377	262.0377	[C$_{13}$H$_9$N$_3$OK]$^+$		48.0
	9a	285.0035	285.0037	[C$_{13}$H$_7$N$_2$O$_2$NaK]$^+$		28.0
	10a	269.0297	269.0297	[C$_{13}$H$_7$N$_2$O$_2$Na$_2$]$^+$		22.0
	11a	169.1083	169.1084	[C$_7$H$_{12}$N$_4$OH]$^+$		10.0
	12a	124.0870	124.0869	[C$_6$H$_{10}$N$_3$]$^+$		5.0
	13a	237.1136	237.1135	[C$_{14}$H$_{13}$N$_4$]$^+$		3.0
	14a	224.0819	224.0818	[C$_{13}$H$_9$N$_3$OH]$^+$		1.5

*Percentage of the signal intensity.
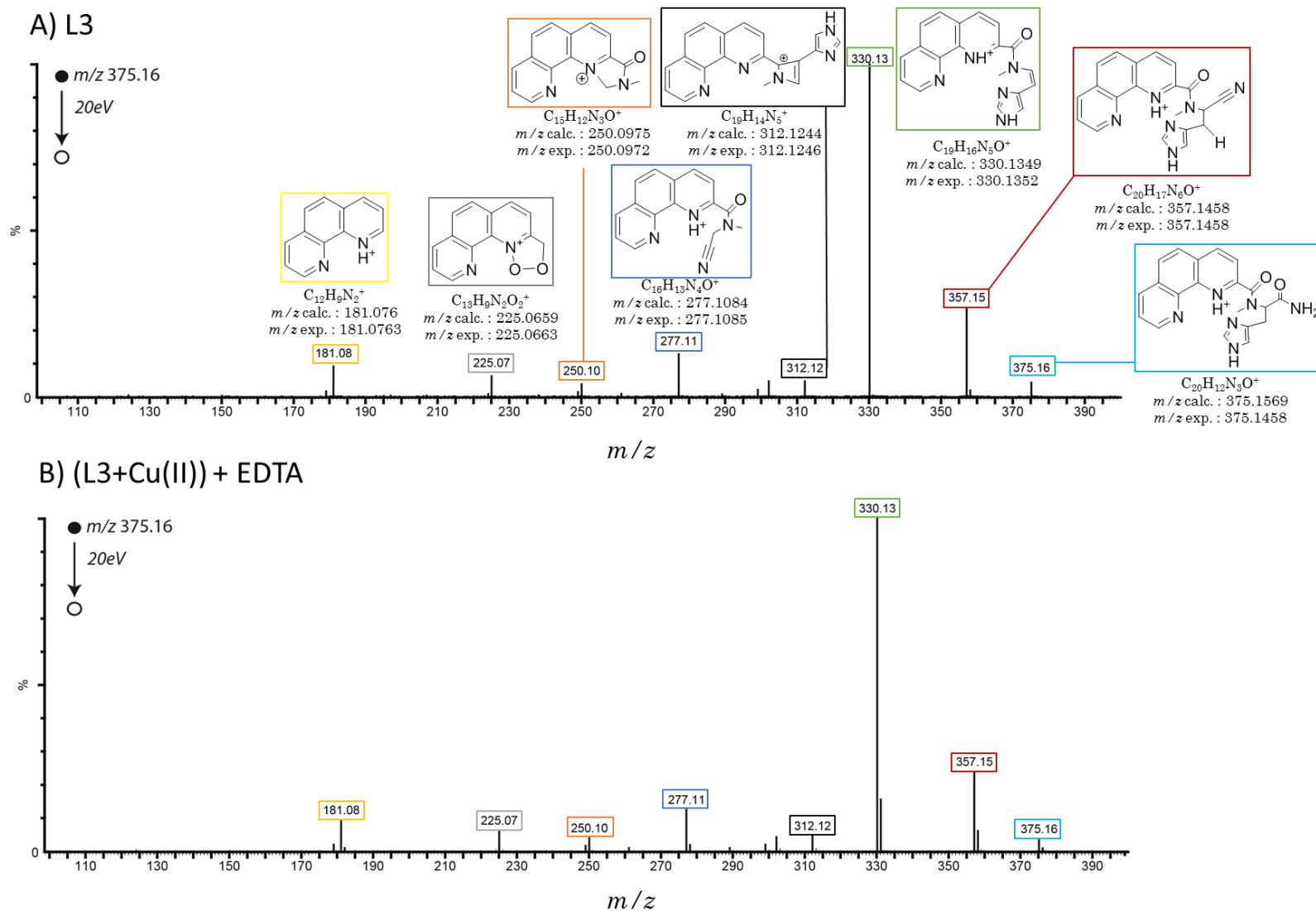
Figure 2.19. ESI/MS/MS fragmentation pattern of **L3** pure (A) and after adding 3 equiv. of EDTA to the solution incubated for 18 h after addition of 1 equiv. of $CuCl_2$ pH 3.0.

To obtain more information about the Cu(II) species present at pH 3.0, the EPR spectra of a solution containing equimolar amounts of **L3** and $CuCl_2$ (1 mM) were recorded at t = 0 and after 18 h (**Figure 2.20**, A). The spectra revealed that there is "free" Cu(II) in solution both at t = 0 and after 18 h. To determine the EPR parameters of the Cu(II) species observed at pH 3.0, the "free" Cu spectrum was subtracted and the final spectrum simulated (**Figure 2.20**, B) The EPR parameters and the approximate quantity of the Cu(II) species are reported in **Table 2.11**.
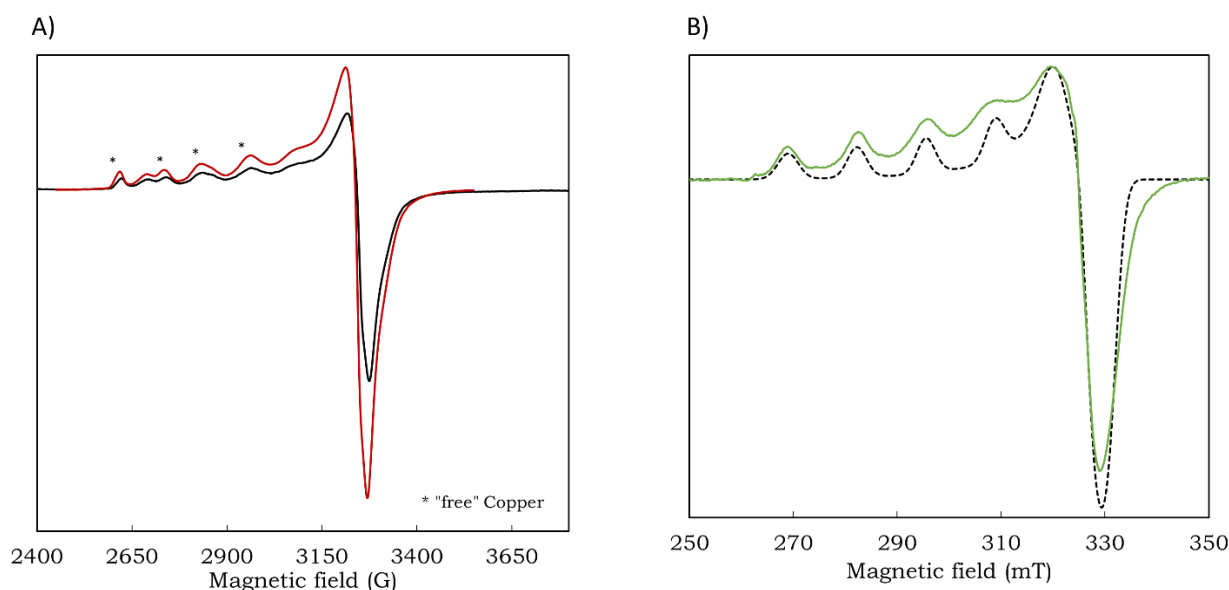
Figure 2.20. EPR spectra of **L3** (1 mM) with 1 equiv. of $CuCl_2$ in H_2O with 10 % glycerol at pH 3.0. A) t = 0 (black curve) and 18 h (red curve). B) The EPR spectrum after subtraction of the "free" Cu(II) (green curve). The dashed curve represents the simulated spectra.

Sagakushi and Addison[24] showed that the $g_{//}/A_{//}$ ratio can be used as a useful empirical index of tetrahedral distortion. The value ranges from approximately 105 to 135 cm for square-planar structure and the quotient increases upon the introduction of tetrahedral distortion contributions. Using this relationship and the parameters obtained from the simulation (**Table 2.11**) we can posit that the species observed at pH 3.0 most likely displays a distorted squared planar or square pyramidal geometry. Additionally, according to Peisach-Blumberg correlations for *g* and *A* values,[25] the equatorial ligands of the Cu(II)

center are most likely 2 N and 2 O donors. This could correspond to a Phen unit and two water molecules.

Table 2.11. EPR parameters obtained at t = 0 after the subtraction of the "free" Cu(II) (**L3** (1 mM) and 1 equiv. of CuCl$_2$ in H$_2$O with 10% glycerol at pH 3.0).

	%	$g_{//}$	$A_{//}$ (10^{-4} cm^{-1})	$g_{x/y}$	$g_{//}/A_{//}$ (10^4 cm)
L3–Cu(II)	50 - 60	2.336	142	2.09/0.06	164.7
Free Cu	40 - 50	2.413	132	2.081/2.081	183.0

These results show that the methylation of the amide N altered totally the stability and coordination properties: while the parent ligand **HL1** is able to coordinate Cu(II) generating stable Cu(II) complexes in the 3.0 to 10.0 pH range, **L3** is not stable in presence of Cu(II) at pH values higher than 4.0 conditions from which the coordination to His and to the carbonyl group of the amide could occur. The mechanism of the degradation of the ligand remains unclear so far. However, the species reported in **Table 2.11** seem to indicate that the amide bond becomes unstable upon the coordination of Cu(II) to **L3**. Under the assumption that Cu(II) will coordinate to the oxygen atom of the amide bond (due to the methylation of the amide nitrogen), the electrophilic character of the carbon atom of the carbonyl group will increase making it more vulnerable to a nucleophilic attack. The results show that molecular oxygen is not involved in the process, and the only presence of Cu(II) and the increase of pH by the addition of base is enough to trigger the reaction. Additionally, the Cu(I) **L3** complex is stable, and the degradation process is only triggered after the oxidation of Cu(I) into Cu(II).

A better strategy for the enhancement of the redox activity of the Cu(II) complexes of the ligands **HL1** and **H₂L2** is needed that will not compromise the stability of the final ligands. In this regard, a potential modification to explore is the replacement of the amide group by a tertiary amine (**Figure 2.21**).
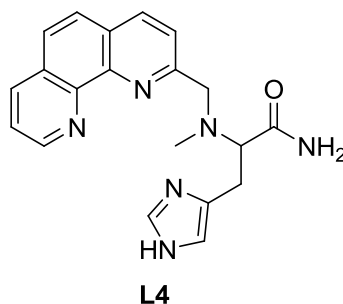
Figure 2.21. Structure of the proposed new ligand **L4**.

2.5. Conclusions and final remarks.

This section was devoted to study in more detail the anticancer properties of the Cu(II) complexes **C1** and **C2** since it was previously reported their cytotoxic activities in A2780 and MCF-7 human cancer cell lines. As DNA stands as one of the most studied targets for many chemotherapeutic compounds, the interactions of **C1** and **C2** with *ct*-DNA were assayed. Results conclude that both complexes interact weakly with *ct*-DNA, most likely through electrostatic interactions and presenting low K_b values (3.47 for **C1** and 3.17 for **C2**). These results agree with the EBr competition studies which reflected their poor DNA intercalation abilities (**Table 2.3**). In order to evaluate their selective cytotoxicity, cytotoxic assays were carried out with the two complexes **C1** and **C2** and their relative ligands (**HL1** and **H₂L2**) in two human normal cell lines (IMR-90 and HUVEC). Additionally, for the sake of comparison (same experimental conditions), we decided to reevaluate their cytotoxic activities in the two human cancer cell lines, A2780 and MCF-7. The results indicate that while the ligands can only slightly inhibit HUVEC cells viability (**Table 2.4**), **C1** and **C2** produce a stronger cytotoxic effect on A2780 than over the two normal cell lines assayed. These results are in line with the data previously reported (**Table 2.1**). However, for MCF-7 cells, the results are

mismatching since the new studies showed no cytotoxic effect by **C2**, which displayed an IC50 value of 88 µM.[1]

The cellular uptake of **C1** and **C2** stablished that these complexes internalize more in normal than in cancer cells, interestingly the cytotoxic effect produced in cancer cells is higher than the one observed in normal cells (**Table 2.6**). On A2780, where the complexes present the higher cytotoxic effect (**Table 2.4**), **C2** internalized 52 % less than **C1**, highlighting the higher cytotoxicity of **C2** in this cell line. The cells with the lowest Cu uptake values were MCF-7, in accordance with the low cytotoxic effect showed.

C1 and **C2** induce intracellular ROS formation in IMR-90, HUVEC and in A2780. For the case of MCF-7, the production of ROS by **C1** and **C2** was low (**Figure 2.9**), these data agree with their low internalization and cytotoxic activity. In A2780, both **C1** and **C2** were able to produce intracellular ROS, comparable to the amounts produced by H_2O_2 and $CuCl_2$. (**Figure 2.10**). This observation correlates with their cytotoxicity values for this cell line (**Table 2.4**). Despite the high internalization of **C1** and **C2** complexes and their ability to generate ROS in normal cells (especially **C1** in HUVEC cells), their cytotoxic properties exhibited in these cells are low compared to the cytotoxic effects produced in A2780 cells, particularly **C2**.

Our data motivated the modification of the complexes via the modification of the correspondent ligands. In this context, the new ligand **L3** was designed. While the addition of 1 equiv. Cu(I) to **L3** at pH 7.0 under anaerobic conditions seems to lead to a stable Cu(I) complex, the addition of Cu(II) produces important irreversible changes in the **L3**. UV-vis shows the appearance an increasing pH-triggered absorption band at 470 nm that increases with time (**Figure 2.14**). This reaction in the ligand is produced also under anaerobic conditions and was observed using H_2O and MeOH as solvents. EPR spectra suggest a complex mixture of Cu(II) species, indicating the destruction of **L3**. This effect is produced only in presence of Cu(II) and it is triggered with the increase of pH. ESI-MS validate these results and indicated that at pH 3.0 it is possible observe the expected *m/z* for the complexation of the unmodified **L3** bound to Cu even after

18 h of exposure (**Table 2.8**). On the contrary, when the complexation is carried out at pH 7.0 it exists a complex mixture of Cu species and fragments of the ligand. ESI-MS and analytical HPLC confirmed the recovery of the intact **L3** after the addition of EDTA to the mixture **L3**-Cu(II) after 18 h at pH 3.0, while at pH 7.0 ESI-MS showed a mixture of different fragments of **L3** (**Table 2.10**). In line with these results, EPR spectra of the solutions concluded the presence of a mixture of Cu(II) species in solution and free Cu(II). At this level of understanding, the mechanism of the degradation of L3 remains unclear.

This work provides important hints in the understanding of the cytotoxic effects of both **C1** and **C2**, which are key to inspire a successful modification of the ligands that allows more selective and effective cytotoxic effects as well as a higher internalization. Further work is necessary to fully understand the behavior of **C1** and **C2** inside cells. Future research must be dedicated to explore the stability of these complexes in presence of the threatening glutathione/metallothionein system described by Santoro *et al.*[26] (see Section 1.2.2.1, Chapter 1), these data could provide additional insights to better understand and control these systems in order to overcome the issues encountered in the field.

2.6. Bibliography.

(1)   Leite, S. M. G.; Lima, L. M. P.; Gama, S.; Mendes, F.; Orio, M.; Bento, I.; Paulo, A.; Delgado, R.; Iranzo, O. Copper(II) Complexes of Phenanthroline and Histidine Containing Ligands: Synthesis, Characterization and Evaluation of Their DNA Cleavage and Cytotoxic Activity. *Inorg. Chem.* **2016**, *55* (22), 11801–11814. https://doi.org/10.1021/acs.inorgchem.6b01884.

(2)   Brandt, W. W.; Dwyer, F. P.; Gyarfas, E. D. Chelate Complexes of 1, 10-Phenanthroline and Related Compounds. *Chem. Rev.* **1954**, *54* (6), 959–1017.

(3)   Sigman, D.; Graham, D.; D'aurora, V.; Stern, A. Oxygen-Dependent Cleavage of DNA by the 1, 10-Phenanthroline. Cuprous Complex. Inhibition of Escherichia Coli DNA Polymerase I. *J. Biol. Chem.* **1979**, *254* (24), 12269–12272.

(4)   Sigel, H.; Martin, R. B. Coordinating Properties of the Amide Bond. Stability and Structure of Metal Ion Complexes of Peptides and Related Ligands. *Chem. Rev.* **1982**, *82* (4), 385–426.

(5)   La Mendola, D.; Magrì, A.; Santoro, A. M.; Nicoletti, V. G.; Rizzarelli, E. Copper(II) Interaction with Peptide Fragments of Histidine-Proline-Rich

Glycoprotein: Speciation, Stability and Binding Details. *J. Inorg. Biochem.* **2012**, *111*, 59–69. https://doi.org/10.1016/j.jinorgbio.2012.02.027.

(6) Pappalardo, G.; Impellizzeri, G.; Bonomo, R. P.; Campagna, T.; Grasso, G.; Saita, M. G. Copper(II) and Nickel(II) Binding Modes in a Histidine-Containing Model Dodecapeptide. *New J. Chem.* **2002**, *26* (5), 593–600. https://doi.org/10.1039/B110655D.

(7) Dey, S.; Sarkar, S.; Paul, H.; Zangrando, E.; Chattopadhyay, P. Copper(II) Complex with Tridentate N Donor Ligand: Synthesis, Crystal Structure, Reactivity and DNA Binding Study. *Polyhedron* **2010**, *29* (6), 1583–1587. https://doi.org/10.1016/j.poly.2010.01.022.

(8) Bravo-Gómez, M. E.; García-Ramos, J. C.; Gracia-Mora, I.; Ruiz-Azuara, L. Antiproliferative Activity and QSAR Study of Copper (II) Mixed Chelate [Cu (N–N)(Acetylacetonato)] NO3 and [Cu (N–N)(Glycinato)] NO3 Complexes,(Casiopeínas®). *J. Inorg. Biochem.* **2009**, *103* (2), 299–309.

(9) Sun, W.-H.; Jie, S.; Zhang, S.; Zhang, W.; Song, Y.; Ma, H.; Chen, J.; Wedeking, K.; Fröhlich, R. Iron Complexes Bearing 2-Imino-1,10-Phenanthrolinyl Ligands as Highly Active Catalysts for Ethylene Oligomerization. *Organometallics* **2006**, *25* (3), 666–677. https://doi.org/10.1021/om050891p.

(10) Chan, W.; White, P. *Fmoc Solid Phase Peptide Synthesis: A Practical Approach*; OUP Oxford, 1999; Vol. 222.

(11) González-Ruiz, V.; Olives, A. I.; Martín, M. A.; Ribelles, P.; Ramos, M. T.; Menéndez, J. C. An Overview of Analytical Techniques Employed to Evidence Drug-DNA Interactions. Applications to the Design of Genosensors. *Biomed. Eng. Trends Res. Technol.* **2011**. https://doi.org/10.5772/13586.

(12) Sirajuddin, M.; Ali, S.; Badshah, A. Drug–DNA Interactions and Their Study by UV–Visible, Fluorescence Spectroscopies and Cyclic Voltametry. *J. Photochem. Photobiol. B* **2013**, *124*, 1–19. https://doi.org/10.1016/j.jphotobiol.2013.03.013.

(13) Kalanur, S.; Katrahalli, Dr. U.; Seetharamappa, J. Electrochemical Studies and Spectroscopic Investigations on the Interaction of an Anticancer Drug with DNA and Their Analytical Applications. *J. Electroanal. Chem.* **2009**, *636*, 93–100. https://doi.org/10.1016/j.jelechem.2009.09.018.

(14) Williams, A. K.; Dasilva, S. C.; Bhatta, A.; Rawal, B.; Liu, M.; Korobkova, E. A. Determination of the Drug–DNA Binding Modes Using Fluorescence-Based Assays. *Anal. Biochem.* **2012**, *422* (2), 66–73.

(15) Bazhulina, N.; Nikitin, A.; Rodin, S.; Surovaya, A.; Kravatsky, Y. V.; Pismensky, V.; Archipova, V.; Martin, R.; Gursky, G. Binding of Hoechst 33258 and Its Derivatives to DNA. *J. Biomol. Struct. Dyn.* **2009**, *26* (6), 701–718.

(16) Suh, D.; Chaires, J. B. Criteria for the Mode of Binding of DNA Binding Agents. *Bioorg. Med. Chem.* **1995**, *3* (6), 723–728.

(17) Peberdy, J. C.; Malina, J.; Khalid, S.; Hannon, M. J.; Rodger, A. Influence of Surface Shape on DNA Binding of Bimetallo Helicates. *J. Inorg. Biochem.* **2007**, *101* (11–12), 1937–1945. https://doi.org/10.1016/j.jinorgbio.2007.07.005.

(18) Puckett, C. A.; Ernst, R. J.; Barton, J. K. Exploring the Cellular Accumulation of Metal Complexes. *Dalton Trans* **2010**, *39* (5), 1159–1170. https://doi.org/10.1039/B922209J.

(19) Cervantes-Cervantes, M. P.; Calderón-Salinas, J. V.; Albores, A.; Muñoz-Sánchez, J. L. Copper Increases the Damage to DNA and Proteins Caused by Reactive Oxygen Species. *Biol. Trace Elem. Res.* **2005**, *103* (3), 229–248.

(20) Yu, Y.; Xu, Q.; He, S.; Xiong, H.; Zhang, Q.; Xu, W.; Ricotta, V.; Bai, L.; Zhang, Q.; Yu, Z. Recent Advances in Delivery of Photosensitive Metal-Based Drugs. *Coord. Chem. Rev.* **2019**, *387*, 154–179.

(21) Panieri, E.; Santoro, M. ROS Homeostasis and Metabolism: A Dangerous Liason in Cancer Cells. *Cell Death Dis.* **2016**, *7* (6), e2253–e2253.

(22) Schumacker, P. T. Reactive Oxygen Species in Cancer Cells: Live by the Sword, Die by the Sword. *Cancer Cell* **2006**, *10* (3), 175–176. https://doi.org/10.1016/j.ccr.2006.08.015.

(23) Hagen, W. R. *Biomolecular EPR Spectroscopy*; CRC press, **2008**.

(24) Sakaguchi, U.; Addison, A. W. Spectroscopic and Redox Studies of Some Copper (II) Complexes with Biomimetic Donor Atoms: Implications for Protein Copper Centres. *J. Chem. Soc. Dalton Trans.* **1979**, No. 4, 600–608.

(25) Peisach, J.; Blumberg, W. Structural Implications Derived from the Analysis of Electron Paramagnetic Resonance Spectra of Natural and Artificial Copper Proteins. *Arch. Biochem. Biophys.* **1974**, *165* (2), 691–708.

(26) Santoro, A.; Calvo, J. S.; Peris-Díaz, M. D.; Krężel, A.; Meloni, G.; Faller, P. The Glutathione/Metallothionein System Challenges the Design of Efficient O2-activating Cu-complexes. *Angew. Chem.* **2020**, ange.201916316. https://doi.org/10.1002/ange.201916316.

CHAPTER 3.

Alzheimer's Disease: A Metal-Related Disease

❝ If you have knowledge,
let others light their candles in it.❞

Margaret Fuller

3.1. Alzheimer's disease.

Responsible for around 60 - 80 % of cases of dementia, Alzheimer disease (AD) is a complex neurodegenerative disease (NDDs),[1] first described by Alois Alzheimer in 1907.[2] It is characterized by the loss of memory, a significant cognitive decline, behavioral and physical disability, dramatic changes in the personality and eventually, death.[3,4] Studies estimates that there were approximately 46.8 million people worldwide affected by AD in 2015. This number is expected to be tripled by 2050.[5,6]

3.2. Symptoms and diagnosis.

Commonly, patients with initial AD symptoms lose the ability to remember new information. This occurs because the first neurons to be damaged are usually in brain regions involved in forming new memories. Other early clinical symptoms include the apathy, depression and the difficulty to remember names, events or conversations. Later symptoms can involve disorientation, confusion, poor judgement, difficulty speaking, and behavior changes.[1] Brain regions responsible for learning and memory processes are decreased in size up to 12 % yearly as a consequence of degeneration of synapses and death of neurons (**Figure 3.1**, A).[7] AD causes a significant decrease of cellular energy metabolism in living patients and this is reflected on a lower glucose uptake (**Figure 3.1**, B). Positron emission tomography (PET) of an AD patient's brain shows the significant decrease in energy metabolism in the frontal cortex (top of the brain) and temporal lobes (sides of the brain).[8]
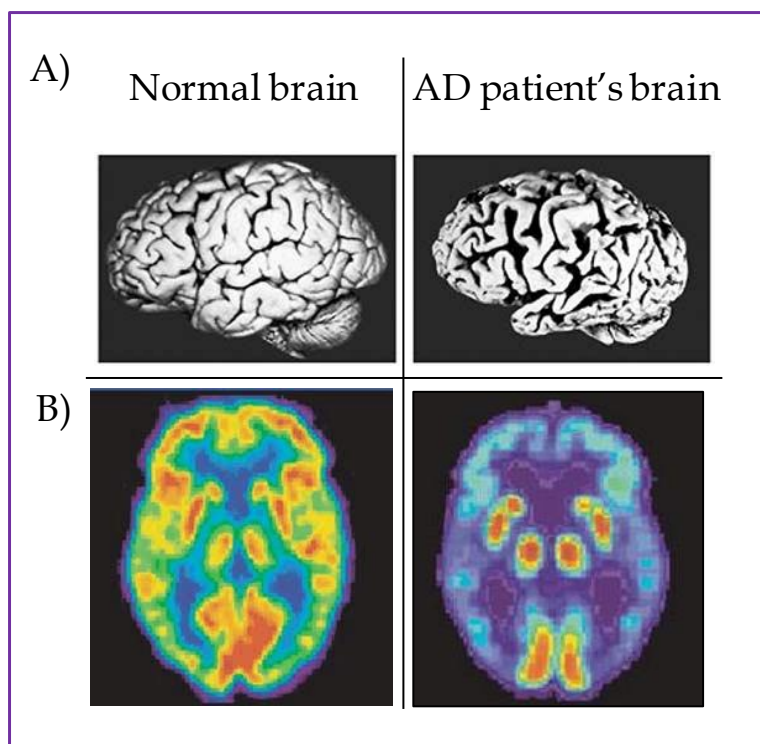
Figure 3.1. A) In comparison with a normal brain (healthy person) the brain of an AD patient reflects important damage in the temporal lobe (lower part of the brain) and frontal lobes (left part of the brain). B) PET images showing glucose uptake (warm colors indicate higher glucose uptake rates) inside a living heathy person's brain (left) and in an AD patient's brain (right).[8]

There are two main histopathological criteria observed for AD: (i) the presence of extracellular deposits of fibrillar peptides called senile plaques and (ii) intracellular fibrillar tangles. The senile plaques (SPs or amyloid plaques) are constituted by the self-aggregation of the amyloid-beta peptide (Aβ), a fragment of 40 to 42 amino acids[9] cleaved from the transmembrane amyloid precursor protein (APP) by the enzymes β-secretase (BACE-1) and γ-secretase (amyloidogenic pathway, **Scheme 3.1**).[10] These aggregates are mostly found extracellularly between neurons and affect the synaptic connections causing significant neuronal damage and eventually death.[11]

A more detailed graphic representation of Aβ peptide aggregation paths is shown on **Scheme 3.2**. Monomeric Aβ random self-assemble can generate

amorphous aggregates, however the well-ordered assemble leads to the formation of amyloid fibrils (fibrilization). The equilibrium between the amyloid fibrillation or amorphous aggregation is affected by different factors such as pH and temperature[12]. This process is responsible for the generation of oligomers and eventually amyloid fibrils, and it can be imaged in post-mortem brains by light microscopy using specific dyes such as thioflavin-T (ThT) or Congo red (CR),[13] two probes widely used in the recognition of Aβ aggregates, including prefibrillar structures. ThT and CR follow the Aβ peptide aggregation by enhancing their fluorescence emission after their intercalation into the Aβ aggregates.
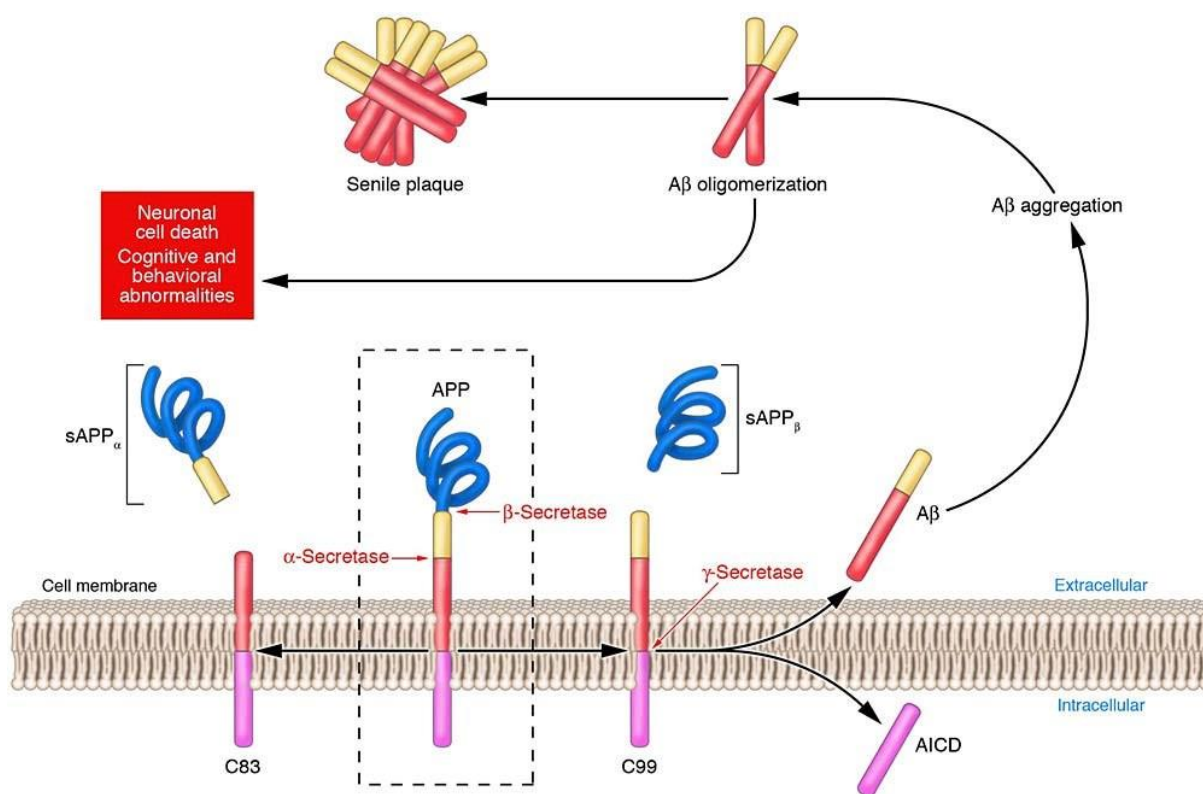
Scheme 3.1. Amyloidogenic and non-amyloidogenic processing pathways of APP cleavage. 1. Amyloidogenic pathway (right) produced by β-secretase generates soluble APP-β and C99, then C99 is cleaved by γ-secretase generating APP intracellular domain (AICD) and Aβ peptide. 2. Non-amyloidogenic pathway (left) by α-secretase generates sAPP-α and C83. Image from reference 14.

The second histopathological criteria for AD is the presence of neurofibrillary tangles (NFTs), which are formed by hyper phosphorylated Tau

protein that aggregates intracellularly in neurons.[11,15] Interestingly, studies have shown that 20 to 40 % of AD unaffected elderly individuals possess enough SPs and NFTs to be diagnosed post-mortem with AD,[16] reflecting that this disease still requiring a better pathogenic understanding.
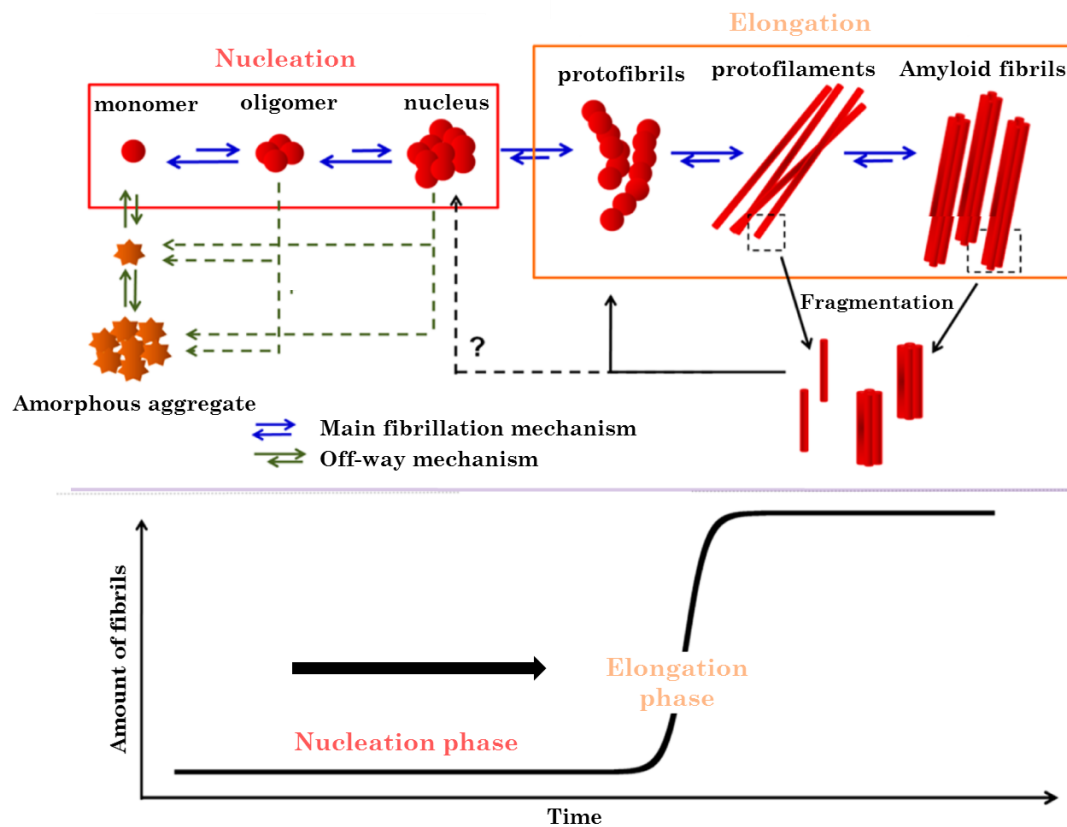
Scheme 3.2. Illustration of the Aβ peptide aggregation (top) and typical evolution describing a sigmoid curve (bottom), representing fibril formation. Figure from refence 17.

Current treatments for AD are only symptom-relieving and typically effective for up to a year at best.[18] Additionally there is no test for AD at early stage, since the differences in brain activity or size are minimal to be detected. Therefore, diagnosing Alzheimer's requires a comprehensive medical evaluation.[1] Diagnosis of AD is realized with 70 % of accuracy with clinical examination in combination with brain imaging techniques. An AD diagnosis includes series of exams as a subjective memory complaint (SMC) test and speech, olfactory, eye and gait testing. Another method for the diagnosis of AD consist in the dosage of AD

biomarkers present in blood such as $A\beta_{1-42}/A\beta_{1-40}$ ratio in the plasma, over expression of cytokines and total cholesterol.[19] The presence of Aβ peptide in the plasma is due to the cerebrospinal fluid absorption in the blood. If the SMC tests are positive, neuroimaging is performed (PET and magnetic resonance imaging, **Figure 3.1**).[20] A definitive AD diagnosis implies post-mortem confirmation by the observation of the two main histopathological criteria of AD (SPs and NFTs).

3.3. Risk factors.

Alzheimer's is a complex multifactorial disease, commonly occurring sporadically with no apparent inheritance.[21] Aging is the main risk factor[10,22] and only 1 % of Alzheimer's cases are estimated as consequence of genetic mutations involving the gene for the APP and the genes for the presenilin 1 and 2, which are constituents of the γ-secretase enzyme complex. Individuals with mutations on these genes exhibit 95 % chance to develop AD symptoms before age 65.

Additionally, exogenous factors such as brain trauma,[1] chronic stress,[23] smoking,[24] obesity,[25] diabetes[26] and hypertension[27] are also involved with the development of AD.[28]

3.4. Amyloid cascade hypothesis.

AD progress involves many factors and consequently, there is still debate about the pathogenesis of the disease. In the last decade diverse hypotheses have emerged including the Aβ peptide cascade hypothesis,[8,10,29] metal ion hypothesis,[30–33] oxidative stress hypothesis,[34,35] Tau hypothesis[36] and inflammation hypothesis.[37,38]

The amyloid cascade hypothesis[29] is one of the most accepted hypothesis and states that the impaired balance between Aβ peptide generation and clearance is the most contributing feature in AD, being the Aβ peptide oligomers the most neurotoxic substances.[39–41] As it was mentioned in Section 3.2, Aβ peptides are cleaved from the APP by the β- and γ-secretases, and diverse proteoforms of different lengths are produced, being $A\beta_{1-40}$ and $A\beta_{1-42}$ the major species (**Figure**

3.2).[9] Disruptions in the balance of the production and clearance of Aβ peptide can be easily produced by alterations over certain conditions, e.g. low pH (γ- secretase have a low pH_{opt}),[42] hypoxia or oxidative stress (enhancing the generation of Aβ peptide by altering β- and γ-cleavage),[43–45] and hypercholesterolemia (reduced cholesterol levels inhibits β- and γ-secretases).[46]
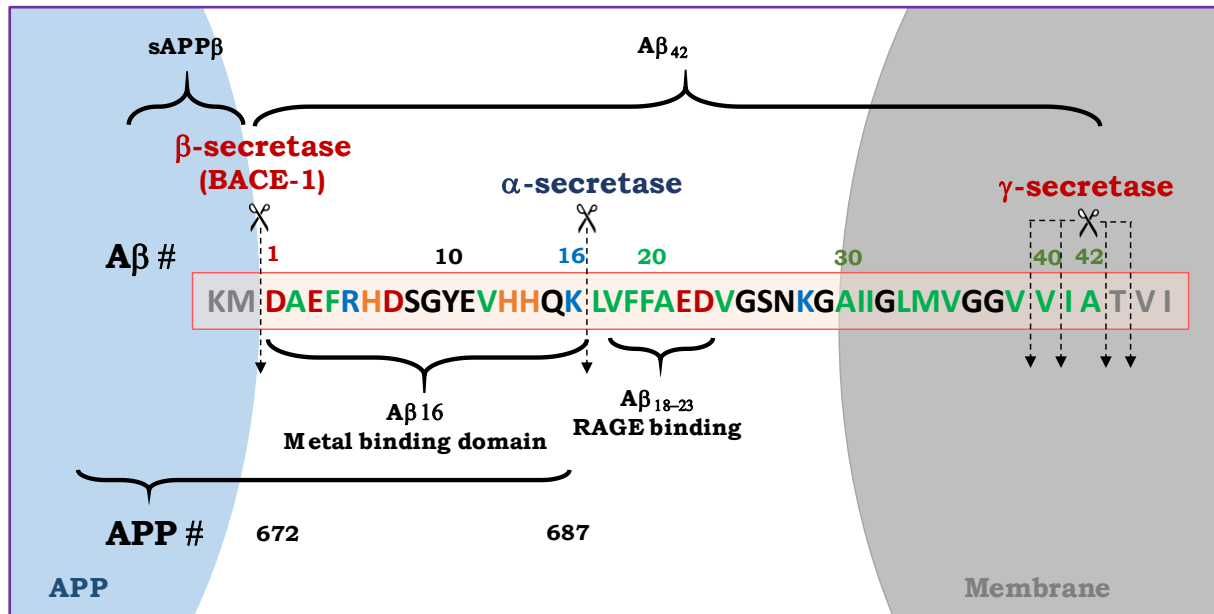
Figure 3.2. Aβ peptide sequence contained by the APP and the two main cleavage positions. Aβ# (above) and APP# (below) numbering is indicated. Amino acid colors represent negative charge (red), positive charge (blue), histidine (orange) and hydrophobic (green).

Moreover, recent studies suggest that the dyshomeostasis of metals (Cu, Zn and Fe) is key in the pathogenesis and development of several neurodegenerative disorders among them AD.[47,48]

3.5.   A link between AD and metal ions.

Metals play very important roles in human metabolism, consequently their homeostasis is critical: deficiency or excess of metal ions are directly linked to the development of many diseases.[49] During the last decades, the interactions between Aβ peptide aggregates and the metal ions has been vastly studied[14,50] since

evidence has indicated that the dyshomeostasis of Cu, Zn and Fe are key in the pathogenesis of AD.[51] It has been reported that the amount of these metal ions in AD patients is 3- to 5-fold higher in comparison with healthy brains.[52,53] They are involved with pathological processes of AD, including Aβ aggregation and oxidative stress,[54,55] and found in SPs, coordinated to the Aβ peptide.[56]

Scheme 3.2 shows the typical evolution of the aggregation process of Aβ peptide. However, evidence suggest that this process can be dramatically affected by the presence of Cu, Fe and Zn ions and that this effect can be modulated by different factors such as pH, temperature or concentrations. These ions can affect the aggregation process in two different ways: (i) binding and subsequent structural changes (excluding covalent modification) and (ii) by altering the peptide through the production of ROS (Cu and Fe).[57–60]

It has been reported that Cu(II) and Zn(II) bind rapidly to the Aβ peptide monomers, specifically to the N-terminal 1-16 (metal binding domain, see **Figure 3.2**), forming M(II)Aβ monomeric complexes. This major complex is the main basic constitutive element for aggregation. Overall, evidence suggest that the presence of Cu(II) and Zn(II) ions affect the kinetics and intermediates (structure and stability), impacting the nucleation phase and the amount and structures of oligomers (**Figure 3.3**).[14]
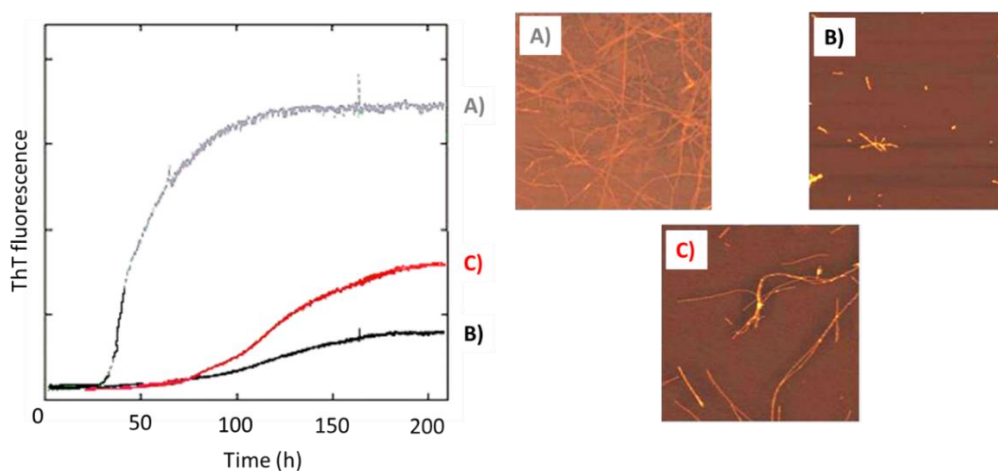
Figure 3.3. Kinetic measurement of Aβ aggregates formation using ThT fluorescence of Aβ (A), Cu(Aβ) (B), Zn(Aβ) (C) and their correspondent atomic force microscopy images (5 μm x 5 μm). [Aβ] = 20 μM, [Cu] = [Zn] 18 μM, [phosphate buffer] = 0.05 M, pH 7.1, T = 37 °C. Figure from reference 61.

Moreover, evidence shows that Cu and Fe[62,63] are associated to ROS generation and therefore, to the oxidative damage caused on phospholipids[64] mitochondria,[65] proteins, DNA[66] and RNA[67,68] as well as to the oxidative damage on the Aβ peptide itself, that can lead to the generation of Aβ peptide forms with enhanced aggregation capabilities (**Scheme 3.3**).
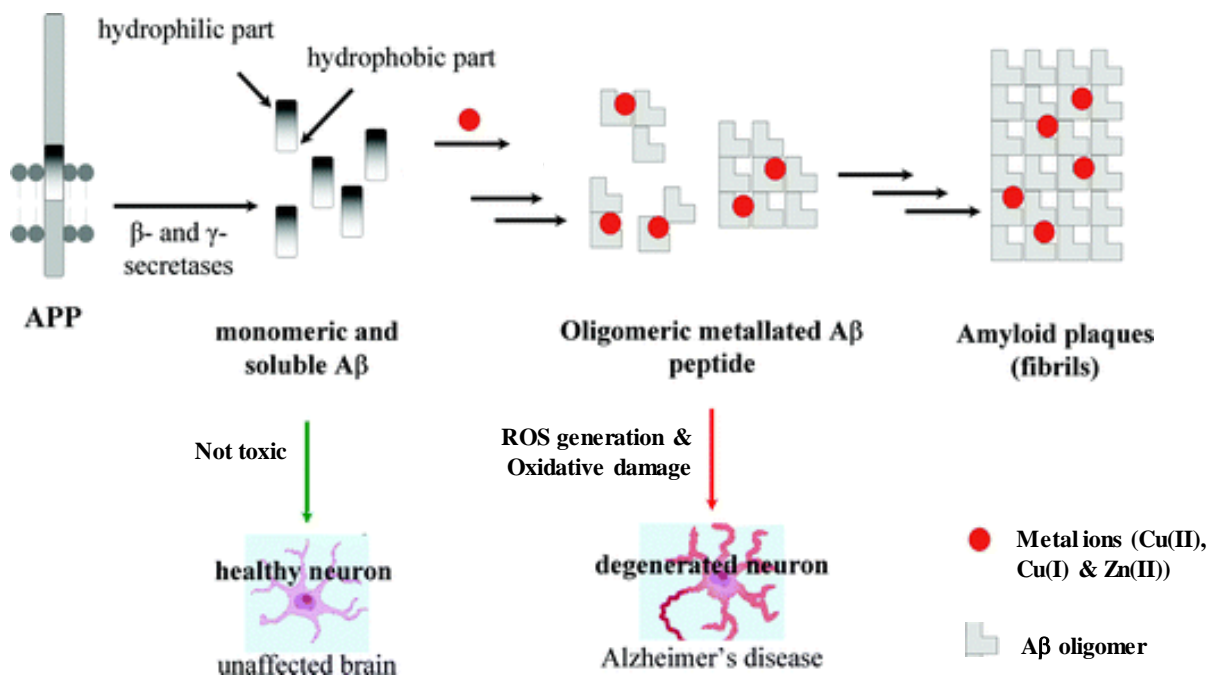
Scheme 3.3. Effects of metal ions in the aggregation of Aβ peptide and ROS production. Figure from reference 69.

The binding of Cu to Aβ peptide, in presence of biological reductants such as ascorbate, which is present in the brain at *ca.* 200 to 400 μM, generates a redox active species able to catalytically cycle between Cu(II)/Cu(I) redox states and produce ROS. The Cu coordination to Aβ plays a critical role in the oxidative damage of AD. Cu(II) binds Aβ at physiological pH in two main binding modes (components I and II) exhibiting both distorted squared planar geometries (**Scheme 3.4**, a).[70,71] Likewise, Cu(I) is coordinated through two of the three His residues present in Aβ sequence in a linear mode (**Scheme 3.4**, b).[72,73]
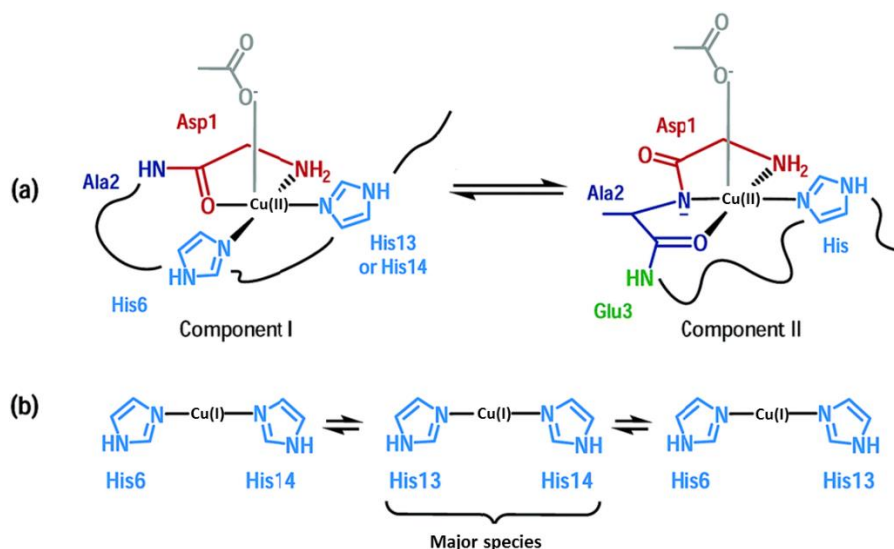
Scheme 3.4. Cu(II) (a) and Cu(I) coordination modes (b) to Aβ peptide in the resting states at near physiological pH. Figure from reference 74.

As previously mentioned, the second main histopathological criteria for AD involves the accumulation of intracellular NFTs, in that context, it has been also stablished that the oxidative stress produced by the Aβ fibrils in presence of these transition metals contribute in the degeneration of tau proteins and consequently in the formation of NFTs.[75–77]

3.6. Therapy approaches for AD treatment.

Although during the last decades large efforts have been devoted to design agents that would provide an efficient treatment against AD, there are still no effective drugs against this neurodegenerative disease. Currently, there exist four FDA approved drugs to treat AD symptoms: tacrine (TAC), donepezil (DNP), galanthamine and rivastigmine (**Figure 3.4**). These drugs help lessen or stabilize symptoms for a limited time,[78] but do not treat the causes involved in AD. These drugs are acetylcholinesterase (AChE) inhibitors. This enzyme is involved in the hydrolysis of choline-based esters, several of which serve as neurotransmitters within the synapsis.[79]
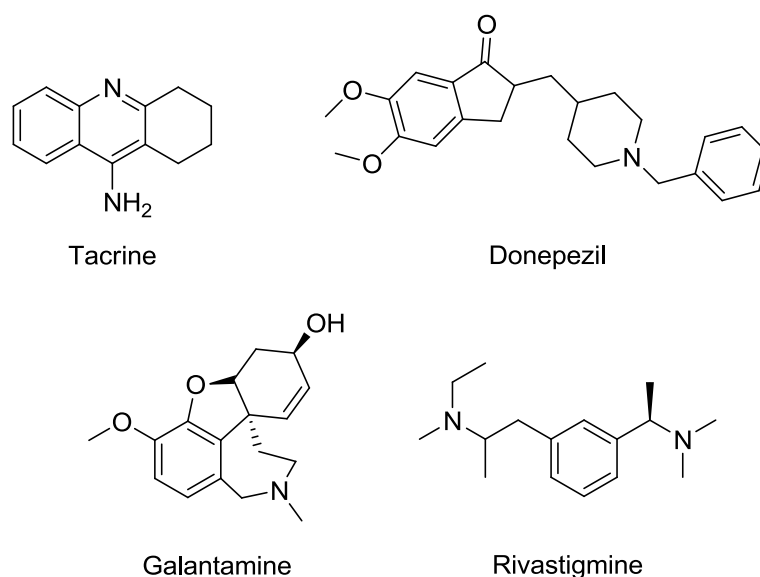
Figure 3.4. FDA approved drugs for treat AD symptoms.

Recently, novel targets including the regulation of Aβ peptide and metal ions concentrations have emerged introducing the next generations of AD therapy approaches. Metal targeted strategies play an important role in the medical treatment of AD given their potential to attenuate the metal mediated effects describe in the previous section, namely the oxidative stress produced by Cu, bound to Aβ peptide.

3.6.1. Copper targeted strategies in AD therapy.

The goal of chelation therapy (or chelatotherapy) is to restore the brain's Cu homeostasis in AD patients to eliminate the toxicity produced by the coordination of this metal to proteins and peptides. In this context, many promising Cu chelating agents has been widely studied, classified and reviewed.[55,80–83] These chelators must be selective for Cu *vs* any other metal ion. This property is defined by the ratio between the affinity values of the ligand for the two metal ions (namely $K_{CuL}/K_{ML} > 100$). Additionally, the ligand must be capable to compete for Cu(II) and Cu(I) against Aβ$_{42}$, ($10^{7.5}$ M^{-1} in HEPES buffer 100 mM at pH 7.1 for Cu(II) and $10^{6.9}$ M^{-1} in HEPES buffer 100 mM at pH 7.4 for Cu(I))[84,85] and maintain its selectivity in presence of Zn (Aβ$_{42}$ affinity constant for Zn is about 10^5 M^{-1} in

HEPES buffer 50 mM at pH 7.4).[86] Moreover, the ligand Cu affinity should not be excessively large in order to avoid competition against essential metalloproteins.[86] The redox silencing of the Cu in both oxidation states and the kinetics of Cu removal are also crucial. Apart from these features, the ideal chelating agent must hold metabolic stability and be innocuous to the cells.

Another important characteristic of chelating agents for neurodegenerative diseases is the brain-blood-barrier (BBB) permeability. The BBB is a highly selective and semipermeable border of endothelial cells that allows the entrance of certain molecules in the circulating blood into the extra cellular fluid of the central nervous system (CNS) and it represents a major pharmacokinetic issue to access the brain.[87]

3.6.1.1. Synthetic Cu ligands.

Despite the numerous chelating agents developed in the last decades, only a few possess favorable pharmacological effects suitable for their use as anti-AD drugs. One of the first and most explored chelating agents in AD is the 8-hydroxyquinoline (8HQ) derivate clioquinol (CQ, **Figure 3.5**) which was formerly used as an antiprotozoal antifungal. CQ is capable to remove Cu(II) and Zn(II) ions from Aβ peptide and SPs formation *in vitro*.[88] A pilot phase IIa clinical trial suggested that CQ can slow cognitive deterioration and decrease the Aβ$_{42}$ levels, however, its phase II clinical trials were suspended due to the neurotoxicity effects exhibited.[89,90] Another issue found on CQ was the low brain-blood-barrier (BBB) permeability. In this regard, PBT2 was designed as a second generation derivate of 8HQ, to improve solubility and brain-blood-barrier permeability (**Figure 3.5**). PBT2 presented promising features such as the ability to remove Cu(II) from Aβ peptide, decrease SPs deposition and a high capacity to interact with Aβ aggregates. Moreover, PBT2 reduced cognitive deterioration in transgenic mice.[89] Further studies suggested that it is safe and well tolerated in AD patients.[91]
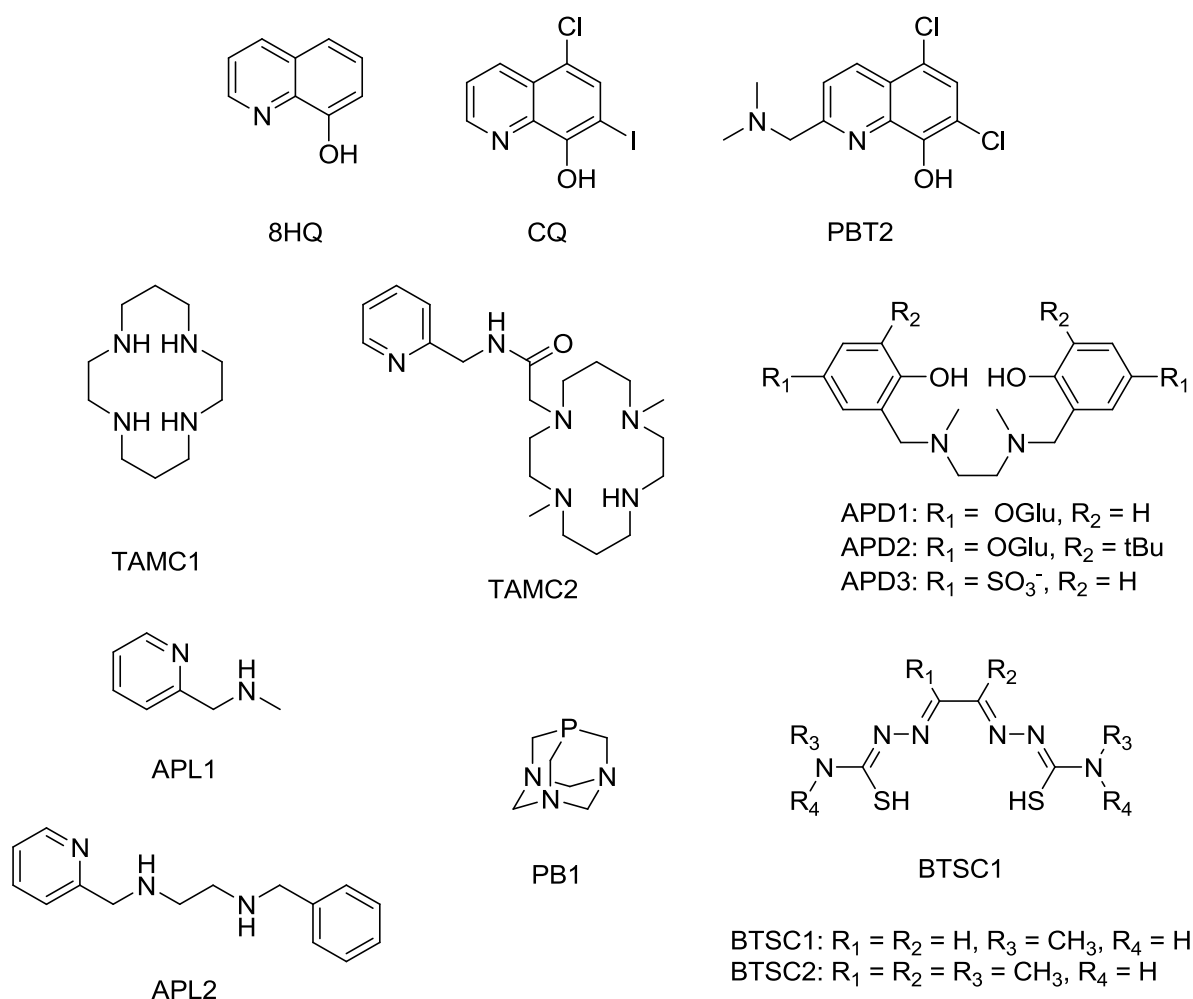
Figure 3.5. Structures of synthetic ligands with anti-AD properties.

Tetraazamacrocycles have been also used as promising scaffolds in AD therapy due to their high metal affinity and their high selectivity for Cu(II) over Zn(II). For instance, TAMC1 (cyclam) has been used as main structural scaffold for several different ligands such as TAMC2 (**Figure 3.5**). TAMC1 can modulate the Aβ peptide aggregation and improve the neuronal cell survival. However, it can only arrest partially the production of ROS.[92] The cyclam derivate (TAMC2) owns a lipophilic pyridine group in order to display improved antioxidant properties and BBB permeability.[93] TAMC2 can modulate Aβ aggregation, decrease the production of H_2O_2 and reduce the toxicity induced by Cu(II)Aβ complex, decreasing intracellular ROS.

Aminophenol derivates such as APD1 and APD2 have been also explored in the context of AD. At neutral pH, APD1 and APD2 exhibit moderate-high Cu(II) affinity (10^{15} M^{-1}), they act as ROS scavengers due to the phenolic moieties while their carbohydrate units provide them with solubility and BBB permeability.[94] APD3, a derivate of APD1 and APD2 (**Figure 3.5**), is capable to stop ROS production and to restore the apo-like type aggregation even in presence of Zn(II).[95]

The aminopyridine based ligand APL1 (**Figure 3.5**) can form Cu(II) and Zn(II) complexes. However, it cannot compete with Aβ peptide for any of these metal ions. APL2, a derivative that has 2 APL1 units in one single molecule, forms more stable Cu(II) and Zn(II) complexes, holding greater affinity values than Aβ peptide at neutral pH (10^{15} and 10^{10} M^{-1} for Cu and Zn, respectively). Additionally, Zn(II) induced aggregation studies reflected that APL2 can solubilize Aβ aggregates.[96]

Considering that Aβ peptide coordinates Cu in both redox states, targeting both Cu(II) and Cu(I) is key in chelation therapy. In this regard, the phosphine derivate PB1 (triaza-7-phosphaadamantane, **Figure 3.5**) has been explored in AD. It is the first ligand reported able to remove Cu(II) and Cu(I) from Aβ peptide. PB1 is able to remove Cu(I) from Aβ peptide and to form an oxidant resistant complex. This effect is maintained even in presence of Zn(II), since the ligand is selective for Cu(I) over Zn(II).[97]

The bis(thiosemicarbazonato) ligands BTSC1 and BTSC1 (**Figure 3.5**) were tested in neuron-like cells and AD animal models. BTSC1 and BTSC2 could solubilize Aβ aggregates and restore cognitive performance in transgenic AD model mice.[98]

3.6.1.2. Peptidic Cu ligands

Peptide and protein scaffolds have been also used in chelatotherapy as Cu ligands in the context of AD since they own many advantages such as water

solubility and a wide structural versatility.[99] Peptides can be easily functionalized and synthetize through standard peptide synthesis protocols.[100]

In this respect, the amino-terminal Cu(II)- and Ni(II)- binding (ACTUN) has inspired several candidates in the context of AD. The ATCUN motif contains the sequence H_2N-Xxx-Zzz-His, being Xxx and Zzz any amino acid (except proline). This motif has higher affinity for Cu(II) than Aβ peptide (about 3 orders of magnitude) and coordinates Cu(II) through 4 N atoms, i.e. the N-terminal amine, the first two amides and the N atom of the imidazole (His). It has been reported that the Cu(II) complexes formed by ATCUN motifs are stable and resistant to reduction to Cu(I).[101] The ATCUN-like tripeptides AL1– AL3 have been reported (**Figure 3.6**).[102] The addition of these peptides at the beginning of the aggregation process can restore the Aβ apo-like type aggregation, meaning indirectly that the tripeptides are able to remove Cu from Aβ peptide. Additionally, these ATCUN-like peptides can reduce moderately the production of ROS.
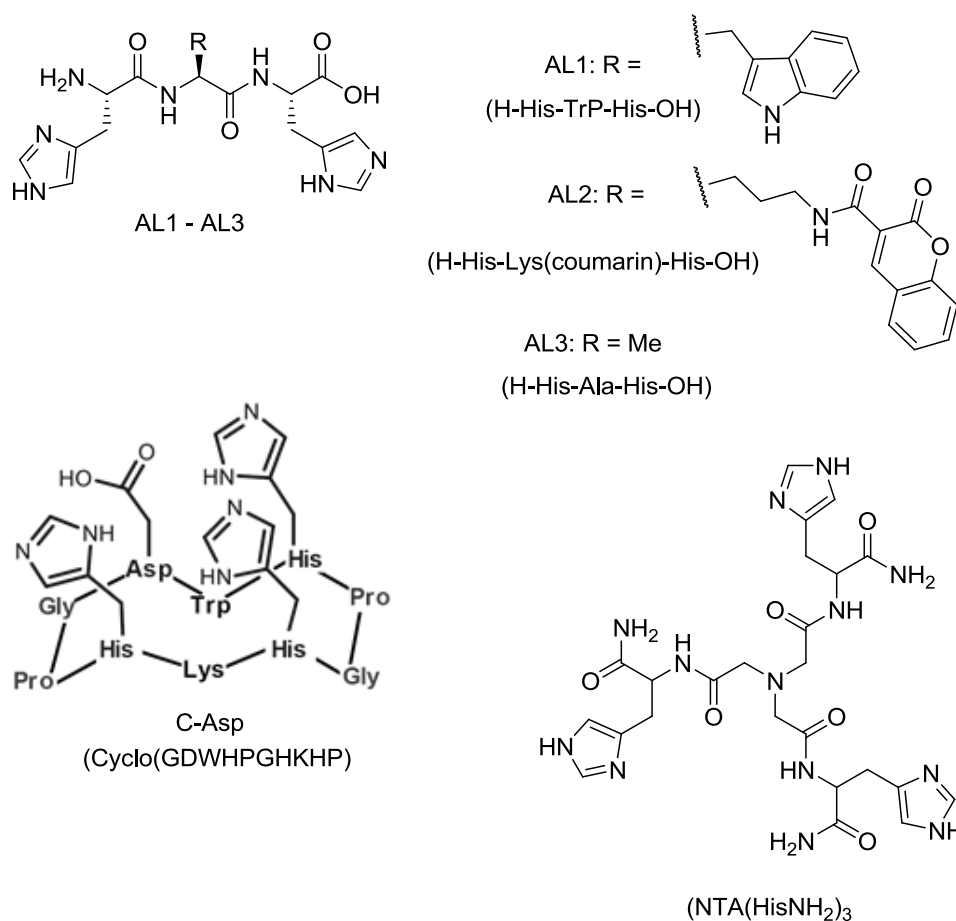
Figure 3.6. Peptide based ligands explored as potential anti-AD agents.

Recently, five His-containing decapeptides structurally preorganized for Cu(II) binding were also explored in the context of AD.[103] Among them, C-Asp (**Figure 3.6**) had the highest Cu(II) affinity and it was capable to compete against Aβ peptide for this metal ion. Furthermore, C-Asp Cu(II) complexation reduced the production of ROS, and *in vitro* aggregation studies indicated that C-Asp avoids the formation of the harmful Cu-stabilized Aβ oligomers easing the apo-like type fibrillation.

The peptide-like ligand, tris-histidine (NTA(HisNH₂)₃ (**Figure 3.6**), is able to chelate both Cu(II) and Cu(I).[104] The ligand is able to coordinate Cu(II) in a squared-planar geometry and Cu(I) in a tetrahedral geometry, the conditional stability constants for Cu(II) and Cu(I) are larger than the ones corresponding to the sequence Aβ$_{1-16}$ (Aβ16 peptide), and the generated Cu(II) and Cu(I) complexes are redox-silent. These properties and the fact that the ligand can be easily functionalized confers special interest in this compound for the AD chemotherapy.

3.6.1.3. Multi-target ligands

The ability to chelate Cu is a crucial property that should be considered in the design of drug candidates for AD treatment. However, due to the complexity of AD, the design of multi-functional metal chelators has become one of the most explored strategies. It involves the combination of two or more molecules with well-known activities in one single molecular system with the purpose of expanding the therapeutical potential. Different scaffolds with the ability to interact with different targets in AD, such as the inhibition of AChE or Aβ aggregates intercalation (**Figure 3.7**) have been functionalized with metal chelators in order to provide further clinical effects. In this context, several multifunctional metal chelators have been described and reviewed by many authors.[80,82,105–108]
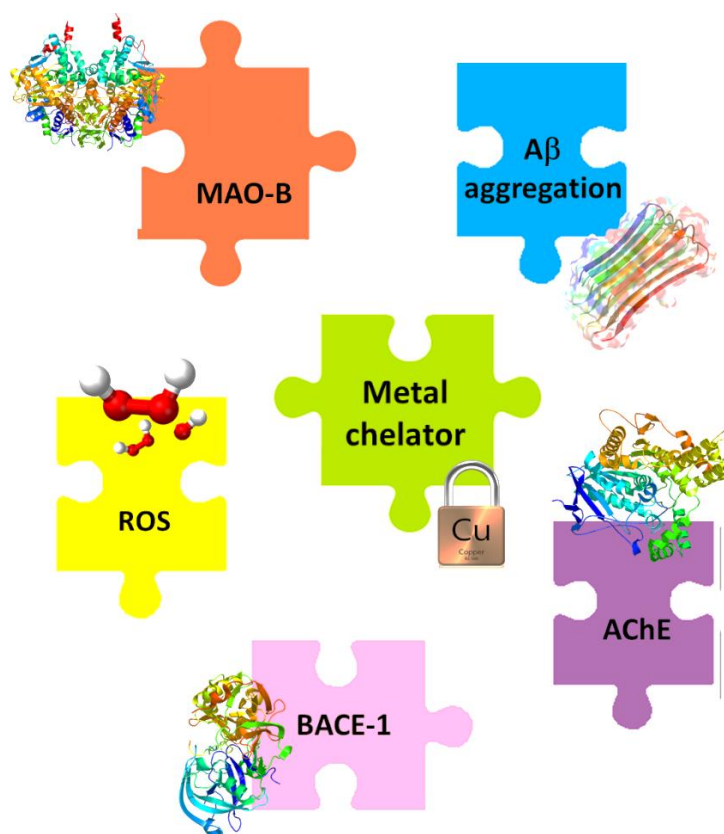
Figure 3.7. Illustration of the most common targets in AD usually linked to metal chelators.

Considering the crucial roles of BACE-1 in the generation of Aβ peptide, the strategy of hybridizing a metal chelator with a BACE-1 inhibitor was utilized by Huang *et al*. to design MCB1 (**Figure 3.8**).[109] MCB1 could chelate Cu(II) and Fe(II) ions, and exhibited higher BACE-1 inhibition potency than the inhibitor alone by forming two hydrogen bonds through the urea group with the catalytic aspartate (Asp228) in BACE-1. Using the same design strategy, the synthesis of MCB2 (**Figure 3.8**) was reported,[110] combining structural scaffolds of different BACE-1 inhibitors and one metal chelator (triazole), in one single molecule. MCB2 exhibited high BACE-1 inhibitory activities due to the hydrogen bond interactions with the Aps32 and Asp 228 within the catalytical cavity of the BACE-1 active site. Moreover, MCB2 could chelate Cu(II) and exhibits moderate antioxidant properties.

Multitarget drugs based on AChE inhibitors have been developed by M. A. Santos *et al.* (**Figure 3.8**, AC1-AC5).[111,112] AC1-AC3 combine the AChE inhibitor TAC (**Figure 3.4**), with a hydroxy benzoyl pyridine (HBP) unit to provide metal chelation capabilities. A similar approach was followed in the design of the compounds AC4 and AC5, combining a TAC moiety with hydroxyphenylbenzimidazole (BIM).[112] The TAC-BIM hybrids showed improved AChE inhibition compared with TAC (IC$_{50}$ 12.5, 208.5 μM and 350 μM, respectively). AC4 and AC5 also displayed 70.9 and 57.4 % of inhibition of the Cu-induced Aβ aggregation and could moderately stop the production of Cu catalyzed ROS.

The neuroprotective properties via inhibition of oxidative stress of MCAP1 (**Figure 3.8**) were reported.[113] MCAP1 combines the radical scavenging properties of the radical scavenger TBA moiety with the chelation abilities of deferiprone (DFP, **Figure 3.8**). The ability to protect cerebellar granule cells from iodoacetate-induced toxicity exhibited by MCAP1 were higher as compared to the administration of TBA and DFP individually..

Examples:
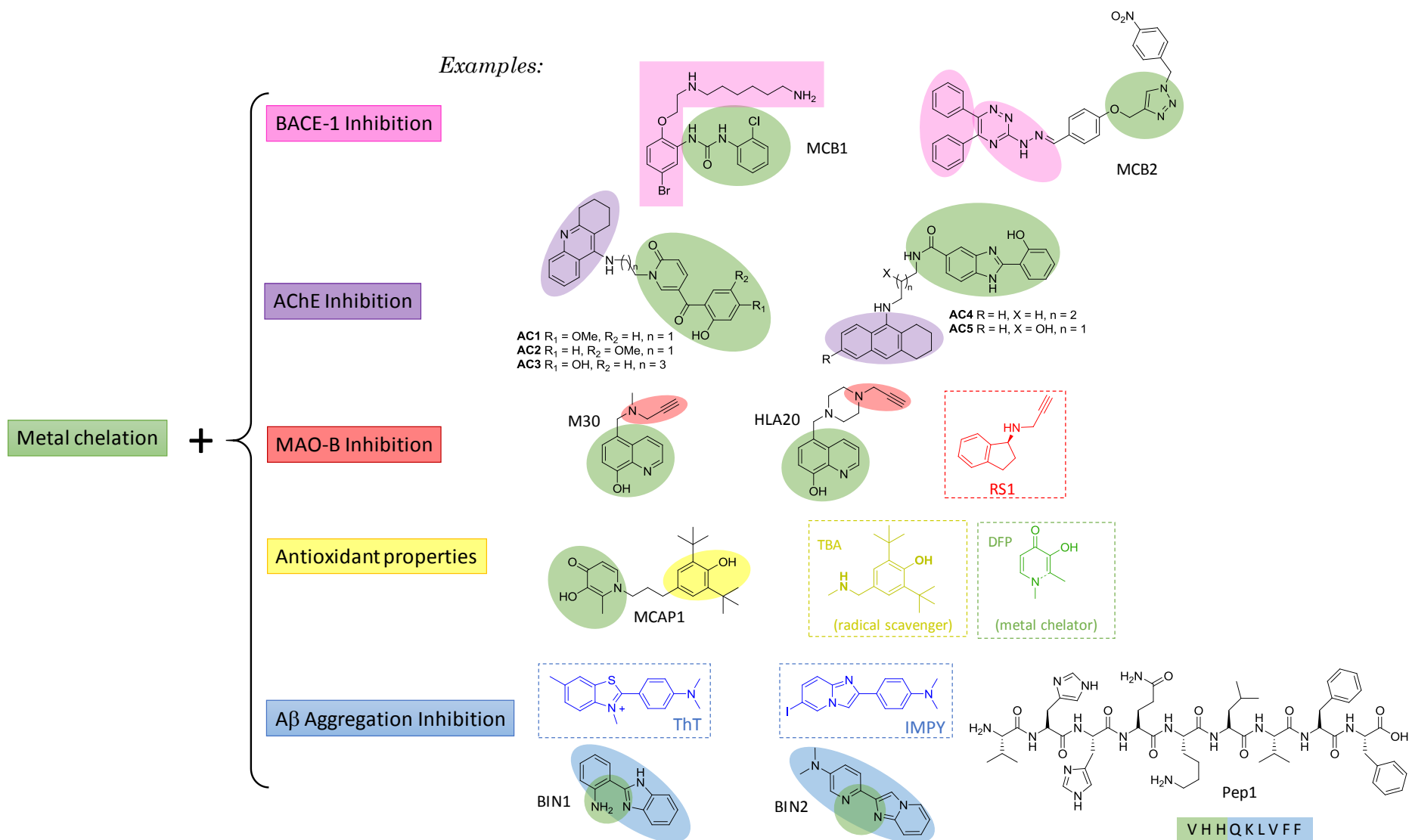
Figure 3.8. Different multifunctional ligands.

The multi-target strategy of the molecules BIN1[114] and BIN2[115] is based on the structure of two Aβ aggregates intercalator dyes, ThT and IMPY (**Figure 3.8**), combined with an aniline or pyridine rings, respectively, to additionally confer Cu chelation. Thus, the resultant BIN1 and BIN2 possess the ability to intercalate in Aβ aggregates and to bind Cu(II) stopping the metal catalyzed production of ROS.

Peptide scaffolds have been also used in multi-targeted strategies to conceive AD drug candidates with different targeting properties or to provide better pharmacokinetic properties.[116]

The design and synthesis of the bifunctional peptide Pep1 (**Figure 3.8**) were reported by Jensen *et al.*[117] The rational design of Pep1 combines two functions in one single peptide i.e. it merges a Cu chelator moiety with the β-sheet breaker moieties of Aβ peptide KLVFF (Aβ$_{16-20}$), a sequence able to inhibit of the formation of Aβ aggregates. The hydrophobic Aβ$_{16-20}$ sequence is related to the formation, oligomerization and fibrilization process by interacting between two Aβ molecules. In Pep1, KLVFF is elongated by four amino acids to include the metal binding domain of Aβ peptide and provide metal chelation properties to the resultant peptide. Pep1 could bind Cu(II) with higher affinity than the native sequence of Aβ$_{42}$ and efficiently suppress the production of ROS. Pep1 exhibited a kinetic effect on the nucleation step of the aggregation of apo-Aβ$_{40}$ retarding the formation of fibrils (see **Scheme 3.2**). Regarding the Cu-induced Aβ aggregation, the presence of Pep1 recuperate the characteristic apo-Aβ aggregation, which is consistent with its capability to remove Cu(II) from Aβ$_{40}$.

Monoamine oxidase B (MAO-B) is another of the most explored targets for the treatment of AD. This enzyme is overexpressed in the frontal cortex and hippocampus in AD patients and it has been associated with regulatory effects on intraneuronal Aβ levels.[118] MAO-B is responsible for the oxidative deamination of neurotransmitters (noradrenalin, dopamine, serotonin) and exogenous amines.[119] Its catalytic activity implicates production of H_2O_2 which increases oxidative stress linked with AD progression. In this regard, M30 and HLA20 molecules (**Figure 3.8**) combine the MAO-B inhibitory moiety (propargyl) of the Parkinson drug RS1 with a Fe chelating scaffold. M30 and HLA20 suppressed iron-induced

lipid-peroxidation in rat brains and displayed greater MAO-B inhibitory potency than RS1.[120] Additionally M30 could effectively reduce Aβ peptide accumulation, revealing promising potential for the treatment of various neurodegenerative disorders including AD.[121]

3.7. Objectives of the study.

The goal of this thesis is to explore the chelating capabilities of His containing Phen based ligands (**L1**, **L2**) as potential candidates for the treatment of AD. For this aim several objectives have been pursued:

i)   Study the antioxidant properties of the Cu(II) complexes of these ligands

ii) Determination of the affinity binding constants of Cu(I), Cu(II) and Zn(II) to the ligand **L1** in order to determine their potential to remove Cu from Aβ peptide.

iii) Evaluate the capabilities of **L1** to remove Cu(I) and Cu(II) from the Aβ peptide in the absence and in the presence of Zn(II) and to arrest the ROS production.

iv) Study the effect of the stoichiometry of **L1** in its effectiveness to stop the ROS production.

v)   Modify **L1** in order to provide enhanced therapeutic potential.

vi) Evaluate the effect that the modification of **L1** produced in its capability to coordinate Cu(II) and to arrest the ROS production.

3.8. Bibliography

(1) Alzheimer's Association. 2017 Alzheimer's Disease Facts and Figures. *Alzheimers Dement.* **2017**, *13* (4), 325–373.

(2) Alzheimer, A. Über Eine Eigenartige Erkrankung Der Hirnrinde (1907). About a Peculiar Disease of the Cerebral Cortex (Translated by L. Jarvik and H. Greenson). *Alzheimer Assoc Disord* **1987**, *1* (1), 3–8.

(3)   Carreiras, M. C.; Mendes, E.; Perry, M. J.; Francisco, A. P.; Marco-Contelles, J. The Multifactorial Nature of Alzheimer's Disease for Developing Potential Therapeutics. *Curr. Top. Med. Chem.* **2013**, *13* (15), 1745–1770. https://doi.org/10.2174/15680266113139990135.

(4)   McKhann, G. M.; Knopman, D. S.; Chertkow, H.; Hyman, B. T.; Jack Jr, C. R.; Kawas, C. H.; Klunk, W. E.; Koroshetz, W. J.; Manly, J. J.; Mayeux, R. The Diagnosis of Dementia Due to Alzheimer's Disease: Recommendations from the National Institute on Aging-Alzheimer's Association Workgroups on Diagnostic Guidelines for Alzheimer's Disease. *Alzheimers Dement.* **2011**, *7* (3), 263–269.

(5)   Prince, M.; Comas-Herrera, A.; Knapp, M.; Guerchet, M.; Karagiannidou, M. World Alzheimer Report 2016: Improving Healthcare for People Living with Dementia: Coverage, Quality and Costs Now and in the Future. **2016**.

(6)   O'Connor, D. World Alzheimer Report 2019: Attitudes to Dementia. 160.

(7)   Jahn, H. Memory Loss in Alzheimer's Disease. *Dialogues Clin. Neurosci.* **2013**, *15* (4), 445–454.

(8)   Mattson, M. P. Pathways towards and Away from Alzheimer's Disease. **2004**, *430*, 10.

(9)   Wildburger, N. C.; Esparza, T. J.; LeDuc, R. D.; Fellers, R. T.; Thomas, P. M.; Cairns, N. J.; Kelleher, N. L.; Bateman, R. J.; Brody, D. L. Diversity of Amyloid-Beta Proteoforms in the Alzheimer's Disease Brain. *Sci. Rep.* **2017**, *7* (1), 9520. https://doi.org/10.1038/s41598-017-10422-x.

(10)   Blennow, K.; de Leon, M. J.; Zetterberg, H. Alzheimer's Disease. *Lancet Lond. Engl.* **2006**, *368* (9533), 387–403. https://doi.org/10.1016/S0140-6736(06)69113-7.

(11)   Silbert, L. C. Does Statin Use Decrease the Amount of Alzheimer Disease Pathology in the Brain? *Neurology* **2007**, *69* (9), E8–E11.

(12)   Roychaudhuri, R.; Yang, M.; Hoshi, M. M.; Teplow, D. B. Amyloid β-Protein Assembly and Alzheimer Disease. *J. Biol. Chem.* **2009**, *284* (8), 4749–4753.

(13)   Reinke, A. A.; Gestwicki, J. E. Insight into Amyloid Structure Using Chemical Probes. *Chem. Biol. Drug Des.* **2011**, *77* (6), 399–411.

(14)   Spies, P. E.; Verbeek, M. M.; van Groen, T.; Claassen, J. A. H. R. Reviewing Reasons for the Decreased CSF Abeta42 Concentration in Alzheimer Disease. *Front. Biosci. Landmark Ed.* **2012**, *17*, 2024–2034. https://doi.org/10.2741/4035.

(15)   Spillantini, M. G.; Goedert, M. Tau Pathology and Neurodegeneration. *Lancet Neurol.* **2013**, *12* (6), 609–622.

(16)   Jack Jr, C. R.; Knopman, D. S.; Jagust, W. J.; Shaw, L. M.; Aisen, P. S.; Weiner, M. W.; Petersen, R. C.; Trojanowski, J. Q. Hypothetical Model of Dynamic Biomarkers of the Alzheimer's Pathological Cascade. *Lancet Neurol.* **2010**, *9* (1), 119–128.

(17)   Faller, P.; Hureau, C.; Berthoumieu, O. Role of Metal Ions in the Self-Assembly of the Alzheimer's Amyloid-β Peptide. *Inorg. Chem.* **2013**, *52* (21), 12193–12206. https://doi.org/10.1021/ic4003059.

(18)   Hansen, R. A.; Gartlehner, G.; Webb, A. P.; Morgan, L. C.; Moore, C. G.; Jonas, D. E. Efficacy and Safety of Donepezil, Galantamine, and Rivastigmine for the Treatment of Alzheimer's Disease: A Systematic Review and Meta-Analysis. *Clin. Interv. Aging* **2008**, *3* (2), 211.

(19) Laske, C.; Sohrabi, H.; Frost, S.; López-de-Ipi-a, K.; Garrard, P.; Buscema, M.; O'Bryant, S. Innovative Diagnostic Tools for Early Detection of Alzheimer's Disease. Alzheimer & Dementia, 11 (5), 561-578. **2015**.

(20) Weiner, M. W.; Veitch, D. P.; Aisen, P. S.; Beckett, L. A.; Cairns, N. J.; Green, R. C.; Harvey, D.; Jack Jr, C. R.; Jagust, W.; Morris, J. C. The Alzheimer's Disease Neuroimaging Initiative 3: Continued Innovation for Clinical Trial Improvement. *Alzheimers Dement.* **2017**, *13* (5), 561–571.

(21) Gatz, M.; Reynolds, C. A.; Fratiglioni, L.; Johansson, B.; Mortimer, J. A.; Berg, S.; Fiske, A.; Pedersen, N. L. Role of Genes and Environments for Explaining Alzheimer Disease. *Arch. Gen. Psychiatry* **2006**, *63* (2), 168–174.

(22) Hebert, L. E.; Weuve, J.; Scherr, P. A.; Evans, D. A. Alzheimer Disease in the United States (2010–2050) Estimated Using the 2010 Census. *Neurology* **2013**, *80* (19), 1778–1783.

(23) Machado, A.; Herrera, A. J.; de Pablos, R. M.; Espinosa-Oliva, A. M.; Sarmiento, M.; Ayala, A.; Venero, J. L.; Santiago, M.; Villarán, R. F.; Delgado-Cortés, M. J. Chronic Stress as a Risk Factor for Alzheimer's Disease. *Rev. Neurosci.* **2014**, *25* (6), 785–804.

(24) Barnes, D. E.; Yaffe, K. The Projected Effect of Risk Factor Reduction on Alzheimer's Disease Prevalence. *Lancet Neurol.* **2011**, *10* (9), 819–828.

(25) Gustafson, D.; Rothenberg, E.; Blennow, K.; Steen, B.; Skoog, I. An 18-Year Follow-up of Overweight and Risk of Alzheimer Disease. *Arch. Intern. Med.* **2003**, *163* (13), 1524–1528.

(26) Mayeux, R. Epidemiology of Neurodegeneration. *Annu. Rev. Neurosci.* **2003**, *26* (1), 81–104.

(27) Launer, L. J.; Ross, G. W.; Petrovitch, H.; Masaki, K.; Foley, D.; White, L. R.; Havlik, R. J. Midlife Blood Pressure and Dementia: The Honolulu–Asia Aging Study☆. *Neurobiol. Aging* **2000**, *21* (1), 49–55.

(28) Kepp, K. P. Bioinorganic Chemistry of Alzheimer's Disease. *Chem. Rev.* **2012**, *112* (10), 5193–5239. https://doi.org/10.1021/cr300009x.

(29) Karran, E.; Mercken, M.; De Strooper, B. The Amyloid Cascade Hypothesis for Alzheimer's Disease: An Appraisal for the Development of Therapeutics. *Nat. Rev. Drug Discov.* **2011**, *10* (9), 698.

(30) Hung, Y. H.; Bush, A. I.; Cherny, R. A. Copper in the Brain and Alzheimer's Disease. *JBIC J. Biol. Inorg. Chem.* **2010**, *15* (1), 61–76.

(31) Barnham, K. J.; Bush, A. I. Metals in Alzheimer's and Parkinson's Diseases. *Curr. Opin. Chem. Biol.* **2008**, *12* (2), 222–228.

(32) Bush, A. I.; Pettingell, W. H.; Multhaup, G.; d Paradis, M.; Vonsattel, J.-P.; Gusella, J. F.; Beyreuther, K.; Masters, C. L.; Tanzi, R. E. Rapid Induction of Alzheimer A Beta Amyloid Formation by Zinc. *Science* **1994**, *265* (5177), 1464–1467.

(33) Bush, A. I. The Metallobiology of Alzheimer's Disease. *Trends Neurosci.* **2003**, *26* (4), 207–214.

(34) Beal, M. F. Aging, Energy, and Oxidative Stress in Neurodegenerative Diseases. *Ann. Neurol.* **1995**, *38* (3), 357–366.

(35) Galindo, M. F.; Ikuta, I.; Zhu, X.; Casadesus, G.; Jordán, J. Mitochondrial Biology in Alzheimer's Disease Pathogenesis. *J. Neurochem.* **2010**, *114* (4), 933–945.

(36) Brier, M. R.; Gordon, B.; Friedrichsen, K.; McCarthy, J.; Stern, A.; Christensen, J.; Owen, C.; Aldea, P.; Su, Y.; Hassenstab, J. Tau and Aß Imaging, CSF Measures, and Cognition in Alzheimer's Disease. *Sci. Transl. Med.* **2016**, *8* (338), 338ra66-338ra66.

(37) Zhang, B.; Gaiteri, C.; Bodea, L.-G.; Wang, Z.; McElwee, J.; Podtelezhnikov, A. A.; Zhang, C.; Xie, T.; Tran, L.; Dobrin, R. Integrated Systems Approach Identifies Genetic Nodes and Networks in Late-Onset Alzheimer's Disease. *Cell* **2013**, *153* (3), 707–720.

(38) Bolós, M.; Perea, J. R.; Avila, J. Alzheimer's Disease as an Inflammatory Disease. *Biomol. Concepts* **2017**, *8* (1), 37–43.

(39) Zhang, Y.; Lu, L.; Jia, J.; Jia, L.; Geula, C.; Pei, J.; Xu, Z.; Qin, W.; Liu, R.; Li, D. A Lifespan Observation of a Novel Mouse Model: In Vivo Evidence Supports Aß Oligomer Hypothesis. *PloS One* **2014**, *9* (1), e85885.

(40) Lee, S. J. C.; Nam, E.; Lee, H. J.; Savelieff, M. G.; Lim, M. H. Towards an Understanding of Amyloid-ß Oligomers: Characterization, Toxicity Mechanisms, and Inhibitors. *Chem. Soc. Rev.* **2017**, *46* (2), 310–323.

(41) Walsh, D. M.; Selkoe, D. J. Aß Oligomers–a Decade of Discovery. *J. Neurochem.* **2007**, *101* (5), 1172–1184.

(42) LaFerla, F. M.; Green, K. N.; Oddo, S. Intracellular Amyloid-ß in Alzheimer's Disease. *Nat. Rev. Neurosci.* **2007**, *8* (7), 499.

(43) Li, L.; Zhang, X.; Yang, D.; Luo, G.; Chen, S.; Le, W. Hypoxia Increases Aß Generation by Altering ß-and γ-Cleavage of APP. *Neurobiol. Aging* **2009**, *30* (7), 1091–1098.

(44) Sun, X.; He, G.; Qing, H.; Zhou, W.; Dobie, F.; Cai, F.; Staufenbiel, M.; Huang, L. E.; Song, W. Hypoxia Facilitates Alzheimer's Disease Pathogenesis by up-Regulating BACE1 Gene Expression. *Proc. Natl. Acad. Sci.* **2006**, *103* (49), 18727–18732.

(45) Tamagno, E.; Guglielmotto, M.; Aragno, M.; Borghi, R.; Autelli, R.; Giliberto, L.; Muraca, G.; Danni, O.; Zhu, X.; Smith, M. A. Oxidative Stress Activates a Positive Feedback between the Γ-and B-secretase Cleavages of the B-amyloid Precursor Protein. *J. Neurochem.* **2008**, *104* (3), 683–695.

(46) Grimm, M. O.; Grimm, H. S.; Tomic, I.; Beyreuther, K.; Hartmann, T.; Bergmann, C. Independent Inhibition of Alzheimer Disease ß-and γ-Secretase Cleavage by Lowered Cholesterol Levels. *J. Biol. Chem.* **2008**, *283* (17), 11302–11311.

(47) Liu, G.; Huang, W.; Moir, R. D.; Vanderburg, C. R.; Lai, B.; Peng, Z.; Tanzi, R. E.; Rogers, J. T.; Huang, X. Metal Exposure and Alzheimer's Pathogenesis. *J. Struct. Biol.* **2006**, *155* (1), 45–51.

(48) Zatta, P.; Lucchini, R.; van Rensburg, S. J.; Taylor, A. The Role of Metals in Neurodegenerative Processes: Aluminum, Manganese, and Zinc. *Brain Res. Bull.* **2003**, *62* (1), 15–28.

(49) Sigel, H.; Sigel, A. The Bio-Relevant Metals of the Periodic Table of the Elements. *Z. Für Naturforschung B* **2019**, *74* (6), 461–471. https://doi.org/10.1515/znb-2019-0056.

(50) Faller, P. Copper and Zinc Binding to Amyloid-ß: Coordination, Dynamics, Aggregation, Reactivity and Metal-Ion Transfer. *ChemBioChem* **2009**, *10* (18), 2837–2845.

(51) Mandel, S.; Amit, T.; Bar-Am, O.; Youdim, M. B. Iron Dysregulation in Alzheimer's Disease: Multimodal Brain Permeable Iron Chelating Drugs, Possessing Neuroprotective-Neurorescue and Amyloid Precursor Protein-Processing Regulatory Activities as Therapeutic Agents. *Prog. Neurobiol.* **2007**, *82* (6), 348–360.

(52) Zatta, P.; Drago, D.; Bolognin, S.; Sensi, S. L. Alzheimer's Disease, Metal Ions and Metal Homeostatic Therapy. *Trends Pharmacol. Sci.* **2009**, *30* (7), 346–355.

(53) Lovell, M. A.; Robertson, J. D.; Teesdale, W. J.; Campbell, J. L.; Markesbery, W. R. Copper, Iron and Zinc in Alzheimer's Disease Senile Plaques. *J. Neurol. Sci.* **1998**, *158* (1), 47–52. https://doi.org/10.1016/s0022-510x(98)00092-6.

(54) Guo, T.; Hobbs, D. W. Development of BACE1 Inhibitors for Alzheimer's Disease. *Curr. Med. Chem.* **2006**, *13* (15), 1811–1829.

(55) Ghosh, A. K.; Kumaragurubaran, N.; Tang, J. Recent Developments of Structure Based ß-Secretase Inhibitors for Alzheimer's Disease. *Curr. Top. Med. Chem.* **2005**, *5* (16), 1609–1622.

(56) Miller, L. M.; Wang, Q.; Telivala, T. P.; Smith, R. J.; Lanzirotti, A.; Miklossy, J. Synchrotron-Based Infrared and X-Ray Imaging Shows Focalized Accumulation of Cu and Zn Co-Localized with ß-Amyloid Deposits in Alzheimer's Disease. *J. Struct. Biol.* **2006**, *155* (1), 30–37.

(57) Viles, J. H. Metal Ions and Amyloid Fiber Formation in Neurodegenerative Diseases. Copper, Zinc and Iron in Alzheimer's, Parkinson's and Prion Diseases. *Coord. Chem. Rev.* **2012**, *256* (19–20), 2271–2284.

(58) You, H.; Tsutsui, S.; Hameed, S.; Kannanayakal, T. J.; Chen, L.; Xia, P.; Engbers, J. D.; Lipton, S. A.; Stys, P. K.; Zamponi, G. W. Aß Neurotoxicity Depends on Interactions between Copper Ions, Prion Protein, and N-Methyl-D-Aspartate Receptors. *Proc. Natl. Acad. Sci.* **2012**, *109* (5), 1737–1742.

(59) Sparks, D. L.; Schreurs, B. G. Trace Amounts of Copper in Water Induce ß-Amyloid Plaques and Learning Deficits in a Rabbit Model of Alzheimer's Disease. *Proc. Natl. Acad. Sci.* **2003**, *100* (19), 11065–11069.

(60) Sanokawa-Akakura, R.; Cao, W.; Allan, K.; Patel, K.; Ganesh, A.; Heiman, G.; Burke, R.; Kemp, F. W.; Bogden, J. D.; Camakaris, J. Control of Alzheimer's Amyloid Beta Toxicity by the High Molecular Weight Immunophilin FKBP52 and Copper Homeostasis in Drosophila. *PloS One* **2010**, *5* (1), e8626.

(61) Conte-Daban, A.; Day, A.; Faller, P.; Hureau, C. How Zn Can Impede Cu Detoxification by Chelating Agents in Alzheimer's Disease: A Proof-of-Concept Study. *Dalton Trans.* **2016**, *45* (39), 15671–15678.

(62) Bousejra-ElGarah, F.; Bijani, C.; Coppel, Y.; Faller, P.; Hureau, C. Iron (II) Binding to Amyloid-ß, the Alzheimer's Peptide. *Inorg. Chem.* **2011**, *50* (18), 9024–9030.

(63) James, S. A.; Volitakis, I.; Adlard, P. A.; Duce, J. A.; Masters, C. L.; Cherny, R. A.; Bush, A. I. Elevated Labile Cu Is Associated with Oxidative Pathology in Alzheimer Disease. *Free Radic. Biol. Med.* **2012**, *52* (2), 298–302.

(64) Sayre, L. M.; Zelasko, D. A.; Harris, P. L.; Perry, G.; Salomon, R. G.; Smith, M. A. 4-Hydroxynonenal-derived Advanced Lipid Peroxidation End Products Are Increased in Alzheimer's Disease. *J. Neurochem.* **1997**, *68* (5), 2092–2097.

(65) Smith, M.; Richey, G.; Sayre, L.; Anderson, V.; Beal, M.; Kowal, N. Test for Oxidative Damage in Alzheimer's. *Nature* **1996**, *382* (6587), 120–121.

(66) Castellani, R. J.; Honda, K.; Zhu, X.; Cash, A. D.; Nunomura, A.; Perry, G.; Smith, M. A. Contribution of Redox-Active Iron and Copper to Oxidative Damage in Alzheimer Disease. *Ageing Res. Rev.* **2004**, *3* (3), 319–326.

(67) Chassaing, S.; Collin, F.; Dorlet, P.; Gout, J.; Hureau, C.; Faller, P. Copper and Heme-Mediated Abeta Toxicity: Redox Chemistry, Abeta Oxidations and Anti-ROS Compounds. *Curr. Top. Med. Chem.* **2012**, *12* (22), 2573–2595.

(68) Nunomura, A.; Perry, G.; Pappolla, M. A.; Wade, R.; Hirai, K.; Chiba, S.; Smith, M. A. RNA Oxidation Is a Prominent Feature of Vulnerable Neurons in Alzheimer's Disease. *J. Neurosci.* **1999**, *19* (6), 1959–1964.

(69) Faller, P.; Hureau, C. Bioinorganic Chemistry of Copper and Zinc Ions Coordinated to Amyloid-ß Peptide. *Dalton Trans* **2009**, No. 7, 1080–1094. https://doi.org/10.1039/B813398K.

(70) Hureau, C. Coordination of Redox Active Metal Ions to the Amyloid Precursor Protein and to Amyloid-ß Peptides Involved in Alzheimer Disease. Part 1: An Overview. *Coord. Chem. Rev.* **2012**, *256* (19), 2164–2174. https://doi.org/10.1016/j.ccr.2012.03.037.

(71) Drew, S. C.; Barnham, K. J. The Heterogeneous Nature of Cu2+ Interactions with Alzheimer's Amyloid-ß Peptide. *Acc. Chem. Res.* **2011**, *44* (11), 1146–1155. https://doi.org/10.1021/ar200014u.

(72) Shearer, J.; Szalai, V. A. The Amyloid-ß Peptide of Alzheimer's Disease Binds CuI in a Linear Bis-His Coordination Environment: Insight into a Possible Neuroprotective Mechanism for the Amyloid-ß Peptide. *J. Am. Chem. Soc.* **2008**, *130* (52), 17826–17835.

(73) Hureau, C.; Balland, V.; Coppel, Y.; Solari, P. L.; Fonda, E.; Faller, P. Importance of Dynamical Processes in the Coordination Chemistry and Redox Conversion of Copper Amyloid-ß Complexes. *JBIC J. Biol. Inorg. Chem.* **2009**, *14* (7), 995–1000.

(74) Cheignon, C.; Jones, M.; Atrián-Blasco, E.; Kieffer, I.; Faller, P.; Collin, F.; Hureau, C. Identification of Key Structural Features of the Elusive Cu–Aß Complex That Generates ROS in Alzheimer's Disease. *Chem. Sci.* **2017**, *8* (7), 5107–5118.

(75) Götz, J.; Chen, F. v; Van Dorpe, J.; Nitsch, R. Formation of Neurofibrillary Tangles in P301L Tau Transgenic Mice Induced by Aß42 Fibrils. *Science* **2001**, *293* (5534), 1491–1495.

(76) Lewis, J.; Dickson, D. W.; Lin, W.-L.; Chisholm, L.; Corral, A.; Jones, G.; Yen, S.-H.; Sahara, N.; Skipper, L.; Yager, D. Enhanced Neurofibrillary Degeneration in Transgenic Mice Expressing Mutant Tau and APP. *Science* **2001**, *293* (5534), 1487–1491.

(77) Zheng, W.-H.; Bastianetto, S.; Mennicken, F.; Ma, W.; Kar, S. Amyloid ß Peptide Induces Tau Phosphorylation and Loss of Cholinergic Neurons in Rat Primary Septal Cultures. *Neuroscience* **2002**, *115* (1), 201–211.

(78)   Alzheimer's Association | Alzheimer's Disease & Dementia Help https://www.alz.org/ (accessed Nov 20, 2019).

(79)   Colovic, M. B.; Krstic, D. Z.; Lazarevic-Pasti, T. D.; Bondzic, A. M.; Vasic, V. M. Acetylcholinesterase Inhibitors: Pharmacology and Toxicology. *Curr. Neuropharmacol.* **2013**, *11* (3), 315–335.

(80)   Santos, M. A.; Chand, K.; Chaves, S. Recent Progress in Multifunctional Metal Chelators as Potential Drugs for Alzheimer's Disease. *Coord. Chem. Rev.* **2016**, *327–328*, 287–303. https://doi.org/10.1016/j.ccr.2016.04.013.

(81)   Sales; Prandi; Castro; Leal; Cunha; Kuca; Ramalho. Recent Developments in Metal-Based Drugs and Chelating Agents for Neurodegenerative Diseases Treatments. *Int. J. Mol. Sci.* **2019**, *20* (8), 1829. https://doi.org/10.3390/ijms20081829.

(82)   Huang, W.; Wei, W.; Shen, Z. Drug-like Chelating Agents: A Potential Lead for Alzheimer's Disease. *RSC Adv* **2014**, *4* (94), 52088–52099. https://doi.org/10.1039/C4RA09193K.

(83)   Alessandro, F.; Maria Elena, F. EDTA Chelation Therapy for the Treatment of Neurotoxicity. *Int. J. Mol. Sci.* **2019**, *20* (5), 1019. https://doi.org/10.3390/ijms20051019.

(84)   Conte-Daban, A.; Borghesani, V.; Sayen, S.; Guillon, E.; Journaux, Y.; Gontard, G.; Lisnard, L.; Hureau, C. Link between Affinity and Cu (II) Binding Sites to Amyloid-β Peptides Evaluated by a New Water-Soluble UV–Visible Ratiometric Dye with a Moderate Cu (II) Affinity. *Anal. Chem.* **2017**, *89* (3), 2155–2162.

(85)   Alies, B.; Badei, B.; Faller, P.; Hureau, C. Reevaluation of Copper(I) Affinity for Amyloid-β Peptides by Competition with Ferrozine-An Unusual Copper(I) Indicator. *Chem. - Eur. J.* **2012**, *18* (4), 1161–1167. https://doi.org/10.1002/chem.201102746.

(86)   Atrián-Blasco, E.; Conte-Daban, A.; Hureau, C. Mutual Interference of Cu and Zn Ions in Alzheimer's Disease: Perspectives at the Molecular Level. *Dalton Trans.* **2017**, *46* (38), 12750–12759. https://doi.org/10.1039/C7DT01344B.

(87)   Daneman, R.; Prat, A. The Blood–Brain Barrier. *Cold Spring Harb. Perspect. Biol.* **2015**, *7* (1), a020412.

(88)   Ferrada, E.; Arancibia, V.; Loeb, B.; Norambuena, E.; Olea-Azar, C.; Huidobro-Toro, J. P. Stoichiometry and Conditional Stability Constants of Cu (II) or Zn (II) Clioquinol Complexes; Implications for Alzheimer's and Huntington's Disease Therapy. *Neurotoxicology* **2007**, *28* (3), 445–449.

(89)   Adlard, P. A.; Cherny, R. A.; Finkelstein, D. I.; Gautier, E.; Robb, E.; Cortes, M.; Volitakis, I.; Liu, X.; Smith, J. P.; Perez, K. Rapid Restoration of Cognition in Alzheimer's Transgenic Mice with 8-Hydroxy Quinoline Analogs Is Associated with Decreased Interstitial Aβ. *Neuron* **2008**, *59* (1), 43–55.

(90)   Budimir, A. Metal Ions, Alzheimer's Disease and Chelation Therapy. *Acta Pharm.* **2011**, *61* (1), 1–14. https://doi.org/10.2478/v10007-011-0006-6.

(91)   Sampson, E. L.; Jenagaratnam, L.; McShane, R. Metal Protein Attenuating Compounds for the Treatment of Alzheimer's Disease. *Cochrane Database Syst. Rev.* **2008**, No. 1.

(92) Chen, T.; Wang, X.; He, Y.; Zhang, C.; Wu, Z.; Liao, K.; Wang, J.; Guo, Z. Effects of Cyclen and Cyclam on Zinc (II)-and Copper (II)-Induced Amyloid β-Peptide Aggregation and Neurotoxicity. *Inorg. Chem.* **2009**, *48* (13), 5801–5809.

(93) Yang, Y.; Chen, T.; Zhu, S.; Gu, X.; Jia, X.; Lu, Y.; Zhu, L. Two Macrocyclic Polyamines as Modulators of Metal-Mediated Aβ40 Aggregation. *Integr. Biol.* **2015**, *7* (6), 655–662.

(94) Rodríguez-Rodríguez, C.; Telpoukhovskaia, M.; Orvig, C. The Art of Building Multifunctional Metal-Binding Agents from Basic Molecular Scaffolds for the Potential Application in Neurodegenerative Diseases. *Coord. Chem. Rev.* **2012**, *256* (19–20), 2308–2332.

(95) Storr, T.; Merkel, M.; Song-Zhao, G. X.; Scott, L. E.; Green, D. E.; Bowen, M. L.; Thompson, K. H.; Patrick, B. O.; Schugar, H. J.; Orvig, C. Synthesis, Characterization, and Metal Coordinating Ability of Multifunctional Carbohydrate-Containing Compounds for Alzheimer's Therapy. *J. Am. Chem. Soc.* **2007**, *129* (23), 7453–7463.

(96) Lakatos, A.; Zsigó, É.; Hollender, D.; Nagy, N. V.; Fülöp, L.; Simon, D.; Bozsó, Z.; Kiss, T. Two Pyridine Derivatives as Potential Cu (II) and Zn (II) Chelators in Therapy for Alzheimer's Disease. *Dalton Trans.* **2010**, *39* (5), 1302–1315.

(97) Atrián-Blasco, E.; Cerrada, E.; Faller, P.; Laguna, M.; Hureau, C. Role of PTA in the Prevention of Cu (Amyloid-β) Induced ROS Formation and Amyloid-β Oligomerisation in the Presence of Zn. *Metallomics* **2019**, *11* (6), 1154–1161.

(98) Crouch, P. J.; Hung, L. W.; Adlard, P. A.; Cortes, M.; Lal, V.; Filiz, G.; Perez, K. A.; Nurjono, M.; Caragounis, A.; Du, T. Increasing Cu Bioavailability Inhibits Aβ Oligomers and Tau Phosphorylation. *Proc. Natl. Acad. Sci.* **2009**, *106* (2), 381–386.

(99) Esmieu, C.; Guettas, D.; Conte-Daban, A.; Sabater, L.; Faller, P.; Hureau, C. Copper-Targeting Approaches in Alzheimer's Disease: How To Improve the Fallouts Obtained from in Vitro Studies. *Inorg. Chem.* **2019**, acs.inorgchem.9b00995. https://doi.org/10.1021/acs.inorgchem.9b00995.

(100) Maude, S.; Tai, L.; Davies, R.; Liu, B.; Harris, S.; Kocienski, P.; Aggeli, A. Peptide Synthesis and Self-Assembly. In *Peptide-Based Materials*; Springer, 2011; pp 27–69.

(101) Gonzalez, P.; Bossak, K.; Stefaniak, E.; Hureau, C.; Raibauta, L.; Balc, W.; Faller, P. N-Terminal Cu Binding Motifs Xxx-Zzz-His (ATCUN) and Xxx-His and Their Derivatives: Chemistry, Biology and Medicinal Applications. *Chem. Weinh. Bergstr. Ger.* **2018**, *24* (32), 8029.

(102) Caballero, A. B.; Terol-Ordaz, L.; Espargaró, A.; Vázquez, G.; Nicolás, E.; Sabaté, R.; Gamez, P. Histidine-Rich Oligopeptides To Lessen Copper-Mediated Amyloid-β Toxicity. *Chem. Eur. J.* **2016**, *22* (21), 7268–7280.

(103) Caballero, A. B.; Iranzo, O.; Hautier, A.; Sabaté, R.; Gamez, P. Peptidic Scaffolds To Reduce the Interaction of Cu(II) Ions with β-Amyloid Protein. *Inorg. Chem.* **2020**, *59* (1), 837–846. https://doi.org/10.1021/acs.inorgchem.9b03099.

(104) Conte-Daban, A.; Boff, B.; Candido Matias, A.; Aparicio, C. N. M.; Gateau, C.; Lebrun, C.; Cerchiaro, G.; Kieffer, I.; Sayen, S.; Guillon, E.; Delangle, P.; Hureau, C. A Trishistidine Pseudopeptide with Ability to Remove Both CuI and CuII from the Amyloid-ß Peptide and to Stop the Associated ROS Formation. *Chem. – Eur. J.* **2017**, *23* (67), 17078–17088. https://doi.org/10.1002/chem.201703429.

(105) Zhang, H.-Y. One-compound-multiple-targets Strategy to Combat Alzheimer's Disease. *FEBS Lett.* **2005**, *579* (24), 5260–5264.

(106) Sharma, A.; Pachauri, V.; Flora, S. J. S. Advances in Multi-Functional Ligands and the Need for Metal-Related Pharmacology for the Management of Alzheimer Disease. *Front. Pharmacol.* **2018**, *9*, 1247. https://doi.org/10.3389/fphar.2018.01247.

(107) Savelieff, M. G.; Nam, G.; Kang, J.; Lee, H. J.; Lee, M.; Lim, M. H. Development of Multifunctional Molecules as Potential Therapeutic Candidates for Alzheimer's Disease, Parkinson's Disease, and Amyotrophic Lateral Sclerosis in the Last Decade. *Chem. Rev.* **2019**, *119* (2), 1221–1322. https://doi.org/10.1021/acs.chemrev.8b00138.

(108) Zhang, P.; Xu, S.; Zhu, Z.; Xu, J. Multi-Target Design Strategies for the Improved Treatment of Alzheimer's Disease. *Eur. J. Med. Chem.* **2019**, *176*, 228–247. https://doi.org/10.1016/j.ejmech.2019.05.020.

(109) Huang, W.; Lv, D.; Yu, H.; Sheng, R.; Kim, S. C.; Wu, P.; Luo, K.; Li, J.; Hu, Y. Dual-Target-Directed 1, 3-Diphenylurea Derivatives: BACE 1 Inhibitor and Metal Chelator against Alzheimer's Disease. *Bioorg. Med. Chem.* **2010**, *18* (15), 5610–5615.

(110) Yazdani, M.; Edraki, N.; Badri, R.; Khoshneviszadeh, M.; Iraji, A.; Firuzi, O. Multi-Target Inhibitors against Alzheimer Disease Derived from 3-Hydrazinyl 1, 2, 4-Triazine Scaffold Containing Pendant Phenoxy Methyl-1, 2, 3-Triazole: Design, Synthesis and Biological Evaluation. *Bioorganic Chem.* **2019**, *84*, 363–371.

(111) Chand, K.; Alsoghier, H. M.; Chaves, S.; Santos, M. A. Tacrine-(Hydroxybenzoyl-Pyridone) Hybrids as Potential Multifunctional Anti-Alzheimer's Agents: AChE Inhibition, Antioxidant Activity and Metal Chelating Capacity. *J. Inorg. Biochem.* **2016**, *163*, 266–277. https://doi.org/10.1016/j.jinorgbio.2016.05.005.

(112) Hiremathad, A.; Keri, R. S.; Esteves, A. R.; Cardoso, S. M.; Chaves, S.; Santos, M. A. Novel Tacrine-Hydroxyphenylbenzimidazole Hybrids as Potential Multitarget Drug Candidates for Alzheimer's Disease. *Eur. J. Med. Chem.* **2018**, *148*, 255–267. https://doi.org/10.1016/j.ejmech.2018.02.023.

(113) Bebbington, D.; Monck, N. J.; Gaur, S.; Palmer, A. M.; Benwell, K.; Harvey, V.; Malcolm, C. S.; Porter, R. H. 3, 5-Disubstituted-4-Hydroxyphenyls Linked to 3-Hydroxy-2-Methyl-4 (1 H)-Pyridinone: Potent Inhibitors of Lipid Peroxidation and Cell Toxicity. J. Med. Chem. **2000**, 43 (15), 2779–2782.

(114) Rodríguez-Rodríguez, C.; Sanchez de Groot, N.; Rimola, A.; Alvarez-Larena, A.; Lloveras, V.; Vidal-Gancedo, J.; Ventura, S.; Vendrell, J.; Sodupe, M.; González-Duarte, P. Design, Selection, and Characterization of Thioflavin-Based Intercalation Compounds with Metal Chelating Properties for Application in Alzheimer's Disease. *J. Am. Chem. Soc.* **2009**, *131* (4), 1436–1451.

(115) Choi, J.-S.; Braymer, J. J.; Park, S. K.; Mustafa, S.; Chae, J.; Lim, M. H. Synthesis and Characterization of IMPY Derivatives That Regulate Metal-Induced Amyloid-β Aggregation. *Metallomics* **2011**, *3* (3), 284–291.

(116) Craik, D. J.; Fairlie, D. P.; Liras, S.; Price, D. The Future of Peptide-Based Drugs. *Chem. Biol. Drug Des.* **2013**, *81* (1), 136–147. https://doi.org/10.1111/cbdd.12055.

(117) Jensen, M.; Canning, A.; Chiha, S.; Bouquerel, P.; Pedersen, J. T.; Østergaard, J.; Cuvillier, O.; Sasaki, I.; Hureau, C.; Faller, P. Inhibition of Cu-Amyloid-β by Using Bifunctional Peptides with Β-Sheet Breaker and Chelator Moieties. *Chem. – Eur. J.* **2012**, *18* (16), 4836–4839. https://doi.org/10.1002/chem.201103546.

(118) Schedin-Weiss, S.; Inoue, M.; Hromadkova, L.; Teranishi, Y.; Yamamoto, N. G.; Wiehager, B.; Bogdanovic, N.; Winblad, B.; Sandebring-Matton, A.; Frykman, S. Monoamine Oxidase B Is Elevated in Alzheimer Disease Neurons, Is Associated with γ-Secretase and Regulates Neuronal Amyloid β-Peptide Levels. *Alzheimers Res. Ther.* **2017**, *9* (1), 57.

(119) Weyler, W.; Hsu, Y.-P. P.; Breakafield, X. O. Biochemistry and Genetics of Monoamine Oxidase. *Pharmacol. Ther.* **1990**, *47* (3), 391–417.

(120) Zheng, H.; Gal, S.; Weiner, L. M.; Bar-Am, O.; Warshawsky, A.; Fridkin, M.; Youdim, M. B. Novel Multifunctional Neuroprotective Iron Chelator-monoamine Oxidase Inhibitor Drugs for Neurodegenerative Diseases: In Vitro Studies on Antioxidant Activity, Prevention of Lipid Peroxide Formation and Monoamine Oxidase Inhibition. *J. Neurochem.* **2005**, *95* (1), 68–78.

(121) Kupershmidt, L.; Amit, T.; Bar-Am, O.; Weinreb, O.; Youdim, M. B. Multi-Target, Neuroprotective and Neurorestorative M30 Improves Cognitive Impairment and Reduces Alzheimer's-like Neuropathology and Age-Related Alterations in Mice. *Mol. Neurobiol.* **2012**, *46* (1), 217–220.

CHAPTER 4.

Exploring the Cu Chelating Capabilities of L1 and L2 in the Context of Alzheimer's Disease

66 *Measure what is measurable,*
and make measurable what is not so."

Galileo Galilei.

4.1. Previous data: Molecular design and synthesis of the ligands L1 and L2.

As described in Chapter 2, **L1** and **L2** (**Figure 4.1**) were previously developed in the group[1] and contain two coordination units: (i) phenanthroline (Phen), classical chelator, capable to coordinate Cu through the nitrogen atoms[2] and (ii) histidine (His), an amino acid that plays significant roles on Cu coordination in metalloproteins and peptides.[3–7]
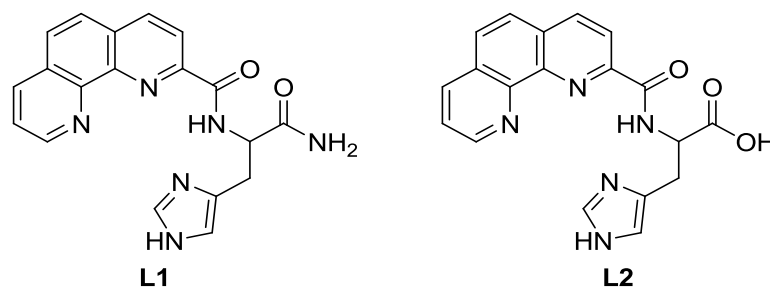
Figure 4.1. Chemical structure of **L1** and **L2** .

Both ligands (**Figure 4.1**) chelate Cu(II) forming a single major species where Cu(II) displays a distorted squared planar geometry. These complexes are stable in a wide range of pH values: from 3.0 to 9.0 for **C1** (**Cu(II)L1**) and from 4.5 to 10.0 for **C2** (**Cu(II)L2**) and their conditional affinity constants (log K_{cond}) at pH 7.4 are 14.55 (**Cu(II)L1**) and 13.89 (**Cu(II)L2**). Please, note that for the sake of simplicity the protonation state of the ligand in the complexes will not be described. Therefore, for the case of L1 the complex Cu(II)L1H$_{-1}$ (deprotonation of the amide)[1] will be denoted as Cu(II)L1. Cyclic voltammetry studies at pH 7.4 revealed a nonreversible redox process Cu(II) $\rightleftarrows$ Cu(I) for both complexes.[8] Namely, **C1** shows a cathodic (E_{pc} = −0.452 V) and an anodic peak (E_{pa} = 0.201 V) with a peak to peak separation $\Delta E_p = E_{pa} - E_{pc}$ = 0.653 V, and likewise, **C2** shows a cathodic (E_{pc} = −0.722 V) and an anodic peak (E_{pa} = 0.181 V) with a Δ_{Ep} = 0.903 V. Taking into account these properties, i.e. high affinity constants for Cu(II), non-reversible Cu(II) $\rightleftarrows$ Cu(I) redox process and the characteristics observed in the Cu chelators reported in literature in the context of Alzheimer's disease (AD), the question that naturally arises is: Are **L1** and **L2** potential Cu chelators in AD therapy?

This chapter focuses therefore on the study of the Cu coordination properties of ligands **L1** and **L2** in the context of AD. Moreover, it explores how the functionalization of **L1** with a carrier peptide known to cross the brain-blood-barrier (BBB) affects these properties.

4.2. Results and discussion.

4.2.1. Evaluation of Reactive Oxygen Species production by L1 and L2.

Oxidative stress is one of the main pathological hallmarks of AD although it is not clear whether this is a cause or a consequence of abnormal processes in the brain.[9] The brain has a rather reductive environment and the synaptic cleft contains *ca.* 200 to 400 µM of ascorbate (AscH$^-$). In the presence of this biological reductant, reactive oxygen species (ROS) such as $O_2^{-\cdot}$, H_2O_2 and HO, can be produced by the redox cycling of Cu(II)/Cu(I) and promote the neuronal damage (**Scheme 4.1**).[10,11]

In vitro ROS formation can either be followed by monitoring HO$^\cdot$ formation through the detection of the fluorescent 7-hydroxyl-coumarin-3-carboxylic acid (7-OH-CCA) dye formed after the reaction of HO$^\cdot$ with the coumarin-3-carboxylic acid (CCA) molecule,[12] or by tracking the AscH$^-$ consumption in UV-vis spectroscopy at 265 nm and correlating the consumption of AscH$^-$ with the generation of ROS. The latter has proven its reliability reflecting effectively the ROS production and it has been widely used in the field.[12–14]
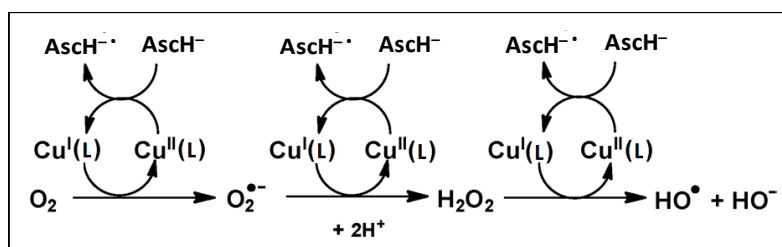
Scheme 4.1. AscH$^-$ oxidation and generation of ROS catalyzed by a redox active Cu complex.

In that regard, the capabilities of **L1** and **L2** to stop the production of ROS were evaluated in two different ways (**Figure 4.2**). (i) Starting from the mixture of Cu(II)/Cu(I) (panel A): in this assay the correspondent ligand is added after the AscH$^-$ consumption has started by the addition of Cu(II) (CuCl$_2$). (ii) Starting only from Cu(I) (panel B): in this experiment Cu(II) is initially reduced to Cu(I) by AscH$^-$ under anaerobic conditions and then the corresponding ligand is added. Subsequently, air (O$_2$) is introduced to the system.

The results obtained (**Figure 4.2**) reflect the Cu(II)/Cu(I) chelation properties of **L1** and **L2** (blue and red lines, respectively) and their different capability to arrest AscH$^-$ consumption. Clearly, the addition of **L1** slows down significantly the AscH$^-$ consumption in both experiments, while the addition of **L2** can only mildly decrease it. Thus, the data indicate that under the tested experimental conditions, **L1** can chelate Cu(II) and Cu(I) and form, respectively, Cu complexes that do not contribute to the formation of ROS. Based on these results **L1**, was selected for further studies. Since the presence of Aβ peptide and other metals (i.e. Zn(II)) can affect this behavior, these factors were studied next.

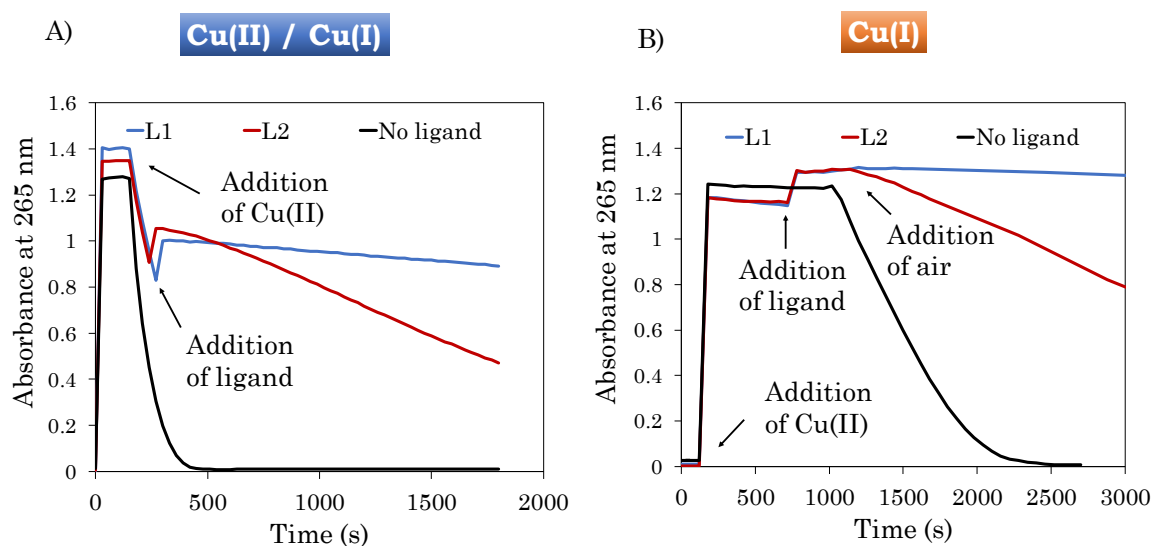**Figure 4.2**. Kinetics of AscH$^-$ consumption by CuCl$_2$ (black lines) followed by UV-vis spectroscopy at the maximum absorbance of AscH$^-$ (265 nm), in presence of **L1** (blue curves) or **L2** (red curves): A) Starting from a mixture Cu(II)/Cu(I), order of additions: AscH$^-$ + Cu(II) + ligand (if any). B) Starting from Cu(I), order of additions: Cu(II) + AscH$^-$ + ligand (if any) + air.

4.2.2. Ability of L1 to remove Cu(II) from Aβ peptide.

4.2.2.1. L1, Aβ peptide and Cu.

As it was described on Section 3.5, the resulting complex formed between Aβ peptide and Cu generates ROS and is considered as one of the main responsible sources of neuronal damage in AD. In this context, the capability of **L1** to sequester Cu(II) ions in the presence of the Aβ peptide was assessed. The soluble and non-aggregating Aβ16 fragment was selected for this study to avoid aggregation-derived interferences in the spectroscopic measurements; this fragment contains the whole metal-binding region of the aggregation-prone Aβ fragments that are responsible for the formation of senile plaques, such as Aβ$_{1-40}$ and Aβ$_{1-42}$ (see **Figure 3.2**, Chapter 3). No significant differences between the short and the full-length Aβ peptides have been observed regarding Cu(II) coordination, binding affinity and ROS production. Therefore, the Aβ16 peptide is used as an appropriate/valuable model for studying metal coordination and ROS production.[15,16]

A way to assay the capability of **L1** to coordinate Cu(II) in presence of Aβ16 peptide is to follow the d-d transition band of the **Cu(II)L1** complex by UV-vis spectroscopy in the absence and presence of Aβ16. A pH titration (from pH 3.0 to pH 10.0) was performed using stoichiometric amounts (1:1, ratio) of **L1**, and Cu(II) (0.5 mM) in absence and presence of 1 equiv. of Aβ16 and following the d-d transition band corresponding to the formation of the **Cu(II)L1** complex (see Annex **Figure A.15** and **A.16**). No significant changes were observed between both sets of spectra. For clarity, only the spectra obtained at pH 7.1 are overlaid and presented here (**Figure 4.3**). The UV-vis spectrum of Cu(II)Aβ16 shows a d-d transition band at 624 nm and the complex **Cu(II)L1** at 605 nm. When the two ligands (**L1** and Aβ16 peptide) are in presence of Cu(II), only the d-d transition band corresponding to the complex **Cu(II)L1** is visible. The data clearly indicate that under these experimental conditions the Aβ16 peptide does not compete with **L1** for Cu(II) coordination.
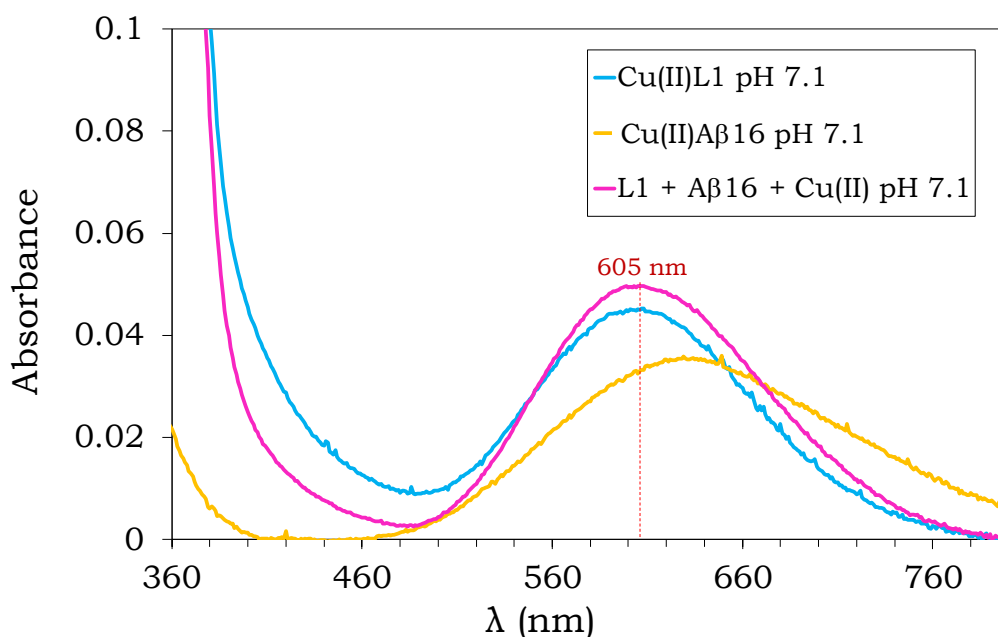
Figure 4.3. Overlay of the UV-vis spectra of **Cu(II)L1**, Cu(II)Aβ16 and Cu(II) in presence of 1 equiv. of **L1** and Aβ16 at 0.5 mM and pH 7.1.

In order to validate the results obtained on UV-vis spectroscopy, the Cu(II) coordination properties of **L1** in the presence of the Aβ16 peptide, were also evaluated using electron paramagnetic resonance (EPR) spectroscopy. For this experiment, two solutions containing 200 μM of Cu(II) in 50 mM HEPES at pH 7.1 and either 1.2 equiv. of Aβ16 or 1.2 equiv. of **L1** were prepared. To an aliquot of the solution containing 1 equiv. of Cu(II) and 1.2 equiv. of **L1**, 1.2 equiv. of Aβ16 peptide were further added. The three solutions were frozen at 120 K in quartz EPR tubes after the addition of 10 % of glycerol as a cryoprotectant. The **Figure 4.4** shows the superimposed EPR data of these solutions. The blue and green curves on **Figure 4.4** represent the mixture of Cu(II) with **L1** or Aβ16, respectively, while the red curve represents the mixture of Cu(II), **L1** and Aβ16 peptide, (in this order of additions) reflecting that the addition of Aβ16 to the solution containing **Cu(II)L1** did not affect the coordination properties of the preformed complex. These data indicate the formation of one single species (**Cu(II)L1**) even in presence of the Aβ16 peptide and confirm what was observed by UV-vis spectroscopy (**Figure 4.3**).
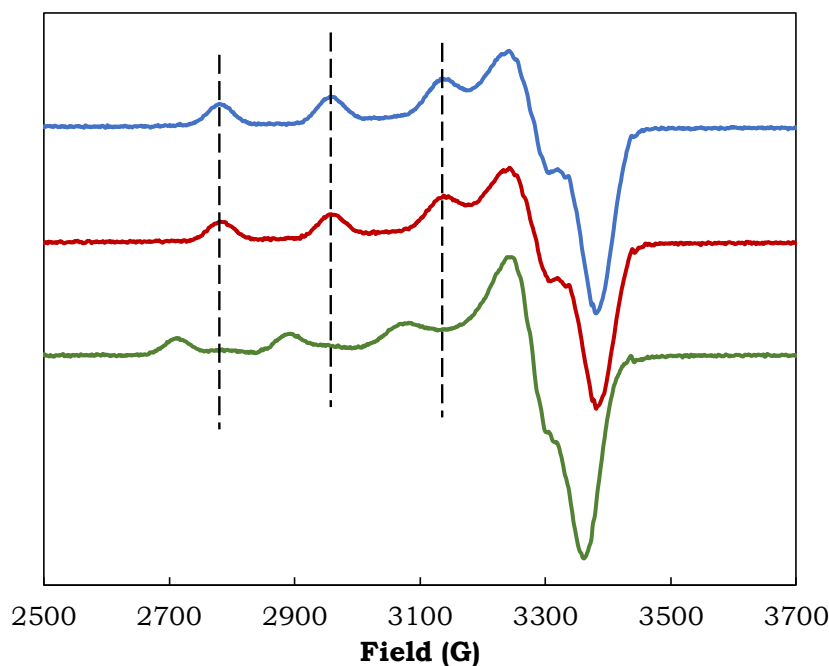
Figure 4.4 Cu(II) competition experiments between Aβ16 peptide and **L1** in 50 mM of HEPES at pH 7.1 and 10 % glycerol. EPR spectra of **Cu(II)L1** [200 μM] (blue curve), Cu(II) [200 μM] + 1.2 equiv. Aβ16 + 1.2 equiv. **L1** (red line) and Cu(II)Aβ16 [200 μM] (green curve).

As described in Section 3.6.1, the Cu(II) binding to Aβ peptide has been deeply studied and reviewed.[13,17–21] The Cu(II) conditional affinity constant of the Aβ16 peptide ($K_{Cu(II)–Aβ16,cond}$) reported is 1.6 x 10^9 M^{-1} at pH 7.1.[21] For the sake of comparison and to get a better insight into the affinity of **L1** for Cu(II) at pH 7.1, the conditional binding constant (K_{cond} = Σ conc. all complex species/[(Σ conc. ligand species not bound to copper) x (Σ conc. copper species not bound to ligand)]) was calculated using the potentiometric data.[1] This value ($K_{Cu(II)-L1,cond}$ = 2.99 x 10^{14} M^{-1}, log $K_{Cu(II)-L1,cond}$ = 14.3) is 5.09 log units higher than the value reported for the binding of Cu(II) to Aβ16 peptide. This means that **L1** has higher affinity for Cu(II) than the Aβ16 and under stoichiometric concentrations, Cu(II) will bind preferentially to **L1**. These observations agree with the UV-vis and EPR experimental data described above.

4.2.2.2. L1, Aβ16 peptide, Cu and Zn.

As it was described on Chapter 3, Section 3.5, Cu has been identified as the main responsible for the oxidative stress caused in the brain,[22] however, it has to be considered that the metal dyshomeostasis observed in AD patients[23,24] affects Cu and Zn concentrations. This implies that Zn(II) can act as a competitor of Cu for the ligand and preclude Cu coordination. Additionally, the Zn(II) concentration within the synaptic cleft is much higher than Cu concentration, namely up to 350 μM for Zn[25] and from 10 to 100 μM for Cu.[26,27] Therefore it is important to study the behavior of these systems in presence of Zn(II).

Initially, the potential of Zn(II) to replace Cu(II) from the complex **Cu(II)L1** was evaluated by UV-vis spectroscopy. Namely, the d-d transition band of the complex **Cu(II)L1** was monitored before and after the addition of 1 equiv. of Zn(II) (Zn(NO$_3$)$_2$) at pH 7.4 (adjusted using NaOH solution).

Panel A in **Figure 4.5** shows the absorption spectra of **L1** (0.5 mM, black line) before and after the addition of 1 equiv. of Cu(II). An absorption band corresponding to the d-d transition of **Cu(II)L1** complex appears at 605 nm with a maximum absorbance of 0.04. No significant changes were observed after the addition of 1 equiv. of Zn(II) (yellow line). The panel B) shows the absorption spectra of **L1** (0.5 mM, black line) before and after the addition of 1 equiv. of Zn(II) (green line). No new bands were detected in the 500 - 700 nm spectral window. It should also be noted that in the 200 - 400 nm window (50 μM), a bathochromic shift is observed on the band correspondent to the free **L1** after the addition of 1 equiv. of Zn(II) indicating the formation of the **Zn(II)L1** complex (see Annex, **Figure A.17**). Lastly, 1 equiv. of Cu(II) was added and the spectrum was recorded again (maximum absorbance 0.04 at 605 nm). These data show no significant differences between the three recorded d-d transition bands (panel C), suggesting that Zn(II) does not interfere with the coordination of Cu(II) to **L1** at 1:1 equiv. ratio.
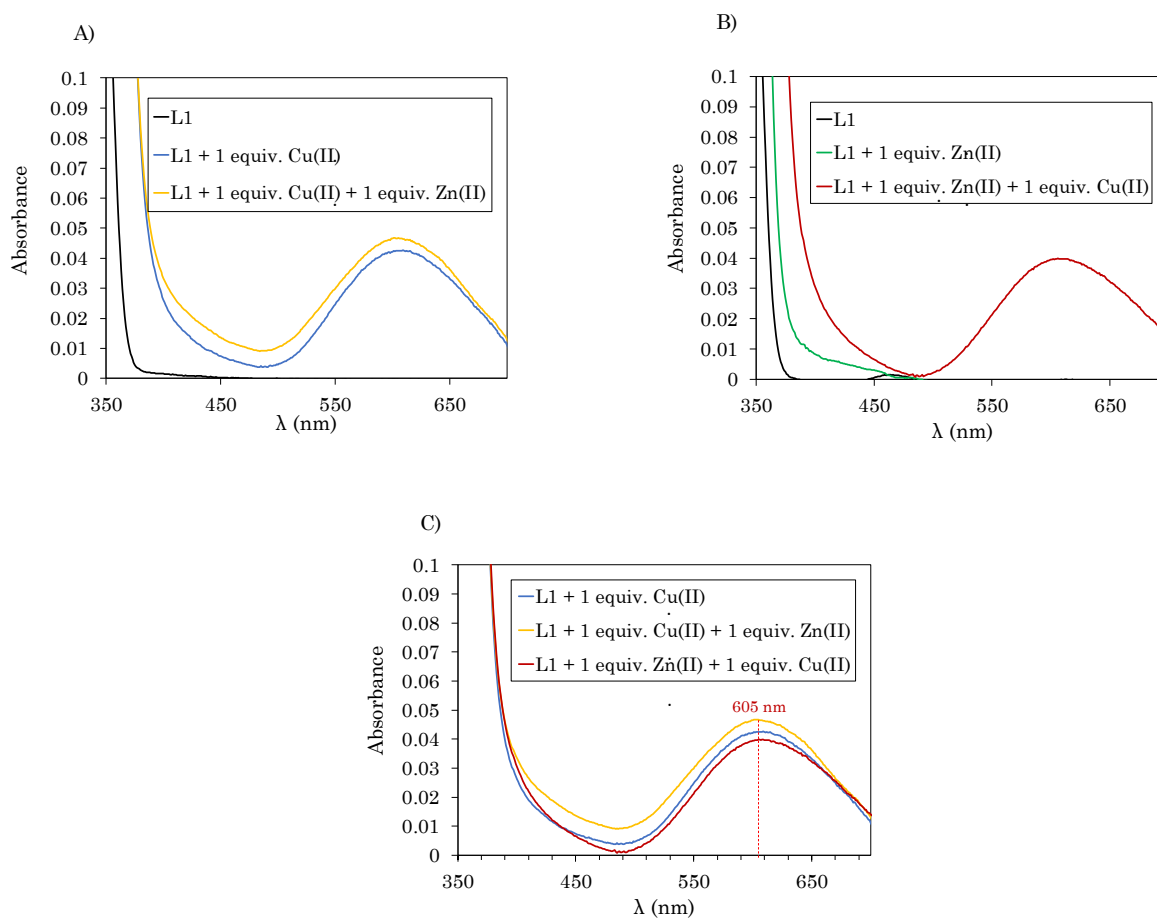
Figure 4.5. Comparison of the Cu(II) d-d transition bands obtained after addition of Cu(II) to **L1** (0.5 mM) at pH 7.4 under different experimental conditions: Panel A) **L1** + 1 equiv. Cu(II) + 1 equiv. of Zn(II). Panel B) **L1** + 1 equiv. Zn(II) + 1 equiv. of Cu(II). Panel C) Overlay of the resulting d-d bands.

The bathochromic shift observed in presence of **L1** with 1 equiv. of Zn(II) suggests the formation of the species **Zn(II)L1**, however the presence of 1 equiv. of Zn(II) does impact the coordination of Cu(II) to **L1**. Considering that Zn(II) concentration within the synaptic cleft is much higher than Cu(II) concentration, a better knowledge of the affinity binding constants of Zn(II) to **L1** is needed to validate the Cu selectivity of **L1** over Zn(II).

4.2.2.2.1. Potentiometric studies.

Potentiometric titrations were initially carried out to determine the affinity binding constant of the Zn(II) complexes of the ligand **L1**. Ratios 1:0.5 and 1:1

(L1:Zn(II), 1 mM) were assayed, but unfortunately the systems could not be studied in the complete pH range as precipitation was observed at pH 6.6. This precluded the determination of the stability constants by potentiometric titrations.

4.2.2.2.2. UV-vis pH titration.

Since the overall formation constants of the Zn(II) complexes with **L1** could not be directly determined by potentiometric titrations due to the precipitation issues, we focused on the apparent binding constant at pH 7.1 ($K_{Zn(II)-L1,app}$), the pH value at which the studies related to ROS formation were carried out. A Zn(II) titration using 50 µM of **L1** was carried out in 100 mM HEPES buffer (pH 7.1). Far UV-vis spectra were recorded upon successive additions of Zn(II) from 0 to 2 equiv. of $Zn(NO_3)_2$ (**Figure 4.6**). A binding curve was obtained by plotting the absorbance at 283 nm vs equiv. of Zn(II) added (inset in **Figure 4.6**) The experimental data were then fit using the **Equation 4.1**,[28–30] where $[L1]_T$ is the total concentration of **L1** (50 µM), $[Zn]$ is the $Zn(NO_3)_2$ concentration in solution at a given point, and A, ε, and ℓ, represent the observed absorbance, the extinction coefficient of the complex and the path length of the UV-vis cell, respectively. The obtained value is shown in **Table 4.1**.

$$A = \epsilon \, \ell \; \frac{\left(\frac{1}{K_{Zn-L1,app}} + [Zn] + [L1]_T\right) - \sqrt{\left(\frac{1}{K_{Zn-L1,app}} + [Zn] + [L1]_T\right)^2 - 4\,[Zn]\,[L1]_T}}{2} \qquad \textbf{(Equation 4.1)}$$
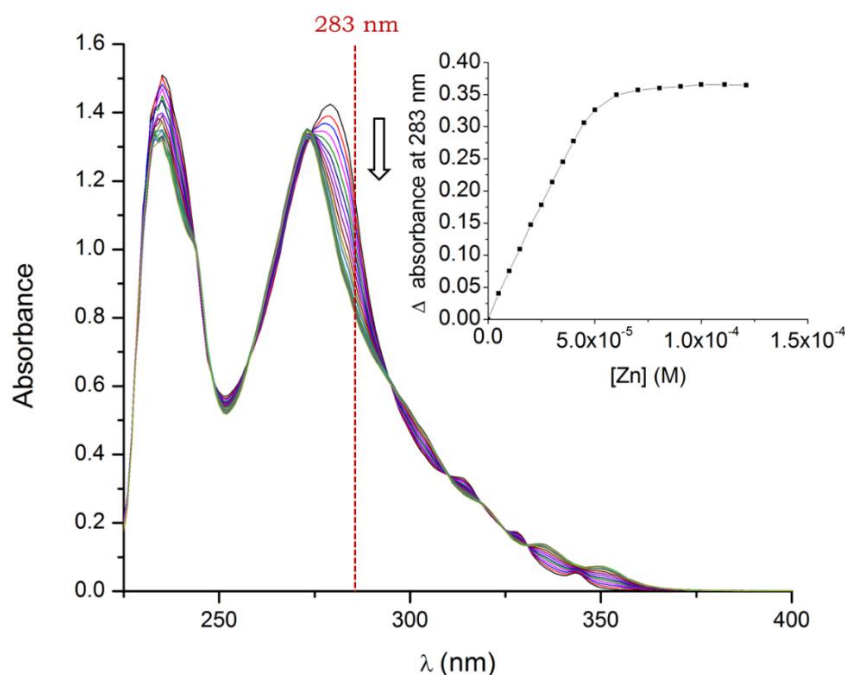
Figure 4.6. UV-vis absorption spectra of the 50 µM **L1** titration with $Zn(NO_3)_2$, from 0 to 2 equiv. of Zn(II) in 100 mM HEPES buffer pH 7.1. The red dashed line indicates the chosen wavelength (283 nm) for the calculations. Inset: experimental binding curve and the fit obtained (black line) using **Equation 4.1**. ΔAbsorbance is defined as the Abs_{283nm} for each addition — Abs_{283nm} when $[Zn] = 0$.

In order to validate the $K_{Zn(II)-L1,app}$ obtained, it was recalculated using a different method, namely HypSpec (HYPERQUAD suit of programs).[31] The two values obtained (**Table 4.1**) are consistent and indicate that the K_{app} of Zn(II) for **L1** is *ca.* 0.2 log unit higher than the one for reported for Aβ16 peptide ($K_{Zn(II)-Aβ16,app} = 5.04$).[32]

Table 4.1. Apparent affinity constants at pH 7.1. (log K_{app}) determined from UV-vis titration data for **Zn(II)L1**.

Method used	log $K_{Zn(II)-L1,app}$
Equation 4.1[28–30]	6.08
HypSpec[31]	5.88

4.2.2.2.3. Comparison of the Cu(II) and Zn(II) affinity constants.

For comparison and to confirm the selectivity of **L1** towards Cu(II), the same protocol was carried out to calculate the K_{app} of Cu(II) to **L1**. Unfortunately, due to the high binding affinity of Cu(II) to **L1** the data obtained were not suitable for the fitting. To overcome this issue, the $K_{Cu(II)-L1,app}$ at pH 7.1 was directly calculated from the $K_{Cu(II)-L1,cond}$ obtained from potentiometric studies (K_{cond} = Σ conc. all complex species / [(Σ conc. ligand species not bound to copper) x (Σ conc. copper species not bound to ligand)],[33] log $K_{Cu(II)-L1,cond}$ = 14.3 at pH 7.1) using the **Equation 4.2**,[34] where [HEPES] = 0.1 M, $\beta_{Cu(II)-HEPES}$ = $10^{3.22}$ and HEPES pK_a = 7.41. This model considers the buffer contributions at a given pH and concentration. The values obtained for Cu(II) and Zn(II) to **L1**, and the respective reported affinity values for Aβ16 are summarized in **Table 4.2**.

$$\log K_{Cu(II)-L1,app} = \log K_{Cu(II)-L1,cond} - \log \left(1 + \beta_{Cu(II)-HEPES} + \frac{[HEPES]}{1+10^{-pH+pKa}}\right) \quad \textbf{(Equation 4.2)}$$

Table 4.2. Apparent affinity constants (K_{app}) of Cu(II) and Zn(II) binding to **L1** and to Aβ16 at pH 7.1 (in 100 mM HEPES buffer unless otherwise noted).

	K_{app} (M^{-1})	log K_{app}
Cu(II)L1 [a]	3.55 x 10^{12}	12.55
Zn(II)L1	7.6 x 10^{5}	5.88
Cu(II)Aβ16 [b]	2.85 x 10^{7}	7.46
Zn(II)Aβ16 [c]	1.1 x 10^{5}	5.04

[a] Calculated from the $K_{Cu(II)-L1,cond}$ obtained by potentiometric studies from reference 1
[b] Calculated from the $K_{Cu(II)-Aβ16,cond}$ reported in reference 21
[c] Value from reference 32, in 50 mM HEPES

The values reported in the **Table 4.2** indicate that under this conditions Cu(II) has more affinity to **L1** than to Aβ16 ($K_{Cu(II)-L1,app} > K_{Cu(II)-A\beta,app}$), and the affinity of Cu(II) to **L1** is greater than the one of Zn(II) ($K_{Cu(II)-L1,app} > K_{Zn(II)-L1,app}$). These results show that Zn(II) is not competing against Cu(II) for binding to **L1**.

All the data reported in Section 4.2.2.2 indicate that **L1** must be capable to remove Cu(II) from Aβ16 peptide even in the presence of Zn(II) and consequently to arrest the generation of ROS. At this point, it was found important to evaluate the affinity constant of Cu(I) to **L1** considering that the ligand Phen can bind Cu(I) with high affinity forming the species Cu(I)(Phen)$_2$.[35]

4.2.3. Determination of the Cu(I) affinity constant of L1.

The affinity values of Cu(I) to **L1** were determined from the UV-vis anaerobic titration of a solution containing 0.2 mM of **L1** in 100 mM HEPES buffer at pH 7.1 with a solution containing 8.5 mM of tetrakis(ACN)Cu(I) hexafluorophosphate. UV-vis spectra were collected after each successive addition from 0 to 4 equiv. of Cu(I) (**Figure 4.7**). The experimental data were analyzed and fit with HypSpec (HYPERQUAD suit of programs).[31] The best fitting considers the formation of the species **Cu(I)(L1)$_2$**, **Cu(I)L1** and **Cu(I)$_2$L1**. The values obtained for the apparent affinity constants are presented in **Table 4.3**. A speciation diagram in the conditions of the titration was obtained using the calculated K_{app} constants with HySS (HYPERQUAD suit of programs) and indicates the changes in speciation across the increase of the Cu(I) concentration[36] (**Figure 4.7, B**).
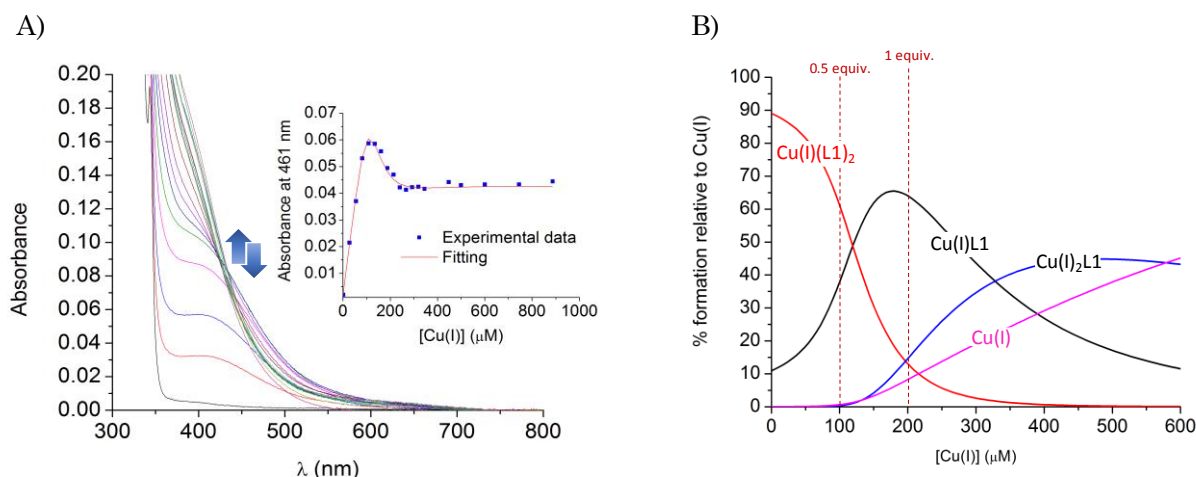
Figure 4.7. UV-vis spectra of **L1** (0.2 mM) titration with Cu(I) (0 to 4 equiv.) in 100 mM HEPES buffer at pH 7.1. Inset: experimental binding curve and fit at 461 nm. B) Speciation diagram of the species in solution relative to Cu(I) in presence of **L1** (0.2 mM) in 100 HEPES at pH 7.1 obtained by HySS.

Table 4.3. Apparent affinity constants (K_{app}) of Cu(I) to **L1** and Aβ16 in 100 mM HEPES buffer at pH 7.1 unless otherwise noted).

	K_{app} (M^{-1})	log K_{app}
Cu(I)L1	1.54 x 10^6	6.19
Cu(I)(L1)$_2$	2.34 x 10^{10}	10.8
Cu(I)$_2$L1	1.07 x 10^{10}	10.03
Cu(I)Aβ16[a]	7.5 x 10^6	6.87

[a] Reported in reference 37 at pH 7.4. This means that this value is an overestimation of the value at pH 7.1.

The speciation diagrams shown that under equimolar conditions of **L1** and Cu(I) the major species in solution correspond to the **Cu(I)L1** species. However, in presence of excess of **L1**, i.e. 100 µM of Cu(I) (0.5 equiv.) and 200 µM of L1, two major species coexists in solution: **Cu(I)L1** and **Cu(I)(L1)$_2$** (**Figure** 4.8).

Cu(I)L1   **Cu(I)(L1)$_2$**
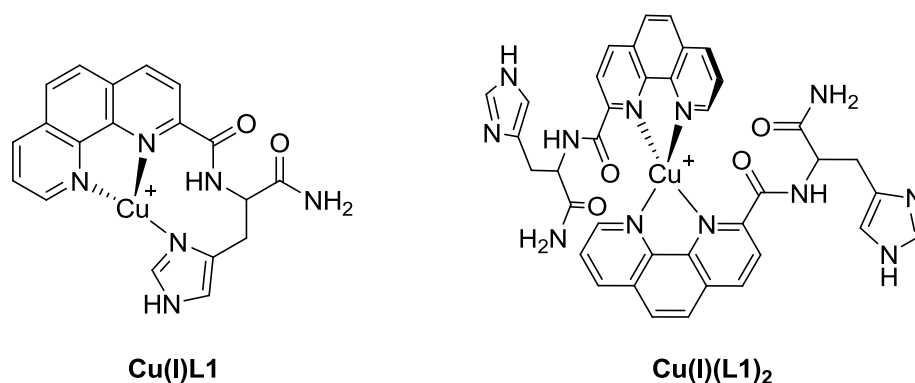
Figure 4.8. Proposed structures for the Cu(I) complexes of **L1**.

These results indicate that **L1** could potentially stop the production of ROS by removing either Cu(II) or Cu(I) from Aβ peptide even in presence of Zn(II). Therefore, to validate this hypothesis, further experiments to explore the production of ROS in presence of Zn(II) and Aβ16 were performed, and they are described next.

4.2.4. Evaluating the L1 capabilities to arrest ROS formation in the absence and presence of Zn(II).

The capacity of **L1** to remove Cu(II) and stop the production of ROS was evaluated in absence and presence of Zn under 3 different conditions: (i) starting from a mixture of Cu(II)/Cu(I) Aβ16 species, (ii) starting from Cu(II)Aβ16 and lastly, (iii) starting from Cu(I)Aβ16. The samples were prepared using the following concentrations: AscH⁻ [100 μM], CuCl$_2$ [10 μM], Aβ16 [12 μM], ZnCl$_2$ [10 μM] and **L1** [12 μM] in 100 mM of HEPES pH 7.1.

4.2.4.1. Absence of Zn(II).

As it was mentioned in Section 4.2.1, the ROS production was evaluated using UV-vis spectroscopy by monitoring the consumption of AscH⁻ at 265 nm (**Figure 4.9**).
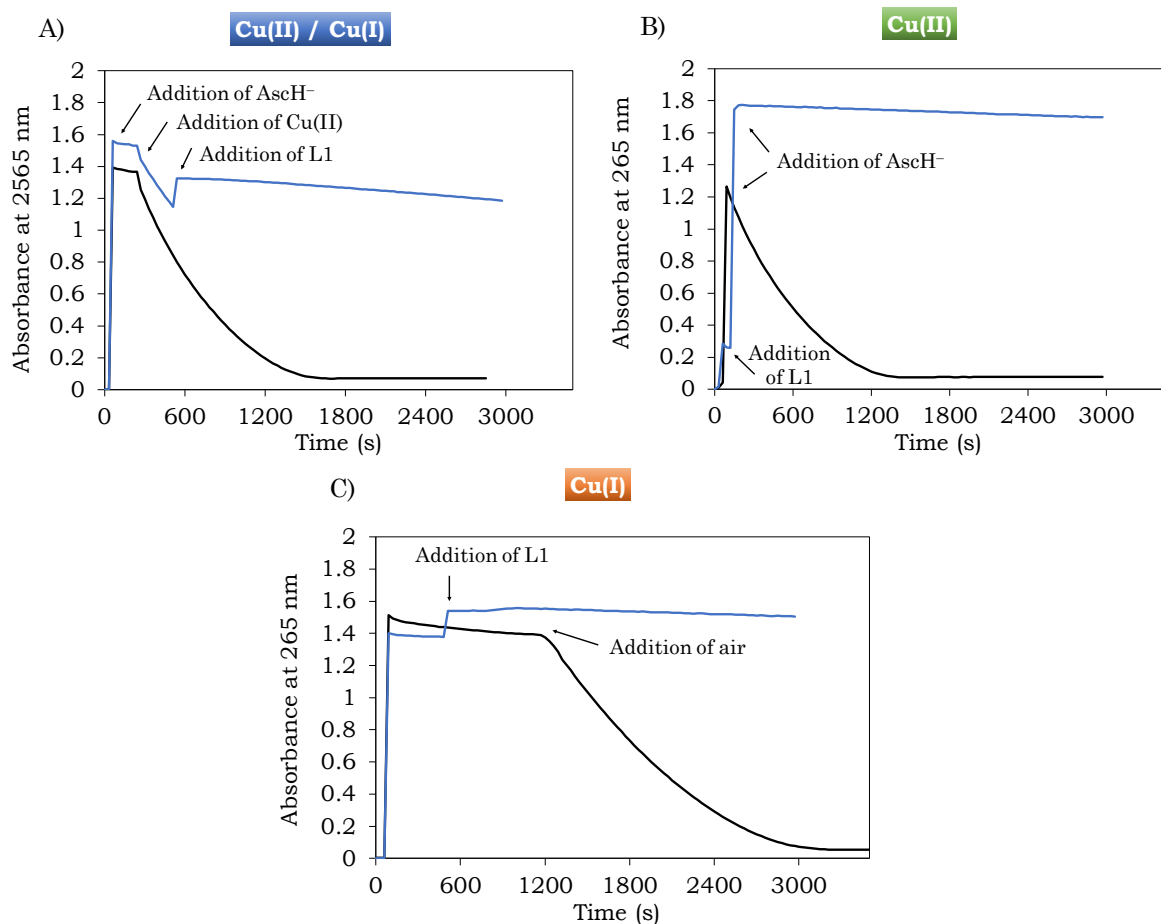
Figure 4.9. Kinetics of AscH$^-$ consumption by CuAβ16 monitored by UV-vis spectroscopy at 265 nm in 100 mM HEPES buffer pH 7.1 in presence (blue curves) and absence (black curves) of **L1**, under three different conditions: Panel A) Starting from Cu(II)/Cu(I) mixture. Panel B) Starting from Cu(II). Panel C) Starting from Cu(I). (Experiments performed in the Laboratoire de Chimie de Coordination (LCC) in Toulouse by Dr. Charlène Esmieu).

(i)   Starting from the mixture of Cu(II)/Cu(I).

In this experiment (**Figure 4.9**, panel A) reagents were added following this order of additions: 1) in presence of **L1** (blue curve): AscH$^-$ + Aβ16 + Cu(II)+ **L1**. 2) positive control (no ligand, black curve): AscH$^-$ + Aβ16 + Cu(II). After the addition of **L1** into the system (blue line), the consumption of AscH$^-$ produced by the redox active complex CuAβ16 was arrested (**Scheme 4.1**), meaning that **L1** is capable to deactivate this complex by removing the Cu ion (either Cu(II) or Cu(I)) from Aβ16 peptide and form **CuL1** species that are redox silent.

(ii)   Starting from Cu(II).

In these experiments (**Figure 4.9**, panel B) the next order of additions was followed: 1) in presence of **L1** (blue curve): Aβ16 + Cu(II) + **L1** + AscH⁻. 2) positive control (no ligand, black curve): Aβ16 +Cu(II) + AscH⁻. For this experiment the ligand was added after the complex Cu(II)Aβ16 was formed, and the AscH⁻ was added at the end. The experimental data reveal that **L1** can remove Cu(II) from the complex Cu(II)Aβ16 and generate a redox silent specie **Cu(II)L1** that doesn't promote the generation of ROS (blue line).

(iii)   Starting from Cu(I).

Cu(II) chelation and the ability to stabilize the corresponding Cu(II) complex are two important features that are key in the development of drug candidates in chelation therapy. However, as it was previously mentioned (Section 3.6.1.1, Chapter 3) the brain has a rather reductive environment[38,39] and consequently it is possible that Cu(I) may be mostly present in the synaptic cleft. Therefore, even the results obtained in (i) seem to indicate that **L1** can sequester Cu(I) from Aβ16 peptide, it was considered critical to explore in more detail the Cu(I) chelation abilities of **L1** in presence of the Aβ16 peptide.

The following set of experiments (**Figure 4.9**, panel C) were performed under anaerobic conditions and the introduction of air to the system is indicated for each case. The additions were performed as follows: 1) in presence of **L1** (blue curve): Cu(II) + AscH⁻+ Aβ16 + **L1** + air; 2) positive control (no ligand, black curve): Cu(II) + AscH⁻+ Aβ16 + air. In these experiments, AscH⁻ was added after Cu(II) under anaerobic conditions in order to reduce all the Cu(II) into Cu(I). Afterwards Aβ16 was added to form the complex Cu(I)Aβ16, and finally **L1** was added. The results indicate that the addition of **L1** stop the consumption of AscH⁻ meaning that **L1** can indeed remove Cu(I) from the Aβ16 peptide.

These results (**Figure 4.9**) are in line with the K_{app} values shown in **Table 4.2** since Cu(II) has a higher affinity for **L1** than for Aβ16 peptide, and thus, **L1** can sequester Cu(II) from the redox active Cu complexes of Aβ16. For the case of Cu(I), the affinity constants of L1 and Aβ16 are similar enough, that besides the

formation of Cu(I)L1, the formation of a ternary species **Cu(I)(L1)(Aβ16**) not efficient in ROS production, is possible. It is worthwhile to mention that the slopes observed for the three experiments are different and this can indicate that the ability of **L1** to chelate Cu(II) and Cu(I) and form the redox silent complexes is different depending on the experimental conditions. In particular, the slope for the experiments starting from Cu(I) is smaller, meaning that **L1** is more efficient to stop the production of ROS when initially there is only Cu(I) coordinated to Aβ16.

4.2.4.2. Presence of Zn(II).

As it was emphasized (Section 4.2.2.2) it is important to study the behavior of **L1** in presence of Zn(II). **Table 4.2** and **Table 4.3** show the different K_{app} values calculated for the binding of Cu(II) and Zn(II) (**Table 4.2**), and Cu(I) (**Table 4.3**) to **L1** and Aβ16 peptide. Since the affinity of Cu(II) and Cu(I) to **L1** is greater than the one of Zn(II) ($K_{Cu(II)-L1,app} > K_{Cu(I)-L1,app} > K_{Zn(II)-L1,app}$), **L1** might be capable to bind Cu even in presence of Zn(II). To confirm the hypothesis the experiments described in Section 4.2.3.1 were repeated in the presence of Zn(II) (**Figure 4.10**).

(i)   Starting from the mixture of Cu(II)/Cu(I).

For this experiment (**Figure 4.10**, panel A) the additions were performed as follows: 1) in presence of **L1** (blue curve): AscH⁻ + Aβ16 + Zn(II) + Cu(II)+ **L1**; 2) positive control (no ligand, black curve): AscH⁻ + Aβ16 + Zn(II) + Cu(II). As it was observed in the previous set of experiments, the addition of **L1** arrests the consumption of AscH⁻, this means that Zn(II) does not interfere with the Cu coordination and **L1** is capable to remove the Cu from Aβ16 peptide to form a redox silent **CuL1** species.
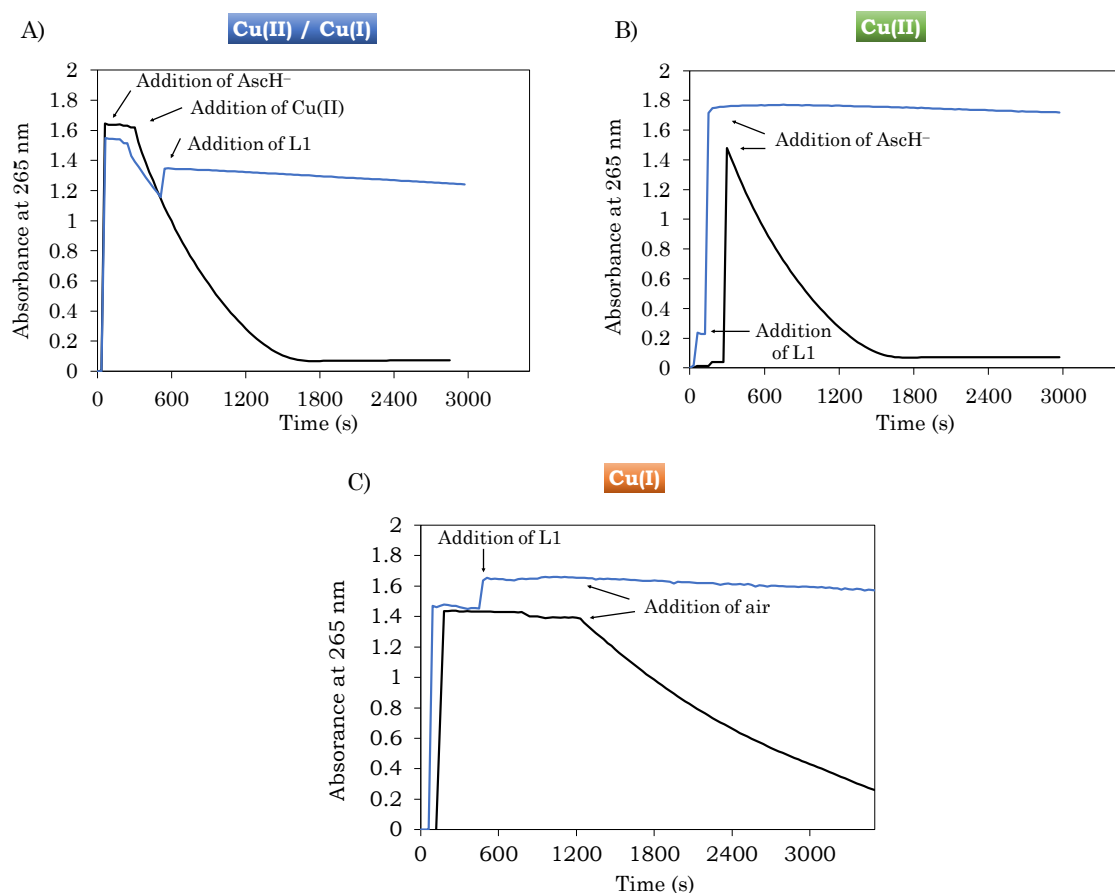
Figure 4.10. Kinetics of AscH⁻ consumption by CuAβ16 in the presence of Zn(II) monitored by UV-vis spectroscopy at 265 nm in 100 mM HEPES buffer pH 7.1, in presence (blue curves)* and absence (black curves) of **L1**, under three different conditions: Panel A) Starting from Cu(II)/Cu(I) mixture. Panel B) Starting from Cu(II). Panel C) Starting from Cu(I). (*Experiments performed at the LCC in Toulouse by Dr. Charlène Esmieu).

(ii)   Starting from Cu(II).

In these experiments (**Figure 4.10**, panel B) the next order of additions was followed: 1) in presence of **L1** (blue curve): Aβ16 + Zn(II) + Cu(II) + **L1** + AscH⁻; 2) positive control (no ligand, black curve): Aβ16 + Zn(II) + Cu(II) + AscH⁻. For this experiment, the ligand is added after the complex Cu(II)Aβ16 is formed, and the AscH⁻ is added at the end. The experiment revealed that **L1** can remove Cu(II) from the complex Cu(II)Aβ16 and generate a redox silent **Cu(II)L1** species that doesn't promote the generation of ROS (blue line).

(iii)   Starting from Cu(I).

In this set of experiments (**Figure 4.10**, panel C) the next order of additions was followed: 1) in presence of **L1** (blue curve): Cu(II) + AscH⁻ + Aβ16 + Zn(II) + **L1** + air; 2) positive control (no ligand, black curve): Cu(II) + AscH⁻+ Aβ16 + Zn(II) + air. This experiment reveals that **L1** can sequester Cu(I) from the initial Cu(I)Aβ16 complex and arrest the consumption of AscH⁻, i.e. production of ROS, by the formation of a redox silent **Cu(I)L1** species.

These experiments highlight the capability of **L1** to bind Cu(II) and Cu(I) and deactivate the redox active complex CuAβ16 even in presence of 1 equiv. Zn(II). These results are in agreement with the fact that the Cu(II) and Cu(I) affinities of **L1** are higher than the one of Zn(II), and that Zn(II) is not competing for L1 with Cu(II) and to a lesser extent with Cu(I). However, as mentioned before the concentrations of Zn(II) in the synaptic cleft are up to one order of magnitude higher than the concentrations of Cu, and these conditions could represent a potential challenge for the efficacy of **L1**. Nonetheless, considering the difference in magnitude for the K_{app} values reported in **Table 4.2** and **Table 4.3**, one can hypothesize that Zn(II) will not represent an issue even in the excess ratio observed in the synaptic cleft.

4.2.5. Evaluation of the formation of ROS in presence of excess of L1.

Since it was observed in Section 4.2.3 that **L1** can form **Cu(I)(L1)₂** complexes, further experiments using larger excess of **L1** were carried out. These experiments were performed under the same conditions used in the previous sections (Sections 4.2.3.1 and 4.2.3.2) and starting from Cu(II), Cu(I) or the mixture Cu(II)/Cu(I) (**Figure 4.11**).

When the AscH⁻ consumption starts from Cu(II) (**Figure 4.11**, A) one can observe that **L1** is more efficient in arresting AscH⁻ at the ratios 1.2:1 (blue curve) than 2:1 (red curve). The same effect is observed when the AscH⁻ consumption starts from Cu(I), although in this case the effect is less pronounced (**Figure 4.11**, B). Interestingly, the effect on the AscH⁻ consumption profiles caused by the

different L:Cu ratios is clearly stronger if the AscH⁻ consumption starts from the mixture Cu(II)/Cu(I). For this case, these experiments were repeated in the presence of Aβ16 peptide and Zn(II) (**Figure 4.12**).

Figure 4.11. Kinetics of AscH⁻ consumption, followed by UV-vis spectroscopy at 265 nm, in presence of **L1** at two different concentrations: 12 μM (ratio: 1.2:1 (L:M), blue curves) and 20 μM (ratio: 2:1, red curves). Panel A): starting from Cu(II), order of additions: Cu(II) + **L1** + AscH⁻. Panel B): starting from Cu(I), order of additions: Cu(II) + AscH⁻ + **L1** + air. Panel C): starting from the mixture Cu(II)/Cu(I), order of additions AscH⁻ + Cu(II) + **L1**. Dashed lines indicate the initial Abs$_{265nm}$. The blue and red arrows indicate the differences in absorbance for ratios 1.2:1 and 2:1, respectively (*Experiments performed at the LCC in Toulouse by Charlène Esmieu).

The **Figure 4.12**, A compares the different AscH⁻ consumption profiles observed for the ratios 1.2:1 and 2:1 in presence of Aβ16 peptide and indicates that the addition of 1 extra equiv. of **L1** reduces the effectiveness of this ligand

compared to the ratio 1.2:1 However, this effect is less pronounced that the one observed in the absence of Aβ16 peptide. When Zn(II) is also present the addition of 1 extra equiv. of **L1** has practically no effect as it is shown in **Figure 4.12**, C. Overall these data highlight that the stoichiometry has an influence on the effectiveness of **L1** to arrest AscH⁻ consumption only in case of Cu(I)/Cu(II) mixture and in absence of Zn(II).
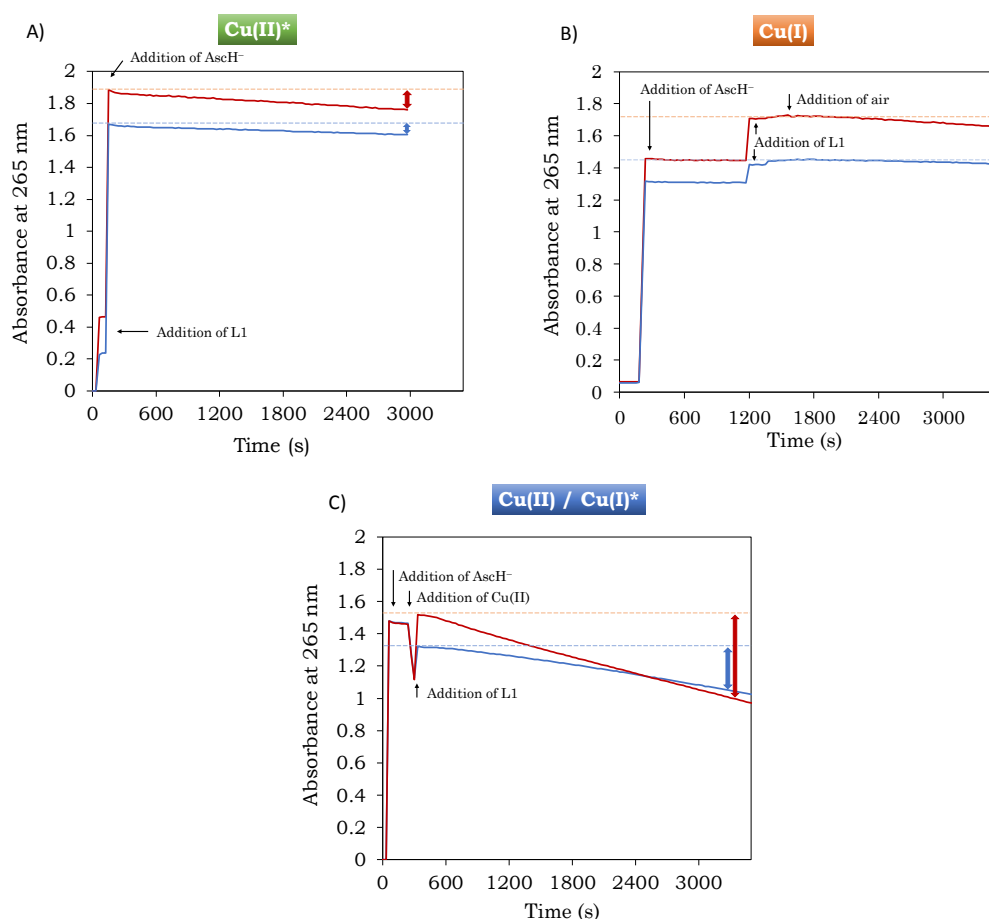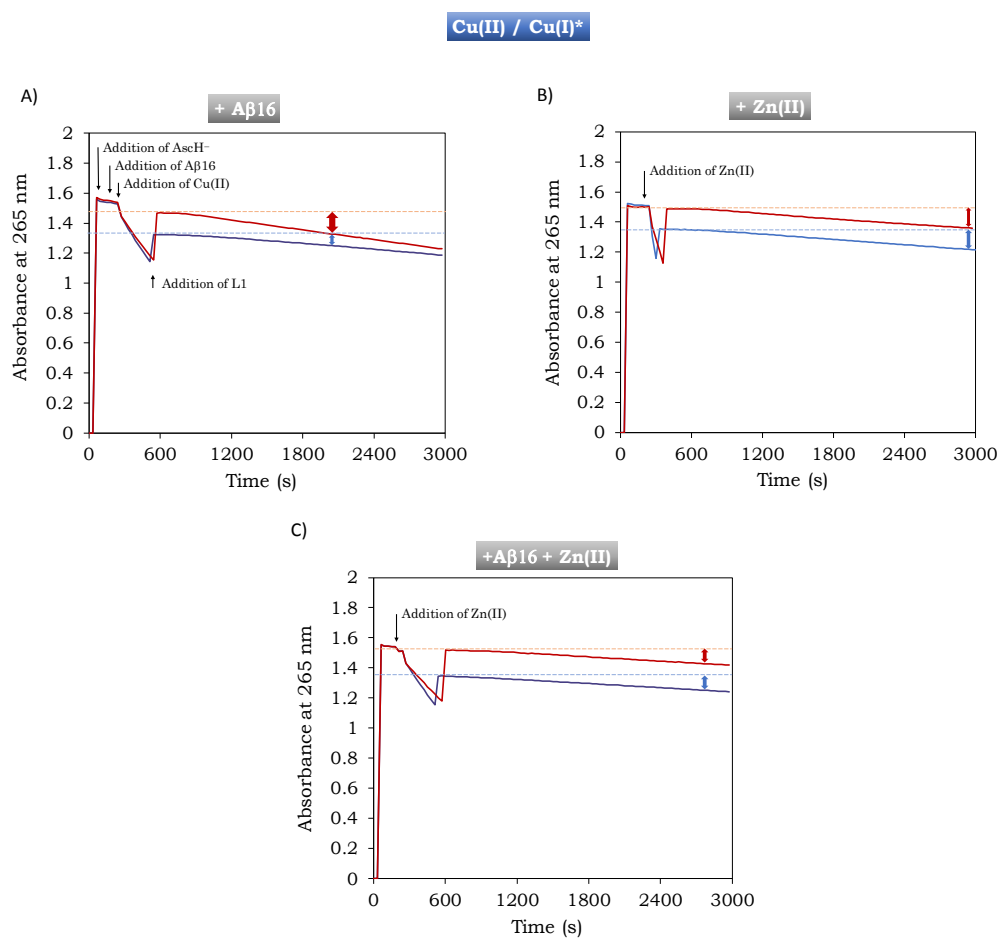

Figure 4.12. Kinetics of AscH⁻ consumption starting from the mixture of Cu(II)/Cu(I), followed by UV-vis spectroscopy at 265 nm, in presence of **L1** at two different concentrations: 12 μM (ratio: 1.2:1, blue curves) and 20 μM (ratio: 2:1, red curves). Panel A) order of additions: AscH⁻ + Aβ16 + Cu(II) + **L1**. Panel B) order of additions: AscH⁻ + Zn(II) + Cu(II) + **L1**. Panel C) order of additions: AscH⁻ + Aβ16 + Zn(II) + Cu(II) + **L1**. Dashed lines indicate the absorbance when **L1** is added. The blue and red arrows indicate, the different slopes for ratios 1.2:1 and 2:1 respectively (*Experiments performed at the LCC in Toulouse by Charlène Esmieu).

4.2.5.1. How is the excess of L1 affecting its effectiveness to stop ROS production?

The effect observed on the effectiveness of **L1** to arrest ROS production between 1.2:1 and 2:1 (L:Cu) ratios is present in the three different conditions tested (**Figure 4.11**). However, this effect is clearly stronger when the kinetics start from the mixture of Cu(II)/Cu(I) (**Figure 4.11**). Considering all the data gathered so far and in order to explain the experimental observations, the mechanism shown in **Scheme 4.2** was proposed, in which for the sake of simplicity **L1** is ascribed simply as L.

According to the K_{app} calculated (**Table 4.3**), the species **Cu(I)(L1)$_2$** is formed even at low excess of **L1** (9.6 % at 1.2 equiv. and 29.1 % at 2 equiv. see Annex **Table A.2**). This species can react with **Cu(II)L1** giving rise to **Cu(I)L1** and **Cu(II)(L1)$_2$** species (**Scheme 4.2**, pathway **(a)**). The latter, can evolve through 2 different pathways that are in competition: via the dissociation of one **L1** (pathway **(b)**) leading to the **Cu(II)L1** (resistant to the AscH$^-$ reduction), or by its AscH$^-$ reduction to form the species **Cu(I)(L1)$_2$** (pathway **(c)**). It is possible to posit that the formation of **Cu(II)L1** from **Cu(II)(L1)$_2$** will imply a strong reorganization of the coordination sphere and that **Cu(II)(L1)$_2$** might keep the same geometry than **Cu(I)(L1)$_2$** (**Figure 4.8**) thus being easily reduced in line with the redox potential values reported for related complexes.[35] The species **Cu(I)L1** formed can be oxidized into **Cu(II)L1** (pathway **(d)**) or it can coordinate an additional **L1**, leading to the formation of **Cu(I)(L1)$_2$** (pathway **(e)**). This redox reaction agrees with the higher consumption of AscH$^-$ observed when the process starts from the mixture Cu(II)/Cu(I). Thus, the formation of the species **Cu(I)(L1)$_2$**, which is the only one that can mediate the reduction of **Cu(II)L1**, is favored when there is excess of **L1**. This explains the increased consumption of AscH$^-$ when there are 2 equiv. of **L1** in comparison with 1.2 equiv.
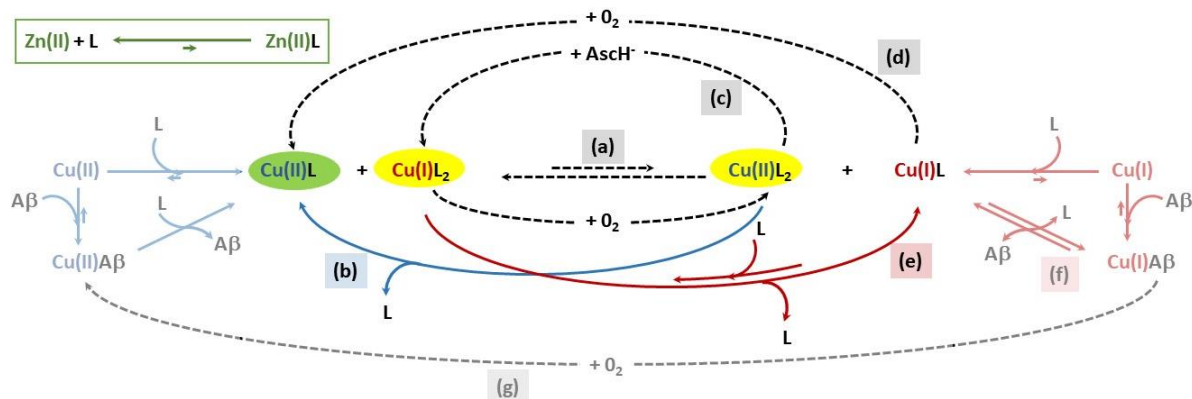
Scheme 4.2. Mechanism proposed to explain the influence of the excess of **L1** (ascribed as L for simplicity) in its effectiveness to arrest the consumption of $AscH^-$. Species containing Cu(II), Cu(I) and Zn(II) are written in blue, red and green respectively. The species resistant to $AscH^-$ reduction (green oval) and $AscH^-/O_2$ consuming species (yellow ovals) are highlighted. Solid and dashed pathways correspond to speciation and redox reactions, respectively. Reactions implying Aβ16 peptide are shaded. For the sake of clarity, only processes key for the ROS production are shown.

In presence of Aβ16 peptide, **L1** lessen the consumption of $AscH^-$ regardless of the conditions (**Figure 4.12**, panel A and panel C). This is in line with the Cu(II) affinity and Cu(II) over Zn(II) selectivity of **L1** (see **Table 4.2**).

The effect observed in presence of Zn(II) (**Figure 4.12**, panel B) is explained by the diminution of the concentration of available **L1** (decrease of stoichiometric excess via the formation of **Zn(II)L1**) that prevents the formation of **Cu(I)(L1)₂**. This is reflected in the weaker $AscH^-$ consumption observed.

Interestingly, the impact of the **L1** excess in presence of Zn(II) is similar with or without Aβ16 (**Figure 4.12**, panels B and C). This indicates that the change of the speciation between **Cu(I)L** and **Cu(I)(L1)₂** due to the presence of Aβ16 (pathway **(f)**, **Table 4.3**) and the quick formation of **Cu(II)L1** via Cu(II)Aβ16 from the oxidation of Cu(I)Aβ (pathway **(g)**) either do not contribute significantly to the main redox reaction (pathway **(a)**) or have counterbalanced effects.

4.2.6. Towards multitarget approach: Functionalization of L1.

As it was previously described, on Chapter 3 (Section 3.3), AD is a complex and multifactorial disease. Consequently, current research for effective

therapeutic agents combines different strategies at once in order to arrest the development of AD. The recent interest in molecules with multitarget features has been widely described and compiled (see Chapter 3, Section 3.6.1). These data indicate the promising outlook of this approach. In this context, we decided to explore the functionalization of the most promising ligand, **L1**, in order to combine its antioxidant activity and its Cu chelation features with two scaffolds that could provide therapeutic added value to the resultant hybrids (**Figure 4.13**).
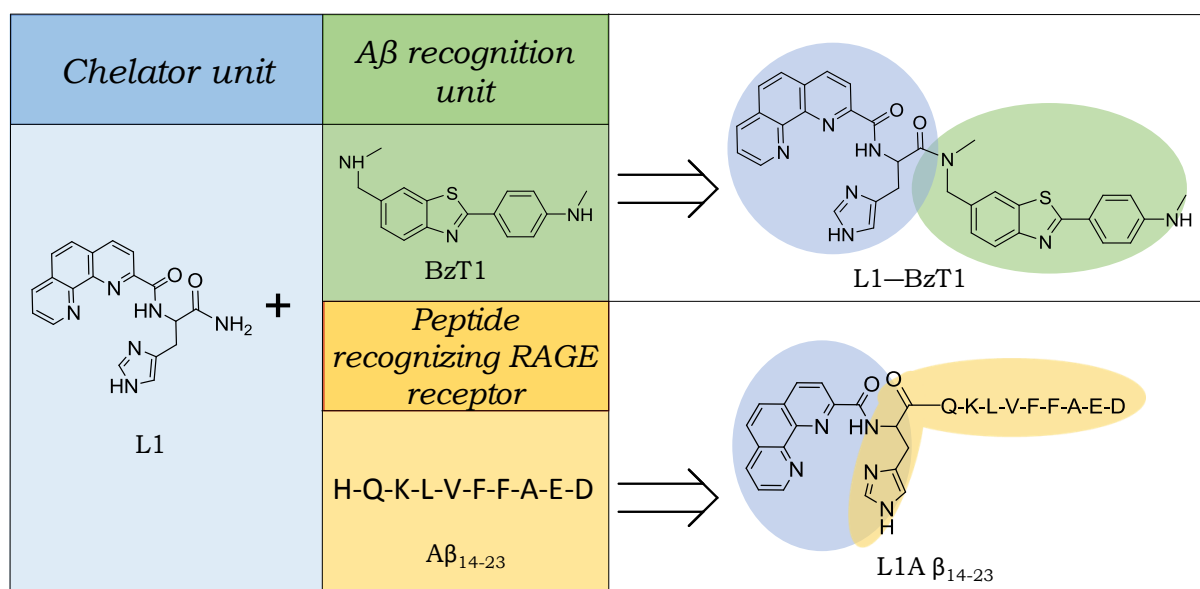
Figure 4.13. Illustration of the two approaches to functionalize **L1**.

The first approach proposes the functionalization of **L1** with the benzothiazole **Bzt1** (**Figure 4.13**). **Bzt1** is a derivate of Thioflavin-T (ThT), a molecular probe able to recognize and interact with Aβ fibrils.[42] The second strategy explores the functionalization of **L1** with a peptide that recognizes the receptor for advanced glycation endproducts (RAGE) and has the capability of surmount one of the most challenging pharmacokinetic issues *in vivo*: crossing the BBB.[43]

4.2.6.1. Functionalization of L1 with the Aβ fibril recognizer BzT1.

In recent years huge efforts have been made to develop markers for Aβ aggregates i.e. derivates of ThT,[44] stilbenes[45] or naphthyl based compounds[46,47] that allow their recognition and *in vivo* detection through imaging.

Herein, the different strategies tested to functionalize **L1** with **Bzt1**, capable to interact with Aβ fibrils,[48] are presented.

Initially, the synthesis of the precursor **L2(Trt)** was carried out. The precursor contains a carboxylic acid for coupling with the free amine of the **Bzt1(Boc)**, and a trityl (Trt) protected His (imidazole ring) to avoid side reactions during coupling. The synthesis was done using SPPS protocols (**Scheme 4.3**), and the 2-chlorotrityl chloride resin, to obtain the correspondent carboxylic acid derivate. Fmoc-His(Trt)-OH (**15**) was coupled to the resin using N,N-diisopropylethylamine (DIEA) (2.5 equiv.) in dichloromethane (DCM). After Fmoc deprotection, the coupling of the 2-carboxy-1,10-phenanthroline (**14**) (synthesis described on Chapter 2, Section 2.1) was performed in dimethylformamide (DMF) using 4 equiv. of benzotriazol-1-yl-oxytripyrrolidinophosphonium hexafluorophosphate (PyBOP) as coupling agent and 8 equiv. of DIEA as base. Finally, **L2(Trt)** was cleaved from the resin by treating the resin for 2 minutes with a solution of 99:1, DCM:TFA. The treatment was done 8 times or until no spot was observed on TLC under a UV-vis lamp. The filtrated liquid, containing the ligand, was neutralized with 400 µL of DIEA and collected. The removal of the solvent was done by rotary evaporation. The residue was dissolved in H_2O and after an organic work up, chloroform ($CHCl_3$) was removed with a rotary evaporator. The product was identified using Proton Nuclear Magnetic Resonance (^{1}H NMR) and mass spectrometry (see Annex **Figures A.18 – A.20**).
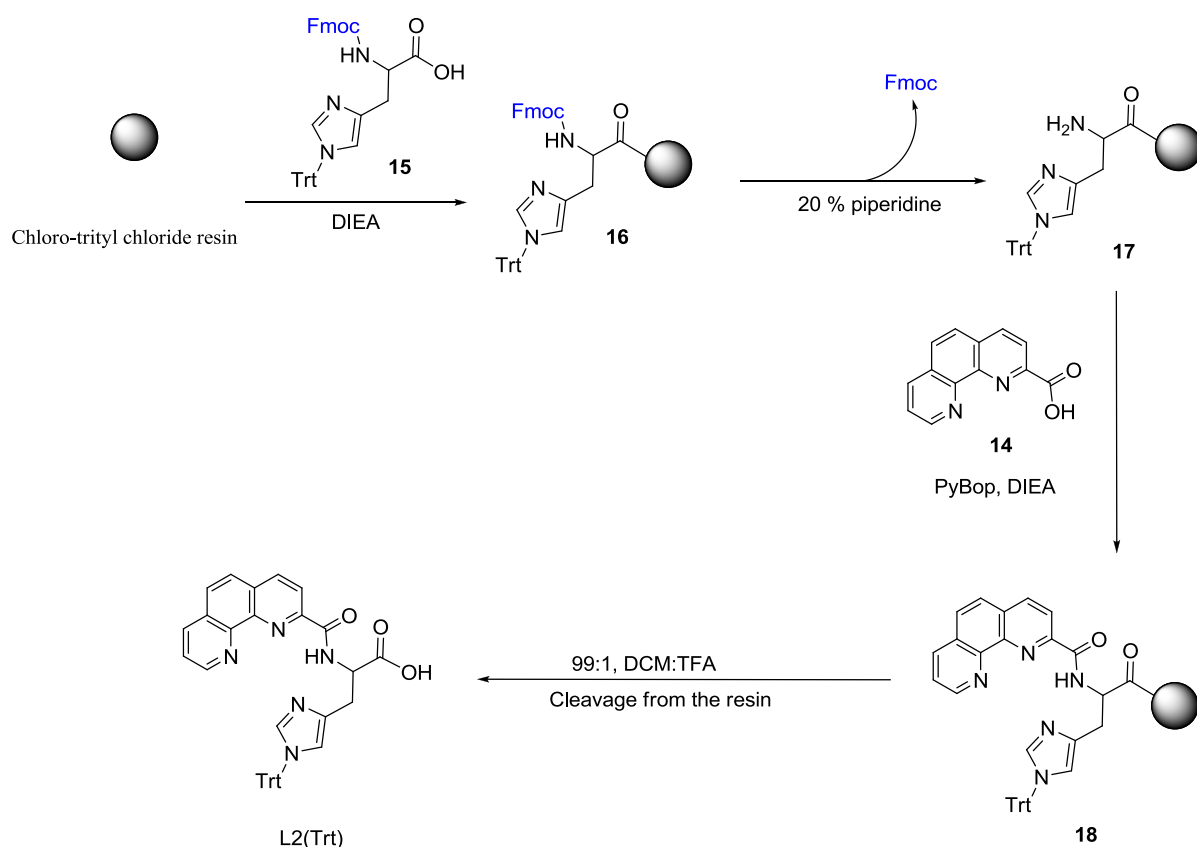
Scheme 4.3. Synthesis of **L2(Trt)**.

Subsequently, **L2(Trt)** and PyBOP (1.1 equiv.) were dissolved in dry DCM with 4 equiv. of DIEA (**Scheme 4.4**). After homogenization, a solution containing 1 equiv. of **Bzt1(Boc)** was added, the mixture was stirred at RT and monitored by thin-layer chromatography (TLC). After 3 h, no major changes were observed. The crude was dissolved in ethyl acetate. After work-up, the organic phase was concentrated and eluted through a chromatographic column (silica gel) using a system 9:2, methanol (MeOH):CHCl$_3$. It was possible to recover the raw material and electrospray ionization mass spectrometry (ESI-MS) confirmed that there were no traces of the expected product **L1-Bzt1(Boc).**
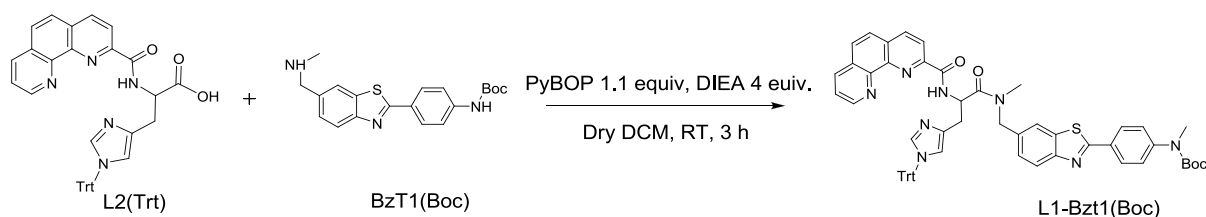
Scheme 4.4. First synthetic strategy to obtain compound **L1-Bzt1(Boc)**.

In a second synthetic strategy (**Scheme 4.5**) PyBOP was replaced by 1-ethyl-3-(3-dimethylaminopropyl)-carbodiimide (EDC) and N-hydroxy-succinimide (NHS), These reagents have been widely used to activate carboxylic groups in diverse applications such as forming amide bonds in peptide synthesis, labeling nucleic acids or attaching drugs to carrier proteins.[49] Thus, 1.0 and 1.4 equiv. of **L2(Trt)** and EDC, respectively, were dissolved and stirred at RT in tetrahydrofuran (THF) for 30 mins. Afterwards, 2 equiv. of dimethyl aminopyridine (DMAP) and 1.3 equiv. of NHS were added to the solution and the mixture was stirred at RT for 2 additional hours. After an extractive work-up, the organic phase was collected and the THF was removed by rotary evaporation. The residue was employed in the next step without further purification, i.e. it was re-dissolved in DCM, and 1.5 equiv. of triethylamine (Et$_3$N) and 1 equiv. of **Bzt1(Boc)** was added to the solution.
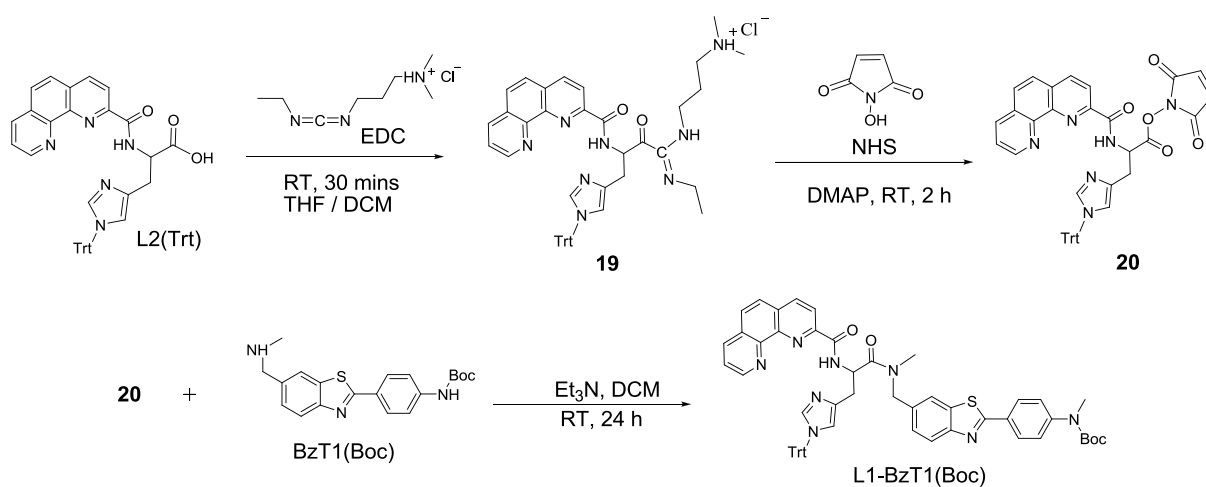
Scheme 4.5. Second synthetic strategy to obtain compound **11**.

The mixture was stirred at room temperature for 24 h and monitored by TLC (system 9:1, $CHCl_3$:MeOH). No significant changes after the 24 h were observed and therefore, the reaction was stopped. After the removal of DCM, a work-up was performed. The organic phase was concentrated and eluted through a chromatographic column (silica gel) using the system 9:2 MeOH:$CHCl_3$, only raw material and side products, that did not correspond to the expected product **L1-BzT1(Boc)**, were obtained. This was confirmed by MS analysis. Changing the order of additions, i.e., adding ET_3N at the end, after addition of **BzT1(Boc)** did not improve the results. Because of the lack of time, the optimal synthetic conditions for the coupling of BzT to **L1** could not be further explored.

4.2.6.2. Functionalization of L1 with a peptide recognizing the receptor for advanced glycation endproducts (RAGE).

One of the main challenges faced by AD drug candidates that renders them ineffective in the treatment of this disease is the lack of the required pharmacokinetic properties, particularly the ability to cross the BBB and access the central nervous system (CNS).[50,51] In this regard, the functionalization of these candidates with molecules that enhance their internalization has become an interesting alternative to overcome this problem.

4.2.6.2.1. Rational design of L1AB: Fighting fire with fire.

Carrier peptides have shown promising results facilitating the entrance of cargo to the CNS.[52,53] Recently, the group reported a peptidic approach to overcome the low permeability of a peptidomimetic β-secretase 1 (BACE-1) inhibitor across the BBB.[43] Using the same approach and rational, **L1** was functionalized with a segment of the Aβ peptide (Aβ$_{14\text{-}23}$, **Figure 4.14**), that contains the hexapeptide sequence known to recognize the receptor for advanced glycation endproducts (RAGE). This 35 kDa trans membrane receptor, characterized by Neeper in 1992,[54] is overexpressed in AD both in BBB and neurons,[55] enabling the entrance into the CNS through receptor mediated-transcytosis. Additionally, the

hexapeptide sequence represents a competitor inhibitor of the internalization of Aβ into cells expressing RAGE[56] and therefore, it could potentially avoid the re-internalization of Aβ peptide into the CNS.[57,58]
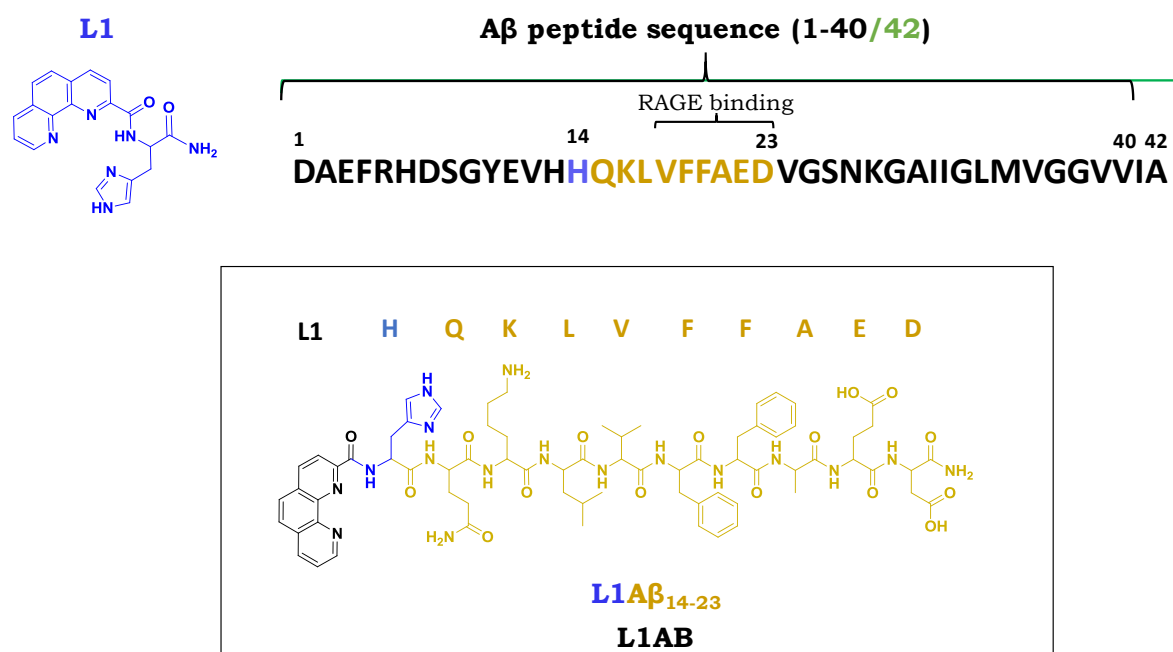
Figure 4.14. Rational design of **L1Aβ14-23** (**L1AB**), based on the combination of **L1** and the sequence Aβ14-23 containing the RAGE binding sequence.

In order to combine **L1** with the RAGE binding sequence and to avoid the modification of the canonical sequence of Aβ peptide, the original RAGE binding sequence, Aβ18-23, was extended to Aβ14-23. The later incorporates the His14 which is one of the two main structural units of **L1** (**Figure 4.14**).

4.2.6.2.2. Synthesis and characterization of L1AB.

The synthesis of the sequence Aβ14-23 was carried out on a Biotage® microwave assisted automatic synthesizer using SPPS standard Fmoc protocols[59] The Fmoc protected Rink Amide MBHA resin (100 - 200 mesh) was used to obtain an amide on the C terminal of the final peptide (**Scheme 4.6**). After amino acids were assembled on the resin and the last Fmoc protecting group was removed (**22**),

an aliquot was taken to simultaneously deprotect and cleave the peptide from the resin, the crude peptide was analyzed by analytical reversed-phase HPLC and MS-ESI to confirm the success of the synthesis and the identity of the expected peptide.
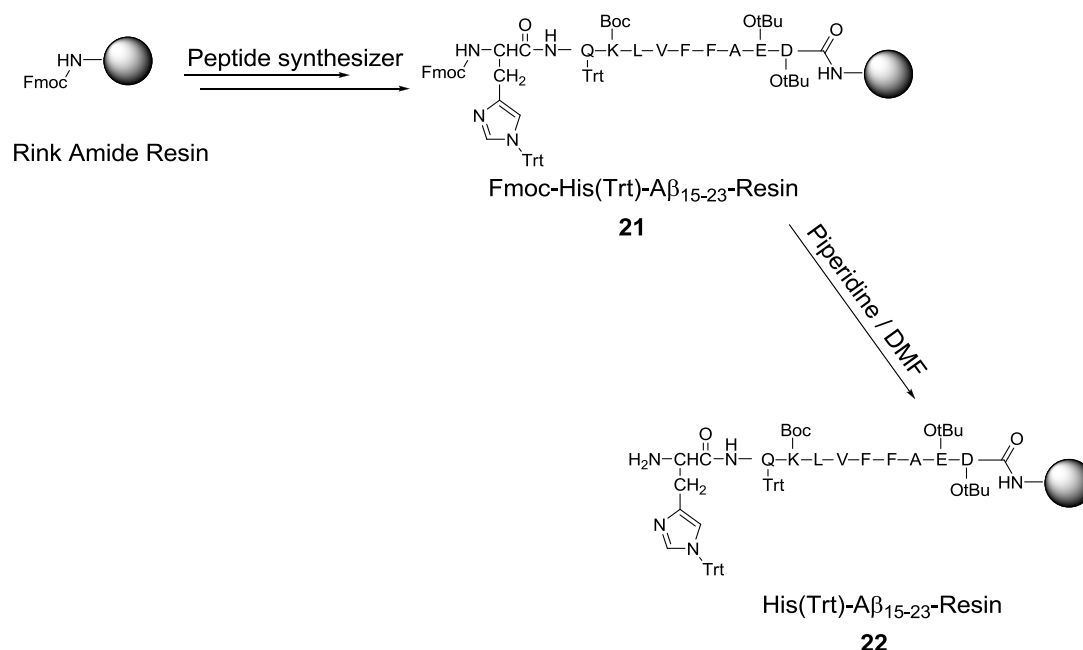
Scheme 4.6. Solid phase synthetic pathway to obtain Aβ$_{14\text{-}23}$ segment on a Rink Amide resin.

Subsequently, the 2-carboxy-1,10-phenanthroline (**14**) was manually coupled to (**22**), using PyBOP as a coupling reagent (**Scheme 4.7**). Afterwards the resin was treated with TFA:TIS:H$_2$O (95:2.5:2.5) solution in order to totally deprotect and cleave **L1AB** peptide from the resin. The resin was filtered out and the acidic solution, containing the product was concentrated under a N$_2$ steam, crude peptide was precipitated and washed with cold diethyl ether. The resulting residue was re-dissolved in water, lyophilized and purified by preparative reversed-phase HPLC.
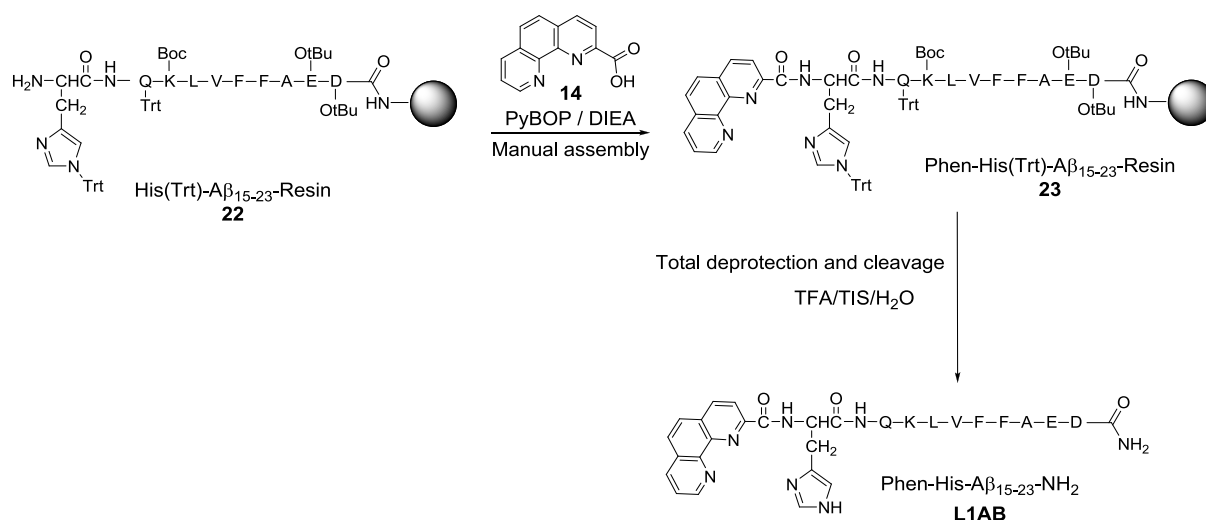
Scheme 4.7. Synthetic strategy to obtain **L1AB** through the coupling between (**17**) and the precursor (**4**).

The purity of **L1AB** was verified by analytical reversed phase HPLC and it was greater than 95 % (see Annex **Figure A.22**), ESI-MS confirmed the identity of the expected product (**Figure 4.15**), $[\textbf{L1AB}+2H]^{2+}$ m/z = 719.8485 Da, (theoretical value for $[\textbf{L1AB}+2H]^{2+}$ m/z = 719.8488 Da) corresponding to 1437.6830 Da. (theoretical for $C_{71}H_{91}N_{17}O_{16}$ = 1437.6830 Da).
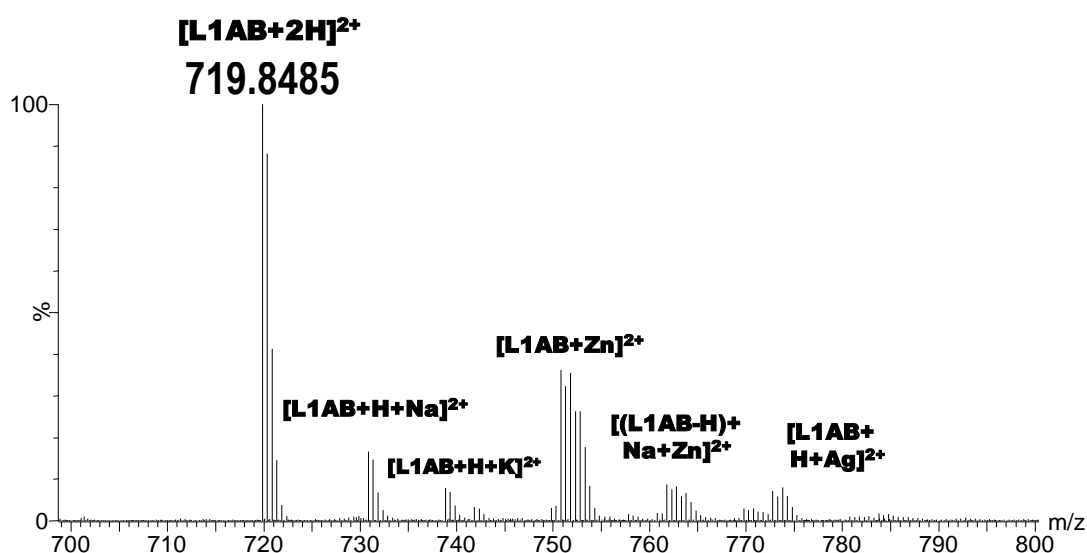

Figure 4.15. ESI-MS spectrum of the pure compound **L1AB** in positive mode (the contamination of the metal ions Na^+, K^+, Ag^+ and Zn^{2+} comes from the ionization source)

4.2.6.2.3. Spectroscopic characterization of the Cu(II) complex of L1AB.

In order to confirm if the Cu(II) coordinating properties of **L1** were maintained after the structural modification, we decided to characterize the correspondent complex **Cu(II)L1AB** by UV-Vis and EPR spectroscopies and compare the spectroscopic data with that of **Cu(II)L1**. **L1AB** possesses a limited water solubility and therefore, the stock solutions of **L1AB** used to generate the aqueous solutions of the following experiments were prepared at 1.5 mM and contain 20 % DMF in H_2O. These issues are associated most likely to the sequence $A\beta_{14\text{-}23}$ (HQKLVFFAED) which includes a highly hydrophobic domain (KLVFFA) responsible for the aggregation of the native Aβ peptide.[60]

The Cu(II) complex of **L1AB** was obtained by mixing 1 equiv. of **L1AB** (0.5 mM) with 1 equiv. of Cu(II) (Cu(NO$_3$)$_2$). UV-vis spectra of the complex were recorded at the initial pH (pH 3.0), pH 7.4 and pH 11.0 (**Figure 4.16**, A). An 0.15 mL aliquot of the solutions were taken at each pH in order to obtain the respective EPR spectra (**Figure 4.16**, B).
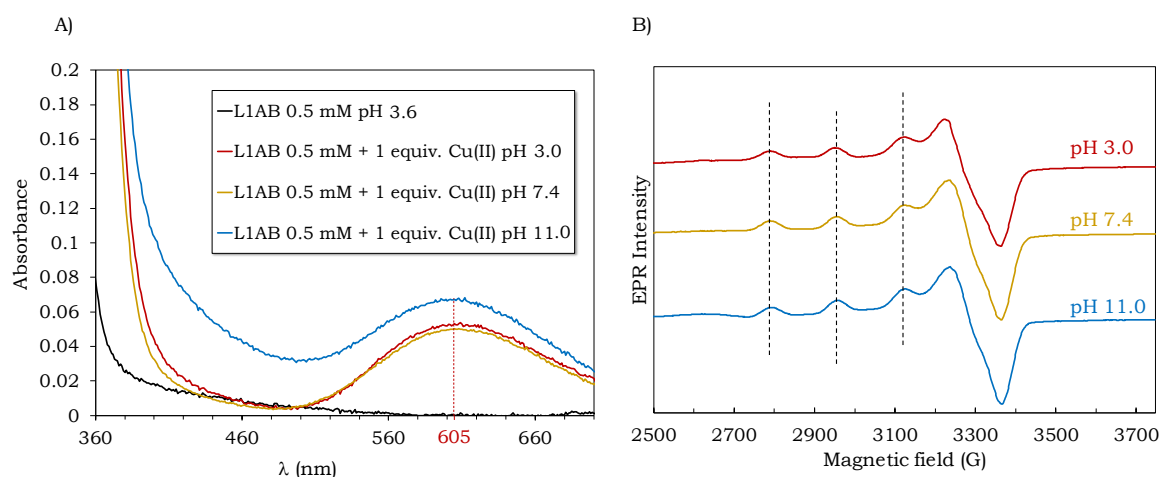

Figure 4.16. Spectroscopic data. A) UV-vis absorption spectra of **L1AB** (black curve) in H_2O (0.5 mM) and of **L1AB** + Cu(II) (1:1) at pH 3.0 (red), pH 7.4 (yellow) and pH 11.0 (blue). B) The X bands EPR spectra of **L1AB** and Cu(II) (1:1) at 0.5 mM, in 10 % glycerol at pH 3.0 (red), pH 7.4 (yellow) and pH 11.0 (blue).

The UV-vis spectra of the **Cu(II)L1AB** show an absorption band on the visible region corresponding to the Cu(II) d-d transitions. Very similar spectra were observed for pH 3.0, 7.4 and 11.0 (**Figure 4.16, A**). The spectrum obtained at pH 11.0 shows a baseline increase that can be attributed to precipitation issues (solution became cloudy). The absorption band at 607 nm does not show significant variations between the different pH values, providing evidence that the same major species is present in solution. Based on the previous data obtained for the parent complex **Cu(II)L1**,[1] the UV-vis spectra suggest an equatorial coordination environment where the nitrogen atoms of the Phen unit, the deprotonated amide and the imidazole of the His are coordinated to Cu(II).

For the sake of comparison, **L1** and **L1AB** were mixed with equimolar amounts of Cu(II) at two different concentrations (50 µM and 0.5 mM). For this case, both ligand stock solutions were prepared at 1.5 mM in 20 % DMF/H_2O to maintain the same amount of DMF for both systems. The pH was adjusted to pH 7.4 and UV-vis spectra were recorded (**Figure 4.17**, A and B). Spectra of **Cu(II)L1** and **Cu(II)L1AB** show no significant differences between them, in both, at the ligand (A) and at the d-d transition (B) regions.
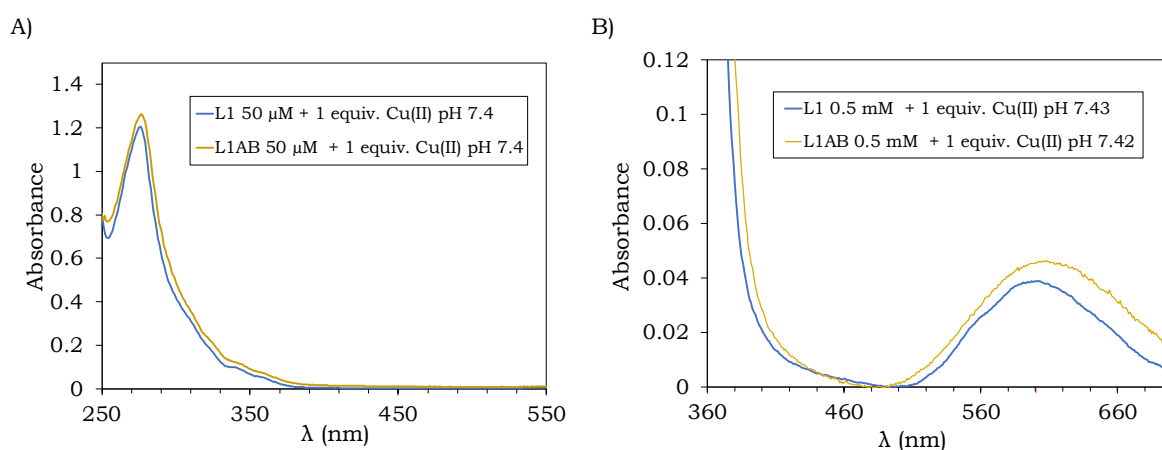

Figure 4.17. Overlapped UV-vis absorption spectra of **L1** (blue) and **L1AB** (yellow) with 1 equiv. of Cu(NO$_3$)$_2$ at pH 7.4. A) 50 µM. B) 0.5 mM.

The EPR spectra in **Figure 4.16** (B), exhibit the four expected lines at low field due to the hyperfine interaction between the unpaired electron of the complex and the copper nucleus. The EPR parameters obtained by simulation of the EPR data at pH 7.4 are shown in **Table 4.4**. These data are consistent with the UV-vis results and with the values reported for the parent **Cu(II)L1** complex at pH 7.4, i.e. the existence of a major Cu(II) species with a square planar or square pyramidal geometry and an N 4 coordination sphere. No significant changes were observed among the different pH values indicating that this species is the main species in this pH range.

Table 4.4. Comparison of the spectroscopic data for the **Cu(II)L1** and **Cu(II)L1AB** at 0.5 mM in aqueous solution, at pH 7.4.

	Cu(II)L1	Cu(II)L1AB
UV-vis		
λ_{max} (nm)	603	607
EPR		
$A_{//}$ (10^{-4} cm^{-1})	175.4*	171.0
$g_{//}$	2.219*	2.219
$g_{\perp}$	2.07, 2.04*	2.05

*Data from reference 1: EPR recorded in water/DMSO (9:1, v:v) solution at 90 K, where $A_{//}$ is reported as A_1, $g_{//}$ as g_1, and $g_{\perp}$ as g_2, g_3.

UV-Vis and EPR spectroscopic data indicate that the ligand **L1AB** preserves the coordination properties of the parent ligand **L1** and the proposed structure for the **Cu(II)L1AB** complex is shown in **Figure 4.18**.
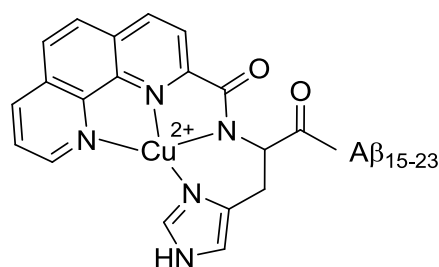
Figure 4.18. Proposed structure for **Cu(II)L1AB** complex at pH 7.4.

4.2.7. Evaluating the L1AB capabilities to arrest ROS formation

After comparing spectroscopic data, we concluded that basically the peptide scaffold does not interfere with the Cu(II) coordination properties of **L1AB**, therefore, the capability of arresting ROS production and the Cu selectivity might not be modified either. The ability of **L1AB** to stop the consumption of AscH⁻ acid was studied as described in Section 4.2.1.

As described in previous sections, the following experiments were performed in 100 mM HEPES at pH 7.1. The solutions were prepared using the corresponding concentrations of AscH⁻ [100 μM], CuCl₂ [10 μM], Aβ16 [12 μM], ZnCl₂ [10 μM] and **L1AB** [12 μM]. The black curves correspond to the respective positive controls for each condition:

(i)   Starting from the mixture Cu(II)/Cu(I).

The blue curve on the **Figure 4.19** represents the kinetic profile of AscH⁻ consumption in presence of **L1AB** (order of additions: AscH⁻ + Cu(II) + **L1AB**). **L1AB** can arrest the consumption of AscH⁻ by chelating Cu(II) and Cu(I). The red curve reflects the kinetic consumption of AscH⁻ in presence of Aβ16 (order of additions: AscH⁻ + Aβ16 + Cu(II)+ **L1AB**). This order of additions allows to pre-form the Cu(II)Aβ16 and Cu(I)Aβ16 complexes that produce ROS as reflected by the consumption of AscH⁻. When **L1AB** is added, the consumption of AscH⁻ is arrested indicating the ability of **L1AB** to remove the Cu(II) and Cu(I) from the Aβ16. The green curve represents the kinetic of AscH⁻ consumption in presence of Aβ16 and Zn(II) (order of additions: AscH⁻ + Aβ16 + Zn + Cu(II) + **L1AB**). The

addition of **L1AB** arrests the formation of ROS meaning that **L1AB** is still capable to remove the Cu(II) and Cu(I) ions from Aβ16 despite the presence of Zn(II).

Figure 4.19. Kinetics of AscH− consumption monitored by UV-vis spectroscopy at 265 nm in 100 mM of HEPES buffer pH 7.1: Blue curve: AscH− + Cu(II) + **L1AB**. Red curve: AscH− + Aβ16 + Cu(II)+ **L1AB**. Green curve: AscH− + Aβ16 + Zn + Cu(II) + **L1AB**. Black curve (positive control) AscH− + Aβ16 + Zn(II) + Cu(II).

(ii)   Starting from Cu(II).

This set of experiments (**Figure 4.20**) analyze the capability to chelate exclusively Cu(II) by performing the addition of **L1AB** when the Cu species in solution correspond to Cu(II), i.e. the complex Cu(II)Aβ16 or free Cu(II). The blue curve in **Figure 4.20** (order of additions: Cu(II) + **L1AB** + AscH−) reveals that **L1AB** can bind to Cu(II) arresting the consumption of AscH−. The red curve represents the kinetics of AscH− consumption when **L1AB** is added after the formation of the complex Cu(II)Aβ16 (order of additions Aβ16 + Cu(II) + **L1AB** + AscH−). Data indicate that **L1AB** can remove Cu(II) from the Cu(II)Aβ16 complex and arrest the ROS production. The green curve represents the kinetic consumption of AscH− in presence of Zn(II) and Aβ16 (order of additions: Aβ16 +

Zn(II) + Cu(II) + **L1AB** + AscH−). The results reveal that Zn(II) does not affect the ability of **L1AB** to remove Cu(II) from Aβ16.

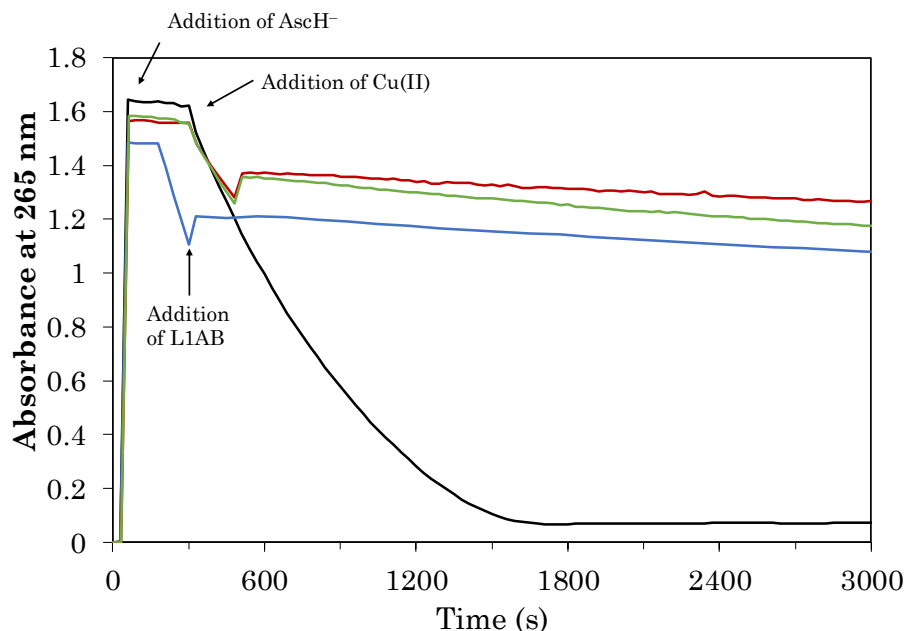**Figure 4.20**. Kinetics of AscH− consumption followed by UV-vis spectroscopy at 265 nm in 100 mM HEPES buffer pH 7.1: Blue curve: Cu(II) + **L1AB** + AscH−. Red curve: Aβ16 + Cu(II) + **L1AB** + AscH−. Green curve Aβ16 + Zn(II) + Cu(II) + **L1AB** + AscH− (green). Positive control, black curve: Aβ16 + Zn(II) + Cu(II) + AscH−.

(iii)   Starting from Cu(I).

The following set of experiments correspond to the study of the Cu(I) chelation capabilities of **L1AB** (**Figure 4.20**). The additions were made under anaerobic conditions and the introduction of air to the system is indicated for each case.
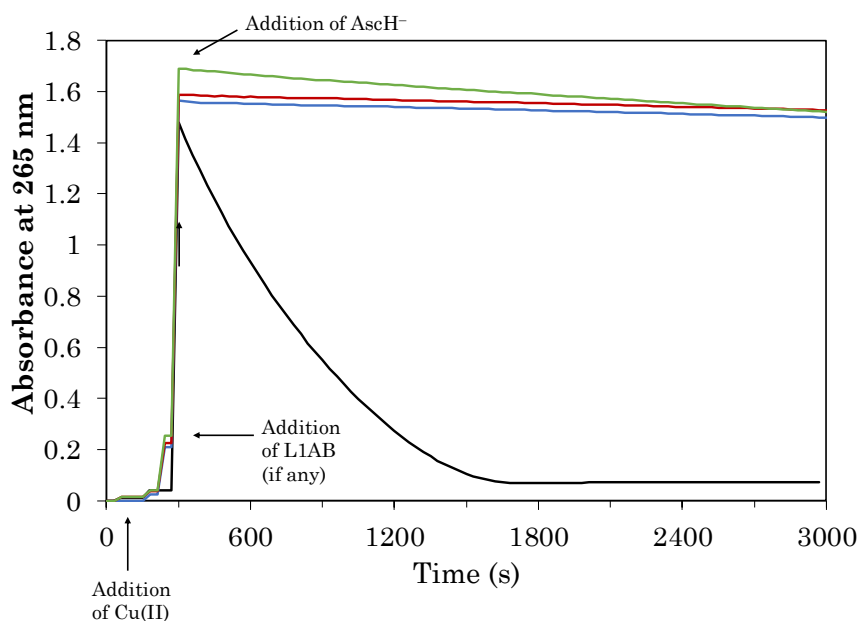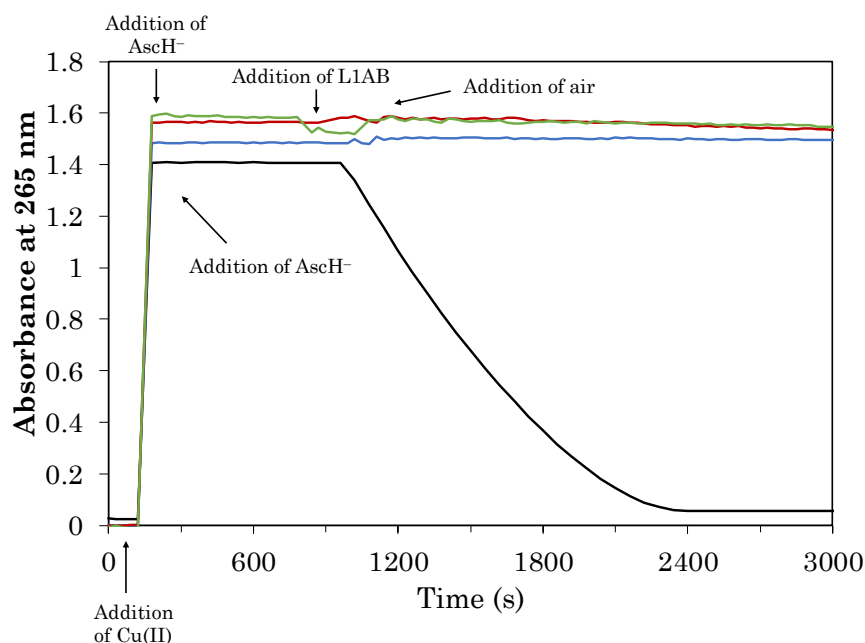
Figure 4.21. Kinetics of AscH⁻ acid consumption followed by UV-vis spectroscopy at 265 nm in 100 mM of HEPES buffer at pH 7.1: Blue curve: Cu(II) + AscH⁻ + **L1AB** + air. Red curve: Cu(II) + AscH⁻ + Aβ16 + **L1AB** + air. Green curve: Cu(II) + AscH⁻ + Aβ16 + Zn(II) + **L1AB** + air. Positive control, black curve: Cu(II) + AscH⁻+ Aβ16 + Zn(II) + air.

The blue curve on **Figure 4.21** represents the kinetic consumption of AscH⁻ when **L1AB** is added to Cu(I) and afterwards air is introduced to the system (order of additions: Cu(II) + AscH⁻ + **L1AB** + air). The data indicate that **L1AB** chelates Cu(I) in solution and generates a **Cu(I)L1AB** species unable to produce ROS. The red curve represents the kinetic profile of AscH⁻ consumption when **L1AB** is added to the complex Cu(I)Aβ16 before the introduction of air (order of additions: Cu(II) + AscH⁻ + Aβ16 + **L1AB** + air). The AscH⁻ consumption is also arrested under these conditions, meaning that **L1AB** can remove Cu(I) from Aβ16.

The green curve represents the kinetic of AscH⁻ consumption in the presence of Zn(II) (order of additions: Cu(II) + AscH⁻ + Zn(II) + Aβ16 + **L1AB** + air). The AscH⁻ consumption is still arrested in presence of Zn(II) meaning that the affinity of Cu(I) to **L1AB** is, most likely, greater than the one of Zn(II).

In summary, the kinetics of AscH⁻ consumption starting from Cu(II), Cu(I) or their mixture reveal that **L1AB** can arrest the production of ROS in the

presence of Aβ16 even in presence of Zn(II) as a competitor. These data indicate that the modification of the parent ligand **L1** by the introduction of the peptide Aβ$_{15-23}$ did not alter its copper coordination properties and that most likely, **L1AB** has similar Cu(II) and Cu(I) affinity constants than **L1** (**Table 4.2** and **Table 4.3**).

4.3. Conclusions and remarks.

The potential of two Phen based ligands as Cu targeting candidates for AD therapy has been studied. The capacities of the ligands **L1** and **L2** to arrest ROS production were initially studied monitoring AscH$^-$ consumption. Data indicated that **L1** performed better than **L2** and its Cu(II) and Cu(I) coordination properties were furthered analyzed under the ROS production experimental conditions. **L1** chelates Cu(II) to give rise to a complex (**Cu(II)L1**) that is hard to reduce by AscH$^-$ and presents high Cu-selectivity *vs.* Zn as reflected by the significant difference between their apparent affinity constants (log $K_{Zn(II)\text{-}L1,app}$ = 6.08 and log $K_{Cu(II)\text{-}L1,app}$ = 12.55). Additionally, this ligand binds Cu(II) with a higher apparent affinity constant than the Aβ16 peptide (log $K_{Cu(II)\text{-}A\beta16,app}$ = 7.46) and therefore, it is be able to remove the Cu(II) from the harmful Cu(II)Aβ complex even in the presence of Zn(II). **L1** binds also Cu(I) forming the **Cu(I)L1** (major) and **Cu(I)(L1)$_2$** (minor) species. In excess of **L1**, the concentration of the species **Cu(I)(L1)$_2$** increases (**Figure 4.7**, **Table A.2**).

L1 is capable of arresting ROS production at 1.2:1 **L1**:Cu ratio independently of the oxidation state of Cu and in presence of Aβ16 peptide and Zn(II). However, this property vanishes when **L1** is present in excess due to the higher formation of the species **Cu(I)(L1)$_2$** that is redox-active and catalyzes the formation of ROS. This species, which is the only species that can mediate the reduction of **Cu(II)L1** in our conditions, gives access to an alternative mechanism (**Scheme 4.2**) that generates ROS. These results highlight the complexity of the multifactorial ROS production process and the importance of carrying out the experiments under conditions closer to the biological relevant ones. Our studies reveal that the speciation of Cu in its different oxidation states with the designed chelator is an important factor. This is rarely investigated but it could be an

important issue if the change in speciation upon redox cycling can generate Cu(I) species that catalyze the formation of ROS. In this case scenario, even if the ligand is able to bind Cu(II) and arrest the production of ROS, the possibility to access to alternative ROS formation pathways when the chelator is present in excess can indeed preclude the potential of the chelator in the context of AD. This highlights the need to develop ligands capable of binding and stabilizing Cu in its two oxidation states (entatic state) without changing complex stoichiometry.[61]

In the second part of this chapter, two strategies to functionalize **L1** were explored to obtain a multitarget system. The functionalization with **Bzt1**, a molecule capable of recognizing Aβ fibrils, was not successful. The synthetic strategies tested where PyBOP and EDC were used as coupling activators did not render the expected final. On the other hand, it was possible to functionalize **L1** with the RAGE binding sequence of the native Aβ peptide (VFFAED) and to obtain **L1AB**. This new ligand merges the Cu coordination properties of **L1** with the BBB permeable capabilities of the peptide scaffold. UV-Vis and EPR spectroscopic data indicate that indeed the modification of **L1** did not affect the Cu(II) coordination properties of **L1**. Accordantly, **L1AB** can arrest the consumption of AscH⁻ and thus ROS production even in presence of Zn(II) and independently of the oxidation state of Cu. Currently, data regarding the Cu(I) and Zn(II) affinity constants of **L1AB** and its capability to arrest ROS production when **L1AB** is present in excess are missing. These experiments will be important to fully understand the **L1AB** behavior and check if the potential ROS active species **Cu(I)(L1AB)₂** could exist. In the case scenario that data indicate that **L1AB** is effective independently of the **L1AB**:Cu ratio used, modifications on the ligand structure will be done to improve its solubility. In the long term, the BBB capabilities of the best final candidate will be tested.

4.4. Bibliography.

(1)   Leite, S. M. G.; Lima, L. M. P.; Gama, S.; Mendes, F.; Orio, M.; Bento, I.; Paulo, A.; Delgado, R.; Iranzo, O. Copper(II) Complexes of Phenanthroline and Histidine Containing Ligands: Synthesis, Characterization and Evaluation of Their DNA Cleavage and Cytotoxic Activity. *Inorg. Chem.* **2016**, *55* (22), 11801–11814. https://doi.org/10.1021/acs.inorgchem.6b01884.

(2)   Brandt, W. W.; Dwyer, F. P.; Gyarfas, E. D. Chelate Complexes of 1, 10-Phenanthroline and Related Compounds. *Chem. Rev.* **1954**, *54* (6), 959–1017.

(3)   Sigel, H.; Martin, R. B. Coordinating Properties of the Amide Bond. Stability and Structure of Metal Ion Complexes of Peptides and Related Ligands. *Chem. Rev.* **1982**, *82* (4), 385–426.

(4)   Gaggelli, E.; Kozlowski, H.; Valensin, D.; Valensin, G. Copper Homeostasis and Neurodegenerative Disorders (Alzheimer's, Prion, and Parkinson's Diseases and Amyotrophic Lateral Sclerosis). *Chem. Rev.* **2006**, *106* (6), 1995–2044.

(5)   La Mendola, D.; Magrì, A.; Santoro, A. M.; Nicoletti, V. G.; Rizzarelli, E. Copper(II) Interaction with Peptide Fragments of Histidine-Proline-Rich Glycoprotein: Speciation, Stability and Binding Details. *J. Inorg. Biochem.* **2012**, *111*, 59–69. https://doi.org/10.1016/j.jinorgbio.2012.02.027.

(6)   Pappalardo, G.; Impellizzeri, G.; Bonomo, R. P.; Campagna, T.; Grasso, G.; Saita, M. G. Copper(II) and Nickel(II) Binding Modes in a Histidine-Containing Model Dodecapeptide. *New J. Chem.* **2002**, *26* (5), 593–600. https://doi.org/10.1039/B110655D.

(7)   Sarkar, B.; Wigfield, Y. The Structure of Copper (II)-Histidine Chelate THE QUESTION OF THE INVOLVEMENT OF THE IMIDAZOLE GROUP. *J. Biol. Chem.* **1967**, *242* (23), 5572–5577.

(8)   Rorabacher, D. B. Electron Transfer by Copper Centers. *Chem. Rev.* **2004**, *104* (2), 651–698.

(9)   Andersen, J. K. Oxidative Stress in Neurodegeneration: Cause or Consequence? *Nat. Med.* **2004**, *10* (7), S18–S25.

(10)   Bondy, S. C.; Guo-Ross, S. X.; Truong, A. T. Promotion of Transition Metal-Induced Reactive Oxygen Species Formation by β-Amyloid. *Brain Res.* **1998**, *799* (1), 91–96.

(11)   Cheignon, C.; Tomas, M.; Bonnefont-Rousselot, D.; Faller, P.; Hureau, C.; Collin, F. Oxidative Stress and the Amyloid Beta Peptide in Alzheimer's Disease. *Redox Biol.* **2018**, *14*, 450–464.

(12)   Chassaing, S.; Collin, F.; Dorlet, P.; Gout, J.; Hureau, C.; Faller, P. Copper and Heme-Mediated Abeta Toxicity: Redox Chemistry, Abeta Oxidations and Anti-ROS Compounds. *Curr. Top. Med. Chem.* **2012**, *12* (22), 2573–2595.

(13)   Alies, B.; Sasaki, I.; Proux, O.; Sayen, S.; Guillon, E.; Faller, P.; Hureau, C. Zn Impacts Cu Coordination to Amyloid-β, the Alzheimer's Peptide, but Not the ROS Production and the Associated Cell Toxicity. *Chem. Commun.* **2013**, *49* (12), 1214–1216.

(14)   Conte-Daban, A.; Boff, B.; Candido Matias, A.; Aparicio, C. N. M.; Gateau, C.; Lebrun, C.; Cerchiaro, G.; Kieffer, I.; Sayen, S.; Guillon, E.; Delangle, P.; Hureau, C. A Trishistidine Pseudopeptide with Ability to Remove Both CuI and CuII from the Amyloid-β Peptide and to Stop the Associated ROS

Formation. *Chem. – Eur. J.* **2017**, *23* (67), 17078–17088. https://doi.org/10.1002/chem.201703429.

(15) Cheignon, C.; Jones, M.; Atrián-Blasco, E.; Kieffer, I.; Faller, P.; Collin, F.; Hureau, C. Identification of Key Structural Features of the Elusive Cu–Aβ Complex That Generates ROS in Alzheimer's Disease. *Chem. Sci.* **2017**, *8* (7), 5107–5118.

(16) Minicozzi, V.; Stellato, F.; Comai, M.; Dalla Serra, M.; Potrich, C. ; Meyer-Klaucke, W.; Morante, S. Identifying the Minimal Copper-and Zinc-Binding Site Sequence in Amyloid-β Peptides. *J. Biol. Chem.* **2008**, *283* (16), 10784–10792.

(17) Drew, S. C.; Barnham, K. J. The Heterogeneous Nature of Cu2+ Interactions with Alzheimer's Amyloid-β Peptide. *Acc. Chem. Res.* **2011**, *44* (11), 1146–1155. https://doi.org/10.1021/ar200014u.

(18) Hureau, C. Coordination of Redox Active Metal Ions to the Amyloid Precursor Protein and to Amyloid-β Peptides Involved in Alzheimer Disease. Part 1: An Overview. *Coord. Chem. Rev.* **2012**, *256* (19), 2164–2174. https://doi.org/10.1016/j.ccr.2012.03.037.

(19) Hureau, C.; Dorlet, P. Coordination of Redox Active Metal Ions to the Amyloid Precursor Protein and to Amyloid-β Peptides Involved in Alzheimer Disease. Part 2: Dependence of Cu (II) Binding Sites with Aβ Sequences. *Coord. Chem. Rev.* **2012**, *256* (19–20), 2175–2187.

(20) Atrián-Blasco, E.; Gonzalez, P.; Santoro, A.; Alies, B.; Faller, P.; Hureau, C. Cu and Zn Coordination to Amyloid Peptides: From Fascinating Chemistry to Debated Pathological Relevance. *Coord. Chem. Rev.* **2018**, *371*, 38–55. https://doi.org/10.1016/j.ccr.2018.04.007.

(21) Conte-Daban, A.; Borghesani, V.; Sayen, S.; Guillon, E.; Journaux, Y.; Gontard, G.; Lisnard, L.; Hureau, C. Link between Affinity and Cu (II) Binding Sites to Amyloid-β Peptides Evaluated by a New Water-Soluble UV–Visible Ratiometric Dye with a Moderate Cu (II) Affinity. *Anal. Chem.* **2017**, *89* (3), 2155–2162.

(22) James, S. A.; Volitakis, I.; Adlard, P. A.; Duce, J. A.; Masters, C. L.; Cherny, R. A.; Bush, A. I. Elevated Labile Cu Is Associated with Oxidative Pathology in Alzheimer Disease. *Free Radic. Biol. Med.* **2012**, *52* (2), 298–302.

(23) Zatta, P.; Drago, D.; Bolognin, S.; Sensi, S. L. Alzheimer's Disease, Metal Ions and Metal Homeostatic Therapy. *Trends Pharmacol. Sci.* **2009**, *30* (7), 346–355.

(24) Lovell, M. A.; Robertson, J. D.; Teesdale, W. J.; Campbell, J. L.; Markesbery, W. R. Copper, Iron and Zinc in Alzheimer's Disease Senile Plaques. *J. Neurol. Sci.* **1998**, *158* (1), 47–52. https://doi.org/10.1016/s0022-510x(98)00092-6.

(25) Frederickson, C. J. Neurobiology of Zinc and Zinc-Containing Neurons. In *International Review of Neurobiology*; Smythies, J. R., Bradley, R. J., Eds.; Academic Press, 1989; Vol. 31, pp 145–238. https://doi.org/10.1016/S0074-7742(08)60279-2.

(26) Hartter, D.; Barnea, A. Brain Tissue Accumulates 67copper by Two Ligand-Dependent Saturable Processes. A High Affinity, Low Capacity and a Low Affinity, High Capacity Process. *J. Biol. Chem.* **1988**, *263* (2), 799–805.

(27) Kardos, J.; Héja, L.; Simon, Á.; Jablonkai, I.; Kovács, R.; Jemnitz, K. Copper Signalling: Causes and Consequences. *Cell Commun. Signal.* **2018**, *16* (1), 1–22. https://doi.org/10.1186/s12964-018-0277-3.

(28) Atwood, J. L.; Lehn, J.-M. *Comprehensive Supramolecular Chemistry*; Pergamon: New York, 1996.

(29) Connors, K. A. *Binding Constants: The Measurement of Molecular Complex Stability*; Wiley, 1987.

(30) Thordarson, P. Determining Association Constants from Titration Experiments in Supramolecular Chemistry. *Chem Soc Rev* **2011**, *40* (3), 1305–1323. https://doi.org/10.1039/C0CS00062K.

(31) Gans, P.; Sabatini, A.; Vacca, A. Investigation of Equilibria in Solution. Determination of Equilibrium Constants with the HYPERQUAD Suite of Programs. *Talanta-Oxf.* **1996**, *43* (10), 1739–1754.

(32) Noël, S.; Bustos Rodriguez, S.; Sayen, S.; Guillon, E.; Faller, P.; Hureau, C. Use of a New Water-Soluble Zn Sensor to Determine Zn Affinity for the Amyloid-β Peptide and Relevant Mutants. *Metallomics* **2014**, *6* (7), 1220. https://doi.org/10.1039/c4mt00016a.

(33) Albelda, M. T.; Bernardo, M. A.; Garcia-España, E.; Godino-Salido, M. L.; Luis, S. V.; Melo, M. J.; Pina, F.; Soriano, C. Thermodynamics and Fluorescence Emission Studies on Potential Molecular Chemosensors for ATP Recognition in Aqueous Solution. *J. Chem. Soc. Perkin Trans. 2* **1999**, No. 11, 2545–2549.

(34) Sokołowska, M.; Bal, W. Cu(II) Complexation by "Non-Coordinating" N-2-Hydroxyethylpiperazine-N′-2-Ethanesulfonic Acid (HEPES Buffer)☆. *J. Inorg. Biochem.* **2005**, *99* (8), 1653–1660. https://doi.org/10.1016/j.jinorgbio.2005.05.007.

(35) James, B. R.; Williams, R. J. P. The Oxidation–Reduction Potentials of Some Copper Complexes. *J Chem Soc* **1961**, *0* (0), 2007–2019. https://doi.org/10.1039/JR9610002007.

(36) Alderighi, L.; Gans, P.; Ienco, A.; Peters, D.; Sabatini, A.; Vacca, A. Hyperquad Simulation and Speciation (HySS): A Utility Program for the Investigation of Equilibria Involving Soluble and Partially Soluble Species. *Coord. Chem. Rev.* **1999**, *184* (1), 311–318.

(37) Alies, B.; Badei, B.; Faller, P.; Hureau, C. Reevaluation of Copper(I) Affinity for Amyloid-β Peptides by Competition with Ferrozine-An Unusual Copper(I) Indicator. *Chem. - Eur. J.* **2012**, *18* (4), 1161–1167. https://doi.org/10.1002/chem.201102746.

(38) Voronova, A.; Meyer-Klaucke, W.; Meyer, T.; Rompel, A.; Krebs, B.; Kazantseva, J.; Sillard, R.; Palumaa, P. Oxidative Switches in Functioning of Mammalian Copper Chaperone Cox17. *Biochem. J.* **2007**, *408* (1), 139–148.

(39) Rice, M. E. Ascorbate Regulation and Its Neuroprotective Role in the Brain. *Trends Neurosci.* **2000**, *23* (5), 209–216. https://doi.org/10.1016/S0166-2236(99)01543-X.

(40) Sigman, D.; Graham, D.; D'aurora, V.; Stern, A. Oxygen-Dependent Cleavage of DNA by the 1, 10-Phenanthroline. Cuprous Complex. Inhibition of Escherichia Coli DNA Polymerase I. *J. Biol. Chem.* **1979**, *254* (24), 12269–12272.

(41)   Santoro, A.; Calvo, J. S.; Peris-Díaz, M. D.; Krężel, A.; Meloni, G.; Faller, P. The Glutathione/Metallothionein System Challenges the Design of Efficient O2-activating Cu-complexes. *Angew. Chem.* **2020**, ange.201916316. https://doi.org/10.1002/ange.201916316.

(42)   Biancalana, M.; Koide, S. Molecular Mechanism of Thioflavin-T Binding to Amyloid Fibrils. *Biochim. Biophys. Acta BBA-Proteins Proteomics* **2010**, *1804* (7), 1405–1412.

(43)   Vila-Real, H.; Coelho, H.; Rocha, J.; Fernandes, A.; Ventura, M. R.; Maycock, C. D.; Iranzo, O.; Simplício, A. L. Peptidomimetic ß-Secretase Inhibitors Comprising a Sequence of Amyloid-ß Peptide for Alzheimer's Disease. *J. Med. Chem.* **2015**, *58* (14), 5408–5418. https://doi.org/10.1021/acs.jmedchem.5b00658.

(44)   Leuma Yona, R.; Mazères, S.; Faller, P.; Gras, E. Thioflavin Derivatives as Markers for Amyloid-ß Fibrils: Insights into Structural Features Important for High-Affinity Binding. *ChemMedChem* **2008**, *3* (1), 63–66. https://doi.org/10.1002/cmdc.200700188.

(45)   Kung, H. F.; Choi, S. R.; Qu, W.; Zhang, W.; Skovronsky, D. 18F Stilbenes and Styrylpyridines for PET Imaging of Aß Plaques in Alzheimer's Disease: A Miniperspective. *J. Med. Chem.* **2010**, *53* (3), 933–941.

(46)   Ono, M. Development of Positron-Emission Tomography/Single-Photon Emission Computed Tomography Imaging Probes for in Vivo Detection of ß-Amyloid Plaques in Alzheimer's Brains. *Chem. Pharm. Bull. (Tokyo)* **2009**, *57* (10), 1029–1039.

(47)   Mathis, C.; Wang, Y.; Klunk, W. Imaging ß-Amyloid Plaques and Neurofibrillary Tangles in the Aging Human Brain. *Curr. Pharm. Des.* **2004**, *10* (13), 1469–1492.

(48)   Cui, M.; Ono, M.; Kimura, H.; Ueda, M.; Nakamoto, Y.; Togashi, K.; Okamoto, Y.; Ihara, M.; Takahashi, R.; Liu, B. Novel 18F-Labeled Benzoxazole Derivatives as Potential Positron Emission Tomography Probes for Imaging of Cerebral ß-Amyloid Plaques in Alzheimer's Disease. *J. Med. Chem.* **2012**, *55* (21), 9136–9145.

(49)   Damink, L. O.; Dijkstra, P.; Van Luyn, M.; Van Wachem, P.; Nieuwenhuis, P.; Feijen, J. In Vitro Degradation of Dermal Sheep Collagen Cross-Linked Using a Water-Soluble Carbodiimide. *Biomaterials* **1996**, *17* (7), 679–684.

(50)   Tang, J.; Ghosh, A. K.; Hong, L.; Koelsch, G.; Turner, R. T.; Chang, W. Study of Memapsin 2 (ß-Secretase) and Strategy of Inhibitor Design. *J. Mol. Neurosci.* **2003**, *20* (3), 299–304.

(51)   Butini, S.; Brogi, S.; Novellino, E.; Campiani, G.; K Ghosh, A.; Brindisi, M.; Gemma, S. The Structural Evolution of ß-Secretase Inhibitors: A Focus on the Development of Small-Molecule Inhibitors. *Curr. Top. Med. Chem.* **2013**, *13* (15), 1787–1807.

(52)   Temsamani, J.; Vidal, P. The Use of Cell-Penetrating Peptides for Drug Delivery. *Drug Discov. Today* **2004**, *9* (23), 1012–1019.

(53)   Pardridge, W. M. Vector-Mediated Peptide Drug Delivery to the Brain. *Adv. Drug Deliv. Rev.* **1995**, *15* (1–3), 109–146.

(54)   Neeper, M.; Schmidt, A.; Brett, J.; Yan, S.; Wang, F.; Pan, Y.; Elliston, K.; Stern, D.; Shaw, A. Cloning and Expression of a Cell Surface Receptor for

Advanced Glycosylation End Products of Proteins. *J. Biol. Chem.* **1992**, *267* (21), 14998–15004.

(55) Han, S.-H.; Kim, Y. H.; Mook-Jung, I. RAGE: The Beneficial and Deleterious Effects by Diverse Mechanisms of Actions. *Mol. Cells* **2011**, *31* (2), 91–97.

(56) Gospodarska, E.; Kupniewska-Kozak, A.; Goch, G.; Dadlez, M. Binding Studies of Truncated Variants of the Aß Peptide to the V-Domain of the RAGE Receptor Reveal Aß Residues Responsible for Binding. *Biochim. Biophys. Acta BBA-Proteins Proteomics* **2011**, *1814* (5), 592–609.

(57) Zlokovic, B. Can Blood-Brain Barrier Play a Role in the Development of Cerebral Amyloidosis and Alzheimer's Disease Pathology. *Neurobiol. Dis.* **1997**, *1* (4), 23–26.

(58) Kim, S.-J.; Ahn, J.-W.; Kim, H.; Ha, H.-J.; Lee, S.-W.; Kim, H.-K.; Lee, S.; Hong, H.-S.; Kim, Y. H.; Choi, C. Y. Two ß-Strands of RAGE Participate in the Recognition and Transport of Amyloid-ß Peptide across the Blood Brain Barrier. *Biochem. Biophys. Res. Commun.* **2013**, *439* (2), 252–257.

(59) Chan, W.; White, P. *Fmoc Solid Phase Peptide Synthesis: A Practical Approach*; OUP Oxford, 1999; Vol. 222.

(60) Enache, T. A.; Chiorcea-Paquim, A.-M.; Oliveira-Brett, A. M. Amyloid–ß Peptides Time-Dependent Structural Modifications: AFM and Voltammetric Characterization. *Anal. Chim. Acta* **2016**, *926*, 36–47.

(61) Esmieu, C.; Guettas, D.; Conte-Daban, A.; Sabater, L.; Faller, P.; Hureau, C. Copper-Targeting Approaches in Alzheimer's Disease: How To Improve the Fallouts Obtained from in Vitro Studies. *Inorg. Chem.* **2019**, acs.inorgchem.9b00995. https://doi.org/10.1021/acs.inorgchem.9b00995.

CHAPTER 5.

General Conclusion

66
There are only two tragedies in life:
one is not getting what one wants,
and the other is getting it."

Oscar Wilde

T he therapeutic potential of the ligands (H)**L1** and (H$_2$)**L2** was explored in two different and contrasting contexts: Cancer and Alzheimer's disease (AD).

For the first approach, we explored into the biological activities of the two Cu(II) complexes of **L1** and **L2** (**C1** and **C2**) to understand their cytotoxicity (Section 2.1.4.1). Data suggested that the cytotoxicity exhibited particularly on A2780 cells might be related to their capabilities to produce ROS inside cells. However, their moderately low cytotoxicity (**C2** more cytotoxic that **C1**) in comparison with Cisplatin (see **Table 2.1**, Section 2.1) highlights the fact that these complexes may not produce ROS efficiently and the ligands need to be optimized to obtain Cu(II) complexes with reversible Cu(II)/Cu(I) redox cycling. In contrast, part of the work regarding AD explored the capability of these ligands to arrest the formation of ROS catalyzed by Cu. These results indicated that the effectiveness of **L1** to arrest the formation of ROS catalyzed by Cu was clearly higher than the one of **L2** (Section 4.2.1). These data are in agreement with the cytotoxic studies mentioned above that revealed that the complex C2 is more active. Further studies indicated that **L1** can arrest ROS production at 1.2:1 L1:Cu ratio independently of the oxidation state of Cu and in presence of Aβ16 peptide and Zn(II). Moreover, it was stablished that the excess of **L1** produces an impact on its effectiveness to arrest the ROS production (Section 4.2.5, Chapter 4), explained by the change in speciation that promotes the formation of the **Cu(I)(L1)$_2$** species, which, in presence of the specie **Cu(II)L1** leads to the formation of **Cu(II)(L1)$_2$** (reducible by AscH$^-$) and **Cu(I)L1** (oxidizable by O$_2$). This effect is lessened by the presence of Zn(II) and Aβ16 peptide by modifying speciation and decreasing the amount of available **L1** to form of the active species (Scheme 4.2, Chapter 4).

Based on all these results, the modification of the ligands took two different directions and purposes. In one way and in the context of cancer, the ligand **L1** (as a probe of concept) was modified with the purpose of generating a more efficient cytotoxic Cu(II) complex, i.e. provide reversibility to their Cu(II) $\rightleftarrows$ Cu(I) redox cycling process. The strategy pursued to optimize **L1** (ligand **L3**) was not successful as data indicated that **L3** is not stable in the presence of Cu(II). On the other hand, and in the context of AD, the purpose was to confer therapeutic added value to the ligand **L1** (the best candidate) without modifying their Cu(II) coordination properties and ROS arrest capabilities. We succeed in this goal but the effectiveness of **L1AB** to arrest ROS under super-stoichiometric ratio of ligand (2:1, L:Cu) was not studied and this indeed will be crucial experiments to be performed in near future.

CHAPTER 6.

Experimental section.

66 Life can only be understood backwards;
but it must be lived forwards.”

Søren Kierkegaard

6.1. Chemicals.

Acetonitrile (ACN), N,N-diisopropylethylamine (DIEA), triisopropylsilane (TIS), diethyl ether (Et_2O), dichloromethane (CH_2Cl_2, N-(3-Dimethylaminopropyl)-N′-ethylcarbodiimide hydrochloride (EDC), N-methyl-2-pyrrolidone (NMP), bathocuproinedisulfonic acid disodium salt, $Cu(NO_3)_2 \cdot 3H_2O$, $CuCl_2$, $Zn(NO_3)_2$, H_2O_2, 1,10-Phenanthroline (Phen), (4-(2-hydroxyethyl)-1-piperazineethanesulfonic acid (HEPES), tris(hydroxymethyl)aminomethane hydrochloride (TRIS-HCl), deoxyribonucleic acid sodium salt from *calf thymus* (*ct*-DNA) ascorbic acid (AscH⁻) and the deuterated solvents for NMR analysis were purchased from Sigma Aldrich - Merck Millipore. Fmoc-His(Trt)-OH, Fmoc-N-Me-His(Trt)-OH, 2-(1H-benzotriazole-1-yl)-1,1,3,3-tetramethyluronium hexafluorophosphate (HBTU), benzotriazole-1-yl-oxy-tris-pyrrolidino-phosphonium hexafluorophosphate (PyBOP), H-Gly-2-chlorotrityl and rink amide MBHA (100-200 mesh) resins were purchased from Novabiochem. Trifluoroacetic acid (TFA), N,N-dimethylformamide, acetic anhydride and piperidine were purchased from Acros Organics. Peptide Aβ16 (DAEFRHDSGYEVHHQK) was bought from Genecust. Suppliers of reagents and cells used for the biological studies (Section 6.7) are indicated in their corresponding sections.

6.2. General Information.

All manipulations of air- or moisture-sensitive compounds were carried out under an atmosphere of nitrogen (N_2) or inside the glovebox.

Preparative reversed-phase high performance liquid chromatography (HPLC) was done on an Agilent Technologies 1200 infinity with a UV-vis detector using the Phenomenex Jupiter Proteo column (250 mm x 21.20 mm, 4 µm, 90 Å) and solvents A (water:TFA, 99.9:0.1, v/v) and B (ACN:water:TFA, 90:9.9:0.1, v/v/v). Analytical reversed-phase HPLC was carried out on an Agilent Technologies 1200 series with a UV-vis detector using the Phenomenex Jupiter Proteo column (250 mm x 4.6 mm, 4 µm, 90 Å) and same solvents A and B.

Solution NMR measurements were done in a Bruker DPX-300 MHz, 400 MHz or 600 MHz NMR spectrometers using $CDCl_3$ or D_2O as a solvent. The ^{1}H and ^{13}C chemical shifts are referenced to the chloroform peak (7.26 ppm for ^{1}H and 77.00 ppm for ^{13}C). 2D NMR NOESY experiment performed on a Bruker DPX-600 MHz spectrometer by Dr. Gaëtan Herbette at Spectropole, the analytical facility of Aix-Marseille University (**Figure A.11**).

The UV-Vis spectroscopy experiments were carried out in different Varian Cary Bio spectrophotometers.

The ESI-Mass Spectrometry studies were performed with a QStar Elite (Applied Biosystems SCIEX) mass spectrometer equipped with a pneumatically assisted atmospheric pressure ionization (API) source. The sample was ionized in positive electrospray mode under the following conditions: electrospray voltage (ISV): 5500 V; orifice voltage (OR): 20 V; nebulization gas pressure (air): 20 psi. Mass spectra (MS) were obtained with a flight time analyzer (TOF). Values are given as m/z. These experiments were performed at Spectropole, the analytical facility of Aix-Marseille University.

6.3. Synthesis of ligands.

6.3.1. Synthesis of the 2-carboxy-1,10-phenanthroline.

The synthesis of 2-carboxy-1,10-phenanthroline was carried out as reported by Sun *et al.*[1] A) 1,10-phenanthroline 1-oxide: 30 mL of 30% H_2O_2 was added dropwise to a solution containing 50 g (0.25 mol) of 1,10-phenanthroline monohydrate in 60 mL of acetic acid (glacial). The mixture was maintained at 75 °C for 3 h Afterwards, 30 mL of H_2O_2 30 % were added dropwise and the heating continued for 3 h. After cooling down the mixture was bisified to pH 10.0 with a saturated solution of KOH and extracted 4 times with chloroform. The combined extractions were dried over anhydrous sodium sulphate and evaporated to obtain a yellow solid. B) 2-Cyano-1,10-phenanthroline: To a solution of 25 g (0.13 mol) of 1,10-phenanthroline 1-oxide and 25 g of potassium cyanide dissolved in 200 mL of water 25 mL of benzoyl chloride were added dropwise during 1 h and the mixture was stirred for 2 additional hours. The precipitated was collected by suction

filtration, washed with water and dried under vacuum. C) 2-carboxy-1,10-phenanthroline: A solution of 10 g of sodium hydroxide in 60 mL of water was added to a solution of 12 g (59 mmol) of 2-cyano-1,10-phenanthroline in 120 mL of 95 % ethanol. The mixture was refluxed for 2 h and after evaporating some ethanol, the solution was slightly acidified with concentrated HCl in an ice-water bath. The precipitate was filtrated, washed with acid water and dried under vacuum obtaining a brown solid (78% yield). %. ^{1}H NMR (400 MHz, D_2O, **Figure A.5**) δ: 8.95 (d, J = 6.0 Hz, 1H), 8.91 (d, J = 8.0 Hz, 1H), 8.14 (t, J = 6.0 Hz, 1H), 8.08 (d, J = 8.2 Hz, 1H), 7.85 (d, J = 8.0 Hz, 1H), 7.78 (d, J = 8.8 Hz, 1H), 7.68 (d, J = 8.6 Hz, 1H). ^{13}C NMR (100 MHz, D_2O, **Figure A.6**) δ: 167.08, 148.18, 146.48, 143.04, 138.34, 136.76, 135.94, 130.30, 129.57, 128.97, 126.90, 125.23, 125.14.

6.3.2. Synthesis of L1 (HL1).

This ligand was prepared manually on a rink amide MBHA resin (0.59 mmol/g, 2 g resin scale synthesis). After removing Fmoc from the resin using 20 % piperidine in dimethylformamide (DMF), the Fmoc-His(Trt)-OH was coupled in DMF using HBTU/HOBt (3.9/4 equiv.) as coupling agent and DIEA as base (8 equiv.). Afterwards, Fmoc deprotection was done by treating the resin with 20 % piperidine in DMF (2 x, 15 min). The 2-carboxy-1,10-phenanthroline unit was coupled in DMF using PyBOP (4 equiv.) as coupling agent and DIEA as base (8 equiv.). The removal of Fmoc and attachment of Fmoc-His(Trt)-OH and 2-carboxy-1,10-phenanthroline were always verified by the Kaiser-test.[2] The ligand was simultaneously deprotected and cleaved from the resin by treatment with the mixture TFA:Triisopropylsilane (TIS):Water (95:2.5:2.5, v/v/v, 20 mL/g of resin) for 2 h at room temperature and under N_2. The resin was filtered and rinsed with 10 mL of TFA. The filtrate and rinses were combined and concentrated with a steam of N_2 to a crude oil, from which a precipitate was obtained by addition of cold diethyl ether (20 mL). After filtration and washing with cold diethyl ether, the precipitate was re-dissolved in the minimum amount of ethanol and concentrated hydrochloric acid was added dropwise until a precipitate appeared. The white-beige solid was dried under vacuum. Average yield: 70%. ^{1}H NMR (400

MHz, D$_2$O, **Figure A.7**) δ: 9.10 (dd, J = 5.4, 1.5 Hz, 1H), 9.03 (dd, J = 8.3, 1.5 Hz, 1H), 8.59−8.44 (m, 2H), 8.26 - 8.16 (m, 2H), 7.98 (s, 2H), 7.30 (d, J = 1.4 Hz, 1H), 4.99 (dd, J = 8.4, 6.4 Hz, 1H), 3.54 - 3.32 (m, 2H). ^{13}C NMR (100 MHz, D$_2$O) δ: 174.01, 164.28, 147.88, 146.44, 143.36, 138.82, 136.36, 135.54, 133.61, 130.52, 129.50, 128.96, 128.46, 126.79, 125.35, 123.15, 117.34, 52.87, 26.81; HR ESI-MS data (**Figure A.8**): m/z 361.1406 [**L1** + H]$^+$ (calc. for [**L1** + H]$^+$ = 361.1408).

6.3.3. Synthesis of L2 (H$_2$L2).

This ligand was manually prepared previously in the group on a 2-chlorotrityl chloride resin (1.22 mmol /g, 2 g resin scale synthesis). The Fmoc-His(Trt)-OH residue was coupled to the 2-chlorotrityl chloride resin using only DIEA (2.5 equiv.) in DCM solution and afterwards the resin was blocked using the mixture DCM/MeOH/DIEA, (80:15:5, v/v/v) stirring for 10 min (3 x). Subsequently the resin was washed with DCM. The deprotection of the Fmoc group was done by treating the resin with 20 % piperidine in DMF (2 x, 15 min). The coupling of the 2-carboxy-1,10-phenanthroline and the total deprotection and cleavage from the resin were done following the same procedure as for **L1** (Section 6.3.2). A final white-beige solid was also obtained. Average yield: 60%. ^{1}H NMR (400 MHz, D$_2$O) δ: 9.22 - 9.13 (m, 2H), 8.62 - 8.55 (m, 1H), 8.50 (s, 1H), 8.33−8.20 (m, 2H), 8.17 (s, 2H), 7.23 (s, 1H), 4.96 (dd, J = 8.9, 5.2 Hz, 1H), 3.52 (dd, J = 15.5, 5.2 Hz, 1H), 3.34 (dd, J = 15.5, 8.9 Hz, 1H); ^{13}C NMR (100 MHz, D$_2$O) δ: 173.91, 164.66, 148.13, 146.79, 143.04, 139.01, 136.76, 136.04, 133.36, 130.94, 129.92, 129.24, 129.00, 126.86, 125.18, 123.17, 117.03, 52.61, 26.60; ESI-MS data: m/z 362.08 [L2 + H]$^+$ (calc. for [L2 + H]$^+$ = 362.13).

6.3.4. Synthesis of L2(Trt).

The synthesis of the ligand **L2(Trt)** was carried out manually using the same protocol than the one used for **L2** with the following changes. The ligand was cleaved from the resin by treating the resin with the mixture DCM/TFA, 99:1, v/v, 8 mL for 2 minutes at room temperature, the resin was filtered, and the solution

collected was immediately neutralized with 400 µL of DIEA. The presence of the compound was verified by thin-layer chromatography (TLC) using the system CHCl$_3$/MeOH (9:1, v/v). This cleavage procedure was repeated until no spot on the TLC was observed. Fractions containing the compound were combined and the solvent was removed in a rotary evaporator. The residue was dissolved in H$_2$O (10 mL) and extracted with CHCl$_3$ (3 x, 20 mL). The organic layers were combined and the CHCl$_3$ was removed under reduced pressure to obtain a white-solid. Average yield 55 %. ^{1}H NMR (400 MHz, CDCl$_3$, **Figure A.18**) δ: 9.49 (d, *J* = 6.2 Hz, 1H), 8.98 (s, 1H), 8.26 (s, 1H), 8.16 (d, *J* = 6.6 Hz, 1H), 8.12 (d, *J* = 6.6 Hz, 1H), 7.68 (s, 2H), 7.51 (s, 1H), 7.05 - 6.87 (m, 15 H) 6.54 (s, 1H), 4.84 (dd, *J* = 7.2, 5.3 Hz, 1H), 3.31 (dd, *J* = 13.8, 5.3 Hz, 1 H), 3.15 (dd, *J* = 13.8, 7.2 Hz, 1H). ^{13}C NMR (100 MHz, CDCl$_3$, **Figure A.19**) δ: 164.7 3, 150.7, 150.17, 145.84, 144.67, 141.87, 137.64, 137.1, 130.48, 130.07, 129.41, 128.62, 128.56, 128.33, 126.81, 124.01, 53.99, 42.34, 12.23. HR ESI-MS data (**Figure A.20**): *m/z* 604.2346 [**L2(Trt)** + H]$^+$ (calc. for [**L2(Trt)** + H]$^+$ = 604.2343).

6.3.5. Compound BzT1(Boc).

This compound was synthetized, characterized purified and provided by Dr. Emmanuel Gras and Alexandre Pocinho (Laboratoire de Chimie de Coordination, LCC).

6.3.6. Synthesis of L3.

The ligand L3 was manually synthetized using a similar protocol as that described for the synthesis of **L1** (Section 6.3.2). Basically, the ligand was assembled on a rink amide MHBA resin (0.56 mmol/g, 2 g scale synthesis). The removal of the temporary Fmoc protecting groups was performed by treating the resin with 20% piperidine (2 x, 15 min) at room temperature and the presence of the free amine was verified by Kaiser-test.[2] The coupling of the Fmoc-N-Me-His(Trt)-OH (2 equiv.) was carried out using HBTU (1.95 equiv.) as a coupling reagent and DIEA (4 equiv.) as base in NMP at room temperature. DMF was

replaced by NMP due to solubility issues with Fmoc-N-Me-His(Trt)-OH. After Fmoc deprotection, the 2-carboxy-1,10-phenanthroline (1.5 equiv.) was coupled in NMP using PyBOP (1.5 equiv.) as coupling agent and DIEA (3 equiv.) as base. The cleavage from the resin and the removal of the Trt protecting group were performed simultaneously by treating the resin with a solution containing TFA/TIS/water, 95:2.5:2.5, v/v/v (15 mL) for 2 h. The resin was filtrated and rinsed with 10 mL of TFA. The two solutions were combined and concentrated by evaporating most of the TFA using a steam of N_2. Cold diethyl ether was added to the oily residue to promote the precipitation of the ligand that was centrifuged and washed with cold diethyl ether (4 x, 10 mL). The yellow residue was dissolved in water and lyophilized. The solid obtained was re-dissolved in 10 % solvent B (1 mg/mL) and purified by preparative reversed-phase HPLC using a linear gradient from 10 to 15 % B in 20 minutes at a flow rate of 10 mL/min (retention time (R_t) = 20.7 min). The purity of the peptide was verified by reversed-phase analytical HPLC and it was greater than 97 % (**Figure A.12**). Average yield 66 %. ^{1}H NMR data at 600 MHz and ^{13}C at 150 MHz in D_2O + Trimethylsilylpropanoic acid (TMSP) at 300 K show two conformers: Conformer A (major, 2/3): ^{1}H NMR (600 MHz, D_2O, **Figure A.9**, **Table A.1**) δ 8.96 (dd, J = 4.5, 1.7 Hz, 1H), 8.52 (d, J = 1.3 Hz, 1H), 8.47 (d, J = 8.9 Hz, 1H), 8.41 (dd, J = 8.1, 1.6 Hz, 1H), 7.86 (d, J = 8.9 Hz, 1H), 7.81 (d, J = 8.9 Hz, 1H), 7.78 (dd, J = 8.1, 4.5 Hz, 1H), 7.69 (d, J = 8.9 Hz, 1H), 3.18 (s, 1H), 7.06 (brt, J = 1.1 Hz, 1H), 5.45 (dd, J = 10.8, 5.1 Hz, 1H), 3.45 (dd, J = 16.0, 10.8 Hz, 1H), 3.22 (ddd, J = 16.0, 5.1, 0.9 Hz, 1H); ^{13}C NMR (150 MHz, D_2O, **Figure A.10**, **Table A.1**) δ 175.5, 173.9, 154.8, 153.4, 152.4, 146.5, 145.6, 143.4, 141.9, 141.1, 136.6, 131.5, 131.3, 129.2, 127.3, 125.6, 120.6, 62.9, 32.4, 26.4. Conformer B (minor, 1/3): ^{1}H NMR (600 MHz, D_2O, **Figure A.9**, **Table A.1**) 9.00 (dd, J = 4.8, 1.7 Hz, 1H), 8.73 (d, J = 1.3 Hz, 1H), 8.53 (dd, J = 8.1, 1.6 Hz, 1H), 8.47 (d, J = 8.9 Hz, 1H), 7.87 (dd, J = 8.1, 4.8 Hz, 1H), 7.86 (d, J = 8.9 Hz, 1H), 7.81 (d, J = 8.9 Hz, 1H), 7.69 (d, J = 8.9 Hz, 1H), 7.52 (brs, 1H), 5.51 (dd, J = 9.5, 5.8 Hz, 1H), 3.61 (ddd, J = 15.6, 5.8, 0.8 Hz, 1H), 3.46 (dd, J = 15.6, 9.5 Hz, 1H), 3.06 (s, 1H). ^{13}C NMR (150 MHz, D_2O, **Figure A.10**, **Table A.1**) δ 175.7, 174.0, 154.8, 154.7, 151.0, 145.0, 145.6, 143.5, 142.9, 141.7, 136.5, 132.3, 131.3, 129.2, 127.3, 125.2, 120.2,

60.9, 37.3, 25.9. HR ESI-MS data (**Figure A.13**): m/z 375.1458 ± 0.5 [**L3** + H]$^+$ (calc. for [**L3** + H]$^+$ = 375.1569).

6.3.7. Synthesis of L1AB.

The peptide containing **L1** was synthesized in two steps: A) Synthesis of the peptide chain (NH$_2$-H(Trt)-Q(Trt)-K(Boc)-L-V-F-F-A-E(OtBu)-D(OtBu)-Resin): the amino acids were assembled on a rink amide MHBA resin (0.56 mmol/g, 0.5 g scale synthesis) using a microwave assisted Biotage Initiator+ Alstra synthesizer and following standard Fmoc solid-phase peptide synthesis (SPPS) techniques.[3] B) Attachment of the 2-carboxy-1,10-phenanthroline: this unit was attached (2 equiv.) manually to the protected resin bound peptide in DMF using PyBOP (4 equiv.) as coupling agent and DIEA as base (8 equiv.). The attachment of 2-carboxy-1,10-phenanthroline was verified by the Kaiser-test.[2] The final peptide was deprotected and cleaved from the resin by treatment with the mixture TFA/TIS/Water (95:2.5:2.5, v/v/v, 20 mL/g of resin) for 2 h at room temperature and under N$_2$. The resin was filtered and rinsed with 10 mL of TFA. The filtrate and rinses were combined and concentrated with a steam of N$_2$ to a crude oil, from which a precipitate was obtained by addition of cold diethyl ether (20 mL). The solid was filtered, washed with cold diethyl ether, lyophilized, re-dissolved in 30 % solvent B (1 mg/mL) and purified by preparative reversed-phase HPLC using a linear gradient from 30 to 40 % B in 15 minutes at a flow rate of 10 mL/min (retention time (R_t) = 10.5 min). The purity of the peptide was verified by reversed-phase analytical HPLC (**Figure A.22**) and it was greater than 97 %. HR ESI-MS data (**Figure A.23**): m/z 1437.6830 ± 0.5 [**L1AB** + H]$^+$ (m/z calc. for [**L1AB** + H]$^+$ = 1437.6830).

6.4. Stock Solutions.

The stock solutions of the purified ligands **L1**, **L2**, and **L3** were prepared for each experiment using Milli-Q-water and the concentrations were determined by UV-vis spectroscopy using the extinction coefficient of the phenanthroline at

pH 7.4 in 100 mM TRIS-HCl buffer ($\varepsilon_{268\,nm}$ = 22 095 M^{-1} cm^{-1}). The stock solution of **L1AB** was prepared in 20 % DMF, firstly dissolving the lyophilized powder on DMF, and after, adding the correspondent 80 % of Milli-Q-water. Its concentration was determined as described before.

The solutions of the complexes **C1**, **C2**, Cu-**L3** and **Cu(II)L1AB** were prepared by mixing the required stoichiometric amounts of the corresponding ligand and the Cu salt.

The stock solutions of Zn(NO$_3$)$_2$ (110 mM), CuCl$_2$ (103 mM) and Cu(NO$_3$)$_2$ (118 mM) were prepared from the analytical grade metal salt and standardized by titration with K$_2$H$_2$EDTA following standard methods.[4] Concentrations of the Cu solutions were confirmed by coupled induced plasma mass spectrometry (ICP-MS) at the Faculty of Pharmacy of Aix-Marseille University.

The stock solution of tetrakis(ACN)Cu(I) hexafluorophosphate (40.1 mM) was prepared in ACN from the analytical grade metal salt and stored under anaerobic conditions (inside a glovebox). The concentration was determined by UV-vis spectroscopy (ε_{483nm} = 13 300 M^{-1} cm^{-1}) using a 4-fold excess of bathocuproine in water as reported by Smith and Wilkins.[5]

Fresh AscH$^-$ solutions were prepared for each experiment at 5 mM by dissolving 9.9 mg in 10 mL of water.

The *ct*-DNA stock solutions (2.8 mM and 1.7 mM) were prepared from its sodium salt in 50 mM NaCl and 5 mM TRIS-HCl buffer (pH 7.4) and standardized by UV-vis spectroscopy (ε_{260nm} = 6 600 M^{-1} cm^{-1}).

The stock solution containing 25 µM of 2′,7′-Dichlorodihydrofluorescein diacetate (DCFDA) in Dulbecco's modified Eagle medium (DMEM) with fetal bovine serum (FBS) was prepared in the darkness by diluting a solution 25 mM DCFDA prepared by weighting 50 mg of DCFDA in 4.1 mL of DMSO.[6]

Aβ16 peptide solution (10 mM) was prepared in water and stored at -25 °C. The concentration was determined by UV-vis spectroscopy using the absorption of Tyr10 considered as free Tyr (at pH 2.0, ε_{276nm}- ε_{296nm} = 1 410 M^{-1} cm^{-1}).

6.5. Spectroscopic studies.

6.5.1. UV-vis spectroscopy.

All spectra were acquired at 298 K using 1 cm path quartz UV-cells.

6.5.1.1. UV-vis pH titrations.

These experiments were performed using a Crison pH-meter Basic 20 with a Biotrode electrode (Hamilton) at 298 K. The required amounts of the ligands and Cu(II) or Zn(II) salts were dissolved in Milli-Q-water and the pH of the solutions was adjusted using NaOH or HCl solutions. UV-vis spectra were recorded on a Varian Cary 50 Bio spectrophotometer.

6.5.1.2. Interaction Studies with DNA.

UV-vis spectra were recorded on a Varian Cary 60 Bio spectrophotometer. The UV-cells were prepared with 30 µM of the correspondent complex in 50 mM NaCl and 5 mM TRIS-HCl buffer (pH 7.32). An additional UV-cell was also prepared excluding the complex, used to subtract the correspondent *ct*-DNA absorption after each addition. The spectra were recorded after each addition of *ct*-DNA (from 0 to 100 µM)[7]. Based upon the variation in absorption, the intrinsic binding constant (K) of the complexes **C1** and **C2** with DNA was calculated using the Benesi–Hildebrand equation (**Equation 2.1**, Section 2.1.2, Chapter 2).[8]

6.5.1.3. Monitoring the production of ROS.

The consumption of ascorbic acid was monitored either on an Agilent 8453 or on a Varian Cary 50 Bio spectrophotometer following the maximum absorbance of ascorbic acid (265 nm). The samples were prepared from stock solutions of ligand, Aβ16 peptide, $CuCl_2$, $Zn(NO_3)_2$ and $AscH^-$, and the final concentrations in the UV-cell were 12, 12, 10, 10 and 100 µM respectively (unless otherwise noted), in 100 mM HEPES buffer solution at pH 7.1.

6.5.1.4.   Determination of the Zn(II) apparent binding constant.

The apparent affinity constant of **L1** for Zn(II) ($K_{Zn(II)-L1,app}$) was calculated in 100 mM HEPES buffer at pH 7.1 on a Varian Cary 60 Bio spectrophotometer. Far UV-vis spectra were recorded upon successive additions of Zn(II) (from 0 to 2 equiv. of Zn(NO$_3$)$_2$) to a solution of 50 μM **L1**. The spectra were analyzed and fit using two methods: HypSpec (HYPERQUAD suit of programs)[9] and the model and equation (**Equation 4.2**) described in Section 4.2.2.2.3, Chapter 4.[10–12]

6.5.1.5.   Determination of the Cu(I) apparent binding constant.

The apparent affinity constant of **L1** for Cu(I) ($K_{Cu(I)-L1,app}$) was calculated in 100 mM HEPES buffer at pH 7.1 on a Varian Cary 60 Bio spectrophotometer. Spectra were recorded upon successive additions of Cu(I) (from 0 to 1.4 equiv.) to a solution containing 200 μM of **L1** under anaerobic conditions (inside a glove box). The spectra were analyzed and fit using HypSpec (HYPERQUAD suit of programs).[9]

6.5.2.   Interaction studies with ethidium bromide (EB).

These experiments were performed on a Perkin Elmer LS 55 50 Hz Fluorescence Spectrometer, connected to a PC system and a water bath temperature controller at 298 K. EBr-DNA competitive assays were carried out on disposable poly(methyl methacrylate) (PMMA) cells with 1 cm path length by following the quenching of the EBr-DNA fluorescence band in 50 mM NaCl and 5 mM TRIS-HCl buffer (pH 7.32) upon increasing complex additions (from 0 to 160 μM). Each spectrum was collected 5 min after each complex addition to allow for signal stabilization. The EBr-DNA ratio used (12.5 μM/2.5 μM) was based on reported literature.[13] To estimate quantitatively the affinity of the different complexes for *ct*-DNA (compared to EBr), their quenching efficiency was calculated using the Stern–Volmer quenching constant (K$_{SV}$) equation (**Equation 2.2**, Section 2.1.3, Chapter 2).[14] Experiments performed by duplicate (n=2) by Joaquim Peña at the Universitat Autonoma de Barcelona.

6.5.3. Electron paramagnetic resonance spectroscopy (EPR).

The X-band EPR spectra were recorded on a Bruker Elexsys E500-9.5/2.7 spectrometer equipped with a BVT 3000 digital temperature controller (100 - 400 K). The spectra were recorded at 120 K in frozen solutions and their simulations were performed using Matlab program package Easyspin.[15] These experiments were performed by Dr. Jalila Simaan at the Institut des Sciences Moléculaires de Marseille (ISM2, Marseille, France).

6.6. High resolution mass spectrometry (HRMS) and tandem mass spectrometry (MS/MS).

These experiments were performed by Dr. Aura Tintaru (Aix-Marseille Université, Institut de Chimie Radicalaire) using a Synapt G2 HDMS quadrupole/time-of-flight (Manchester, UK) equipped with an electrospray source operating in positive mode. A quadrupole was used for selection of precursor ions to be further submitted to collision induced dissociation (CID) in MS/MS experiments. Samples were introduced at 10 µL/min flow rate (capillary voltage + 2.8 kV, sampling cone voltage: varied between + 20 V and + 60 V) under a curtain gas (N_2) flow of 100 L/h heated at 35 °C. Accurate mass experiments were performed using reference ions from CH_3COONa internal or external standard. The samples were dissolved and further diluted in methanol (Sigma-Aldrich, St-Louis - MO, USA) doped with formic acid (1 % v/v) prior to analysis. MS/MS experiments were performed at variable collision energy (5 to 15 eV laboratory frame, using argon as the collision gas. The precursor ion was used as the reference for accurate measurements of product ion m/z value in MS/MS spectra. Data analyses were conducted using MassLynx 4.1 programs provided by Waters.

6.7. Biological studies.

6.7.1. Cell culture.

Routine cell culture was performed as previously described.[16] Cancer cells used were human ovarian cancer cells A2780 (from Sigma Aldrich, Lyon, France) and human breast cancer cells MCF-7 (ATCC® HTB22). Normal human cells used were human normal endothelial cells (Human Umbilical Vein Endothelial Cells, HUVEC) (ECACC, Sigma-Aldrich, Lyon, France), and human lung fibroblasts IMR-90 (ATCC® CCL186). A2780 cells were cultured in RMPI-1640 supplemented with 10% FBS, 1% L-glutamine, and 1% antibiotics (all from Invitrogen (Carlsbad, CA, USA)). IMR-90 and MCF-7 cells were grown in DMEM supplemented with 10% FBS, 1% L-glutamine, and 1% antibiotics. HUVEC cells were cultured in specific medium (Endothelial Cell Growth Medium from Sigma Aldrich, Lyon, France). Cells were routinely grown on 25 cm^2 flasks and maintained in a 5% CO_2 incubator at 37 °C. For ROS production and uptake assay, cells grown on 25 cm^2 flasks were detached using trypsin-EDTA solution (from Thermofisher), counted using Malassez counting chamber, diluted in appropriate culture media and seeded into either 6- or 96-well cell culture plates (Greiner bio-one) at the corresponding cells density. These experiments were performed in collaboration with Dr. Marc Maresca at the Institut des Sciences Moléculaires de Marseille (ISM2, Marseille, France).

6.7.2. Cellular uptake studies (Cu internalization).

Uptake assay was performed as previously described.[17] Briefly, human cells were seeded onto 6-well plates at 10^6 cells per well in 2 mL and left to incubate overnight for optimal adherence. The next day, medium was aspirated, and cells were washed once with sterile phosphate buffer saline containing calcium and magnesium (PBS++, pH 7.4) (from Thermofisher, Les Ulis, France). Wells were emptied and 1 mL of 200 µM solutions diluted in pre-warmed PBS++ of **C1**, **C2**, **L1**, **L2**, $CuCl_2$ and H_2O_2 were added to each well. After 4 h incubation in CO_2 incubator at 37 °C, 200 µL of cell medium were collected and stored at -80°C before copper's quantification, and the cells were scraped in 200 µL of nitric acid (67 % Suprapur

Merck). Cell lysates were stored at -80°C before copper quantification. Uptake was normalized to protein content present into the wells. The amount of protein was measured using the standard Bradford method[18] (Bradford Ultra purchased from Expedeon). These experiments were performed in triplicate (n=3) and in collaboration with Dr. Marc Maresca at the Institut des Sciences Moléculaires de Marseille (ISM2, Marseille, France).

Measurements were carried out by ICP-MS. Before analysis, cell lysates (200 µL in nitric acid 67 % Suprapur Merck) were diluted with 1800 µL of ultrapure water (18 MΩ.cm) and the supernatants were diluted with 200 µL of nitric acid (67% Suprapur Merck) and 200 µL of ultrapure water (18 MΩ.cm). Quantification was carried out on ICAP Q ICP-MS equipped with a collision cell to reduce interference (Thermo Electron). Before each batch of analysis, the measurement conditions were optimized using a reference solution containing 1 ppb of different elements (Co, In, Ba) (Analytika). The calibration of the ICP-MS was carried out during each group of measurements by analysis of standard copper solutions (from 0.5 to 500 µg/L) obtained by dilution of a certified multi-element solution (Sigma Aldrich). A reference solution (SCP Sciences water) is analyzed as a control sample. The masses (m/z) retained for copper analysis are 63 and 65. The data were analyzed and processed using Qtegra software (ThermoElectron). These experiments were performed in triplicate (n=3) by Dr. Florence Chaspoul at the Faculty of Pharmacy at the University Aix-Marseille.

6.7.3. Cytotoxic studies (MTT assay).

Measurement of the toxicity of ligands, their respective complexes, $CuCl_2$ and H_2O_2 was performed as previously reported.[17,19] Briefly, human cells grown on 25 cm² flasks were detached using trypsin-EDTA solution (from Thermofisher). After counting using Malassez chamber, cells were diluted in appropriate culture media, seeded into 96-well cell culture plates (Greiner bio-one, Paris, France) at approximately 104 cells per well in 200 µL of medium and left to incubate overnight for optimal adherence. The next day, medium was aspirated and 200 µL of a dilution series from 200 to 3 µM of the compounds, (stock solutions prepared

fresh) in appropriate medium, were added before incubation for 72 h at 37 °C/5 % CO_2. At the end of the incubation period, medium was aspirated and replaced by 200 µL of MTT solution (final concentration of 500 µg/mL in sterile phosphate buffer saline containing calcium and magnesium (PBS++, pH 7.4) (from Thermofisher, Les Ulis, France). After 4 h incubation at 37 °C in 5 % CO_2, the medium was aspirated, and the purple formazan crystals formed into the cells were dissolved in 200 µL of DMSO using orbital shaking. Absorbance was finally measured at 570 nm using a plate spectrophotometer (Synergy™ Mx Monochromator-Based Multi-Mode Microplate Reader). The cell viability was calculated as percentage of the control wells. For analysis, the non-linear fit curve method was used via GraphPad Prism version 7.00 for Windows (GraphPad Software, La Jolla California USA, www.graphpad.com). Experiments were performed in triplicate (n=3) by Dr. Marc Maresca at the Institut des Sciences Moléculaires de Marseille (ISM2, Marseille, France).

6.7.4. Measurement of intracellular ROS production.

For this experiment 20 000 cells per well of the respective cell line (A2780, MCF-7, IMR-90 and HUVEC) were incubated at 37 °C in the dark with 100 µL of a solution containing 25 µM of DCFDA (Sigma-Aldrich) in DMEM with FBS. After 30 minutes the medium was removed and 100 µL of the respective complex or ligand solutions in PBS were added to the well, assaying concentrations from 200 to 0.3 µM. Additionally, $CuCl_2$ and H_2O_2 solutions were also assayed as controls. Readings of fluorescence were recorded at initial time, 4 and 72 h (λ_{exc} = 485 nm, λ_{em} = 535 nm) on a Synergy™ Mx Monochromator-Based Multi-Mode Microplate Reader. These experiments were performed in triplicate (n=3) and in collaboration with Dr. Marc Maresca at the Institut des Sciences Moléculaires de Marseille (ISM2, Marseille, France

6.8. Bibliography.

(1) Sun, W.-H.; Jie, S.; Zhang, S.; Zhang, W.; Song, Y.; Ma, H.; Chen, J.; Wedeking, K.; Fröhlich, R. Iron Complexes Bearing 2-Imino-1,10-Phenanthrolinyl Ligands as Highly Active Catalysts for Ethylene Oligomerization. *Organometallics* **2006**, *25* (3), 666–677. https://doi.org/10.1021/om050891p.

(2) Kaiser, E.; Colescott, R. L.; Bossinger, C. D.; Cook, P. I. Color Test for Detection of Free Terminal Amino Groups in the Solid-Phase Synthesis of Peptides. *Anal. Biochem.* **1970**, *34* (2), 595–598.

(3) Chan, W.; White, P. *Fmoc Solid Phase Peptide Synthesis: A Practical Approach*; OUP Oxford, 1999; Vol. 222.

(4) Complexometric titrations [by] G. Schwarzenbach & H. Flaschka. (Book, 1969) [WorldCat.org] https://www.worldcat.org/title/complexometric-titrations-by-g-schwarzenbach-h-flaschka/oclc/639841806 (accessed Aug 2, 2019).

(5) Smith, G. F.; Wilkins, D. H. New Colorimetric Reagent Specific for Cooper. *Anal. Chem.* **1953**, *25* (3), 510–511. https://doi.org/10.1021/ac60075a037.

(6) Yoon, D. S.; Lee, M.-H.; Cha, D. S. Measurement of Intracellular ROS in Caenorhabditis Elegans Using 2′,7′-Dichlorodihydrofluorescein Diacetate. *Bio-Protoc.* **2018**, *8* (6). https://doi.org/10.21769/BioProtoc.2774.

(7) Sirajuddin, M.; Ali, S.; Badshah, A. Drug–DNA Interactions and Their Study by UV–Visible, Fluorescence Spectroscopies and Cyclic Voltametry. *J. Photochem. Photobiol. B* **2013**, *124*, 1–19. https://doi.org/10.1016/j.jphotobiol.2013.03.013.

(8) Benesi, H. A.; Hildebrand, J. H. A Spectrophotometric Investigation of the Interaction of Iodine with Aromatic Hydrocarbons. *J. Am. Chem. Soc.* **1949**, *71* (8), 2703–2707. https://doi.org/10.1021/ja01176a030.

(9) Gans, P.; Sabatini, A.; Vacca, A. Investigation of Equilibria in Solution. Determination of Equilibrium Constants with the HYPERQUAD Suite of Programs. *Talanta-Oxf.* **1996**, *43* (10), 1739–1754.

(10) Thordarson, P. Determining Association Constants from Titration Experiments in Supramolecular Chemistry. *Chem Soc Rev* **2011**, *40* (3), 1305–1323. https://doi.org/10.1039/C0CS00062K.

(11) Atwood, J. L.; Lehn, J.-M. *Comprehensive Supramolecular Chemistry*; Pergamon: New York, 1996.

(12) Connors, K. A. *Binding Constants: The Measurement of Molecular Complex Stability*; Wiley, 1987.

(13) Brissos, R. F.; Torrents, E.; Mariana dos Santos Mello, F.; Carvalho Pires, W.; de Paula Silveira-Lacerda, E.; Caballero, A. B.; Caubet, A.; Massera, C.; Roubeau, O.; Teat, S. J.; Gamez, P. Highly Cytotoxic DNA-Interacting Copper Coordination Compounds. *Metallomics* **2014**, *6* (10), 1853–1868. https://doi.org/10.1039/C4MT00152D.

(14) Liu, H.-K.; Sadler, P. J. Metal Complexes as DNA Intercalators. *Acc. Chem. Res.* **2011**, *44* (5), 349–359. https://doi.org/10.1021/ar100140e.

(15) Stoll, S.; Schweiger, A. EasySpin, a Comprehensive Software Package for Spectral Simulation and Analysis in EPR. *J. Magn. Reson.* **2006**, *178* (1), 42–55.

(16) Olleik, H.; Nicoletti, C.; Lafond, M.; Courvoisier-Dezord, E.; Xue, P.; Hijazi, A.; Baydoun, E.; Perrier, J.; Maresca, M. Comparative Structure-Activity Analysis of the Antimicrobial Activity, Cytotoxicity, and Mechanism of Action of the Fungal Cyclohexadepsipeptides Enniatins and Beauvericin. *Toxins* **2019**, *11* (9). https://doi.org/10.3390/toxins11090514.

(17) Razafimanjato, H.; Garmy, N.; Guo, X.-J.; Varini, K.; Di Scala, C.; Di Pasquale, E.; Taïeb, N.; Maresca, M. The Food-Associated Fungal Neurotoxin Ochratoxin A Inhibits the Absorption of Glutamate by Astrocytes through a Decrease in Cell Surface Expression of the Excitatory Amino-Acid Transporters GLAST and GLT-1. *Neurotoxicology* **2010**, *31* (5), 475–484.

(18) Bradford, M. M. A Rapid and Sensitive Method for the Quantitation of Microgram Quantities of Protein Utilizing the Principle of Protein-Dye Binding. *Anal. Biochem.* **1976**, *72*, 248–254. https://doi.org/10.1006/abio.1976.9999.

(19) Leite, S. M. G.; Lima, L. M. P.; Gama, S.; Mendes, F.; Orio, M.; Bento, I.; Paulo, A.; Delgado, R.; Iranzo, O. Copper(II) Complexes of Phenanthroline and Histidine Containing Ligands: Synthesis, Characterization and Evaluation of Their DNA Cleavage and Cytotoxic Activity. *Inorg. Chem.* **2016**, *55* (22), 11801–11814. https://doi.org/10.1021/acs.inorgchem.6b01884.

ANNEX.

Supplementary Information.

a) Supplementary information relative to Chapter 2.

    i) Speciation diagrams of C1 and C2.

A)
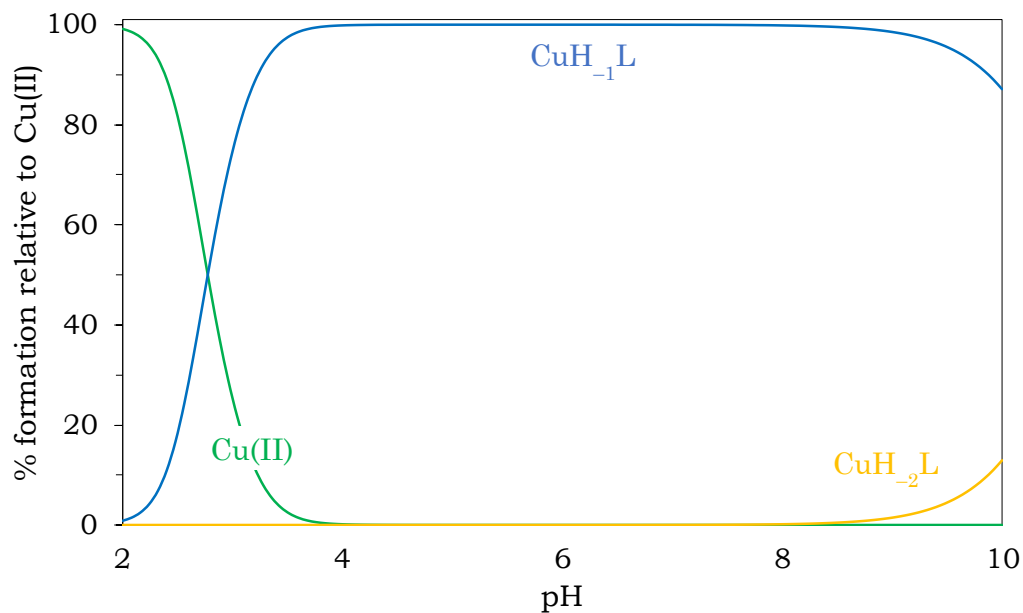
B)
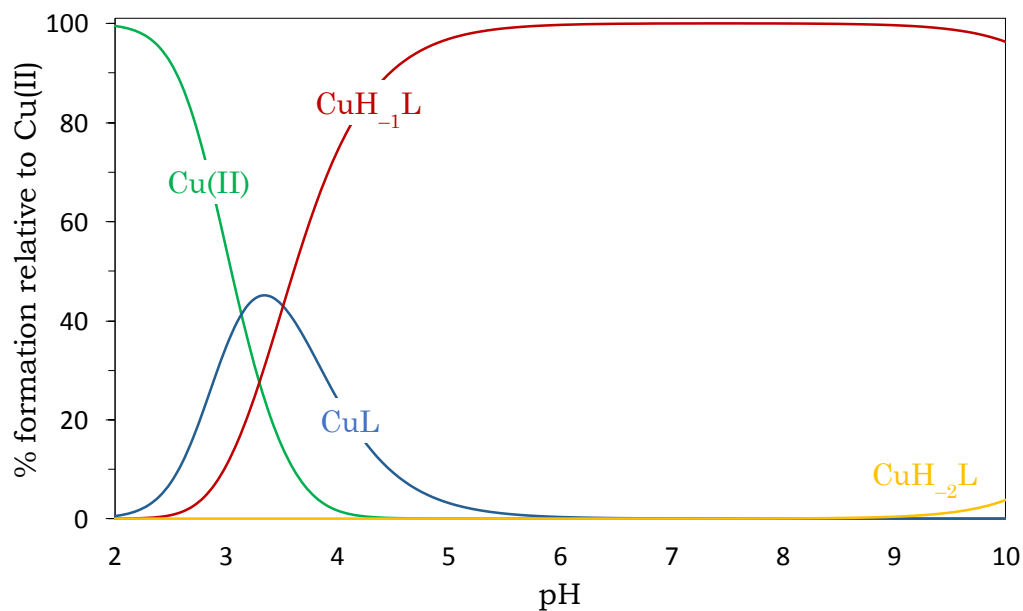
Figure A.1. Species distribution diagrams for the correspondent Cu(II) complexes of A) **HL1** and B) **H₂L2** in aqueous solution at 298 K. (I = 0.1 M KNO3), [L] = Cu(NO₃)₂ = 0.2 mM.

ii) Cu uptake in cells.
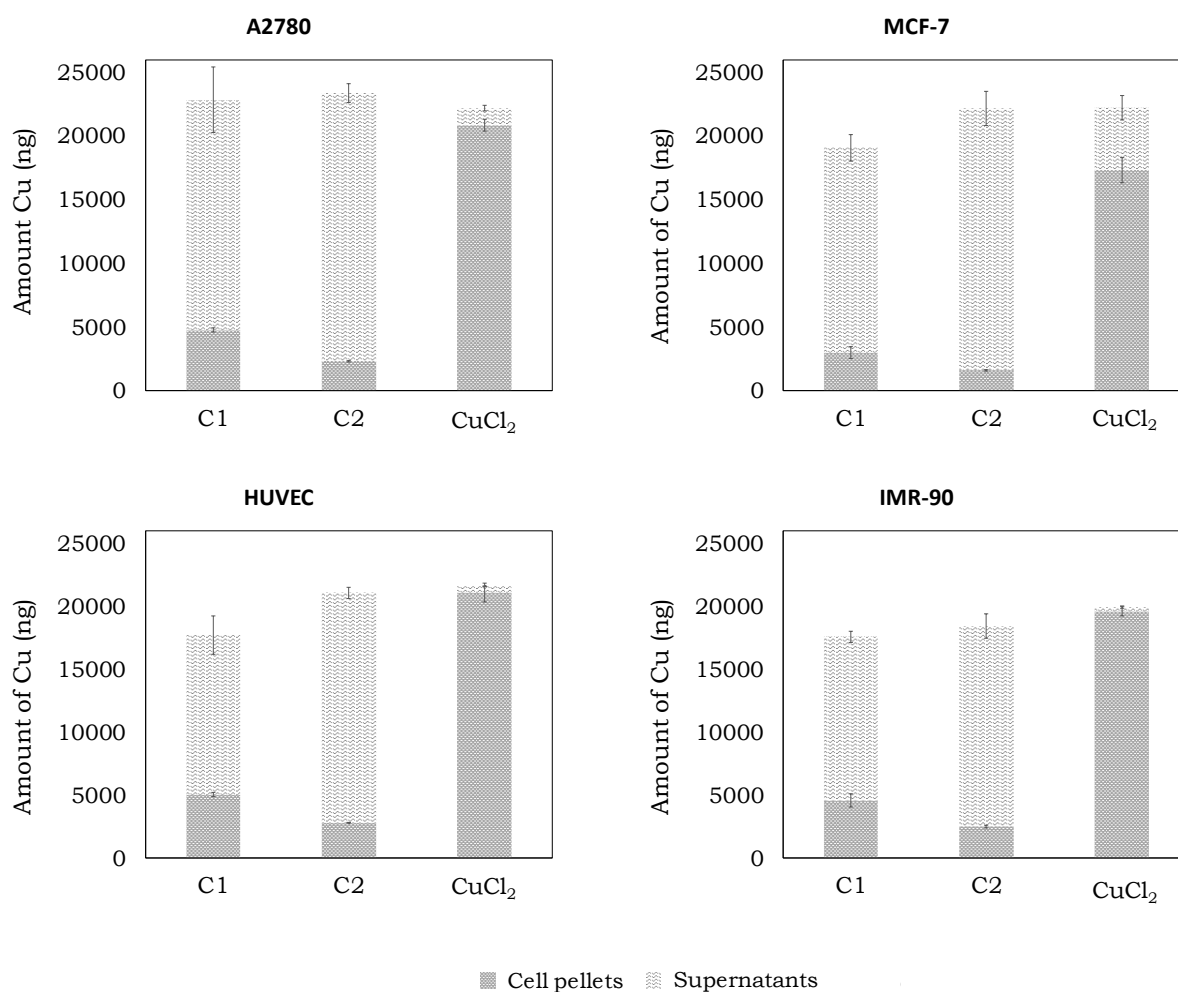
Figure A.2. Cu accumulation and distribution displayed by **C1**, **C2** and $CuCl_2$ on cancer (A2780, MCF-7) and normal (HUVEC, IMR-90) cell lines.

iii)   Measurement of intracellular ROS by **HL1**, **H₂L2**, **C1** and **C2** on A2780, MCF-7, IMR-90 and HUVEC.
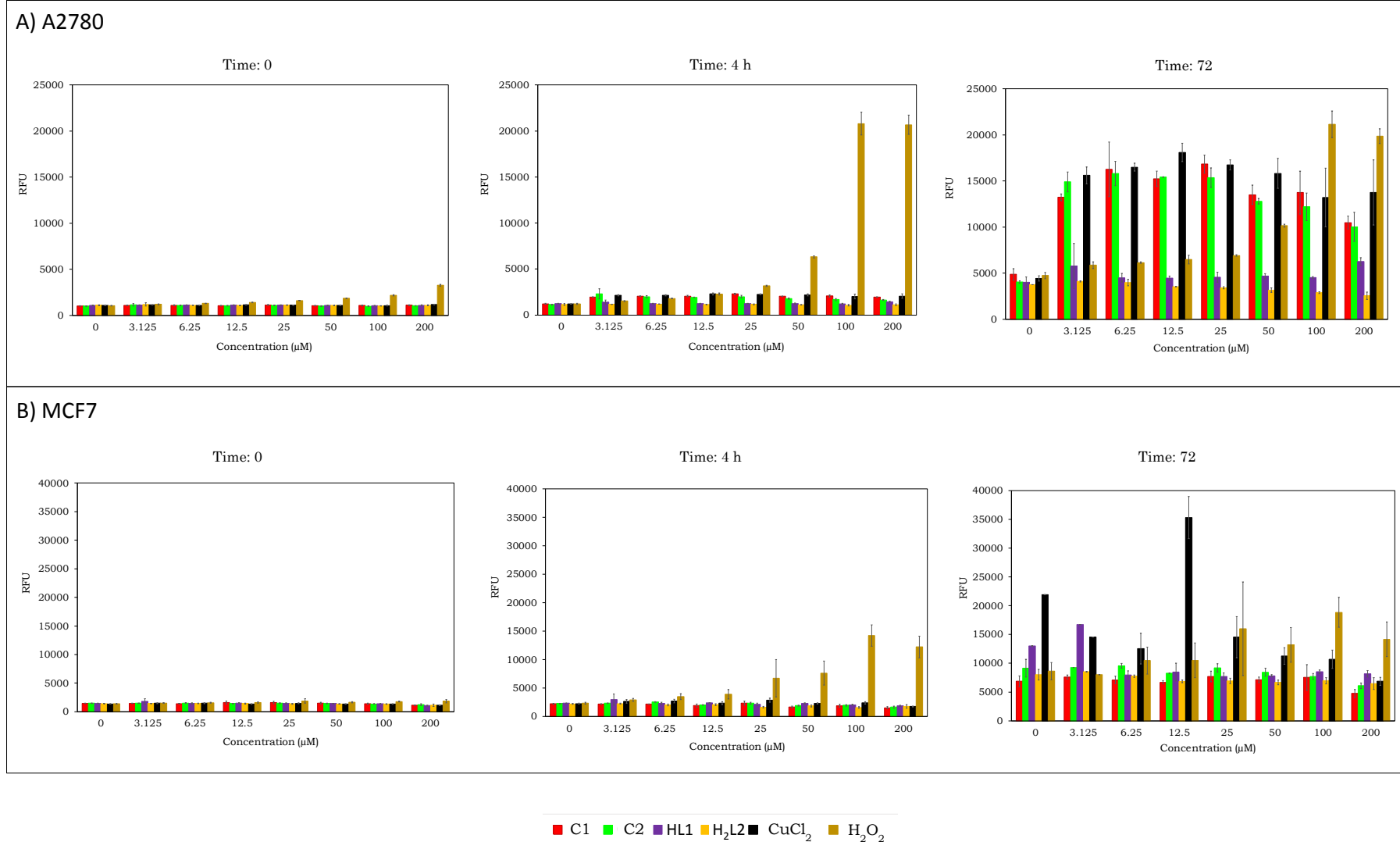
Figure A.3. Intracellular induced ROS production assayed with DCFDA on A2780 and MCF7 cells after different incubation times with the ligands **HL1**, **H₂L2**, their respective Cu(II) complexes **C1** and **C2**, and the controls H_2O_2 and CuCl2 at different concentrations.
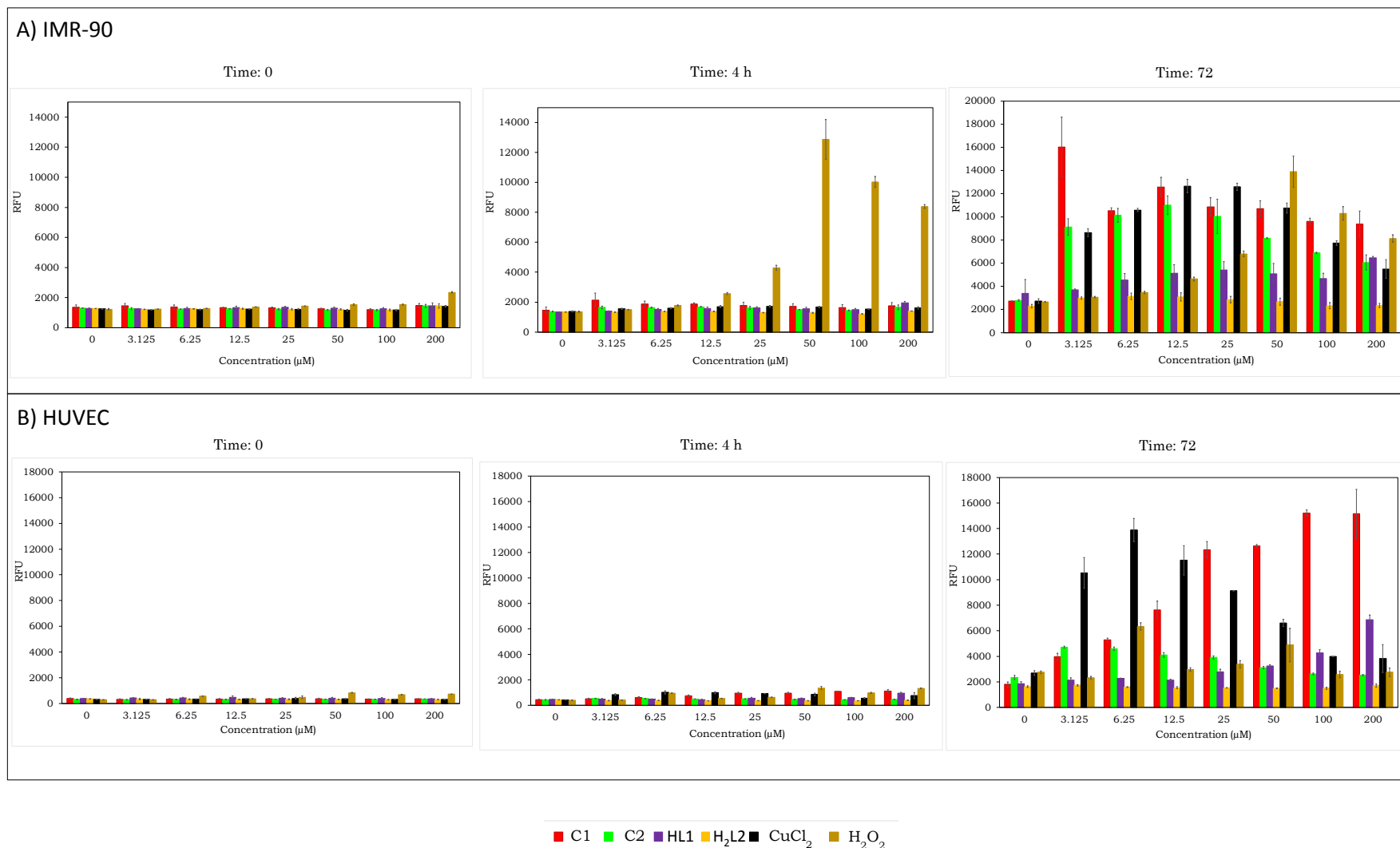
Figure A.4. Intracellular induced ROS production assayed with DCFDA on IMR-90 and HUVEC cells after different incubation times with the ligands **HL1**, **H₂L2**, their respective Cu(II) complexes **C1** and **C2**, and the controls H_2O_2 and CuCl2 at different concentrations.

iv) NMR spectroscopy of PhenCOOH.
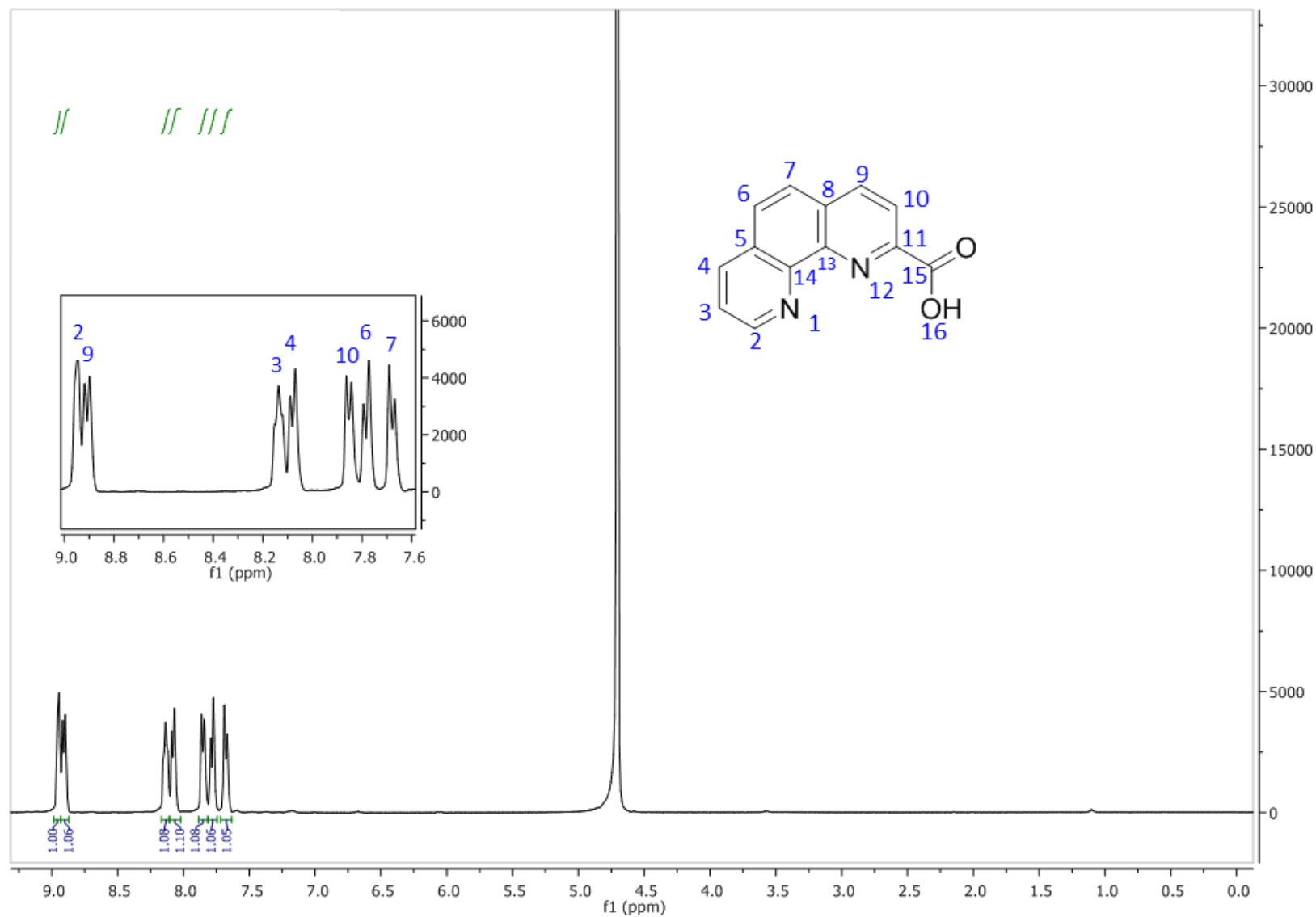
Figure A.5. ^{1}H NMR spectrum (400 MHz, D$_2$O) of PhenCOOH.
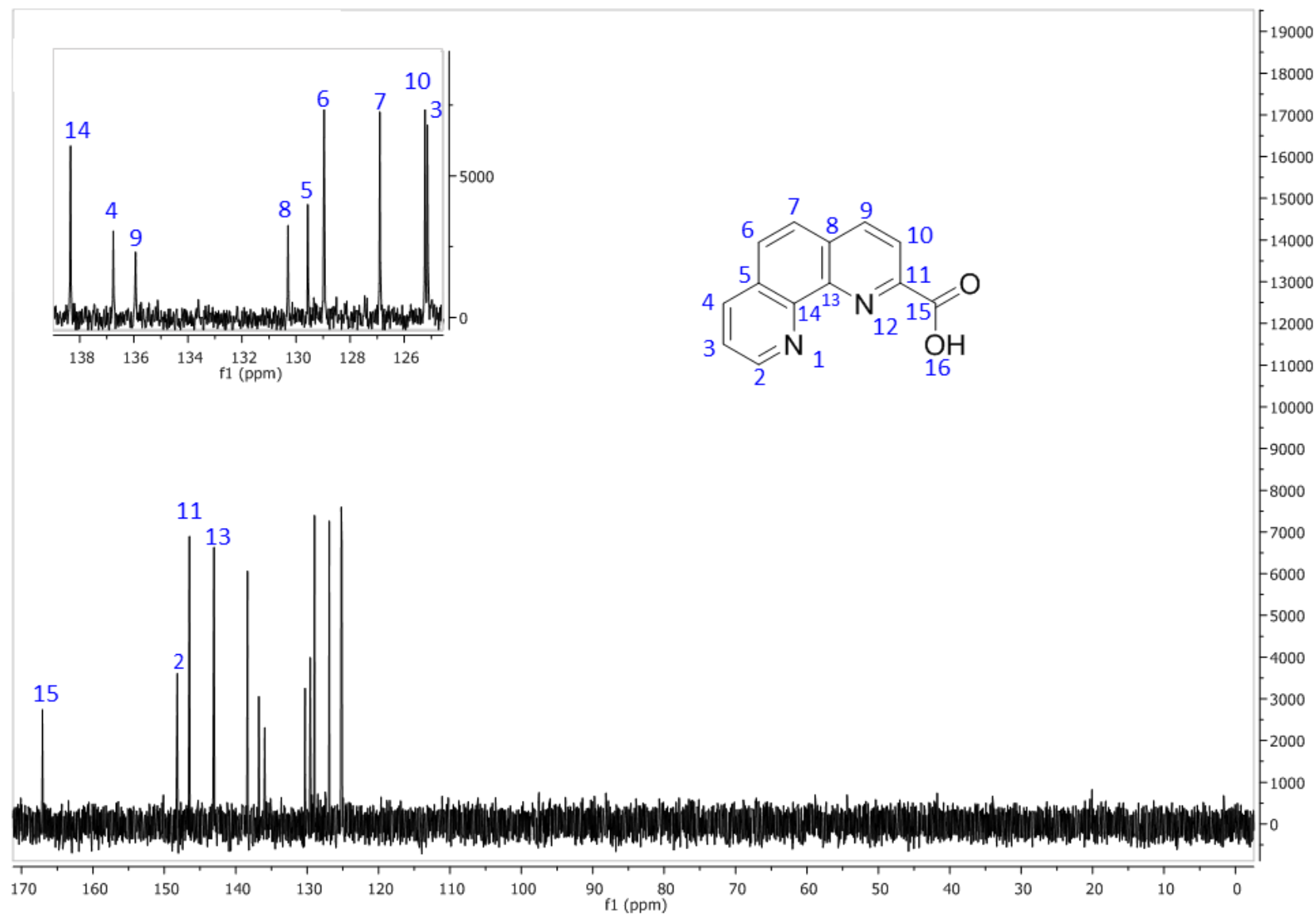
Figure A.6. ^{13}C NMR spectrum (100 MHz, D$_2$O) of PhenCOOH.

v) ¹H NMR and HR ESI-MS of **HL1**.
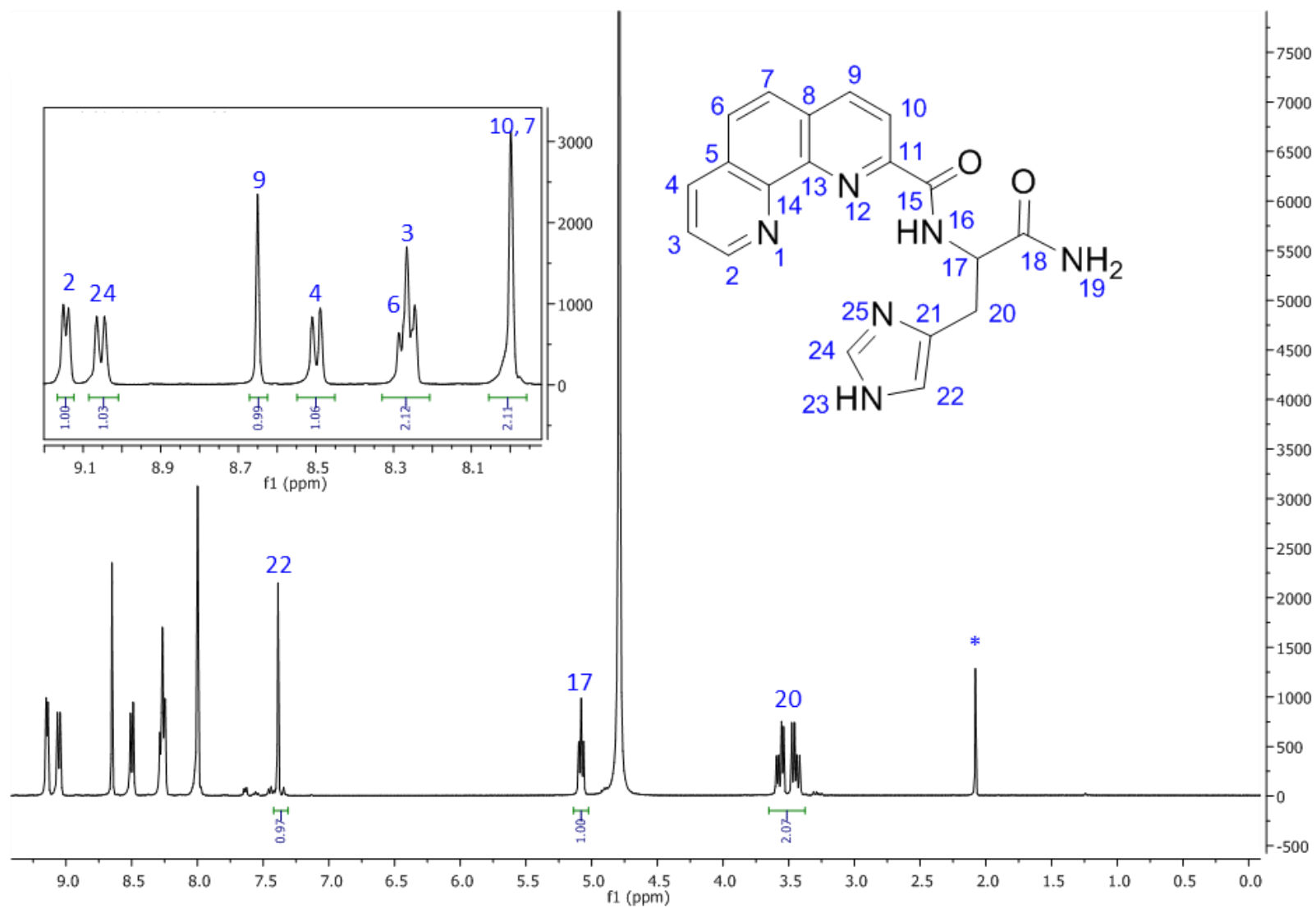
**Figure A.7**. ¹H NMR spectrum (400 MHz, D₂O) of **HL1** (*ACN signal).
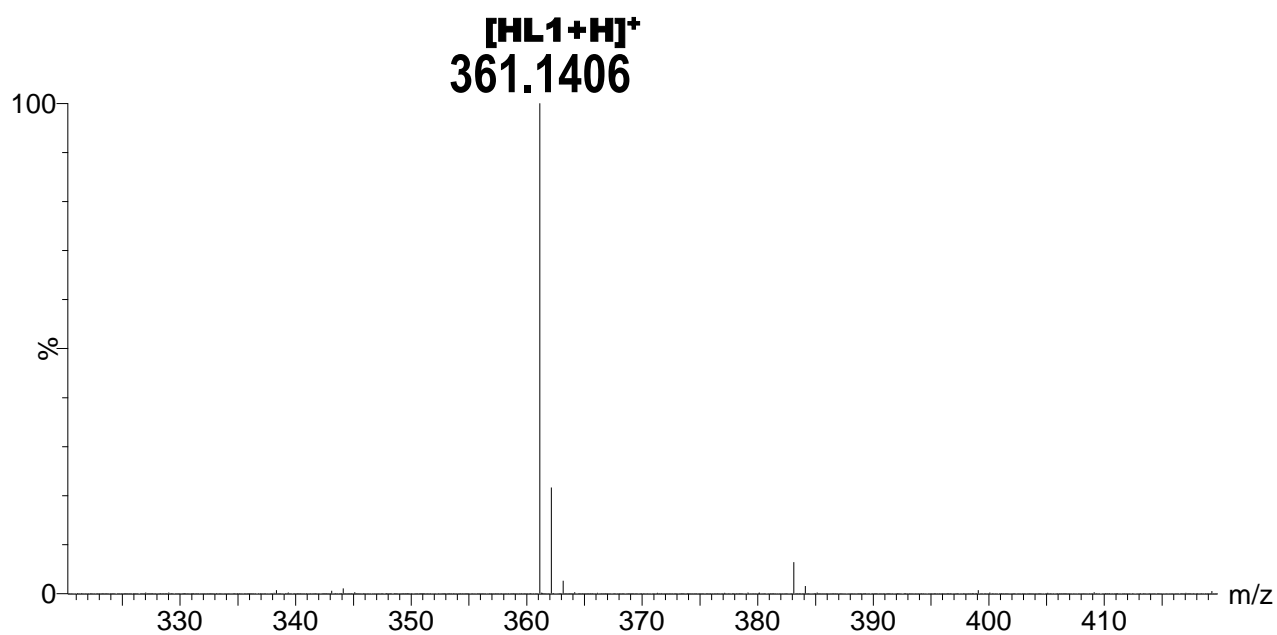
Figure A.8. HR ESI-MS spectrum of **HL1** (positive mode electrospray ionization).

vi) ¹H, ¹³C NMR, HR ESI-MS and analytical HPLC chromatogram of **L3**.
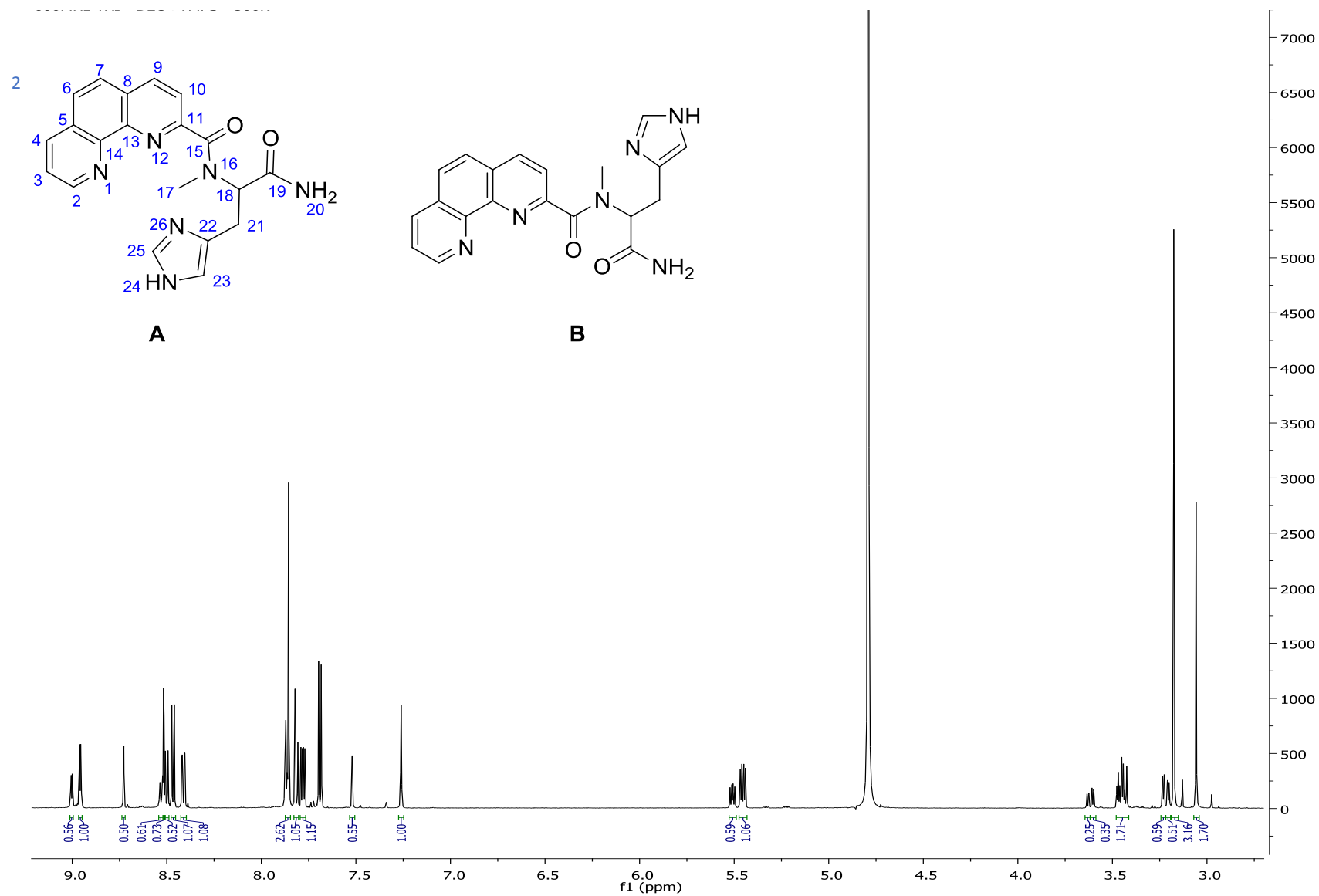
Figure A.9. ¹H NMR spectrum (600 MHz, D₂O) of **L3.**
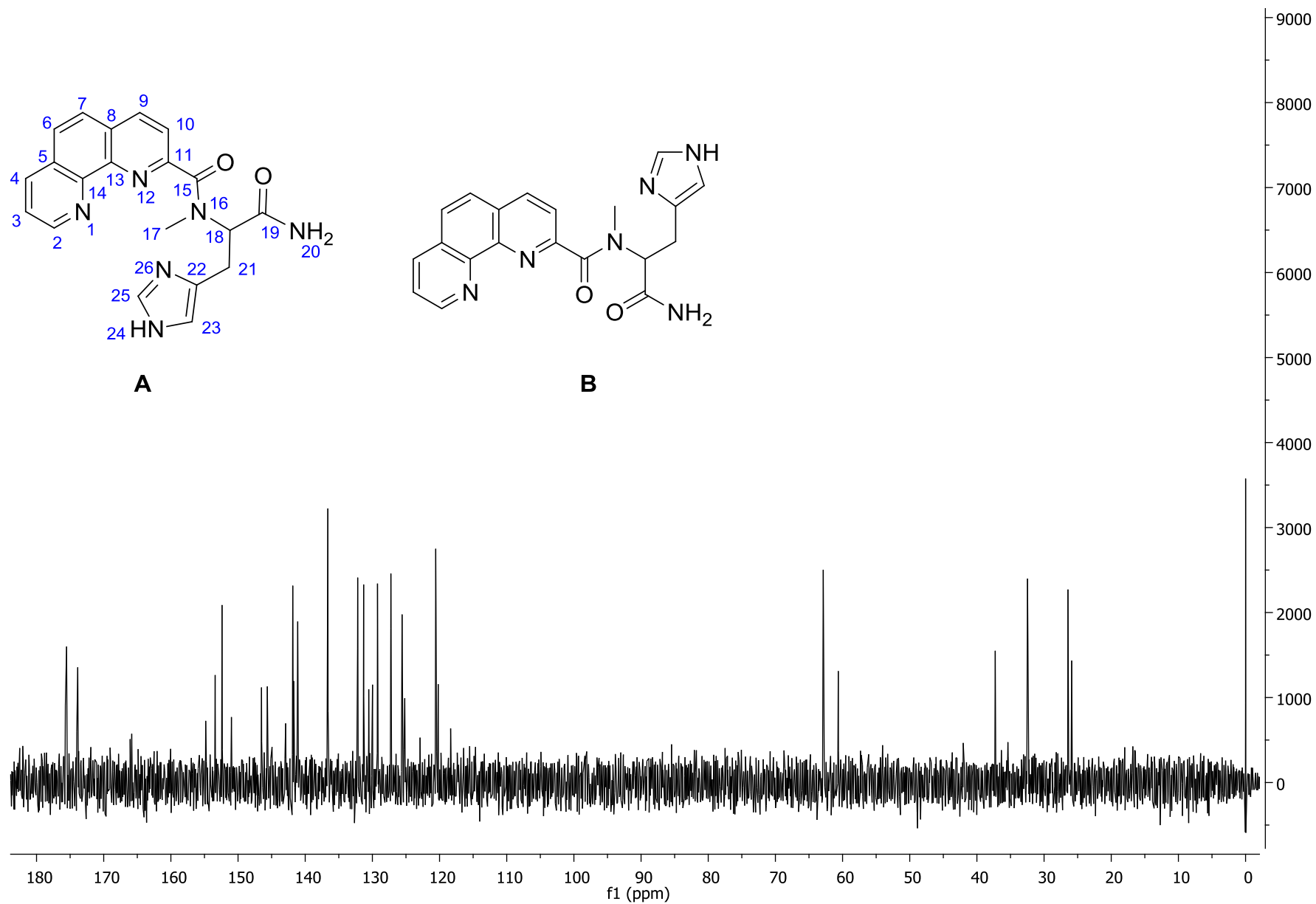
Figure A.10. ^{13}C NMR spectrum (150 MHz, D$_2$O) of **L3**.
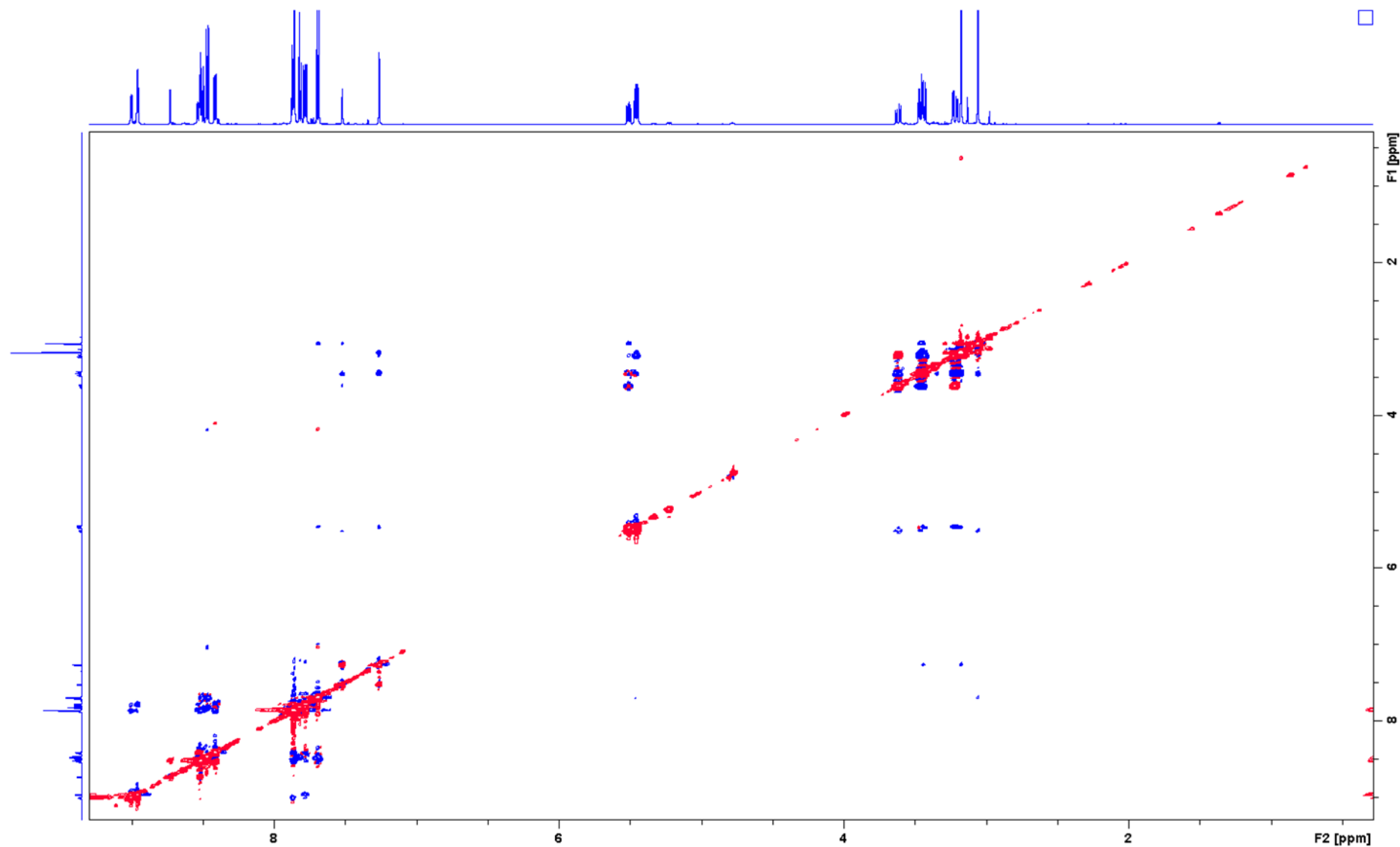
Figure A.11. The 2D NOESY spectrum of **L3** in D2O at 600 MHz. Scalar coupled partners are shown in red while NOE cross peaks are shown in blue.

Table A.1. NMR chemical shifts of ligand **L3** for ^{1}H (600 MHz) and ^{13}C (150 MHz in D_2O at 300 K.

Position	Major specie (A)		Minor specie (B)	
	δ_{1H}	δ_{13C}	δ_{1H}	δ_{13C}
2	8.96 (dd, 4.5, 1.7)	152.4	9.00 (dd, 4.8, 1.7)	151.0
3	7.78 (dd, 8.1, 4.5)	127.3	7.87 (dd, 8.1, 4.8)	127.3
4	8.41 (dd, 8.1, 1.6)	141.1	8.53 (dd, 8.1, 1.6)	142.9
5	-	154.8	-	154.8
6	7.86 (d, 8.9)	131.3	7.86 (d, 8.9)	131.3
7	7.81 (d, 8.9)	129.2	7.81 (d, 8.9)	129.2
8	-	153.4	-	154.7
9	8.47 (d, 8.9)	141.9	8.51 (d, 8.9)	141.7
10	7.69 (d, 8.9)	125.6	7.69 (d, 8.9)	125.2
11	-	143.4	-	143.5
13	-	145.6	-	145.6
14	-	146.5	-	145.0
15	-	173.9	-	174.0
17	3.18 (s)	32.4	3.06 (s)	37.3
18	5.45 (dd, 10.8, 5.1)	62.9	5.51 (dd, 9.5, 5.8)	60.9
19	-	175.5	-	175.7
21	3.22 (ddd, 16.0, 5.1, 0.9)	26.4	3.61 (ddd, 15.6, 5.8, 0.8)	25.9
	3.45 (dd, 16.0, 10.8)		3.46 (dd, 15.6, 9.5)	
22	-	131.5	-	132.3
23	7.26 (brt, 1.1)	120.6	7.52 (brs)	120.2
25	8.52 (d, 1.3)	136.6	8.73 (d, 1.3)	136.5

s: single, d: doublet, t: triplet, br: broad
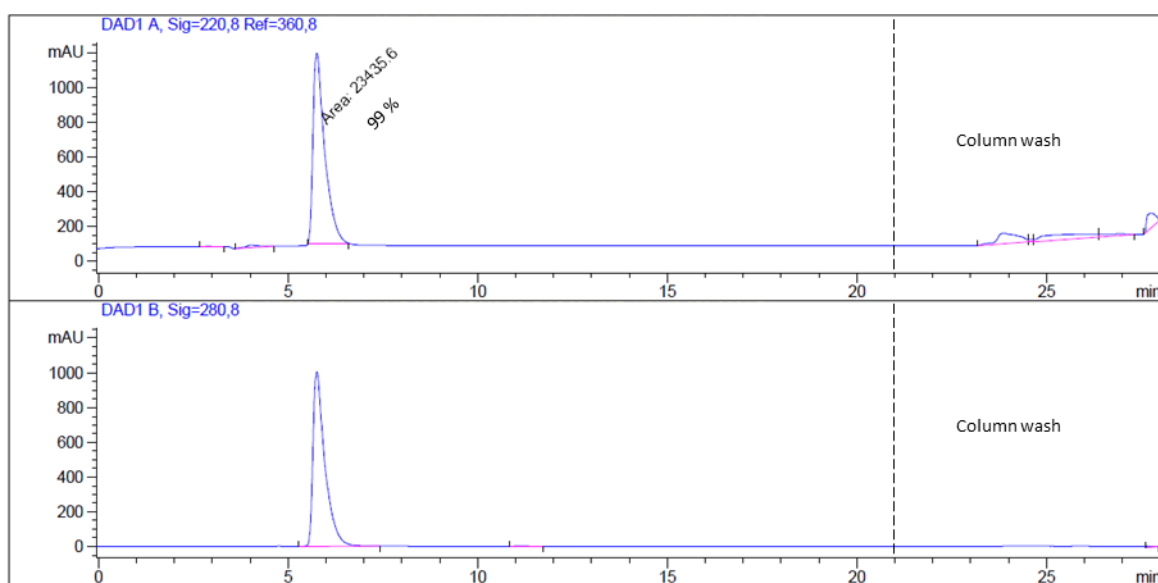
Figure A.12. Analytical reversed phase HPLC chromatogram of **L3** after purification. Upper 220 nm, bottom 280 nm. Method: 10 to 15 % of solvent B in 20 min, flux: 1 mL/min, Column: Phenomenex Jupiter Proteo column (250 mm × 4.6 mm, 4 µm, 90 Å).
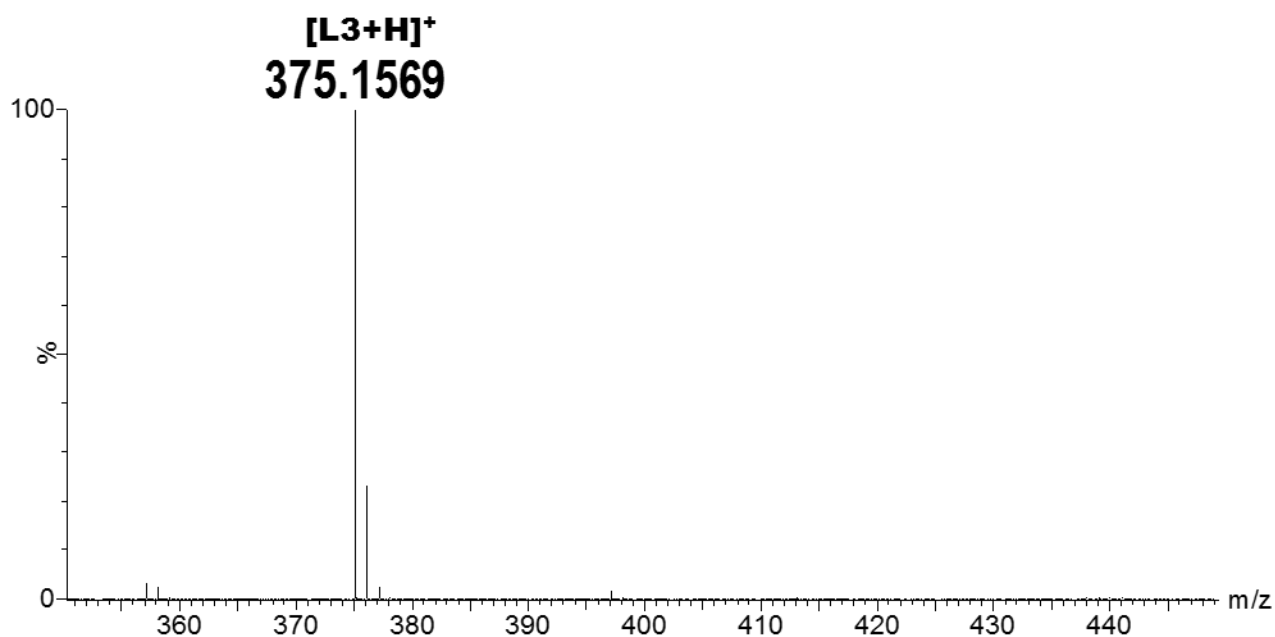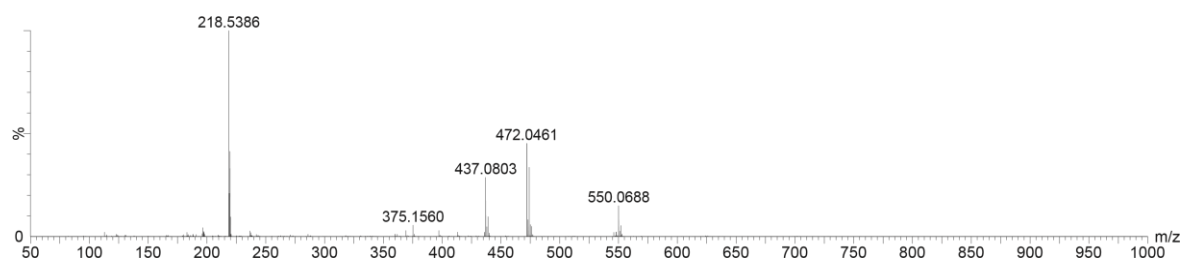

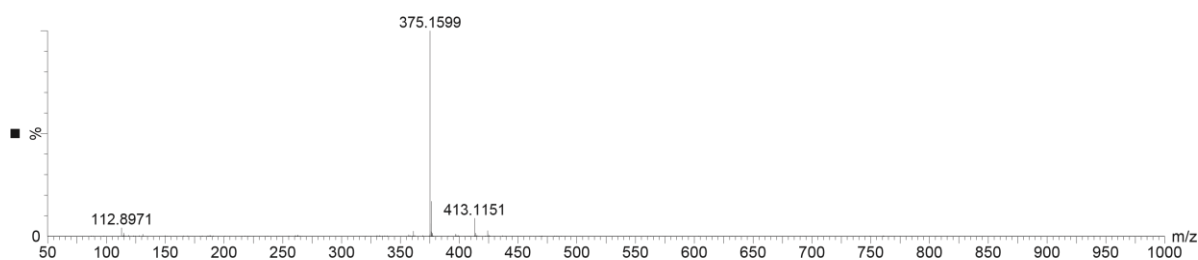**Figure A.13**. HR ESI-MS spectrum of **L3** (positive mode electrospray ionization).

vii)   ESI-MS analyses of L3 + Cu(II)

A) T$_0$
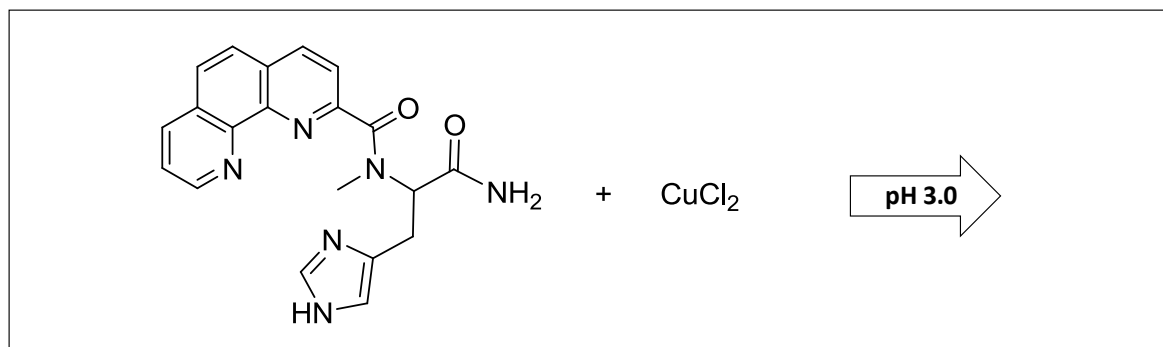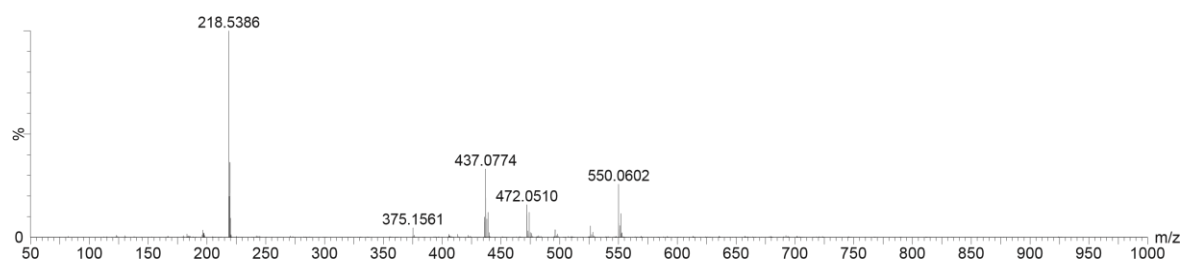
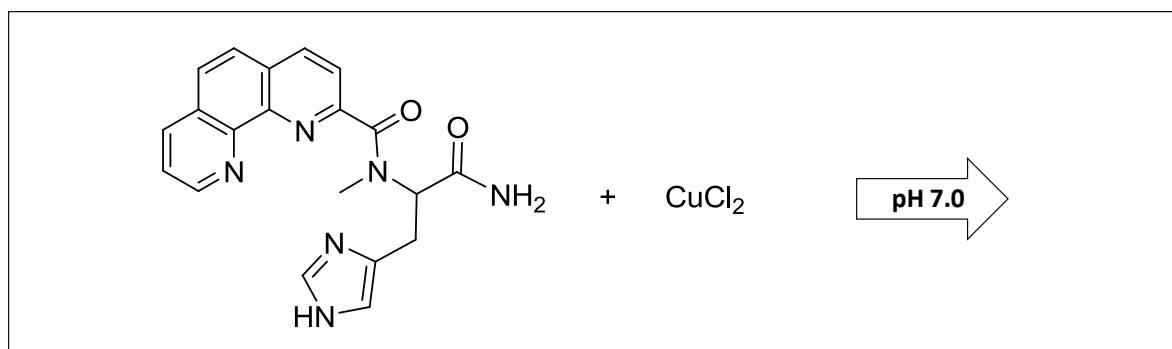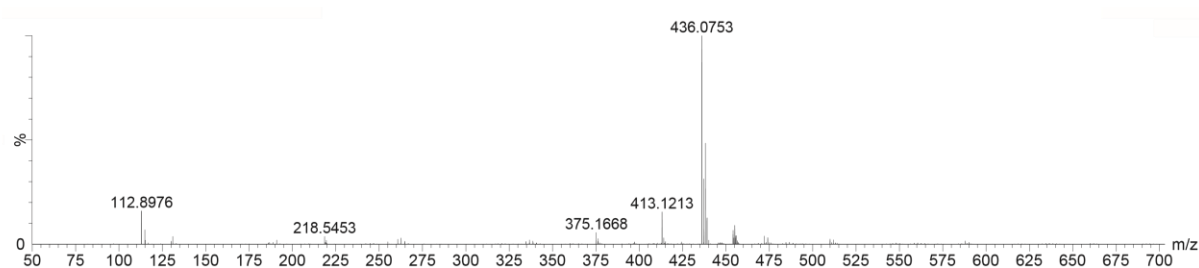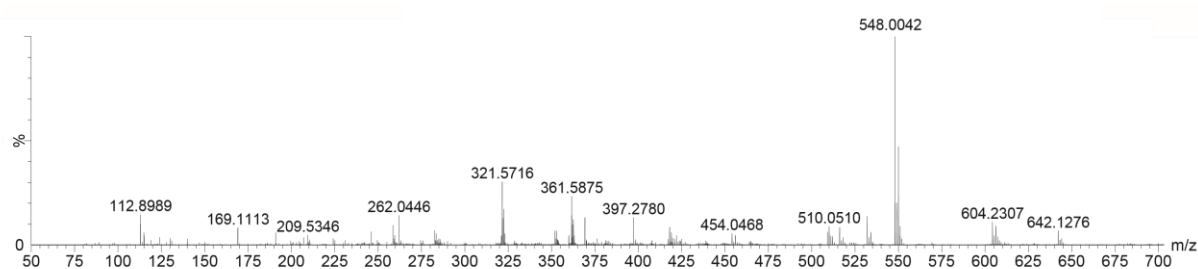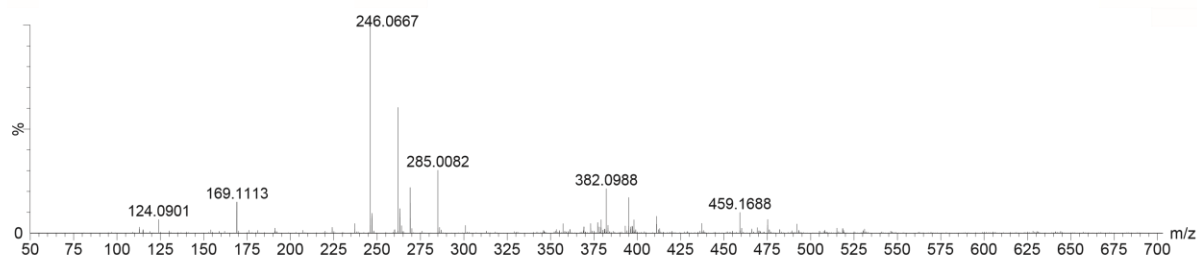B) After 18 h incubation

C) After 18 h incubation upon removal of Cu (+ EDTA)

Scheme A.1. HR ESI-MS spectrum (positive mode electrospray ionization) of **L3** + CuCl$_2$ at pH 3.0 at T$_0$ (A), after 18 h incubation (B) and after the addition of EDTA (C).

A) T$_0$

B) After 18 h incubation

C) After 18 h incubation upon removal of Cu (+ EDTA)

Scheme A.2. HR ESI-MS spectrum (positive mode electrospray ionization) of **L3** + CuCl$_2$ at pH 7.0 at T$_0$ (A), after 18 h incubation (B) and after the addition of EDTA (C).

viii) Analytical HPLC of **L3** + Cu(II) (and references) after 18 h at pH 3.0 and pH 7.0.
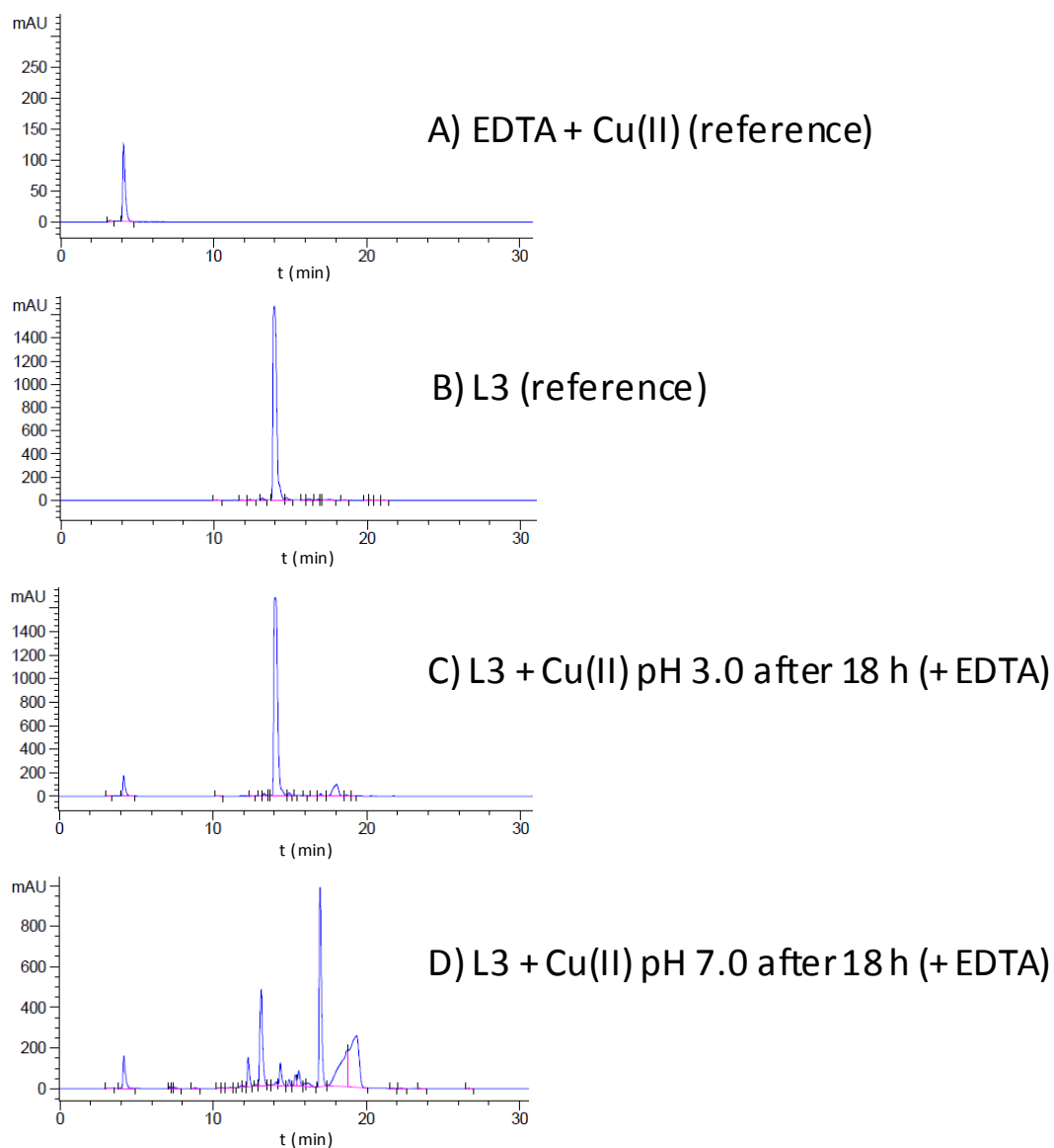
Figure A.14. Comparison of the chromatograms (analytical HPLC, monitoring at 280 nm) of the solutions containing **L3** + 1 equiv. of Cu(II) at pH 3.0 (c) and pH 7.0 (d) after 18 h *vs* **L3** (A) and EDTA + Cu (B) references. (Method: 0 to 40 % of solvent B in 15 min, flux: 1 mL/min).

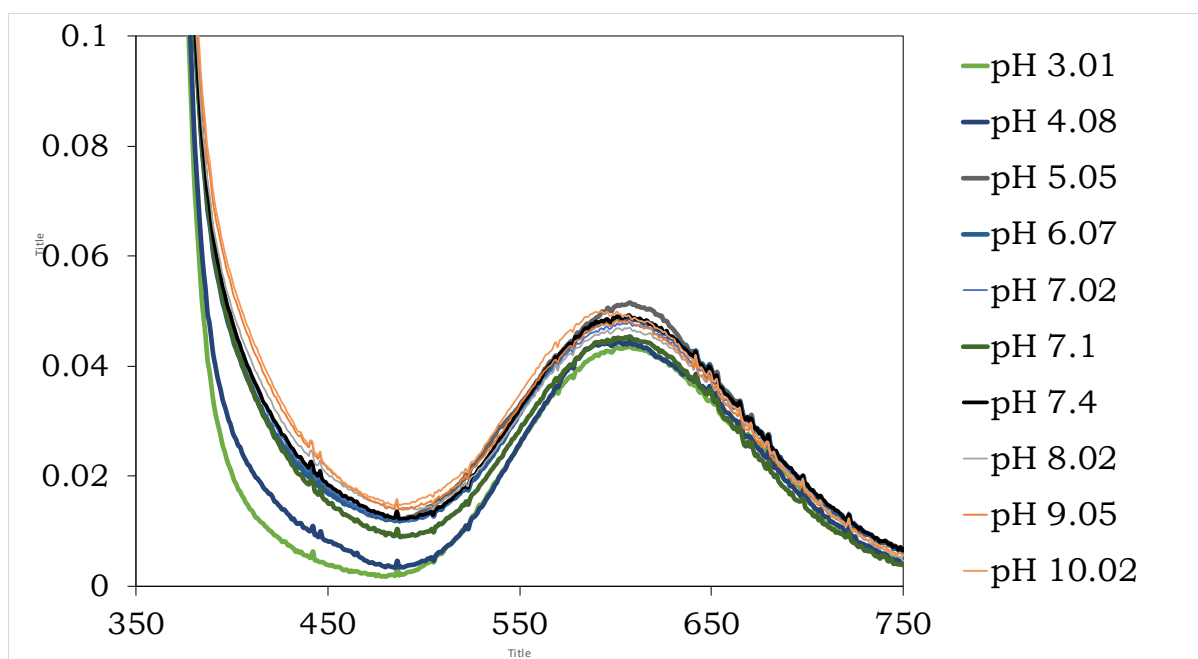b) Supplementary information relative to Chapter 4.[a]

    i) UV-vis spectra.

Figure A.15. UV-vis pH titration of **L1** (0.5 mM) in presence of 1 equiv. of Cu(II).
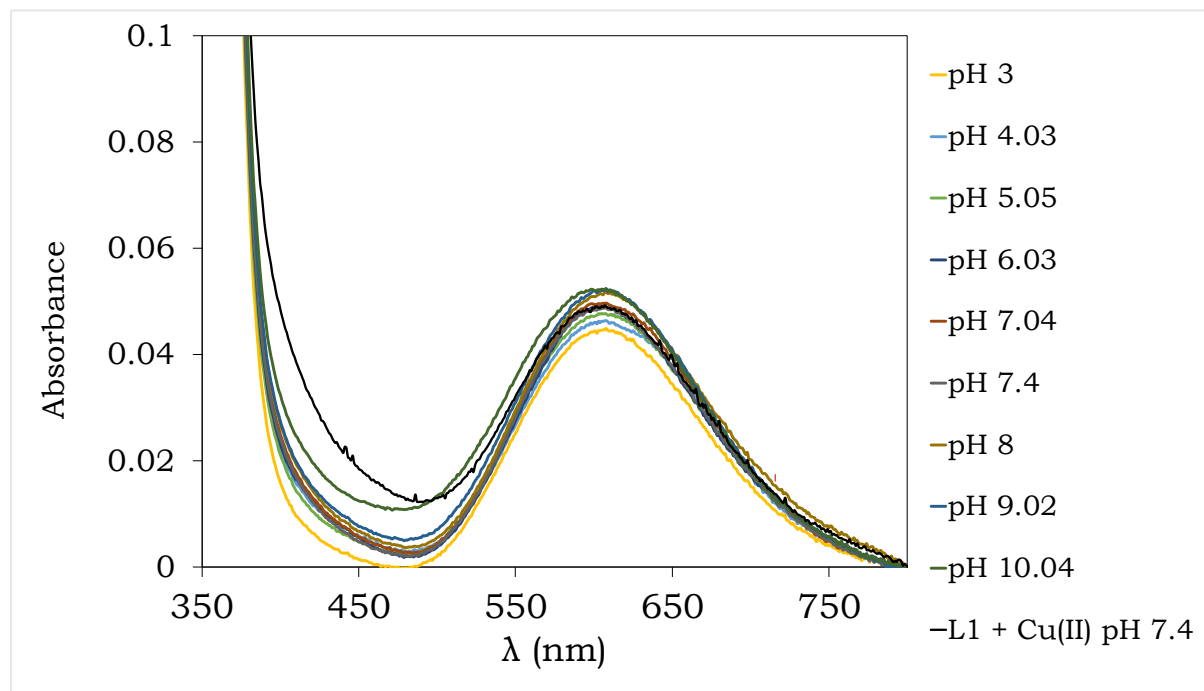

Figure A.16. UV-vis pH titration of **L1** (0.5 mM) in presence of 1 equiv. of Aβ16 and Cu(II). The black curve represents the UV-vis absorption spectra of the complex **Cu(II)L1** at 0.5 mM.

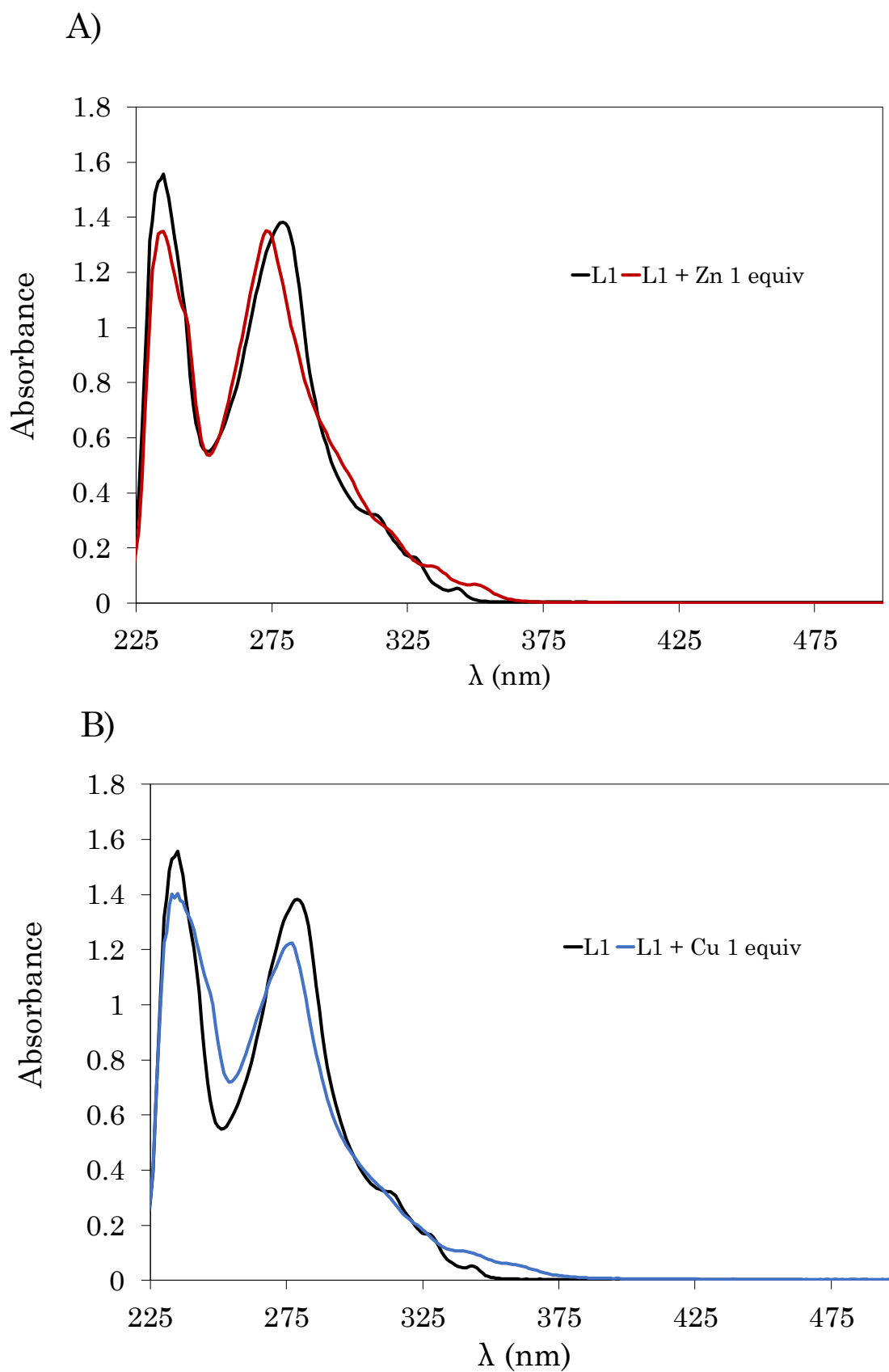[a] For this section, **HL1** and **H₂L2** are nominated simply as **L1** and **L2**.

A)

B)

Figure A.17. UV-vis spectra overlay of: Panel A): 50 μM **L1** and **Cu(II)L1** complex at pH 7.1. Panel B): 50 μM L1 and **Zn(II)L1** at pH 7.1.
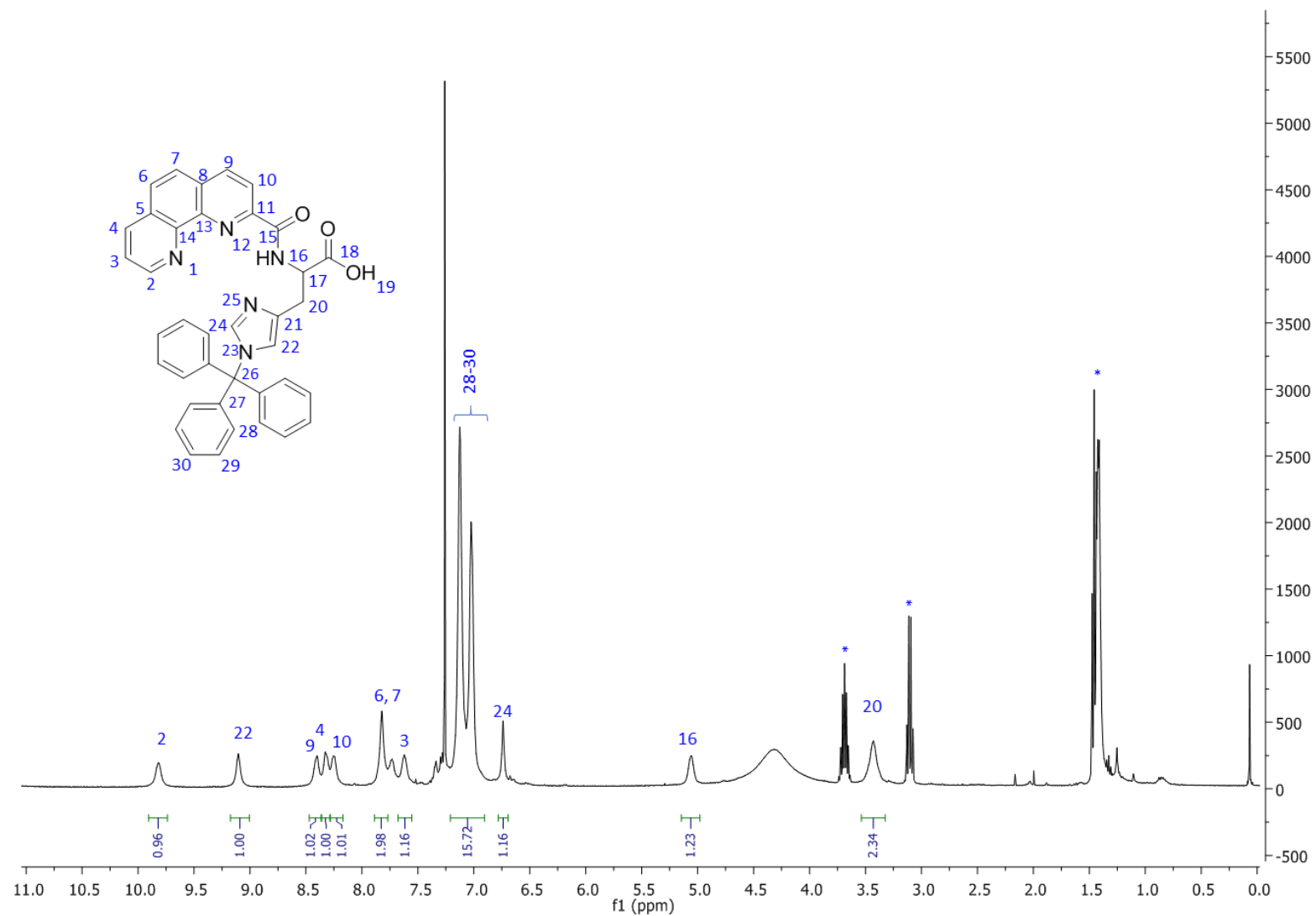
ii) ^{1}H, ^{13}C NMR and HR ESI-MS of L2(Trt).

Figure A.18. ^{1}H NMR spectrum (400 MHz, CDCl$_3$) of **L2(Trt)** (*DIEA signals).
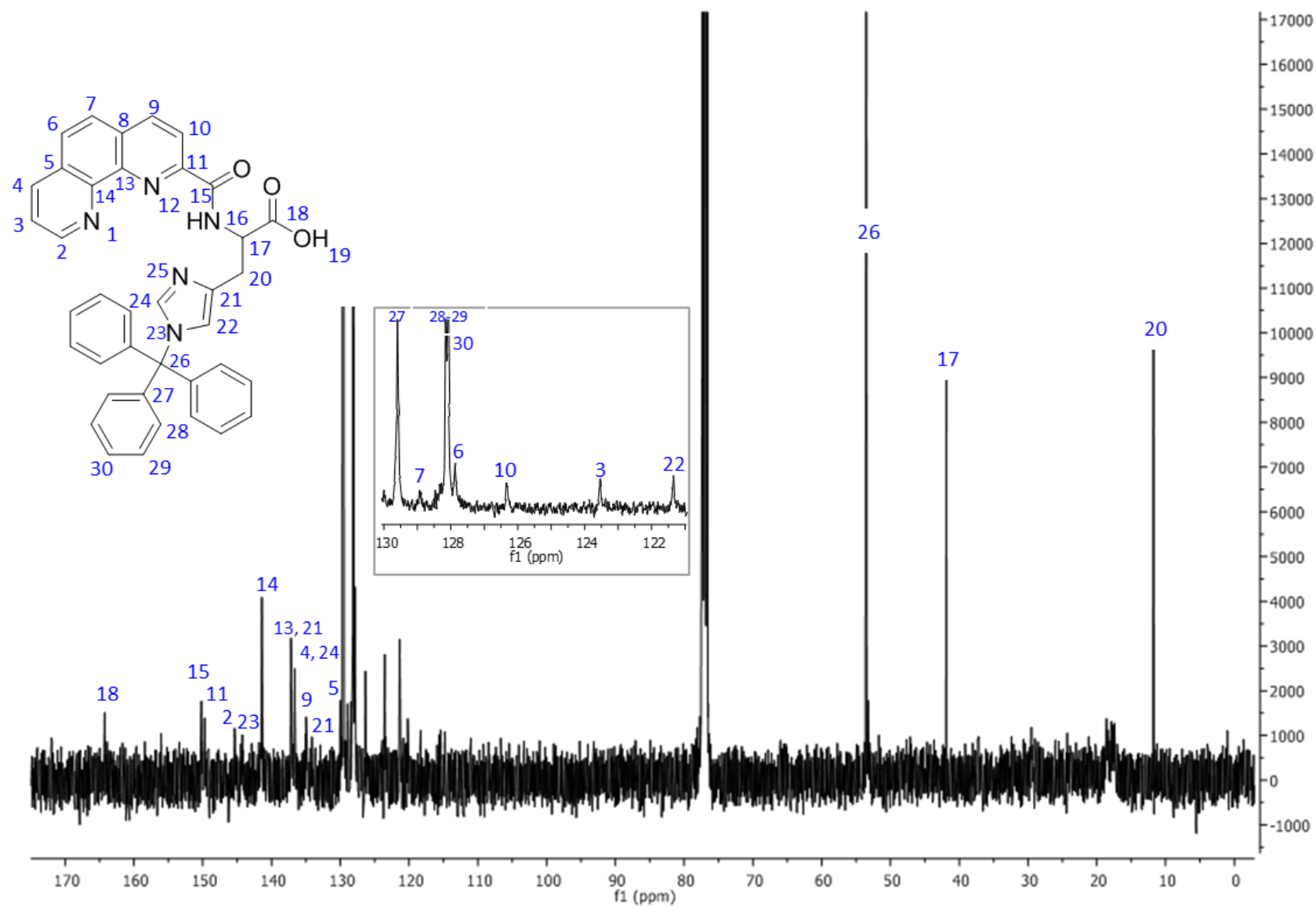
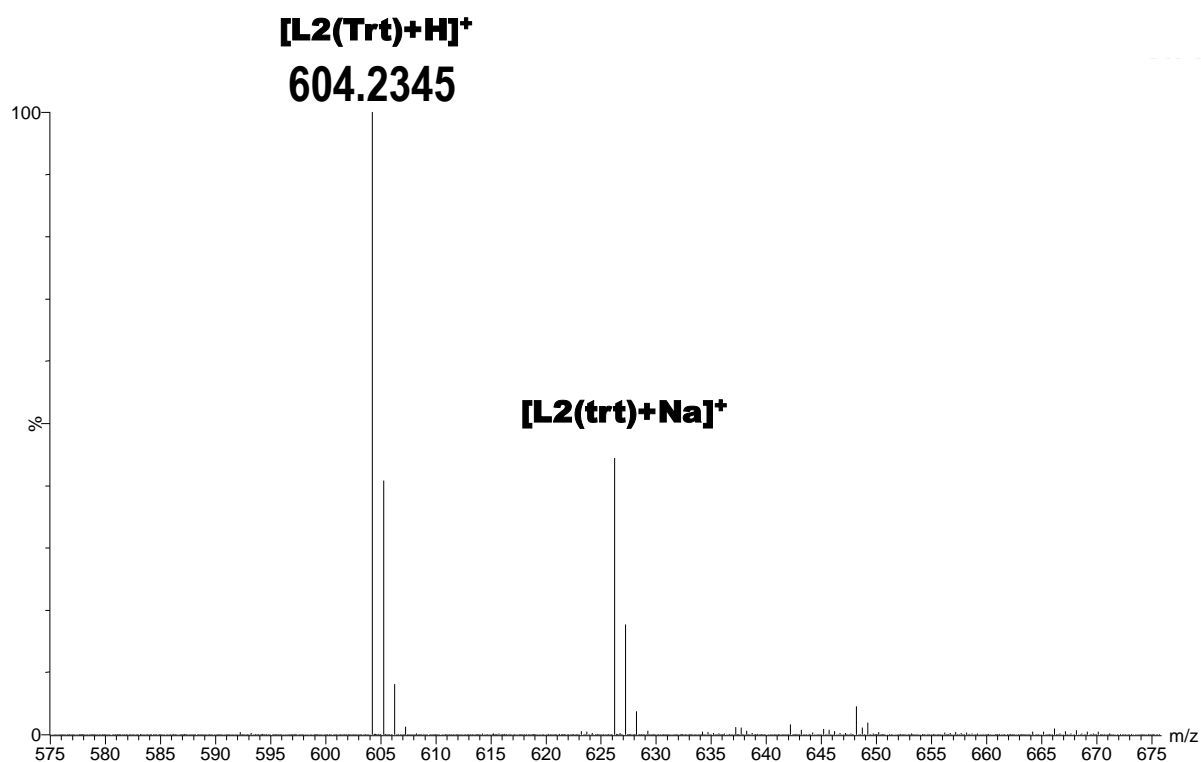**Figure A.19**. ^{13}C NMR spectrum (100 MHz, CDCl$_3$) of **L2(Trt)**.

Figure A.20. HR ESI-MS spectrum of **L2(Trt)** (positive mode electrospray ionization).

Table A.2. % of Cu(I) species present in solution at pH 7.1 at diferent **Cu(I):L1** ratios ([Cu(I)] = 10 μM). Values were calculated using the K_{app} reported in **Table 4.3** and the HYSS program.

Species	Ratio L1:Cu(I)	
	1.2:1	**2:1**
Cu(I)L1	77.9	67.8
Cu(I)(L1)₂	9.6	29.1
Cu(I)₂L1	1.0	0.2

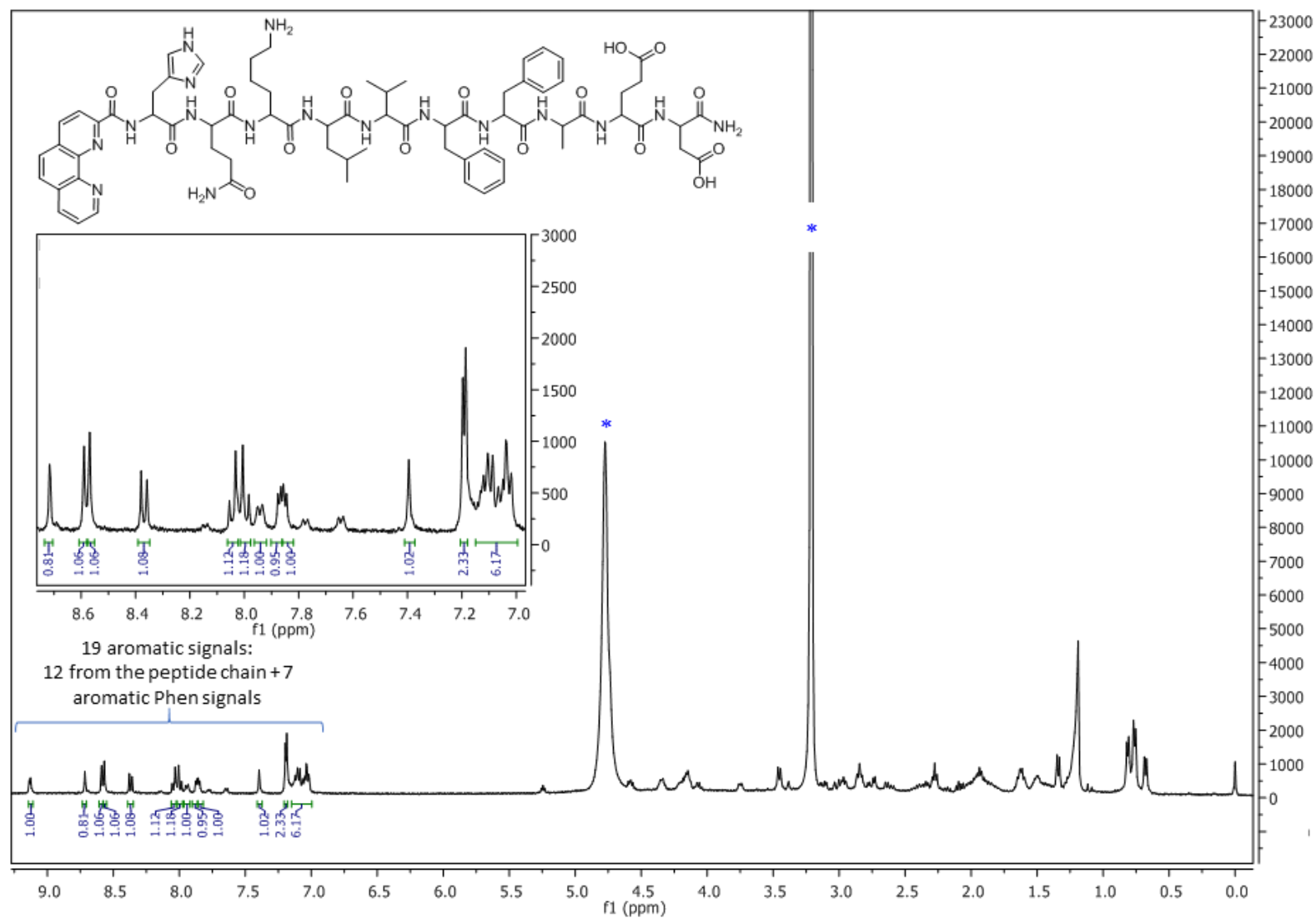iii) ¹H NMR, analytical HPLC chromatogram and HR ESI-MS of L1AB.

Figure A.21. ¹H NMR spectrum (400 MHz, MeOD) of **L1AB** (*MeOH signals).
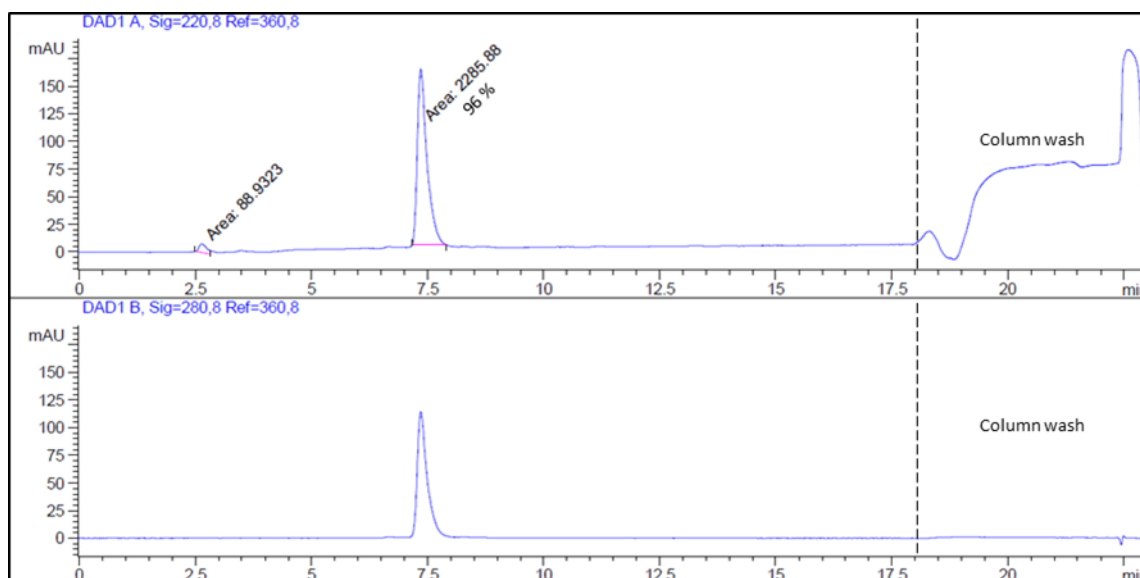
Figure A.22. Analytical reversed phase HPLC chromatogram of **L1AB** after purification. Upper 220 nm, bottom 280 nm. (Method: 30 to 40 % of solvent B in 15 min, flux: 1 mL/min, Column: Phenomenex Jupiter Proteo column).
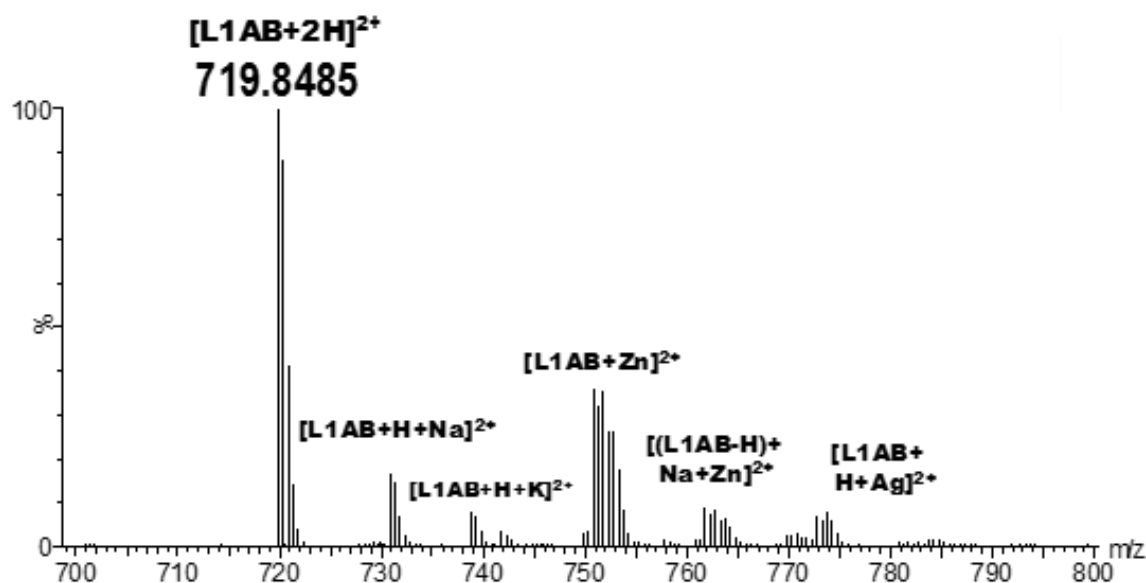

Figure A.23. HR ESI-MS spectrum of **L1AB** (positive mode electrospray ionization, the contamination of the metal ions Ag^+, Ka^+ and Na^+ comes from the ionization source).

66 …eternity asks you and every one of these millions of millions, just one thing: whether you have lived in despair or not…

If then, if you have lived in despair, then whatever else you won or lost, for you everything is lost, eternity does not acknowledge you, it never knew you, or, still more dreadful, it knows you as you are known, it manacles you to yourself in despair."

Søren Kierkegaard

Résumé

Le cuivre (Cu) est un métal endogène et redox actif présent dans plusieurs protéines et enzymes essentielles à la vie et joue un rôle important dans différents processus biologiques. Cependant, son activité redox rend également le Cu potentiellement toxique car il peut favoriser la formation d'espèces réactives de l'oxygène (ROS). Ce comportement à double tranchant intéresse les chercheurs depuis longtemps et son exploitation est cruciale pour développer des complexes de Cu aux propriétés biologiques, catalytiques, diagnostiques et thérapeutiques uniques. Dans ce travail de thèse, différents ligands pour la coordination du Cu ont été conçus et explorés dans deux contextes différents : le cancer et la maladie d'Alzheimer (MA). La première partie de cette thèse est consacrée à approfondir les connaissances relatives aux effets cytotoxiques produits par les complexes de Cu(II) (C1, C2) de deux ligands (L1, L2). Bien que les complexes aient montré de faibles interactions avec l'ADN, des études *in vitro* réalisées sur des lignées cellulaires normales (IMR-90, HUVEC) et cancéreuses (A2780, MCF-7) ont indiqué que C1 et C2 internalisaient les cellules et favorisaient la formation de ROS. Bien que les effets cytotoxiques n'aient pas été détectés dans les cellules MCF-7, ceux-ci étaient plus élevés dans A2780 que dans les cellules normales. L1 et L2 ont été modifiés afin d'améliorer la cytotoxicité. La deuxième partie de la thèse évalue les capacités de chélation du Cu de L1 et L2 en tant qu'agents thérapeutiques potentiels pour la MA. Les données ont montré que L1 peut arrêter efficacement la production de ROS catalysée par Cu(I)/Cu(II) en présence et en l'absence de peptide Aβ16 et de zinc. Les données suggèrent que le rapport L1 : Cu joue un rôle important dans l'efficacité de L1 pour arrêter la production de ROS. L1 a été modifié avec succès sans altérer ses propriétés de chélation du Cu pour fournir une perméabilité à la barrière hémato-encéphalique.

Abstract

Copper (Cu) is a versatile redox active endogenous metal that is present in many proteins and enzymes critical for life and plays important roles in different biological processes. However, its redox activity also renders Cu potentially toxic because it can promote the formation of reactive oxygen species (ROS). This double-edged sword behavior has interested researchers for long time and its harnessing is crucial to develop Cu complexes with unique biological, catalytic, diagnostic and therapeutic properties. In this Ph.D. thesis different ligands for Cu coordination have been designed and explored in two different contexts: cancer and Alzheimer disease (AD). The first part of this thesis is devoted to providing more insights into the cytotoxic effects produced by the Cu(II) complexes (C1, C2) of two ligands (L1, L2). The complexes showed weak interactions with DNA, but in vitro studies performed in normal (IMR-90, HUVEC) and cancer cell lines (A2780, MCF-7) indicated that C1 and C2 internalize into the cells and promote the production of ROS. While cytotoxic effects were not detected in MCF-7 cells, in line with very low internalization, they were higher in A2780 than in normal cells. L1 and L2 were further modified to improve cytotoxicity. The second part of the thesis evaluates the Cu chelating abilities of L1 and L2 as potential therapeutic agents for AD. Data showed that L1 can arrest efficiently the generation of ROS catalyzed by Cu(I)/Cu(II) in presence and absence of Aβ16 peptide and zinc. The presence of excess of L1 lessened this effect but it was counterbalanced by the co-presence of Zn. A mechanism that involves the redox reaction between Cu(II)L1 and Cu(I)(L1)$_2$ is proposed to explain this behavior. L1 was successfully modified, without altering its Cu chelating properties and ROS arresting capabilities, to attain blood-brain-barrier permeability.